University of Sussex

The matter and halo power spectra in redshift space using effective field theory

Lucía Fonseca de la Bella

Submitted for the degree of Doctor of Philosophy

University of Sussex

March 2018

Declaration

I hereby declare that this thesis has not been and will not be submitted in whole or in part to another University for the award of any other degree.

The original concepts for the projects in this thesis were proposed by Dr David Seery, and have been carried out by myself in collaboration with Dr David Seery, Dr Donough Regan, Dr Shaun Hotchkiss and Dr David Parkinson. Chapters 2 and 3 of this thesis are based on the following publications:

- Lucía Fonseca de la Bella, Donough Regan, Shaun Hotckiss and David Seery, "The matter power spectrum in redshift space using effective field theory", JCAP doi 10.1088/1475-7516 (2017). This paper was written by Dr David Seery. The calculations and numerical analysis were performed independently by myself, Dr David Seery and Dr Donough Regan. The suite of custom N-body simulations was provided by Dr Shaun Hotchkiss.

- Lucía Fonseca de la Bella, David Parkinson, Donough Regan and David Seery, "Impact of bias and redshift-space modelling for the halo power spectrum", arXiv 1805.12394. This paper was mainly written by myself and has been submited to JCAP. The analytical calculations were performed independently by myself, Dr David Seery and Dr Donough Regan. The numerical analysis was performed independently by myself and Dr David Seery. The **WizCOLA** simulations were provided by Dr David Parkinson.

Signature:

Lucía Fonseca de la Bella

UNIVERSITY OF SUSSEX

Lucía Fonseca de la Bella,

Doctor of Philosophy

The matter and halo power spectra in redshift space using effective field theory

Summary

The imminent era of large galaxy surveys (Dark Energy Survey, Euclid and Dark Energy Spectroscopic Instrument, among others) will soon drive a step change in our understanding of the standard cosmological model. Analytic control has traditionally come from the use of perturbation theory, but its reach is limited in scale and excludes a significant fraction of the modes visible to the surveys. *N*-body simulations could provide an alternative, but their computational time is extremely long. These pressures have produced research to enhance the standard perturbation theory and to appropriately model the *redshift-space distortion* power spectra that real surveys produce.

The analysis performed in this thesis is based on the *effective field theory of large-scale structure* (EFT). This yields encouraging results for the *dark matter power spectrum*, at the cost of adjustable counterterms that we estimate from a suite of custom *N*-body simulations performed using the **gevolution** numerical relativity code. We extend our analysis to *haloes* –concept used to refer to a more general notion: *tracers of large-scale structures*. There exists a statistical relation between the distribution of dark matter and haloes given by a set of bias parameters. As part of this analysis, we utilise the **WizCOLA** simulations –created to obtain covariance matrices for the WiggleZ survey.

In summary, we are in broad agreement with other methods employed in the literature. We include for the first time the full time dependence of the one-loop matter power spectrum using EFT and we are capable of probing smaller scales, $k \lesssim 0.74h/\mathrm{Mpc}$. Moreover, we achieve, for $k \lesssim 0.4h/\mathrm{Mpc}$, a $\sim 2\%$ level of accuracy in real space and $\sim 5\%$ for the monopole in redshift space. We also quantify how more complex modelling improves the fit for the halo multipoles. For future work, we find it relevant to use real observational data, e.g. WiggleZ dataset.

Acknowledgements

First and foremost, I would like to thank my supervisor Dr David Seery for his patient guidance, encouragement and advice provided throughout my time as his PhD student — especially for his forbearance in helping me debug my very entangled code. I am also thankful to Dr Donough Regan for his patience in double-checking my never-ending calculations. My gratitude, as could not be otherwise, to my collaborators Dr Hotchkiss and Dr Parkinson, and to all staff members at the University of Sussex for all those insightful conversations and discussions that have helped me broaden my understanding of our universe.

I must express my infinite gratitude to my family: to my parents for their immeasurable love and support — had it not been for you, I would not be the person I am, the scientist I have become; and neither in this life nor in all of eternity will I be able to say thank you enough —; to Cuchy, my twin, my copy, my clone, my everything: I feel the most fortunate person in this universe for having you in my life; and to my grandparents, for I know they have been watching over me and guiding my way throughout these years. And, of course, to my dearest Data, Zack and my late Fluffies. To my dearest friends: Mari & Raúl, Inma and Ortiz, for they looked after me and cared for me when I needed them the most. To Carmelitö (Yipee ki-yay!), my dearest brother, for all those moments watching "Die hard!" together. To Nick ♪♩♫, my partner, my significant other, my everlasting friend whose unconditional love and support mean everything to me, all my warmest gratitude for always believing in me and for bringing my smile back upon my face.

To my dearest friends at Sussex whose long-lasting friendship I will cherish for ever: to Zé & Ana for revealing me the truth on how Portugal is far greater than Spain and for all those wonderful times having *alot*[1] of fun; to Jesús & Kathryn for those more than interesting coffee breaks and for encouraging me never to give up; to Scotty, my dear friend, we have been through difficult times but you can be sure there will always be a special place for you in my heart; and Michaela & Mark, for making me discover the splendorous taste of marmite. To my colleagues Benoît, Ridwan, Alex, Daniel, Sam, Mateja, Tick,

[1] For the origin of this, the reader can refer to *The Alot*.

Wissarut, Peter, Pippa, Jess, Sunayana, and to all my students. Also, my very special gratitude to all my Marseillaise friends: Huong & Benny –my lovely nephew–, Luciana, Louis and Criss. A special mention to Estrella, UCOfísic@s, Dr Luis Garay, Dr Guillermo Mena, and to all the staff at the University of Aix-Marseille for marking my first steps into science. Likewise, my utmost cosmological farewells to our late Dr Stephen Hawking, *live long and prosper*[2]. And last but certainly not least, my warmest gratitude to every member of the gospel choir of Brighton, *BGG*, especially to our beloved First Lady Lou, our heart-warming choir director Daniel and our dearest music director Jason, for they have been my British family and supported me throughout the most difficult times. Keep shinning on!

[2] Vulcan salute

Contents

List of Tables

List of Figures

"Porque el conocimiento nos hará libres".

"The truth will set us free".

To my parents.

Chapter 1

Introduction

The main purpose of the following historical review [39] is to enlighten our perspective and insight into the centenarian research field of large-scale structure, and to contextualise the content of this thesis and the contribution of my research to the scientific community. In addition, the reader can find in this chapter all the basic tools for cosmology. A brief description of the main eras of the universe can be found in section 1.2, a derivation of the fundamental equations of cosmology in section 1.3, and the basic theoretical tools for linear clustering can be read in section 1.4, as well as higher-order clustering, section 1.5.

1.1 Historical background

The founding fathers of astronomy date back to the time of the Babylonians, Hypatia, Aristotle, Ptolomy and scholars from the Medieval Period; without neglecting the outstanding work of Copernicus, Tycho Brahe and Keppler. Most of them strongly believed in a finite universe surrounded by a vault of fixed stars. Not before the XVI century was this idea replaced by the notion of an infinity of stars uniformly distributed across the firmament (Digges 1576). This idea was supported by Newton himself in 1692. The next revolutionary idea, ascribed to Swedenborh [175], Lambert [113], Wright [194] and Kant [105], was the concept of *island universes* or *nebulae*, recognising the finite size of our galaxy and conjecturing the existence of similar celestial systems far out in space. The great observational supporter of such nebulae was Herschel in 1785 [85], whose main achievements where collected by Agnes Clerke in her book *" A popular History of Astronomy during the Nineteenth Century"*. A century later, Slipher was the first to measure the Doppler-shift shown in the nebulae spectra [171], known later on as the *redshift*.

The foundations for modern cosmology were laid by Einstein in 1917 when he published his research on *'Cosmological Considerations in the General Theory of Relativity'* [56] and established the first relativistic model of the universe: the Einstein's static universe. By then, our Galaxy was thought to compose the entirety of the universe, until the "Great Debate" of 1920. A revolutionary notion of the universe was presented, leading to a heated exchange between the astronomers Shapley and Curtis. The former argued that the so-called "spiral nebulae" were just nearby gas clouds and the universe was composed only of one big galaxy [169], whereas the latter defended that the universe was composed of many galaxies [45]. Two years later, the exact solutions to the Einstein equations describing an expanding, homogeneous and isotropic universe were independently discovered by Friedmann [68] (Soviet Union) and Lemaître [114] (Belgium), whereas the standard form of the metric was proposed by both Robertson [153] (United States) and Walker [87] (United Kingdom) a few years later.

In 1926, Edwin Hubble [88] concluded that "galaxies are uniformly distributed in space" after analysing 400 "extragalactic nebulae" of his catalogue. Conversely, in 1932 Shapley and Ames [168] noted "the general unevenness in distribution" of the galaxies projected onto the sky and the factor of two difference in the number of galaxies in the northern and southern hemisphere by analysing their catalogue of bright galaxies. A couple of years later, Hubble [90], using the same Shapley-Ames catalogue, came to a similar conclusion, observing that on angular scales $\lesssim 10^{\,o}$ there was an excess in the number counts of galaxies above what would be expected for a random Poisson distribution — similar to a Gaussian distribution on larger scales and clumpier on smaller scales.

Further galaxy catalogues and surveys flourished in the 60's, shedding light on the understanding of the structure of the universe. For instance, the Lick galaxy catalogue (Shane and Wirtanen 1967 [167]) with a million of galaxies recorded; and the Zwicky et al. catalogue in 1968 [198]. Almost a decade later, Peebles in 1975 [144] showed that the angular two-point correlation function roughly followed a power law distribution over very small angular scales (large scales) and the clustering amplitude was lower for fainter galaxy populations, likely due to larger projection effects along the line of sight — faint galaxies typically lie at larger distances, the projected clustering integrates over a wider volume of space and therefore dilutes the effect. These results spurred the first large-scale structure redshift surveys which obtained optical spectra of individual galaxies to measure

the redshift and spatial distribution of large galaxy samples. Along these lines, Seldner et al. in 1977 [163] (from the Lick catalogue) produced maps of the counts of galaxies in angular cells across the sky displaying with great detail the projected distribution of galaxies on the plane of the sky, exhibiting a foam-like pattern far from uniform. Subsequently, one year later Gregory and Thompson [79] mapped the 3D spatial distribution of 238 galaxies around and towards the Coma/Abell 1367 supercluster, naming regions with very few galaxies as "voids". Likewise, Joeveer et al. (1978) [97] described "filaments" as chains of galaxy clusters.

During the last quarter of the 20^{th} century, 3D surveys were developed. Authors of the KOS survey (1978) [108] studied the 3D spatial distribution of galaxies and got amused by their conclusion: "although not entirely unexpected, it is striking how strongly clustered our galaxies are in velocity space". The CfA survey (1982) [47] quantified clusters of galaxies in 3D and compared the so-called "complex topology" of the large-scale structure with that seen in N-body dark matter simulations. The second CfA survey 1985-1995 revealed the existence of the "Great Wall": supercluster of galaxies that extended over $170h^{-1}$Mpc. Further research, such as Gott et al. in 1986 [78], supported the idea of a sponge-like pattern to the distribution of galaxies.

The beginning of the new century brought the development of multi-object spectrographs, allowing rapid progress of redshift surveys and simultaneous observations of hundreds of galaxies. In addition, the construction of larger telescopes enabled deeper surveys of lower luminosity nearby galaxies and more luminous distant galaxies. The large redshift surveys at low redshift — the Two Degree Field Galaxy Redshift Survey ('2dfGRS' 2001) [41] and the Sloan Digital Sky Survey ('SDSS' 2000) [196] — undoubtedly revealed the foam-like pattern of the structure, and clearly observed voids of $\sim 10h^{-1}$Mpc, as well as filaments stretching greater than $\sim 10h^{-1}$Mpc surrounding voids and connecting galaxy groups and clusters.

Currently, the standard theoretical paradigm regarding large-scale structure (for example, reference [13]) claims that fluctuations in the energy density of the early universe — seen as temperature deviations in the cosmic microwave background — grow through gravitational instability into the structure seen today in the galaxy density field. Moreover, the features of large-scale structure are understood to depend on cosmological

parameters as well as on the physics of galaxy formation and evolution. Nowadays, cosmologists are first-hand witnesses of an imminent ground-breaking era of large galaxy surveys [149, 12, 101, 139, 48] — Dark Energy Survey ('DES'), Euclid and Dark Energy Spectroscopic Instrument, ('DESI'), Large Synoptic Survey Telescope, ('LSST'), Square Kilometer Array, ('SKA') and 4-metre Multi Object Spectroscopic Telescope) ('4MOST') — in which cutting-edge research is to be conducted. This era will soon drive a step change in our understanding of the standard cosmological model.

1.2 Chronology of the universe

Our universe has experienced different epochs throughout its fourteen billion years of existence. According to the big-bang theory (see [184] and references therein), the main cosmological eras[1] are the following:

Very early universe

All started with a big-bang[2] and, during the very first seconds, the universe was governed by quantum effects, this is the so-called *Planck epoch* ($< 10^{-43}s$, $> 10^{32}K$, $> 10^{19}$GeV). Right after, the *grand unification epoch* took place ($< 10^{-36}s$, $> 10^{16}$GeV) during which the three forces of the standard model were unified. Then, the universe expanded exponentially and its temperature dropped drastically during *cosmic inflation* ($< 10^{-32}s$, $10^{28} - 10^{22}K$). Finally, the cooling of the universe allowed the strong nuclear force and the electroweak force to emerge.

Radiation domination

During the *quark epoch* ($> 10^{-12}s$, $10^{12}K$), the forces of the standard model became independent and the universe was dominated by a quark-gluon plasma, displaying the highest energies currently observable by the *Large Hadron Collider* [1]. As temperature and energy dropped, quarks started binding into hadrons ($10^{-6} - 1s$, $10^{10}K$); the slight matter-antimatter asymmetry (*baryon asymmetry*) eliminated any trace of anti-hadrons; the interaction between neutrinos and baryonic matter stopped ($1s$, $1MeV$, $10^{10}K$), decoupling and travelling freely; and leptons and anti-leptons remained in thermal equilibrium, leading to a *photon epoch* ($10 - 10^{13}s$, $10^{9} - 10^{4}K$) dominated by a nuclei-electron-photon plasma. Finally, during the so-called *big-bang nucleosynthesis* ($10 - 10^{3}s$,

[1] The reader can refer to Table 1.1 and Figure 1.1 in section 1.3

[2] The Big-Bang Theory

$10MeV - 100keV$, $10^{11} - 10^9 K$), protons and neutrons started to form primordial atomic nuclei.

Matter domination

At the beginning of this era, matter density and radiation density were equal and the expansion of the universe was decelerating at a faster rate. The universe kept cooling down allowing the creation of hydrogen and helium atoms — this is the *recombination time*. Photons were no longer in thermal equilibrium, hence matter and light became free, releasing the first-seen light in the universe and producing the cosmic microwave background radiation. At the end of recombination, most of protons were bound up in neutral atoms. The time between recombination and the formation of first stars is referred to as the *dark ages*, during which the only additional radiation emitted was the 21 cm spin line of neutral hydrogen. It follows the *re-ionization epoch*, when the earliest modern Population III stars were formed — and, therefore, the currently observed most distant astronomical objects. Then galaxies coalesced into proto-clusters, clusters and super-clusters, forming the large structures of the universe.

Late-time acceleration

Finally, the universe was coldest as ever and a new accelerating expansion phase began, sourced by some exotic component (called dark energy) which behaves similarly to a cosmological constant. Coincidentally, this happened roughly by the time the Solar System and life appeared, establishing one of the major puzzles in cosmology: the *cosmological coincidence problem* [185].

1.3 Background cosmology

This section, is devoted to the revision of basic cosmology. The fundamental principles of physical cosmology are

1. **Statistical isotropy**: the universe looks the same regardless the direction.
2. **Statistical homogeneity**: on large scales the matter distribution is uniform.

These two statements combined lead to the *Copernican principle*, which states that we are not in a special location in the universe. Nevertheless, on smaller scales the universe bears structure — taking various forms, such as galaxies and clusters of galaxies —, breaking these principles.

1.3.1 Dynamics of the universe

Fundamental equations of cosmology are derived from general relativity, however analogous equations can be obtained from thermodynamics and Newtonian dynamics. Considering a homogeneous universe composed of a pressureless fluid and a spherically symmetric shell of radius a, the volume element of the shell can be written as $\mathrm{d}V = 4\pi a^2 da$, whereas the inner mass is constant, $M = (4\pi/3)a^3\rho$ — being ρ the matter density. *Gauss's theorem* establishes that the inner volume does not feel any gravity from the shell, unlike the shell itself which does feel the gravitational attraction from the particles in the inner shell. Therefore, each particle in the shell feels an acceleration given by *Newton's second law*

$$\ddot{a} = -\frac{GM}{a^2} \tag{1.1}$$

where G is *Newton's constant* of gravity. Integrating this equation over the whole volume, the *Friedmann equation* is obtained

$$H^2 \equiv \left(\frac{\dot{a}}{a}\right)^2 = \frac{8\pi G}{3}\rho - \frac{K}{a^2} \tag{1.2}$$

where K is an integration constant and $H = \dot{a}/a$. This equation above can be interpreted as the equation for the expansion rate of the universe — represented by the *Hubble parameter* H — with spatial curvature K, where a is the scale factor of the universe, driven by the energy budget of the universe, ρ — defined as the sum of the energy densities of every independent component. This equation derived in the Newtonian regime is also exact in general relativity, being obtained from the 00 component of the Einstein equations for a perfect fluid in an expanding homogeneous and isotropic universe described by the Friedman-Lemaître-Robertson-Walker metric [87].

The first law of thermodynamics determines the energy budget of a system. In this case, we consider an independent fluid component with energy

$$\mathrm{d}E = -p\mathrm{d}V + T\mathrm{d}S \tag{1.3}$$

where E is the total energy, p the pressure, V the volume, T the temperature and S the entropy of the system. Since the universe does not exchange any form of heat with any other system, the expansion of the universe is considered to be adiabatic, $T\mathrm{d}S = 0$, and, therefore, the whole energy budget is given by the work term in the equation above, $\mathrm{d}E = -p\mathrm{d}V$. In units of $c = 1$, the Einstein equation for the energy also reads as $E = \rho V$. Taking its differential form and considering the work contribution to the energy budget,

the following differential equation is satisfied

$$\mathrm{d}\rho + (p+\rho)\frac{\mathrm{d}V}{V} = 0, \tag{1.4}$$

leading to the *continuity equation*

$$\dot{\rho} = -3H(\rho + p), \tag{1.5}$$

which determines energy-momentum conservation. Equation (1.5) can also be obtained by using the covariant conservation of the stress-energy tensor for a perfect fluid, $\nabla_\mu T^{\mu 0} = 0$.

At this point, the equation of state parameter is commonly defined as the pressure-to-density ratio

$$\omega \equiv \frac{p}{\rho}\,. \tag{1.6}$$

Different fluid components are characterised by their particular equation of state parameter. For a fluid element with $\omega =$ constant, the solution to equation (1.5) reads

$$\rho_x = \rho_{0,x}\left(\frac{a_0}{a}\right)^{3(1+\omega_x)} \tag{1.7}$$

where $\rho_{0,x}$ is the mean density for that particular element x and a_0 is the scale factor of the universe today. It is also convenient to define the energy budget of a fluid element as $\Omega_x \equiv \rho_x/\rho_c$ being the critical density $\rho_c = 3H^2/8\pi G$ for a flat universe. hence the contribution of every fluid component to the total energy budget of a flat universe is $1 = \Sigma_x \Omega_x$. Moreover, from the Friedmann equation (1.2) for an expanding flat universe, the scale factor yields

$$a(t) = a_0\left(\frac{t}{t_0}\right)^{\frac{2}{3(1+\omega_x)}}, \tag{1.8}$$

and for $\omega_x \neq -1$, the Hubble parameter reads

$$H = \frac{2}{3(1+\omega_x)t}. \tag{1.9}$$

Examples for non-relativistic pressureless matter, relativistic particles such as radiation and dark energy or cosmological constant can be read on Table 1.1 and Figure 1.1.

As a direct consequence of the Friedmann equation (1.2) and the continuity equation (1.5), the Raychaudhury equation yields

$$\frac{\ddot{a}}{a} + \frac{4\pi G}{3}(\rho + 3p) = 0. \tag{1.10}$$

This describes the acceleration of the universe as a competition between pressure and energy density. Equation (1.10) can also be obtained from the ii component of the Einstein

COMPONENT	ω_x	ρ_x	$a(t)$	$H(t)$
Radiation	1/3	$\rho_{r,0}(a_0/a)^4$	$a_0(t/t_0)^{1/2}$	$1/2t$
Matter	0	$\rho_{m,0}(a_0/a)^3$	$a_0(t/t_0)^{2/3}$	$2/3t$
Dark energy or cosmological constant	-1	$\rho_{\Lambda,0}$	$a_0 e^{H_0(t-t_0)}$	$H_0 = \sqrt{8\pi G\rho_{\Lambda,0}/3}$

Table 1.1: Equation of state parameter, energy density, scale factor and Hubble parameter for the three main components of the universe.

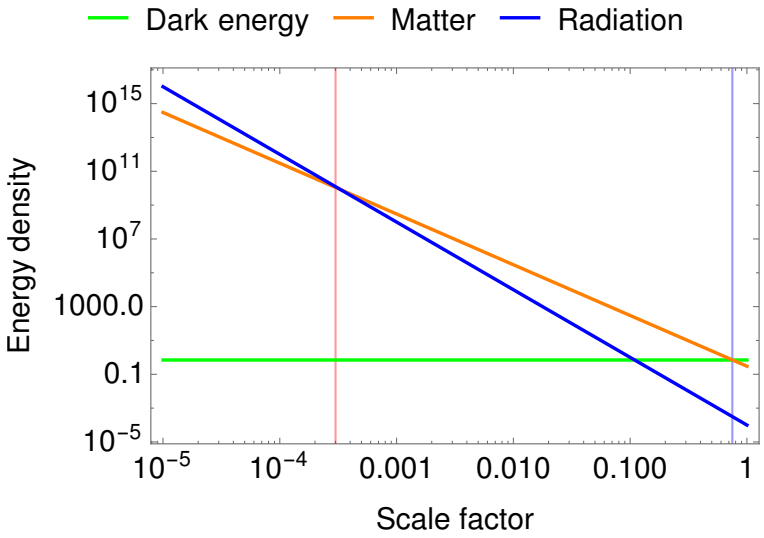

Figure 1.1: Representation of the different behaviours of the fluid energy density as a function of the scale factor. A scale factor of 1 represents the present time, whereas smaller values represent the past. The red line marks the radiation-matter equality, separating radiation domination and matter domination. Likewise, the blue line refers to the time when the late-time acceleration era begins.

equations combined with the Friedmann equation (1.2).

As mentioned, the dynamics of the main equations describing the evolution of our universe can be derived in the Newtonian regime. However, this approximation is only valid at sub-horizon scales[3], so general relativity is a more suitable framework. Along

[3]After inflation and before the late-time acceleration era, co-moving scales are entering the Hubble horizon, which is the scale associated to the Hubble parameter $k_{entry} = aH$, such that smaller scales enter earlier than larger scales. Scales inside the horizon, $k \gg aH$, are referred to as sub-horizon scales and can be described within the Newtonian limit. Conversely, super-horizon scales, $k \ll aH$, or scales outside the horizon need to be described by general relativity.

these lines, the Friedman-Lemaître-Robertson-Walker metric [87] is defined as the metric describing an expanding, homogeneous and isotropic universe with spatial curvature K — describing $K < 0$ a closed universe, $K = 0$ a spatially flat universe, and $K > 0$ an open universe. In spherical coordinates, this is given by

$$\mathrm{d}s^2 = -\mathrm{d}t^2 + a(t)^2 \left[\frac{\mathrm{d}r^2}{1 - Kr^2} + r^2 \left(\mathrm{d}\theta^2 + \sin^2\theta \mathrm{d}\varphi^2 \right) \right]. \tag{1.11}$$

This equation (1.11) is solution to the Einstein equations [190]

$$G_{\mu\nu} = 16\pi G T_{\mu\nu} \tag{1.12}$$

where $G_{\mu\nu}$ is the so-called Einstein tensor and $T_{\mu\nu}$, the stress-energy tensor. For the concrete case of a perfect fluid

$$T_{\mu\nu} = (\rho + p) u_\mu u^\nu + p \delta^\nu_\mu, \tag{1.13}$$

u_μ being the four-velocity of the fluid and δ^ν_μ a Kronecker delta.

1.3.2 The Hubble flow

Distances

Fundamental observers are defined as those whose coordinates do not change with the expansion of the universe, defining a co-moving coordinate system (refer to the grid in Figure 1.2). The distance between each cell of the grid defines the so-called *co-moving distance*, χ. The Friedman-Lemaître-Robertson-Walker (1.11) for a spatially flat universe in terms of co-moving coordinates reads

$$\mathrm{d}s^2 = \mathrm{d}t^2 - a(t)^2 [\mathrm{d}\chi^2 + \chi^2 \mathrm{d}\Omega^2]. \tag{1.14}$$

Therefore, since photons following a radial trajectory satisfy the geodesic equation $\mathrm{d}s^2 = 0$, the co-moving distance covered by photons between t_0 and t is given by

$$\chi = \int_{t_0}^{t} \frac{\mathrm{d}t'}{a(t')}, \tag{1.15}$$

which is time independent and, consequently, relates to the physical distance through the scale factor, $a(t)$:

$$d(t) = a(t)\chi. \tag{1.16}$$

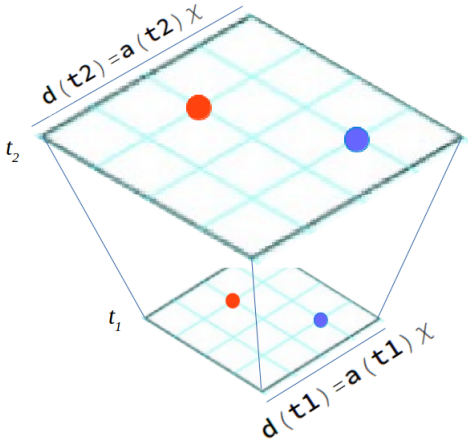

Figure 1.2: Representation of co-moving and real distances in cosmology at different cosmic times.

Cosmological redshift

In observing the universe, the information extracted from a particular object under study sheds light not only on its spectral intensity and chemical composition; but also tells us about motion, distance and time. In order to perform observations, astronomers employ type Ia supernovae since the light produced from these explosions can outshine a whole galaxy for several weeks or months, releasing the same amount of light and intensity. This type of supernovae is also referred to as *standard candles*. The emission lines, in comparison with the emitted for the same object in a rest frame, appear to be shifted either to the left or to the right (blue or red part) of the spectrum, implying that the source is moving either towards the observer or away from the observer. This effect is defined as the *cosmological redshift*

$$z + 1 = \frac{\lambda_{obs}}{\lambda_{em}}, \tag{1.17}$$

where λ_{obs} and λ_{em} are the observed and emitted wavelength of the light ray, respectively.

By considering the emission of photons from one object along the line of sight, the emitted radiation follows the geodesic equation $\mathrm{d}^2 s = 0$ and, by using the metric (1.14),

$$\mathrm{d}t = a(t)\mathrm{d}\chi. \tag{1.18}$$

Integrating over the total travelling time from $\chi = 0$ to $\chi = \chi_0$

$$\int_{t_{em}}^{t_{obs}} \frac{\mathrm{d}t}{a(t)} = \int_0^{\chi_0} \mathrm{d}\chi. \tag{1.19}$$

Regarding another set of photons emitted an infinitesimal time after the first one, i.e. $t_{em} + \mathrm{d}t_{em}$, the above relation would look like

$$\int_{t_{em}+\mathrm{d}t_{em}}^{t_{obs}+\mathrm{d}t_{obs}} \frac{\mathrm{d}t}{a(t)} = \int_0^{\chi_0} \mathrm{d}\chi. \tag{1.20}$$

Since the co-moving coordinate of the object is the same throughout this event, equations (1.19) and (1.20) are equal. Therefore

$$\int_{t_{em}}^{t_{obs}} \frac{\mathrm{d}t}{a(t)} = \int_{t_{em}+\mathrm{d}t_{em}}^{t_{obs}+\mathrm{d}t_{obs}} \frac{\mathrm{d}t}{a(t)}, \tag{1.21}$$

leading to

$$\frac{\mathrm{d}t_{obs}}{\mathrm{d}t_{em}} = \frac{a(t_{obs})}{a(t_{em})} \equiv \frac{\lambda_{obs}}{\lambda_{em}}. \tag{1.22}$$

Moreover, from the definition of cosmological redshift (1.17),

$$\frac{a(t_{em})}{a(t_{obs})} = \frac{1}{1+z}, \tag{1.23}$$

and setting at the present time, $z = 0$, $a(t_0) = 1$, the relation between redshift and scale factor yields

$$1 + z = \frac{1}{a(t)}. \tag{1.24}$$

The Hubble's law

In general, there exists an overall red-shifting of galaxy spectra, meaning that our universe is expanding at a rate given by the Hubble parameter, $H = \dot{a}/a$. The *recession velocity* at which an object moves due to the Hubble flow can be derived from the time derivative of the physical distance (1.16)

$$v_r \equiv \dot{d}(t) = \frac{\dot{a}(t)}{a(t)} d(t) = H(t) d(t). \tag{1.25}$$

The equation above is called the *Hubble law*, and establishes the relation between redshift and distances. In an isotropic and homogeneous universe, from equations (1.24) and (1.25), the redshift of a photon emitted at $t_{em} = t_{obs} - \mathrm{d}t$, but detected at the present time, $t_{obs} = t_0$, reads

$$1 + z \sim \frac{a_0}{a_0 - \dot{a}(t_0)\mathrm{d}t} \sim 1 + H_0 \mathrm{d}t, \tag{1.26}$$

therefore,

$$z \sim \frac{H_0}{c} c\mathrm{d}t = \frac{H_0}{c} d(t_0). \tag{1.27}$$

This fundamental prediction was empirically confirmed by Hubble in 1929 [89].

Additionally, local mass concentrations perturb the isotropic picture, causing perturbations in the Hubble flow. That is, the recession velocity (1.25) will have an extra contribution, the so-called *peculiar velocity*, coming from the time derivative of the co-moving distance and describing the random motion of an object with respect to the local Hubble flow. That is,

$$v_r = H(t)d(t) + v_p. \tag{1.28}$$

1.4 Linear Clustering measurements

The observed *structure* in the universe [121] is associated with the inhomogeneous distribution of matter which evolved from initial scalar perturbations of the gravitational potential of the Hubble flow. In over-dense regions, the expansion of gravitating matter slows down, comes to rest and is superseded by a collapse. The initial stage of collapse proceeds mainly along one of three directions and leads to self-crossings and the formation of one-dimensional oppositely directed flow. Later on, the regions of self-confined matter relax and gradually acquire a spherical shape and form multi-stream systems trapped by gravity, *matter haloes*.

Nowadays, well-developed non-linear structures are present in our universe, showing a wide diversity of shapes: from galaxy haloes, groups and clusters of galaxies (scales $\sim$ 10Mpc), to super-clusters and voids (scales $\sim$ 100Mpc). Furthermore, sheet-like formations called *walls* can be seen, exhibiting a collection of elongated *filaments* which may intersect and form *nodes* –where rich galaxy clusters can be found.

1.4.1 Fluid equations

By assuming a spatially flat universe and working in the conformal-Newtonian gauge[4], the Einstein equations lead to the fluid equations which describe the density, ρ_m, and velocity

[4]The conformal-Newtonian gauge, also known as the longitudinal gauge or the null-shear gauge, is defined by

$$\mathrm{d}s^2 = -(1+2\Phi)\mathrm{d}t^2 + a^2(1+2\Psi)(\mathrm{d}x^2 + \mathrm{d}y^2 + \mathrm{d}z^2),$$

where $\Phi(t,\mathbf{x})$ and $\Psi(t,\mathbf{x})$ are the Bardeen potentials —the former usually called the Newtonian potential—. In addition, a perfect fluid verifies $\Phi = \Psi$.

of dark matter, $\mathbf{u}$, bound to the Newtonian gravitational potential $\tilde{\Phi}$. These read

$$\dot{\rho}_m + \nabla \cdot (\rho_m \mathbf{u}) = 0, \tag{1.29a}$$

$$\dot{\mathbf{u}} + (\mathbf{u} \cdot \nabla)\mathbf{u} + \frac{1}{\rho_m}\nabla p + \nabla\tilde{\Phi} = 0, \tag{1.29b}$$

$$\nabla^2\tilde{\Phi} = 4\pi G\rho_m. \tag{1.29c}$$

Considering small perturbations,

$$\rho_m(t, \mathbf{r}) = \rho_0 + \delta\rho(t, \mathbf{r}), \tag{1.30a}$$

$$p_m(t, \mathbf{r}) = p_0 + \delta p(t, \mathbf{r}), \tag{1.30b}$$

$$\mathbf{u}(t, \mathbf{r}) = H(t)\mathbf{r} + \mathbf{v}(t, \mathbf{r}), \tag{1.30c}$$

$$\tilde{\Phi}(t, \mathbf{r}) = \tilde{\Phi}_0(\mathbf{r}) + \Phi(t, \mathbf{r}). \tag{1.30d}$$

Regarding matter distribution, we denote ρ_0 as the background matter density — expected density of matter in a uniform and homogeneous universe governed by a Poisson distribution. The excess of matter is given by $\delta\rho \equiv \rho - \rho_0$. Thus, a dimensionless quantity can be defined: the *density contrast* — measure of the deviation or fluctuation of the matter density in a region with respect to the mean density —

$$\delta = \frac{\delta\rho}{\rho_0}. \tag{1.31}$$

The rest of the background quantities in equation (1.30) are p_0, $H(t)\mathbf{r}$ and $\tilde{\Phi}_0(\mathbf{r})$; whereas the rest of the small inhomogeneous perturbations are $\delta p(t, \mathbf{r})$, $\mathbf{v}(t, \mathbf{r})$ and $\Phi(t, \mathbf{r})$. Finally, the perturbed fluid equations can be written

$$\dot{\delta} + 3H\delta + H\mathbf{r} \cdot \nabla\delta + \nabla \cdot \mathbf{v} = 0, \tag{1.32a}$$

$$\dot{\mathbf{v}} + H\mathbf{v} + H\mathbf{r} \cdot \nabla\mathbf{v} + \frac{1}{\rho_0}\nabla\delta p + \nabla\Phi = 0, \tag{1.32b}$$

$$\nabla^2\Phi = 4\pi G\rho_0\delta. \tag{1.32c}$$

The first equation (1.32a) is the continuity equation for the density contrast, equation (1.32b) is the so-called Navier-Stokes equation for the velocity inhomogeneity, and equation (1.32c) is the Poisson equation.

In general, for adiabatic perturbations of a non-relativistic single-component fluid, the equations of motion (1.32) for the density perturbation yield

$$\ddot{\delta}_k + 2H\dot{\delta}_k + \left[\left(\frac{c_s}{a}\right)^2 k^2 - 4\pi G\rho_0\right]\delta_k = 0 \tag{1.33}$$

where dot refers to time derivatives, H is the Hubble parameter, a is the scale factor of the universe, G is the gravitational constant and c_s[5] is the speed of sound parameter. This equation is the so-called *Jeans' equation* [93] for an expanding fluid, and its solution is fully determined by the sign of the factor in brackets. Namely, if the pressure term is dominant against the compression term, the solution is oscillatory, otherwise gravity dominates and perturbations grow. The characteristic scale which separates these behaviours is the Jeans' scale:

$$k_J = \frac{a}{c_s}\sqrt{4\pi G\rho_0}. \tag{1.34}$$

For scales significantly smaller than the Jeans' length, the oscillations are damped, therefore their amplitude decreases with time and there is no growth of structure for sub-Jeans scales (virialised structures). On the other hand, for scales larger than the Jeans' length (but still sub-horizon, $aH \ll k \ll k_J$), the general solution to the equation has two contributions, a growing mode and a decaying mode. After some time, the decaying mode dies out and the perturbations grow.

In particular, dark matter has no pressure and, therefore, its perturbation do not present an oscillatory behaviour but a growing trend which, during matter domination, is directly proportional to the scale factor of the universe. From (1.33) and table 1.1

$$\ddot{\delta}_{\mathbf{k}} + \frac{4}{3t}\dot{\delta}_{\mathbf{k}} - \frac{2}{3t^2}\delta_{\mathbf{k}} = 0, \tag{1.35}$$

whose general solution is

$$\delta(\mathbf{k}, t) = A_1 t^{2/3} + A_2/t. \tag{1.36}$$

The first term is the growing mode and the second one is the decaying mode. Therefore, after some time, the matter density perturbations during matter domination grow proportionally to the scale factor, $\delta(\mathbf{k}, t) \propto t^{2/3} \propto a$.

1.4.2 The two-point correlation function

The two-point correlation function, $\xi(r)$, is a quantitative measure of large-scale structure which traces the amplitude of galaxy clustering as a function of distance, r, which is generally a co-moving length with units of h^{-1}Mpc. This quantity is defined as the measure of the excess probability, $\mathrm{d}\mathbb{P}$, above what is expected for an unclustered random Poisson distribution, of finding a galaxy in a volume element $\mathrm{d}V$ at a distance r from the nearest

[5] This is defined by $c_s^2 = \left(\frac{\partial p}{\partial \rho}\right)_s$, at constant entropy.

galaxy

$$\mathrm{d}\mathbb{P} = n[1 + \xi(r)]\mathrm{d}V, \tag{1.37}$$

where n is the mean number galaxy density [146]. On scales smaller than $10h^{-1}$Mpc, the two-point correlation function seems to be well-described by a power law

$$\xi(r) \sim \left(\frac{r}{r_0}\right)^{-\alpha}, \tag{1.38}$$

with $\alpha > 0$, being r_0 the correlation length. For $r < r_0$, the probability of finding a galaxy at a distance r is significantly larger than for a random Poisson distribution, causing an over-dense region. Therefore, in terms of the density contrast, the correlation between the density at one location of space and the density at a distance r is given by the two-point correlation function

$$\xi(r) = \langle \delta(\mathbf{x})\delta(\mathbf{x} + \mathbf{r})\rangle. \tag{1.39}$$

This quantity relates to the *power spectrum* via the Fourier transform

$$\xi(r) = \int \frac{\mathrm{d}^3k}{(2\pi)^3} P(k)\mathrm{e}^{-\mathbf{i}\mathbf{k}\cdot\mathbf{r}}, \tag{1.40}$$

which in terms of the density contrast reads

$$\langle \delta(\mathbf{k}_1)\delta(\mathbf{k}_2)\rangle = (2\pi)^3\delta_D(\mathbf{k}_1 + \mathbf{k}_2)P(k). \tag{1.41}$$

Additionally, before recombination, baryon matter and photons coupled together to form a two-component fluid with a high sound speed —since photons provided most of the density and pressure. According to the equation above (1.33), the pressure term dominated and the baryon-photon fluid propagated as an expanding spherical sound wave. After recombination, photons were set free and travelled at the speed of light — rewarding us with the first light of the universe and the cosmic microwave background [122] —, whereas baryons were trapped within dark matter potential wells. This phenomenon is known as "baryon acoustic oscillations". Until this occurred, the sound wave covered a determined distance, $\sim 5 \cdot 10^8$ light years, producing an enhanced number of galaxy pairs separated by this scale [58] (refer to figure 1.3). Such increase of matter density interestingly reveals a well-defined single peak in the matter correlation function given by equation (1.39) [124]. The characteristic scale of baryon acoustic oscillations remains constant throughout the evolution of the universe so that it is used as a *standard ruler* in cosmology.

1.4.3 Linear matter power spectrum

In the linear regime —on large scales where perturbations are very small—, the matter power spectrum is fully determined by the transferred primordial power spectrum. After

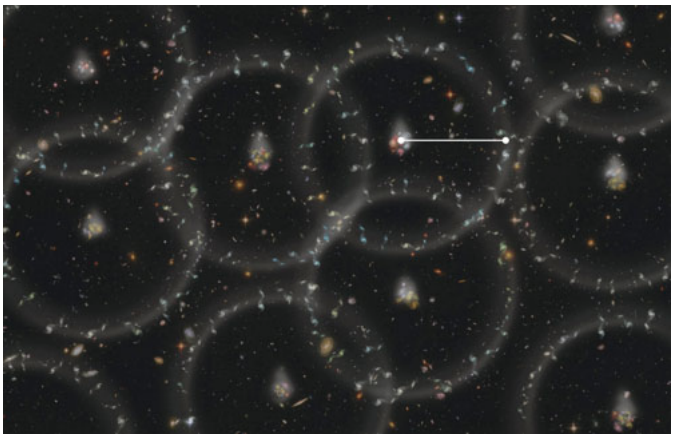

Figure 1.3: Illustration of the spheres of baryon acoustic oscillations around the initial dark matter clumps by the BOSS project.

inflation, fluctuations of the primordial gravitational potential, Φ, are considered the seed of structure formation. The initial power spectrum, according to equation (1.41), is now defined by

$$\langle \Phi(\mathbf{k}_1)\Phi(\mathbf{k}_2)\rangle \equiv (2\pi)^3 \delta_D(\mathbf{k}_1+\mathbf{k}_2) P_*(k), \tag{1.42}$$

and takes the form of nearly a power law

$$P_*(k) \sim A^2 \Big(\frac{k}{k_0}\Big)^{n_s-1} \tag{1.43}$$

where A is the amplitude of the initial fluctuations at the pivot scale k_0, and n_s is the spectral index. When $n_s - 1 = 0$, the power spectrum is scale invariant, otherwise the power spectrum is tilted. For $n_s - 1 < 0$, the power spectrum is called red and there are more structures at large scales. Conversely, the power spectrum is called blue if $n_s - 1 > 0$ and there are more structures at small scales.

After inflation and after reheating, all the information regarding structure evolution is stored in the so-called *transfer function*, $T(k,t)$, for large scales, $k \ll k_{eq}$[6], which entered the horizon during matter domination. Therefore, there exists a linear relation between the perturbations of the primordial gravitational potential, $\delta^* \equiv \Delta\Phi/\Phi_0$, and the matter density contrast:

$$\delta(\mathbf{k},t) = T(k,t)\delta^*(\mathbf{k}). \tag{1.44}$$

Hence the power spectrum on large scales yields

$$P(k,t) = T(k,t)^2 P_*(k). \tag{1.45}$$

[6]The sub-index *"eq"* refers to the equivalent time when matter density equalled radiation density $k_{eq} = aH(t_{eq}) \sim \Omega_m h^2/14$.

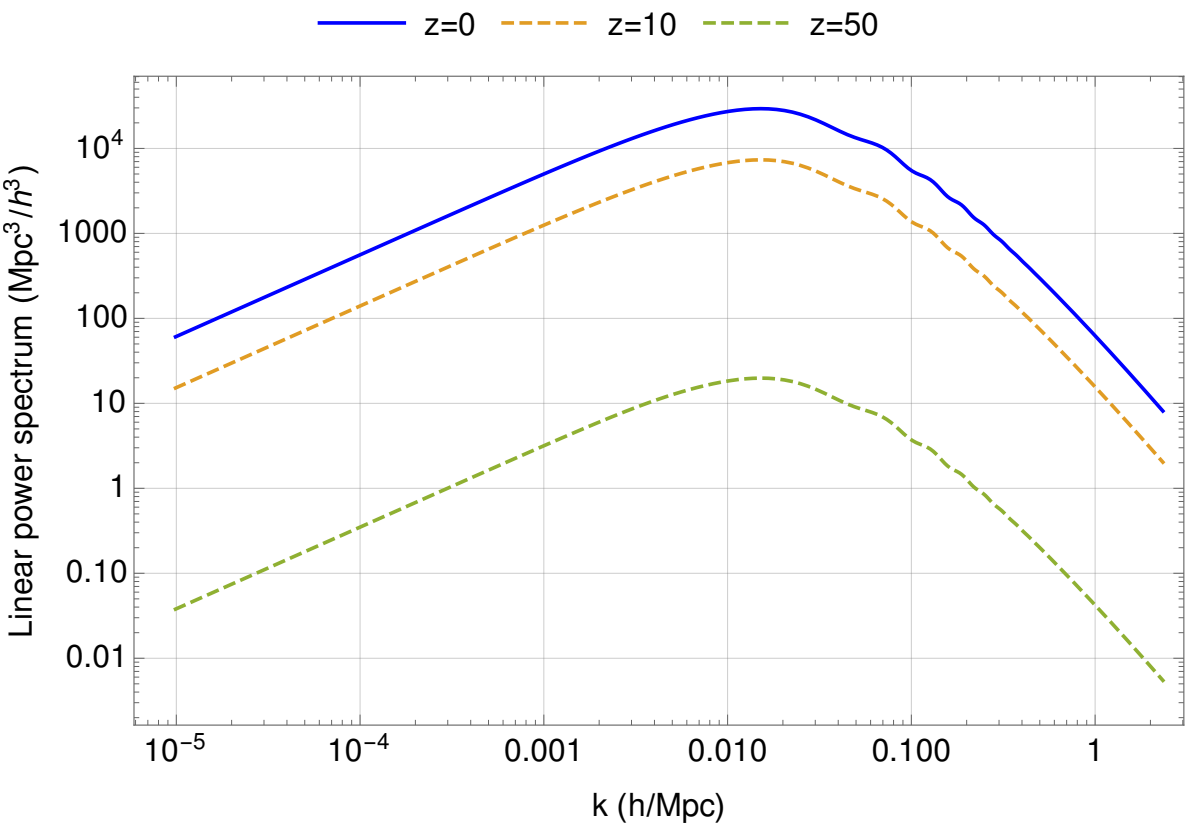

Figure 1.4: Linear matter power spectra for different epochs, namely redshift 0, 10 and 50. Today, there exists more growth of structure in the universe, hence the amplitude of the power spectrum is larger. The noticeable wiggles on scales $\sim 0.1h$/Mpc represent the baryon acoustic oscillations, and the turnabout scale corresponds to that of equivalent time, $k_{eq} \sim 0.01h$/Mpc.

Figure 1.4 clearly pictures the transmission of structure information from the past to the present time, showing how the amplitude of the matter power spectrum becomes larger as more structures are seen in the universe today. On large scales, the matter power spectrum rises quite steeply, turning at $k \sim k_{eq}$. On smaller scales, the growth is much slower due to the fact that the growth of density perturbations was inhibitied while the perturbations were inside the horizon during the era of radiation domination. Finally, non-linearities begin to dominate and the linear matter power spectrum becomes inexorably unable to describe the perturbation features. Consequently, higher-order corrections to linear theory ought to be sought.

1.5 Higher-order clustering measurements

1.5.1 Eulerian standard perturbation theory

On small scales, matter perturbations are no longer small and the linear approximation breaks down. Therefore, higher order corrections to equation (1.33) are necessary — further details can be found in Chapter 2 [13, 49]. The equations of motion read

$$\dot{\delta}_k + \theta_k = -\int \frac{\mathrm{d}^3k_1\mathrm{d}^3k_2}{92\pi)^6}(2\pi)^3\delta_D(\mathbf{k}-\mathbf{k}_{12})\alpha(\mathbf{k_1},\mathbf{k_2})\theta_{k_1}\delta_{k_2} \tag{1.46a}$$

$$\dot{\theta}_k - 2H\theta_k + \frac{3}{2}H^2\Omega_m\delta_k = -\int \frac{\mathrm{d}^3k_1\mathrm{d}^3k_2}{(2\pi)^6}(2\pi)^3\delta_D(\mathbf{k}-\mathbf{k}_{12})\beta(\mathbf{k}_1,\mathbf{k}_2)\theta_{k_1}\theta_{k_2} \tag{1.46b}$$

where θ is the velocity divergence, and the kernels

$$\alpha(\mathbf{k_1},\mathbf{k_2}) \equiv \frac{\mathbf{k}_{12}\cdot\mathbf{k}_1}{k_1^2}, \quad \beta(\mathbf{k_1},\mathbf{k_2}) \equiv \frac{k_{12}^2\,\mathbf{k}_1\cdot\mathbf{k}_2}{2k_1^2k_2^2} \tag{1.47}$$

encode the non-linearity of the fluid equations where $\mathbf{k}_{12} = \mathbf{k}_2 - \mathbf{k}_1$. The general n^{th}-order solution yields

$$\delta^{(n)}(\mathbf{k}) = \int \mathrm{d}^3q_1 \ldots \int \mathrm{d}^3q_n\delta_D(\mathbf{k}-\mathbf{q}_{1\ldots n}F_n(\mathbf{q}_1,\ldots,\mathbf{q}_n)\delta^{(1)}_{\mathbf{q}_1}\ldots\delta^{(1)}_{\mathbf{q}_1}, \tag{1.48a}$$

$$\theta^{(n)}(\mathbf{k}) = \int \mathrm{d}^3q_1 \ldots \int \mathrm{d}^3q_n\delta_D(\mathbf{k}-\mathbf{q}_{1\ldots n}G_n(\mathbf{q}_1,\ldots,\mathbf{q}_n)\theta^{(1)}_{\mathbf{q}_1}\ldots\theta^{(1)}_{\mathbf{q}_1}. \tag{1.48b}$$

where the different kernels in the Einstein-de Sitter approximation [57] (i.e., $\Omega_m = 1$) are

$$F_n(\mathbf{q}_1,\ldots,\mathbf{q}_n) = \sum_{m=1}^{n-1}\frac{G_m(\mathbf{q}_1,\ldots,\mathbf{q}_m)}{(2n+3)(n-1)}\Big[(2n+1)\alpha(\mathbf{k}_1,\mathbf{k}_2)F_{n-m}(\mathbf{q}_{m+1},\ldots,\mathbf{q}_n) \tag{1.49a}$$

$$+ 2\beta(\mathbf{k}_1,\mathbf{k}_2)G_{n-m}(\mathbf{q}_{m+1},\ldots,\mathbf{q}_n), \tag{1.49b}$$

$$G_n(\mathbf{q}_1,\ldots,\mathbf{q}_n) = \sum_{m=1}^{n-1}\frac{G_m(\mathbf{q}_1,\ldots,\mathbf{q}_m)}{(2n+3)(n-1)}\Big[3\alpha(\mathbf{k}_1,\mathbf{k}_2)F_{n-m}(\mathbf{q}_{m+1},\ldots,\mathbf{q}_n) \tag{1.49c}$$

$$+ 2n\beta(\mathbf{k}_1,\mathbf{k}_2)G_{n-m}(\mathbf{q}_{m+1},\ldots,\mathbf{q}_n), \tag{1.49d}$$

being $\mathbf{k}_1 = \mathbf{q}_1 + \ldots + \mathbf{q}_m$ and $\mathbf{k}_2 = \mathbf{q}_{m+1} + \ldots + \mathbf{q}_n$, $\mathbf{k} = \mathbf{k}_1 + \mathbf{k}_2$. For example, $F_1 = G_1 \equiv 1$ and

$$F_2(\mathbf{k}_1,\mathbf{k}_2) = \frac{5}{7} + \frac{2}{7}\frac{(\mathbf{k}_1\cdot\mathbf{k}_2)^2}{k_1^2k_2^2} + \frac{\mathbf{k}_1\cdot\mathbf{k}_2}{2}\left(\frac{1}{k_1^2}+\frac{1}{k_2^2}\right), \tag{1.50a}$$

$$G_2(\mathbf{k}_1,\mathbf{k}_2) = \frac{3}{7} + \frac{4}{7}\frac{(\mathbf{k}_1\cdot\mathbf{k}_2)^2}{k_1^2k_2^2} + \frac{\mathbf{k}_1\cdot\mathbf{k}_2}{2}\left(\frac{1}{k_1^2}+\frac{1}{k_2^2}\right). \tag{1.50b}$$

For specific derivation of these functions refer to [13] and references therein.

There exist three contributions to the one-loop power spectrum, conventionally labelled P_{11}, P_{22} and P_{13} (see figure 1.5),

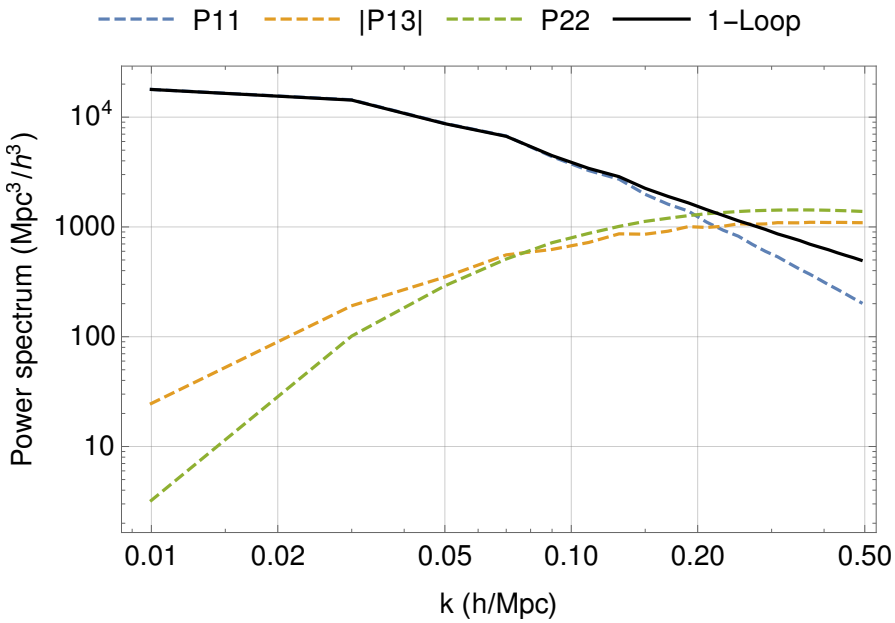

Figure 1.5: One-loop matter power spectra using standard perturbation theory and constructed as the addition of the linear, P_{11}, the quadratic, P_{22}, and the cubic contribution, P_{13}.

$$\langle \delta_{\mathbf{k}_1,1} \delta_{\mathbf{k}_2,1} \rangle = (2\pi)^3 \delta(\mathbf{k}_1 + \mathbf{k}_2) P_{11}(k), \tag{1.51a}$$

$$\langle \delta_{\mathbf{k}_1,2} \delta_{\mathbf{k}_2,2} \rangle = (2\pi)^3 \delta(\mathbf{k}_1 + \mathbf{k}_2) P_{22}(k), \tag{1.51b}$$

$$\langle \delta_{\mathbf{k}_1,1} \delta_{\mathbf{k}_2,3} + \delta_{\mathbf{k}_1,3} \delta_{\mathbf{k}_2,1} \rangle = (2\pi)^3 \delta(\mathbf{k}_1 + \mathbf{k}_2) P_{13}(k). \tag{1.51c}$$

In general, the complexity incidental to perturbation theory lies in the fact that solutions at each order become non-separable functions of time (redshift) and wavemodes. hence the use of approximations for the time-dependent functions becomes highly common in the literature[7]. Broadly used is the Einstein-de Sitter approximation [57] in which the non-linear growth functions are set proportional to powers of the linear growth function — this procedure becomes exact for matter domination when most of the energy budget of the universe is that of dark matter.

Further complications regarding divergences in the non-linear regime and some issues related to the amplitude of the baryon acoustic oscillations may be encountered. Concerning the ultra-violet divergences, non-linear physics make a considerable impact on the distribution of dark matter on small scales. Unfortunately, standard perturbation theory

[7] One of the results presented in chapter 2 [49] is the derivation, for the first time in the literature, of the full time dependence of the growth functions of the one-loop matter power spectrum within standard perturbation theory.

seems to be limited in accounting for such physical phenomena, leading to deviations of the fluctuations from the actual amplitude and shape of the matter perturbations, making this theory unpredictable and inaccurate on such scales. Consequently, further extensions and corrections to the standard framework become evidently necessary. One workaround on scales where non-linear physics dominate is the use of the effective field theory with counterterms encoding all of the microscopic phenomena. Conversely, on scales where standard perturbation theory is valid, one well-known alternative to resolve the limitations of perturbation theory would be the use of simulations. However, perturbation theory is still much faster to compute plus it seems very difficult for simulations to capture effects on the very largest scales. The main reason is that in order to simulate enough long modes one would need an extremely large box. Additionally, if one wishes to explore small scales, then the simulations become prohibitively expensive. Moreover, once the observables are computed in perturbation theory, it becomes very easy to change the initial conditions and even the physics. Changing initial conditions becomes very difficult with simulations because one would need to ensure that the new conditions are statistical compatible with the power spectrum and other physical observables. Likewise, changing the physics would mean reconstructing the code from scratch. In addition, concerning the baryon acoustic oscillations, standard perturbation predictions also appear to over-magnify some features on larger scales. In dealing with this over-magnification, the literature is replete with alternatives and practical re-summation schemes [189, 188, 166] in charge of damping the wiggle components of the matter perturbations. We will review theses effects deeply in chapter 2.

1.5.2 Effective field theory

The effective field theory formalism [11, 34, 33] is borrowed from particle physics to handle the ultra-violet divergences appearing in standard perturbation theory. Predictions from the standard theory seem to work extremely well within the linear regime —up to a certain cut-off scale. However, the new era of redshift surveys — such as Dark Energy Survey, Euclid, Dark Energy Spectroscopy Instrument or the Square Kilometre Array — permits cosmologists to probe increasingly smaller scales. The range of newly visible scales lie on the so-called *mild non-linear regime*, where dark matter fluctuations grow extremely large. Therefore, the use of a more accurate and robust theoretical framework becomes essential. This would be the *effective field theory* formalism, which enables us to handle our ignorance of an ultimate high-energy theory, and to find a workaround to the complex

modelling of non-linear physics associated with haloes, galaxy formation, gas dynamics or feedback from active galactic nuclei.

This theoretical tool has been traditionally utilised in cosmology [38, 82], introducing the notion of counter-terms. From the particle physics perspective, these counter-terms can be understood as indispensable factors that renormalise the matter density bare operator — which need to be fixed by real observational data or, alternatively, by simulations. Likewise, employing a more cosmology-like language, these counter-terms can be thought of as corrections to the perfect fluid approximation, leading to an effective energy-momentum tensor and new contributions to the fluid equations. In this sense, counter-terms parametrise all the unknown non-linear physics occurring on small scales and affecting macroscopic quantities such as matter density. The full description of this methodology can be found in chapter 2 of this thesis.

1.6 Redshift space clustering

Measurements of the two-point correlation function use the redshift of a galaxy, not its distance, to infer its location along the line of sight. This introduces two complications:

Alcock-Paczinski effect.—A cosmological model has to be assumed in order to convert measured redshifts to inferred distances [120]. Fortunately, errors on the assumed cosmology seem to be generally subdominant.

Redshift space distortions.—The gravitational redshift is function of the relative velocity of galaxies with respect to the observer, including Hubble recession and peculiar velocity effects. Peculiar velocities are unknown to redshift surveys and, therefore, only Hubble recession can be considered. In doing so, when converting from redshift space to real space, the distribution of matter appears radially distorted. That is,

- On small scales, $r \lesssim 1h^{-1}$Mpc, galaxies embedded in collapsed virialised overdensities — groups and clusters of galaxies — have large random motions relative to each other. That is, galaxies in a cluster have roughly the same distance from the observer but they have different redshifts. This is the effect known as *"fingers of god"*, FoG[8], an elongation in redshift space maps along the line of sight where groups

[8]The finger-of-god effect is modelled by a multiplicative damping exponential $\sim \mathrm{e}^{-\mu^2 f^2 k^2 \sigma^2}$, where μ is the cosine of the angle of the line of sight, f is the linear growth function and σ represents the amplitude of the perturbations.

and clusters appear radially extended towards the observer [183], see Figure 1.6.

- On large scales, $r \gtrsim 1h^{-1}$Mpc, the opposite effect can be observed due to streaming motions of galaxies infalling onto still collapsing structures. Adjacent galaxies will be moving in the same direction leading to coherent motion and causing an apparent contraction along the line of sight in redshift space [102].

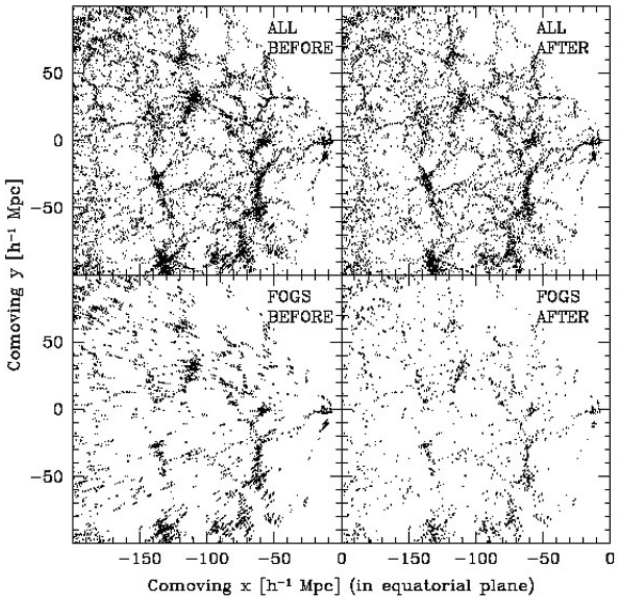

Figure 1.6: Image reprinted from [183], showing all galaxies from the SDSS survey (top row), and galaxies identified as having FoG effect (bottom row). The right column ("after") refers to the distribution of galaxies after modelling and removing such effect.

The mapping between real space coordinates, $\mathbf{r}$, and redshift space coordinates, $\mathbf{s}$, is given by the following Doppler formula,

$$\mathbf{s} = \mathbf{r} + (\hat{\mathbf{r}} \cdot \mathbf{v})\hat{\mathbf{r}}, \tag{1.52}$$

where $\hat{\mathbf{r}}$ is a unit vector along the line-of-sight, and $\mathbf{v}$ is the peculiar velocity of the galaxy in Hubble units. The real-space matter over-density $\delta(\mathbf{r})$ and the redshift-space over-density $\delta_s(\mathbf{s})$ are related by mass conservation, because the real-to-redshift mapping only moves mass around; it does not change its concentration. Therefore

$$\rho_s(\mathbf{s})\,\mathrm{d}^3 s = \rho(\mathbf{r})\,\mathrm{d}^3 r, \tag{1.53}$$

where ρ_s and ρ are the full density in redshift space and real space, respectively. hence to first order in perturbations,

$$\rho_{0,s}(\mathbf{s})\Big[1 + \delta_s(\mathbf{s})\Big]\,\mathrm{d}^3 s = \rho_0(\mathbf{r})\Big[1 + \delta(\mathbf{r})\Big]\,\mathrm{d}^3 r. \tag{1.54}$$

The background density — in real and redshift space, $\rho_{0,s}$ and ρ_0, respectively — is conserved, that is, in the absence of perturbations, matter fields are uniformly and homogeneously distributed in both real and redshift space. hence

$$1+\delta_s(\mathbf{s}) = \Big[1+\delta(\mathbf{r})\Big]\det\left(\frac{\partial \mathbf{s}}{\partial \mathbf{r}}\right)^{-1}, \tag{1.55}$$

where $\det\left(\frac{\partial \mathbf{s}}{\partial \mathbf{r}}\right) \equiv \det J$ represents the determinant of the Jacobian of the linear transformation, being $\det J = \det\left(\delta^i_k + \hat{r}^i\hat{r}^j\partial_k v_j + O(v^2)\right) \simeq 1 + \hat{r}^i\hat{r}^j\partial_i v_j$, under the *distant observer approximation*[9].

Within the linear regime, the linear redshift-space matter power spectrum yields

$$P_s(k,\mu) = \left(1+f\mu^2\right)^2 P(k) \tag{1.56}$$

where f is the linear growth function and μ refers to the cosine of the angle between the wave-vector $\mathbf{k}$ and the line of sight. Additionally, redshift galaxy surveys do not measure the redshift-space matter power spectrum itself but its multipole components. Consequently, in order to compare with data, the theoretical prediction for the power spectrum must be decomposed into multipole moments [94] by using the Legendre polynomials, $\mathcal{L}_l(\mu)$,

$$P_s(k,\mu) = \sum_{l=0}^{2l} P_l(k)\mathcal{L}_l(\mu)^{10}, \tag{1.57}$$

where multipole moments are given by

$$P_l(k) = \frac{2l+1}{2}\int_{-1}^{1} P^s(k,\mu)\mathcal{L}_l(\mu)\,\mathrm{d}\mu. \tag{1.58}$$

Although the introduction of redshift space distortions may augment the complexity of analytical and numerical computations, this effect becomes worth measuring in order to constrain cosmological parameters, as well as to retrieve the underlying real-space correlation function, allowing cosmologists to reach higher accuracy in their theoretical predictions. The analysis of this effect within the effective field theory framework motivates my work in chapter 2 [49].

[9] The *distant observer* or plane-parallel approximation establishes that observed galaxies are sufficiently far away that their separations subtend a very small angle at the observer, implying that displacements in redshift space caused by peculiar velocities may be treated as parallels.

[10] The anisotropy in $P(\mathbf{k})$ is symmetric in μ, $P(k,\mu) = P(k,-\mu)$. This is why only even values are summed over.

1.7 Galaxy bias

Galaxy surveys do not measure the distribution of matter fields but the distribution of galaxies and further tracers — extremely non-linear objects. Nonetheless, there exists a statistical relationship between the distribution of galaxies[11] and dark matter. This relationship originates from convoluted formation processes, highly complex and far from being completely understood. Alternatively, on quasi-linear scales, galaxy formation physics can be absorbed by a finite set of parameters [51], the so-called *bias parameters*.

The relation between the halo density contrast and the underlying over-density of dark matter and further fields, φ, is generally unknown. Therefore, a perturbative expansion may be performed, provided the fluctuations of the different fields are small enough

$$\delta_h(\mathbf{x},t) = \mathtt{F}[\delta(\mathbf{x},t),\varphi(\mathbf{x},t)] \sim \mathtt{F}_\delta(0,0)\delta(\mathbf{x},t) + \mathtt{F}_\varphi(0,0)\varphi(\mathbf{x},t) + \dots\,, \tag{1.59}$$

being $\mathtt{F}_\delta$ and $\mathtt{F}_\varphi$ the derivative of the functional $\mathtt{F}$ with respect to matter and the rest of fields, respectively. Considering $\delta(0,0) \equiv 0$, $\varphi(0,0) \equiv 0$, and, in consequence, $\delta_h(0,0) = 0$, equation (1.59) can be written

$$\delta_h(\mathbf{x},t) = \sum_{\mathcal{O}} b_{\mathcal{O}} \mathcal{O}(\mathbf{x},t) \tag{1.60}$$

where $\mathcal{O}$ is an operator representing every field, δ and φ; and $b_{\mathcal{O}} \equiv \mathtt{F}_{\mathcal{O}}(0,0)$ is the bias parameter associated with the operator $\mathcal{O}$ absorbing our ignorance about the functional $\mathtt{F}$.

Additionally, regardless whether the bias parameters appearing in equation (1.60) are scale dependent or scale independent, there exist two main categories[12]:

Local bias.—This form of bias only take into account the local effect of the gravitational potential of the underlying dark matter perturbations. This category includes operators involving two spatial derivatives for the gravitational potential, $\partial^2\Phi$[13].

[11] The concept of *galaxy* is used in the literature to refer a more general notion, *tracers of large-scale structure* — whose definition encompasses a diverse variety of objects such as galaxies, groups and clusters of galaxies, voids, quasars, the Lyman-α forest, radiation from 21 *cm* hydrogen hyperfine structure transition, etcetera.

[12] Other classifications can be found in the review by Desjacques et al [51].

[13] Local bias do not include first derivatives and terms directly proportional to the field itself since they are not allowed by the *equivalence principle*. The *weak equivalence principle* states that laws of freely-falling particles are the same in a gravitational field and a uniformly accelerated frame, on small enough regions of space-time. The generalisation of this statement is the so-called *Einstein's equivalence principle* which claims that on small enough regions of space-time, the laws of physics reduce to those of special relativity since it is impossible to detect the existence of a gravitational field.

The simplest example of local bias is the *linear bias* for which the statistical relation between haloes and the underlying dark matter perturbations becomes linear, $\delta_h(\mathbf{k}) = b_1\delta(\mathbf{k})$ [46]. The use of this model seems appealing because of its simplicity and the very low number of constraining parameters.

Non-local bias.—This form of bias account for physics affecting the collpased object within its mass scale, k_M. Moreover, it includes operators involving exactly two spatial derivatives for the gravitational potential, $\partial^2\Phi$, powers of the tidal field and time derivatives of both the density and the tidal field.

One example is the McDonald and Roy model [126] who consider that the collapsed object is affected not only by the local gravitational potential but for the physics happening in its vicinity. McDonald et al. also work under the premise that, in order to be consistent, the order in the bias expansion should match that of preturbation — meaning that if one works up to one-loop in perturbation theory, one should expand up to third-order in bias. The halo density contrast reads

$$\delta_h(\mathbf{k}) = b_1\delta(\mathbf{k}) + \frac{b_2}{2!}\delta^2(\mathbf{k}) + \frac{b_{s^2}}{2!}s^2(\mathbf{k}) + b_{3nl}[\sigma_3\delta]_{\mathbf{k}}. \tag{1.61}$$

Another example is the model constructed by Saito et al. [154], the *co-evolution model*, which also follow these premises

$$\delta_h(\mathbf{k}) = b_1^{(L)}\delta(\mathbf{k}) + \frac{b_2^{(L)}}{2}\delta^2(\mathbf{k}). \tag{1.62}$$

More complex models not only systematically construct all the one-loop contributions to the bias, but also consider time non-locallity [37, 164] — the same way there exists space non-locallity, the tracer ought to be affected by the history of the collapsed object. The description of such space non-local and time non-local bias model within the effective field theory formalism motivates our chapter 3.

1.8 Overview of this thesis

After reviewing the literature on the large-scale structure, it becomes clear that there is a need to revisit the use of the effective field theory framework in real space in order to deal with ultra-violet divergences and to probe smaller scales within the so-called mildly non-linear regime — scales visible by the modern surveys — where standard perturbation theory breaks down and stops producing reliable predictions. As a step forward in this research field, in chapter 2, we analyse the one-loop matter power spectrum, including for the first time the full-time dependence of the relevant growth functions; as well as

redshift space distortions, making the analytical and numerical computations far more complex but enabling us to extract priceless information about the velocity dispersions within clusters.

Leaning on the redshift-space matter power spectrum results using effective field theory, the next logical step is the analysis of halo bias. In chapter 3, we shed some light on the question about model selection to analyse observational data. Moreover, information in galaxy surveys comes at a price, meaning that the observables have to be modelled, so there is a tradeoff between the accuracy of the model and the constraining power of the data. The model has to be accurate enough, but it should not contain unphysical degrees of freedom, and it should have as few parameters as possible so that data is not "wasted" in constraining them. In this chapter, we intend to address the question *what is the appropriate level of complexity for a present-day analysis of a galaxy survey?*

The final chapter of this thesis, chapter 4, is devoted to the general conclusions extracted from my research, as well as future prospects and further investigation. Finally, references are included.

Chapter 2

Matter power spectrum in redshift space using effective field theory

Abstract

The use of Eulerian 'standard perturbation theory' to describe mass assembly in the early universe has traditionally been limited to modes with $k \lesssim 0.1h/\mathrm{Mpc}$ at $z = 0$. At larger k the SPT power spectrum deviates from measurements made using N-body simulations. Recently, there has been progress in extending the reach of perturbation theory to larger k using ideas borrowed from effective field theory. We revisit the computation of the redshift-space matter power spectrum within this framework, including for the first time the full one-loop time dependence. We use a resummation scheme proposed by Vlah et al. to account for damping of baryonic acoustic oscillations due to large-scale random motions and show that this has a significant effect on the multipole power spectra. We renormalize by comparison to a suite of custom N-body simulations matching the MultiDark MDR1 cosmology. At $z = 0$ and for scales $k \lesssim 0.4h/\mathrm{Mpc}$ we find that the EFT furnishes a description of the real-space power spectrum up to $\sim 2\%$, for the $\ell = 0$ mode up to $\sim 5\%$, and for the $\ell = 2, 4$ modes up to $\sim 25\%$. We argue that, in the MDR1 cosmology, positivity of the $\ell = 0$ mode gives a firm upper limit of $k \approx 0.75h/\mathrm{Mpc}$ for the validity of the one-loop EFT prediction in redshift space using only the lowest-order counter-term. We show that replacing the one-loop growth factors by their Einstein-de Sitter counterparts is a good approximation for the $\ell = 0$ mode, but can induce deviations as large as 2% for the $\ell = 2, 4$ modes. An accompanying software bundle, distributed under open source licenses, includes Mathematica notebooks describing the calculation, together with parallel pipelines capable of computing both the necessary one-loop SPT integrals and the effective field theory counterterms.

2.1 Introduction

The long dominance of the cosmic microwave background (CMB) as our principal source of information regarding the early universe will soon come to an end, displaced by new datasets from large galaxy redshift surveys. In addition to present-day surveys such as the Dark Energy Survey, the list will expand over the next decade to include at least Euclid, the Dark Energy Spectroscopic Instrument, the Large Synoptic Survey Telescope, the Square Kilometer Array, and the 4-metre Multi Object Spectroscopic Telescope. The ensemble of Fourier modes visible to each of these instruments carries information about *both* (i) the gravitational potentials— presumably generated by inflation — that seeded structure formation, and (ii) the effective force laws that operated while matter was drawn into these potential wells and condensed into halos. This sensitivity to a rich range of physical processes means that the imminent era of large galaxy surveys should drive a step change in our understanding of the standard cosmological model —and especially its poorly-understood early- and late-time accelerating phases.

The price to be paid for access to this information is an obligation to connect our theoretical description with observation by carrying out sophisticated modelling of both gravitational potentials and force laws. Analytic control has traditionally come from the use of perturbation theory [100, 187, 69, 77, 17, 174, 123, 13], but its reach is limited in scale to $k \lesssim 0.1h/\mathrm{Mpc}$ at $z = 0$ and therefore excludes a significant fraction of the modes visible to the surveys listed above. Large N-body simulations provide an alternative, but although Moore's Law has significantly reduced their time cost they are still expensive—certainly too expensive to be considered routine for extensions of the standard cosmological model that entail a significant increase in the parameter space. These pressures have produced a large literature based on enhancements of standard perturbation theory ('SPT') that extend its reach to moderate k in the approximate range $0.1h/\mathrm{Mpc}$ to $0.5h/\mathrm{Mpc}$. One such approach is based on modern ideas from effective field theory [11, 34, 33, 151, 166, 165, 189, 188], leading to the so-called 'effective field theory of large-scale structure'. This has yielded encouraging results for the matter power spectrum and bispectrum, at the cost of adjustable counterterms that must be estimated from observation or from N-body simulations.

Redshift space effects.—In this chapter we revisit the application of these ideas to the *redshift-space* power spectrum. Real surveys must estimate the radial distance to a source from its redshift, and therefore do not measure the galaxies' true spatial configuration. Unknown peculiar velocities associated with each source bias our distance estimate, in-

troducing a systematic 'redshift space distortion' that must be modelled appropriately if we are to extract reliable results [92]. This is both a challenge and an opportunity. While redshift-space effects complicate the analysis, they enable us to measure correlations between densities and velocities that carry information about the effective gravitational force law on cosmological scales. In Einstein gravity, for the non-relativistic regime applicable to large-scale structure, this effective force is composed of an attractive $1/r^2$ component that is offset by a repulsive contribution from the cosmological expansion. In non-Einstein gravities the competition between these effects may be altered, or the scale-dependence of the force law may itself be modified due to processes involving exchange of new force-carrying particles.

These non-Einstein gravities could be constrained by precise measurements of the effective force law on cosmological scales, but only if its scale-dependence can be separated from uncertainties in our computation of its behaviour in the standard cosmological model. For this purpose effective field theory should be a helpful tool, enabling us to extend the range of wavenumbers that can be reached analytically and used for comparison. Senatore & Zaldarriaga [165] and later Lewandowski et al. [116] provided an analysis of the redshift-space matter power spectrum within such an effective description. More recently, Perko et al. extended this analysis to include biased tracers of the dark matter distribution [148] (see also Refs. [7, 76]). By itself, the dark matter can be measured only through its impact on cosmological weak lensing.

In this paper we revisit the redshift-space analysis for the pure matter power spectrum. Our computation is similar to that of Lewandowski et al., with which it shares a common language and point of departure. However, it differs in certain technical details such as construction of the counterterms, our procedure for estimating their numerical values, and our procedure for resumming large loop-level terms involving integrals over the infrared part of the power spectrum. Moreover we compute all time dependent terms exactly, rather than approximating them as powers of the Einstein-de Sitter growth function $D(z)$. This enables us to assess the accuracy of the Einstein–de Sitter approximation. We renormalize to a suite of custom N-body simulations performed using the **gevolution** numerical relativity code.

As part of our analysis we describe some computational innovations that we believe to be improvements over the traditional methods used by Matsubara to compute the redshift-space power spectrum in standard perturbation theory [125]. One such innovation is an algorithm to extract the explicit μ-dependence[1] of the redshift-space power spectrum

[1] Here, $\mu = \hat{\mathbf{k}} \cdot \hat{\mathbf{n}}$ is the orientation of a $\mathbf{k}$ mode contributing to the matter density field relative to the

using the Rayleigh plane-wave expansion and analytic formulae for weighted integrals over products of two or three spherical Bessel functions. A procedure to compute these three-Bessel integrals was described by Gervois & Navelet [74], and more recently by Fabrikant [62]. However, their results do not yet seem to have entered the cosmological literature.[2]

Code availability.—To assist those who wish to replicate or extend our analysis, we have made our computer codes and supporting datasets available as part of a software bundle accompanying this work. These include the parameter files needed to reconstruct our initial linear power spectra, the settings files required to reproduce our **gevolution** simulations, and databases containing the loop integrals and one-loop power spectra evaluated using the EFT. Each of these products can be downloaded by following the links given in Appendix 2.C.

Summary.—Our presentation is organized as follows. In §2.2 we fix notation by summarizing the construction of the renormalized real-space matter power spectrum, originally described by Carrasco et al. [34, 33]. In §2.2.1 we collect the equations of structure formation during the matter era and describe their non-relativistic limit. In §2.2.2 we construct Eulerian perturbation theory based on these equations and compute the one-loop correction to the power spectrum of the density contrast $\delta = \delta\rho/\rho$. The time-dependent factors $D_A, \ldots, D_J$ and the loop integrals $P_{AA}, \ldots, P_{BB}, P_D, \ldots, P_{J_1}, P_{J_2}$ are the key results from this section. They are re-used extensively in §2.3.

In §2.2.3 we briefly summarize the use of effective field-theory methods to parametrize the unknown ultraviolet parts of these loop integrals. In §2.2.4 we describe renormalization of the velocity field, and explain how to relate the perspective used in this paper to the 'smoothing' prescription for renormalized operators used in Refs. [11, 34, 33, 132] and elsewhere. In §2.2.5 we introduce a scheme proposed by Vlah, Seljak, Chu & Feng to resum the damping effect of displacements on large scales and assess its impact on the real-space power spectrum. We conclude this section by describing the renormalization of the power spectrum at redshift $z = 0$ (§2.2.6), and compare our results with those already reported in the literature.

---

line of sight $\hat{\mathbf{n}}$ from Earth.

[2] Certain three-Bessel integrals were computed as long ago as 1936 by Bailey [9]. However, Bailey's method (and its descendents) required a triangle inequality to be satisfied by the arguments of the Bessel functions. To be effective our algorithm requires knowledge of the integral for any values of the arguments and not just those that satisfy the triangle inequality. It is for this extension that we require the more advanced methods of Refs. [74, 62].

This section can be read as a mini-primer on the use of effective field-theory methods. Readers already familiar with their application to large-scale structure may wish to focus on §2.2.2—which introduces our notation for time-dependent factors, the SPT kernels, and loop integrals—and §2.2.5, which describes our resummation prescription. These summarize the principal technical differences between our formalism and the existing literature.

In §2.3 we describe the renormalization of the redshift-space power spectrum. In §2.3.1 we write down an expression suitable for computing the redshift-space density contrast δ_s up to one-loop and discuss the counterterms needed to renormalize it. In §2.3.2 we describe the calculation of the δ_s power spectrum up to one-loop, introducing a new method to simplify evaluation of the tensor integrals that appear at this order. We extend the Vlah et al. resummation scheme to redshift space in §2.3.3 and comment on its relation to empirical schemes for capturing the suppression of power on small scales due to randomized virial motions within halos. In §2.3.4 we describe the construction of the Legendre multipoles. A significant advantage of the Vlah et al. resummation scheme is that this can be done *analytically*, reducing the requirement for expensive numerical computation. The N-body simulations needed to obtain non-linear measurements of these multipoles are described in §2.3.5. We comment on a number of difficulties encountered when extracting reliable estimates of the redshift-space multipoles. Finally, in §2.3.6 we fit for the counterterms of the effective description and discuss the resulting power spectra. We assess the accuracy of the Einstein–de Sitter approximation and comment on the time-dependence of the EFT counterterms. We conclude in §2.4. A number of Appendices extend the discussion presented in the main text.

Notation.—We use units in which $c = \hbar = 1$ and define the reduced Planck mass to be $M_{\rm P} = (8\pi G)^{-1/2}$. Our Fourier convention is $f(\mathbf{x}) = \int \mathrm{d}^3k\,(2\pi)^{-3}\,f(\mathbf{k})\mathrm{e}^{\mathrm{i}\mathbf{k}\cdot\mathbf{x}}$.

Latin indices a, b, …, from the beginning of the alphabet range over spacetime coordinates (t, x, y, z) or $(0, 1, 2, 3)$. Latin indices i, j, …, from the middle of the alphabet range over spatial indices only. Repeated spacetime indices are taken to be contracted with the metric g_{ab}. Repeated spatial indices all in the 'up' or 'down' position are contracted with the three-dimensional Euclidean metric δ_{ij}, so that (for example) $v^2 = v^i v^i = \delta_{ij} v^i v^j = \sum_i (v^i)^2$, and likewise for $v_i v_i = \delta^{ij} v_i v_j$.

2.2 One-loop renormalization of the matter power spectrum in real space

In this section we briefly recapitulate the construction of the one-loop matter power spectrum, neglecting the complexities of redshift-space distortions. The material presented here is a review of the theory developed by Baumann et al. [11], Carrasco et al. [34, 33] and Mercolli & Pajer [132], although some results are new (including renormalization of the velocity accounting for its full time dependence), and parts of our presentation are different to discussions that have already appeared in the literature. We develop the formalism in detail because we will rely on the notation and methodology developed here when we study the power spectrum in redshift space.

2.2.1 Matter equations of motion

Initially we work in a non-linear Newtonian gauge for which the metric can be written

$$\mathrm{d}s^2 = -\mathrm{e}^{2\Psi}\,\mathrm{d}t^2 + a^2\,\mathrm{e}^{2\Phi}\,\mathrm{d}\mathbf{x}^2. \tag{2.1}$$

The comoving dark matter velocity satisfies $u^a = \mathrm{e}^{-\Psi}\gamma(1,\mathbf{v})$, where $\gamma = (1-v_{\mathrm{phys}}^2)^{-1/2}$ is the special-relativistic Lorentz factor and $v_{\mathrm{phys}} = a\mathrm{e}^{\Phi-\Psi}v$ is the physical peculiar 3-velocity. To obtain the true physical velocity for a source at distance d we should add v_{phys} to the Hubble flow $v_{\mathrm{H}} = Hd$. In this metric, the continuity equation for a perfect fluid with pressure p and density ρ can be written

$$\partial_t\Big(\gamma^2(p+\rho)-p\Big)+\nabla\cdot\Big(\gamma^2(p+\rho)\mathbf{v}\Big)+\gamma^2(p+\rho)\Big(\mathbf{v}\cdot\nabla(\Psi+3\Phi)+(H+\dot\Phi)(4-\gamma^{-2})\Big) = 0, \tag{2.2}$$

and the Euler equation is

$$\begin{aligned}\partial_t\Big(\gamma^2\mathbf{v}(p+\rho)\Big) + (\mathbf{v}\cdot\nabla)\Big(\gamma^2\mathbf{v}(p+\rho)\Big) + \frac{1}{a^2}\mathrm{e}^{2\Psi-2\Phi}\nabla p \\ + \gamma^2\mathbf{v}(p+\rho)\Big(\nabla\cdot\mathbf{v} + 5(H+\dot\Phi) + 5\mathbf{v}\cdot\nabla\Phi - \mathbf{v}\cdot\nabla\Psi - \dot\Psi\Big) \\ + \frac{1}{a^2}\mathrm{e}^{2\Psi-2\Phi}(p+\rho)\Big(\gamma^2\nabla\Psi - (\gamma^2-1)\nabla\Phi\Big) = 0\end{aligned} \tag{2.3}$$

An overdot denotes a derivative with respect to time t. The gravitational potentials satisfy the Poisson constraint,

$$\begin{aligned}\frac{1}{a^2}\nabla^2\Phi + \frac{1}{2a^2}\nabla\Phi\cdot\nabla\Phi = -\frac{\mathrm{e}^{2\Phi}}{2M_{\mathrm{P}}^2}\Big(\gamma^2(p+\rho) - p - 3Ha^2\mathrm{e}^{-2\Psi}\nabla^{-2}\nabla\cdot[\gamma^2\mathrm{e}^{2\Phi}(p+\rho)\mathbf{v}]\Big) \\ + \mathrm{e}^{2\Phi-2\Psi}\Big(\frac{3}{2}H^2 + 3H\nabla^{-2}[(H+\dot\Phi)\nabla^2\Psi + \nabla\dot\Phi\cdot\nabla\Psi] + \frac{3}{2}\dot\Phi^2\Big).\end{aligned} \tag{2.4}$$

Finally, for Einstein gravity coupled to a perfect fluid, the gravitational potentials will be related by the no-slip condition $\Psi = -\Phi$. All these equations are exact. In particular, they do not assume that the density and pressure are perturbatively small or that velocities are non-relativistic.

Non-relativistic limit.—Up to this point we have retained all terms in order to make clear what is entailed by our approximations. We wish to use these equations to describe deposition of matter by a gravitationally-driven flow within the potential wells associated with Φ and Ψ. Assume that the flow carries density $\rho_{\rm f}$ which is deposited onto a condensation of density $\rho_{\rm c}$. Therefore the density contrast δ is approximately $\rho_{\rm c}/\rho_{\rm f}$. In a static Newtonian universe the flow velocity at distance R from the condensation is roughly

$$v \sim \frac{R}{t_{\rm ff}}\frac{\rho_{\rm c}}{\rho_{\rm f}} \sim \frac{R}{t_{\rm ff}}\delta, \tag{2.5}$$

where $t_{\rm ff} \approx (G\rho_{\rm f})^{-1/2}$ is the free-fall time associated with the flow. This correlation between v and δ is characteristic of an inverse-square-law force. It continues to apply in an expanding universe described by Einstein gravity, adjusted by a scale-independent constant of order unity that accounts for competition between Newtonian attraction and cosmological repulsion. In a non-Einstein gravity we should expect its R dependence or the overall constant of proportionality to receive corrections. Ultimately, it is these corrections that we wish to explore using redshift-space distortions.

Returning to Einstein gravity and temporarily restoring factors of c we conclude that v/c scales like $t_R/t_{\rm ff}$, where $t_R = R/c$ is the light-crossing time at distance R. In the case of cosmological structure formation the flow density $\rho_{\rm f}$ is the background matter density and $t_{\rm ff}$ is of order a Hubble time. Therefore $t_R/t_{\rm ff} \ll 1$ on any scale well inside the Hubble radius, making $v/c \ll 1$. On these scales it follows that relativistic corrections $\sim \mathcal{O}(\gamma)$ will be negligible. A similar discussion was given by Fry [69].

On the other hand, terms of order $\nabla\mathbf{v} \sim t_{\rm ff}^{-1}\rho_{\rm c}/\rho_{\rm f}$ need not be suppressed. In combination with a time derivative such as $\dot\rho$ or $\dot{\mathbf{v}}$ the relative importance of such terms will be of order $t_{\rm ff}\nabla\mathbf{v} \sim \rho_{\rm c}/\rho_{\rm f}$, which need not be especially small. Therefore it is meaningful to develop a series expansion in $\nabla\mathbf{v}$ while neglecting relativistic corrections from terms of order v^2 and higher. This is standard perturbation theory or 'SPT'. Specializing to matter domination, in which the gravitational potentials are determined by the matter density fluctuation, and keeping only terms linear in $\Phi = -\Psi$, Eqs. (2.2)–(2.4) for pressureless

cold dark matter reduce to

$$\dot{\delta} + \nabla \cdot \Big((1+\delta)\mathbf{v} \Big) = 0 \tag{2.6a}$$

$$\dot{\mathbf{v}} + (\mathbf{v}\cdot\nabla)\mathbf{v} + 2H\mathbf{v} - \frac{1}{a^2}\nabla\Phi = 0 \tag{2.6b}$$

$$\frac{1}{a^2}\nabla^2\Phi = -\frac{3H^2}{2}\Omega_m\delta, \tag{2.6c}$$

where we have decomposed the density as $\rho = \rho_0 + \delta\rho$, with ρ_0 the homogeneous background, and $\delta = \delta\rho/\rho$ is the density contrast. The quantity $\Omega_m = \rho_m/(3H^2M_{\rm P}^2)$ is the redshift-dependent matter density parameter.

Radial inflow approximation.—On large scales the flow $\mathbf{v}$ will be oriented nearly radially into a nearby potential well and the vorticity $\boldsymbol{\omega} = \nabla\times\mathbf{v}$ will be very small. In this 'potential flow' region the velocity can be written as a gradient $\mathbf{v} = \nabla\nabla^{-2}\theta$, where $\theta = \nabla\cdot\mathbf{v}$ is the velocity divergence. In this approximation, after translation to Fourier space, Eqs. (2.6a)–(2.6c) become

$$\dot{\delta}_{\mathbf{k}} + \theta_{\mathbf{k}} = -\int \frac{{\rm d}^3q\,{\rm d}^3s}{(2\pi)^6}\,(2\pi)^3\delta(\mathbf{k}-\mathbf{q}-\mathbf{s})\alpha(\mathbf{q},\mathbf{s})\theta_{\mathbf{q}}\delta_{\mathbf{s}}, \tag{2.7a}$$

$$\dot{\theta}_{\mathbf{k}} - 2H\theta_{\mathbf{k}} + \frac{3H^2}{2}\Omega_m\delta_{\mathbf{k}} = -\int \frac{{\rm d}^3q\,{\rm d}^3s}{(2\pi)^6}\,(2\pi)^3\delta(\mathbf{k}-\mathbf{q}-\mathbf{s})\beta(\mathbf{q},\mathbf{s})\theta_{\mathbf{q}}\theta_{\mathbf{s}}, \tag{2.7b}$$

where the dimensionless kernels $\alpha(\mathbf{q},\mathbf{s})$ and $\beta(\mathbf{q},\mathbf{s})$ satisfy

$$\alpha(\mathbf{q},\mathbf{s}) = \frac{\mathbf{q}\cdot(\mathbf{q}+\mathbf{s})}{q^2}, \tag{2.8a}$$

$$\beta(\mathbf{q},\mathbf{s}) = \frac{\mathbf{q}\cdot\mathbf{s}}{2q^2s^2}(\mathbf{q}+\mathbf{s})^2. \tag{2.8b}$$

Notice that β is symmetric but α is not. For future use it is helpful to define a symmetrized version of weight unity,

$$\bar{\alpha}(\mathbf{q},\mathbf{s}) = \frac{1}{2}\alpha(\mathbf{q},\mathbf{s}) + \frac{1}{2}\alpha(\mathbf{s},\mathbf{q}). \tag{2.9}$$

We also define a third kernel $\gamma(\mathbf{q},\mathbf{s})$ to be a sum of the α and β kernels,

$$\gamma(\mathbf{q},\mathbf{s}) = \alpha(\mathbf{q},\mathbf{s}) + \beta(\mathbf{q},\mathbf{s}). \tag{2.10}$$

Like α, it can be symmetrized to give $\bar{\gamma}(\mathbf{q},\mathbf{s})$. Observe that the linear part of Eq. (2.7a) reads $\theta_{\mathbf{k}} = -\dot{\delta}_{\mathbf{k}}$, which replicates our conclusion above that $\nabla\mathbf{v} \sim t_{\rm ff}^{-1}\rho_{\rm c}/\rho_{\rm f} \sim H\delta$.

Combining Eqs. (2.7a)–(2.7b) to eliminate $\theta_{\mathbf{k}}$ and obtain a single second-order equation for $\delta_{\mathbf{k}}$, and exchanging cosmic time t for redshift z, defined by

$$1 + z = \frac{a_0}{a}, \tag{2.11}$$

where $a_0 = a(t_0)$ is the present-day value of the scale factor, we find

$$\begin{aligned}\delta_{\mathbf{k}}'' - \frac{1-\epsilon}{1+z}\delta_{\mathbf{k}}' - \frac{3}{2}\frac{\Omega_m}{(1+z)^2}\delta_{\mathbf{k}} \\ = -\int \frac{\mathrm{d}^3q\,\mathrm{d}^3s}{(2\pi)^6}(2\pi)^3\delta(\mathbf{k}-\mathbf{q}-\mathbf{s})S_2(\mathbf{q},\mathbf{s}) \\ -\int \frac{\mathrm{d}^3q\,\mathrm{d}^3s}{(2\pi)^6}(2\pi)^3\delta(\mathbf{k}-\mathbf{q}-\mathbf{s})\int \frac{\mathrm{d}^3t\,\mathrm{d}^3u}{(2\pi)^6}(2\pi)^3\delta(\mathbf{s}-\mathbf{t}-\mathbf{u})S_3(\mathbf{q},\mathbf{s},\mathbf{t},\mathbf{u}) \\ +\mathcal{O}(\delta^4).\end{aligned} \tag{2.12}$$

We have retained terms only up to $\mathcal{O}(\delta^3)$; those of higher order do not contribute to the one-loop power spectrum. A prime $'$ denotes a derivative with respect to z. The quantity ϵ is defined by $\epsilon = -\dot{H}/H^2$ and can be related to the deceleration parameter. The source terms S_2 and S_3 satisfy

$$S_2(\mathbf{q},\mathbf{s}) = \bar{\gamma}(\mathbf{q},\mathbf{s})\delta_{\mathbf{q}}'\delta_{\mathbf{s}}' + \frac{3}{2}\frac{\Omega_m}{(1+z)^2}\bar{\alpha}(\mathbf{q},\mathbf{s})\delta_{\mathbf{q}}\delta_{\mathbf{s}}, \tag{2.13}$$

and

$$S_3(\mathbf{q},\mathbf{s},\mathbf{t},\mathbf{u}) = \alpha(\mathbf{s},\mathbf{q})\beta(\mathbf{t},\mathbf{u})\delta_{\mathbf{q}}\delta_{\mathbf{t}}'\delta_{\mathbf{u}}' + 2\beta(\mathbf{q},\mathbf{s})\alpha(\mathbf{t},\mathbf{u})\delta_{\mathbf{q}}'\delta_{\mathbf{t}}'\delta_{\mathbf{u}} + \alpha(\mathbf{s},\mathbf{q})\alpha(\mathbf{t},\mathbf{u})\delta_{\mathbf{q}}'\delta_{\mathbf{t}}'\delta_{\mathbf{u}}. \tag{2.14}$$

2.2.2 Eulerian perturbation theory

The most straightforward approach to solution of Eq. (2.12) is via an expansion in powers of δ. The outcome of this procedure is described as Eulerian perturbation theory.

Linear solution.—First consider the linear term, which does not require the sources S_2 and S_3. Because Eq. (2.12) applies only during matter domination we should suppose the initial condition $\delta_{\mathbf{k}} = \delta_{\mathbf{k}}^*$ to be set at some redshift $z = z^*$ that is well within the matter era, but still early enough that terms of order $(\delta_{\mathbf{k}}^*)^2$ or higher can be neglected. For practical calculations we normally set $z^* \approx 50$.

The linear solution is $\delta_{\mathbf{k}}(z) = D(z)\delta_{\mathbf{k}}^*$, where the growth function $D(z)$ satisfies

$$D'' - \frac{1-\epsilon}{1+z}D' - \frac{3}{2}\frac{\Omega_m}{(1+z)^2}D = 0. \tag{2.15}$$

If the initial time z^* is chosen sufficiently early then the initial condition requires that $D(z)$ is approximately given by the matter-dominated solution $D(z) \approx a(z)/a(z^*)$. Notice that $D^* = D(z^*) = 1$. Solutions to this equation were studied by Mészáros [133] and Groth & Peebles [81]. The velocity can be determined from the linear part of Eq. (2.7a), yielding

$$\theta_{\mathbf{k}} = -fH\delta_{\mathbf{k}} \tag{2.16}$$

where the growth factor $f(z)$ is defined to be

$$f \equiv -(1+z)\frac{D'}{D} = \frac{\mathrm{d}\ln D}{\mathrm{d}\ln a}. \tag{2.17}$$

Eqs. (2.16)–(2.17) are nothing more than the estimate (2.5) in this model, with $t_{\mathrm{ff}} = 1/H$ and $R \sim 1/k$, and f representing a scale-independent damping of the gravitational force due to cosmological expansion. In the matter-only Einstein–de Sitter model we have $f = 1$ and there is no damping of the correlation between $\mathbf{v}$ and δ; the effect of the expansion is only to soften exponential growth of δ into a power-law. For $\Omega_m < 1$ there is extra suppression which can be estimated in Einstein gravity by $f \approx \Omega_m^{5/9}$ [119].

Second-order solution.—To distinguish the different contributions to $\delta_{\mathbf{k}}$ and $\theta_{\mathbf{k}}$ we attach a label n indicating the order in perturbation theory. The linear solution described above gives the first-order component $\delta_{\mathbf{k},1}$. The second-order component $\delta_{\mathbf{k},2}$ is generated by insertion of linear solutions into the quadratic source S_2. It gives

$$\delta_{\mathbf{k},2} = \int \frac{\mathrm{d}^3 q\, \mathrm{d}^3 s}{(2\pi)^6} (2\pi)^3 \delta(\mathbf{k}-\mathbf{q}-\mathbf{s}) \delta^*_{\mathbf{q}} \delta^*_{\mathbf{s}} \Big(D_A(z)\bar{\alpha}(\mathbf{q},\mathbf{s}) + D_B(z)\bar{\gamma}(\mathbf{q},\mathbf{s}) \Big), \tag{2.18}$$

for which the spatial average $\mathbf{k} = 0$ mode vanishes because $\alpha(\mathbf{q},-\mathbf{q}) = \beta(\mathbf{q},-\mathbf{q}) = \gamma(\mathbf{q},-\mathbf{q}) = 0$. The time-dependent growth functions $D_A(z)$ and $D_B(z)$ are analogues of the linear growth function $D(z)$. They are solutions to the equations

$$D_A'' - \frac{1-\epsilon}{1+z} D_A' - \frac{3}{2}\frac{\Omega_m}{(1+z)^2} D_A = \frac{3}{2}\frac{\Omega_m}{(1+z)^2} D^2 \tag{2.19a}$$

$$D_B'' - \frac{1-\epsilon}{1+z} D_B' - \frac{3}{2}\frac{\Omega_m}{(1+z)^2} D_B = (D')^2. \tag{2.19b}$$

We choose initial equations so that D_A and D_B match the corresponding growth functions in a matter-only model at the initial redshift $z = z^*$. This makes our results practically independent of the choice of z^*, provided it is taken to be sufficiently early.

Third-order solution.—The third-order solution is sourced by insertion of linear solutions into the cubic term S_3 together with insertion of one linear and one second-order solution in the quadratic term S_2. It can be written

$$\begin{aligned}
\delta_{\mathbf{k},3} = \int \frac{\mathrm{d}^3 q\, \mathrm{d}^3 s\, \mathrm{d}^3 t}{(2\pi)^9} (2\pi)^3 \delta(\mathbf{k}-\mathbf{q}-\mathbf{s}-\mathbf{t}) \delta^*_{\mathbf{q}} \delta^*_{\mathbf{s}} \delta^*_{\mathbf{t}} \\
\times \Big(2[D_D(z) - \mathcal{D}(z)] \bar{\gamma}(\mathbf{s}+\mathbf{t},\mathbf{q}) \bar{\alpha}(\mathbf{s},\mathbf{t}) + 2 D_E(z) \bar{\gamma}(\mathbf{s}+\mathbf{t},\mathbf{q}) \bar{\gamma}(\mathbf{s},\mathbf{t}) \\
+ 2[D_F(z) + \mathcal{D}(z)] \bar{\alpha}(\mathbf{s}+\mathbf{t},\mathbf{q}) \bar{\alpha}(\mathbf{s},\mathbf{t}) + 2 D_G(z) \bar{\alpha}(\mathbf{s}+\mathbf{t},\mathbf{q}) \bar{\gamma}(\mathbf{s},\mathbf{t}) \\
+ \mathcal{D}(z) \Big[\alpha(\mathbf{s}+\mathbf{t},\mathbf{q}) \bar{\gamma}(\mathbf{s},\mathbf{t}) - 2\alpha(\mathbf{s}+\mathbf{t},\mathbf{q}) \bar{\alpha}(\mathbf{s},\mathbf{t}) \Big] \Big).
\end{aligned} \tag{2.20}$$

	A	B	D	E	F	G	J
growth function D_i	$\frac{3}{7}D^2$	$\frac{2}{7}D^2$	$\frac{2}{21}D^3$	$\frac{4}{63}D^3$	$\frac{1}{14}D^3$	$\frac{1}{21}D^3$	$\frac{1}{9}D^3$
growth factor f_i	$2f$	$2f$	$3f$	$3f$	$3f$	$3f$	$3f$

Table 2.1: Relation between the non-linear growth functions D_i and their Einstein–de Sitter counterparts, which can be expressed as powers of the linear growth function D.

The new growth functions D_D, D_E, D_F, D_G and Đ satisfy

$$D_D'' - \frac{1-\epsilon}{1+z}D_D' - \frac{3}{2}\frac{\Omega_m}{(1+z)^2}D_D = D'D_A' \tag{2.21a}$$

$$D_E'' - \frac{1-\epsilon}{1+z}D_E' - \frac{3}{2}\frac{\Omega_m}{(1+z)^2}D_E = D'D_B' \tag{2.21b}$$

$$D_F'' - \frac{1-\epsilon}{1+z}D_F' - \frac{3}{2}\frac{\Omega_m}{(1+z)^2}D_F = \frac{3}{2}\frac{\Omega_m}{(1+z)^2}DD_A \tag{2.21c}$$

$$D_G'' - \frac{1-\epsilon}{1+z}D_G' - \frac{3}{2}\frac{\Omega_m}{(1+z)^2}D_G = \frac{3}{2}\frac{\Omega_m}{(1+z)^2}DD_B \tag{2.21d}$$

$$\text{Đ}'' - \frac{1-\epsilon}{1+z}\text{Đ}' - \frac{3}{2}\frac{\Omega_m}{(1+z)^2}\text{Đ} = (D')^2 D. \tag{2.21e}$$

As above, each D_i should be solved subject to the boundary condition that it matches a matter-only model at $z = z^*$.

Einstein–de Sitter approximation.—It is common to simplify Eqs. (2.18) and (2.20) by exchanging the non-linear growth functions D_i for powers of the linear growth function D. (See Appendix B.3 of Scoccimarro et al. [159].) This procedure is exact for the $\Omega_m = 1$ Einstein–de Sitter model. If we define a growth factor f_i for each D_i by analogy with Eq. (2.17),

$$f_i \equiv -(1+z)\frac{D_i'}{D_i}, \tag{2.22}$$

then the solutions for D_i and f_i in an Einstein–de Sitter model are given in Table 2.1. With these choices the combination $D_A\bar{\alpha}(\mathbf{q},\mathbf{s}) + D_B\bar{\gamma}(\mathbf{q},\mathbf{s})$ in Eq. (2.18) becomes the standard kernel $D^2F_2(\mathbf{q},\mathbf{s})$ and the kernel in Eq. (2.20) becomes $D^3F_3(\mathbf{q},\mathbf{s},\mathbf{t})$ [100, 187, 77, 193, 123, 162, 161]. In Fig. 2.1 we plot the time evolution of the D_i and f_i, calculated for a Planck2015 cosmology [4], relative to the 'Einstein–de Sitter approximation' computed using Table 2.1.[3] At large z the growth functions match the Einstein–de Sitter values

[3] To be clear, note that what we describe as the *Einstein–de Sitter approximation* consists of taking the D_i and f_i to satisfy the relations of Table 2.1 using the appropriate linear $D(z)$ for the cosmology under discussion. We do not use the specific $D(z)$ corresponding to an $\Omega_m = 1$, $\Omega_\Lambda = 0$ Einstein–de Sitter model.

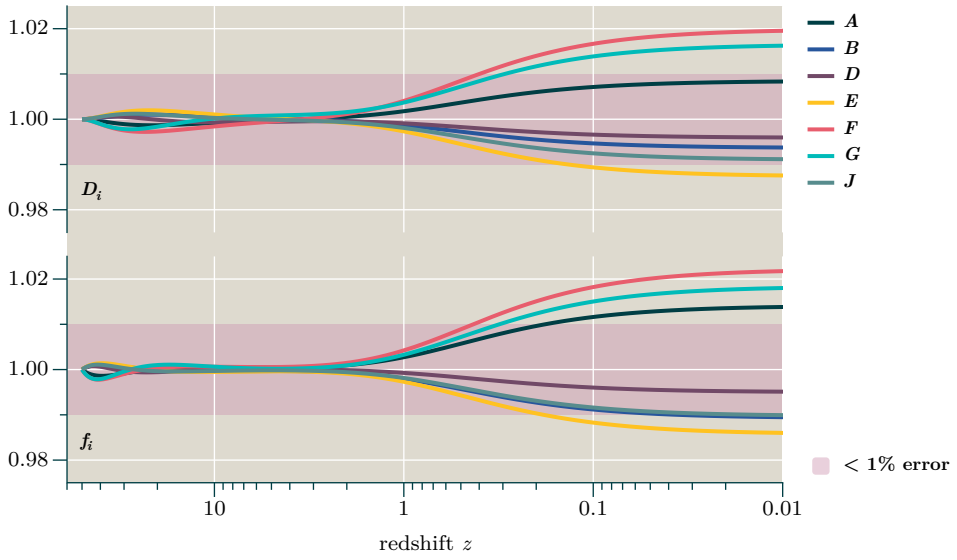

Figure 2.1: Time evolution of the growth functions D_i and growth factors f_i for Planck2015 parameter values [4] relative to the Einstein-de Sitter approximations of Table 2.1. The light pink shaded region shows where the Einstein–de Sitter approximation is accurate to better than 1%. Some jitter is visible near the initial redshift $z^* = 50$, which is caused by slight inaccuracies in our initial conditions. These are set assuming matter domination and neglect the radiation component. The effect is negligible for $z < 1$.

rather closely [159]. At $z \sim 2$, where the vacuum energy becomes significant, they begin to deviate from the Einstein–de Sitter prediction. At low redshift $z \sim 0$ the largest discrepancies are roughly 2%, implying that the full time dependence may be required for very accurate calculations.

In this paper we retain the distinction between the different growth functions, and in §2.3.6 we will quantify the error incurred by the Einstein–de Sitter approximation.

Power spectra.—The two-point function following from Eqs. (2.15), (2.18) and (2.20) was computed by Suto & Sasaki [174], and later for the velocity power spectrum by Makino, Sasaki & Suto [123]; see also Scoccimarro & Frieman [162, 161] and Scoccimarro [158]. Assuming $\delta^*_{\mathbf{k}}$ to be a Gaussian random field there are three contributions, conventionally labelled P_{11}, P_{22} and P_{13},

$$\langle \delta_{\mathbf{k}_1,1} \delta_{\mathbf{k}_2,1} \rangle = (2\pi)^3 \delta(\mathbf{k}_1 + \mathbf{k}_2) P_{11}(k) \tag{2.23a}$$

$$\langle \delta_{\mathbf{k}_1,2} \delta_{\mathbf{k}_2,2} \rangle = (2\pi)^3 \delta(\mathbf{k}_1 + \mathbf{k}_2) P_{22}(k) \tag{2.23b}$$

$$\langle \delta_{\mathbf{k}_1,1} \delta_{\mathbf{k}_2,3} + \delta_{\mathbf{k}_1,3} \delta_{\mathbf{k}_2,1} \rangle = (2\pi)^3 \delta(\mathbf{k}_1 + \mathbf{k}_2) P_{13}(k), \tag{2.23c}$$

where k is the common magnitude of the wavevectors $\mathbf{k}_1$ and $\mathbf{k}_2$, and to prevent clut-

ter we have suppressed the z-dependence of each quantity. The linear contribution P_{11} is described as the tree-level power spectrum, and the sum $P_{22}+P_{13}$ is the one-loop contribution. Defining the initial power spectrum $P^*(k)$ to satisfy $\langle\delta^*_{\mathbf{k}_1}\delta^*_{\mathbf{k}_2}\rangle = (2\pi)^3\delta(\mathbf{k}_1+\mathbf{k}_2)P^*(k)$, these different contributions can be written

$$P_{11}(k) = D^2P^*(k) \tag{2.24a}$$

$$P_{22}(k) = D_A^2P_{AA}(k) + D_AD_BP_{AB}(k) + D_B^2P_{BB}(k) \tag{2.24b}$$

and

$$\begin{aligned}P_{13}(k) = DP^*(k)\Big[&(D_D-\breve{D})P_D(k) + D_EP_E(k) + (D_F+\breve{D})P_F(k)\\ &+ D_GP_G(k) + \frac{\breve{D}}{2}\big[P_{J2}(k) - 2P_{J1}(k)\big]\Big].\end{aligned} \tag{2.24c}$$

The quantities P_i appearing in these expressions are defined by

$$P_{AA} \equiv 2\int\frac{\mathrm{d}^3q}{(2\pi)^3}\bar{\alpha}(\mathbf{k}-\mathbf{q},\mathbf{q})^2P^*(\mathbf{q})P^*(\mathbf{k}-\mathbf{q}) \tag{2.25a}$$

$$P_{AB} \equiv 4\int\frac{\mathrm{d}^3q}{(2\pi)^3}\bar{\alpha}(\mathbf{k}-\mathbf{q},\mathbf{q})\bar{\gamma}(\mathbf{k}-\mathbf{q},\mathbf{q})P^*(\mathbf{q})P^*(\mathbf{k}-\mathbf{q}) \tag{2.25b}$$

$$P_{BB} \equiv 2\int\frac{\mathrm{d}^3q}{(2\pi)^3}\bar{\gamma}(\mathbf{k}-\mathbf{q},\mathbf{q})^2P^*(\mathbf{q})P^*(\mathbf{k}-\mathbf{q}) \tag{2.25c}$$

$$P_D \equiv 8\int\frac{\mathrm{d}^3q}{(2\pi)^3}\bar{\gamma}(\mathbf{k}-\mathbf{q},\mathbf{q})\bar{\alpha}(\mathbf{k},-\mathbf{q})P^*(\mathbf{q}) \tag{2.25d}$$

$$P_E \equiv 8\int\frac{\mathrm{d}^3q}{(2\pi)^3}\bar{\gamma}(\mathbf{k}-\mathbf{q},\mathbf{q})\bar{\gamma}(\mathbf{k},-\mathbf{q})P^*(\mathbf{q}) \tag{2.25e}$$

$$P_F \equiv 8\int\frac{\mathrm{d}^3q}{(2\pi)^3}\bar{\alpha}(\mathbf{k}-\mathbf{q},\mathbf{q})\bar{\alpha}(\mathbf{k},-\mathbf{q})P^*(\mathbf{q}) \tag{2.25f}$$

$$P_G \equiv 8\int\frac{\mathrm{d}^3q}{(2\pi)^3}\bar{\alpha}(\mathbf{k}-\mathbf{q},\mathbf{q})\bar{\gamma}(\mathbf{k},-\mathbf{q})P^*(\mathbf{q}) \tag{2.25g}$$

$$P_{J1} \equiv 8\int\frac{\mathrm{d}^3q}{(2\pi)^3}\alpha(\mathbf{k}-\mathbf{q},\mathbf{q})\bar{\alpha}(\mathbf{k},-\mathbf{q})P^*(\mathbf{q}) \tag{2.25h}$$

$$P_{J2} \equiv 8\int\frac{\mathrm{d}^3q}{(2\pi)^3}\alpha(\mathbf{k}-\mathbf{q},\mathbf{q})\bar{\gamma}(\mathbf{k},-\mathbf{q})P^*(\mathbf{q}) \tag{2.25i}$$

If we replace the growth functions D_i by their Einstein–de Sitter counterparts of Table 2.1 then Eqs. (2.24a)–(2.25i) reproduce the one-loop δ power spectrum reported by Suto et al. [174].

Infrared safety.—Each of these integrals converges individually in the infrared region $q \ll k$ provided $P^*(k)$ is no more divergent than $1/k$ at small k, which is amply satisfied for realistic power spectra. We discuss the ultraviolet region $q \gg k$ in detail in §2.2.3 below.

If $P^*(k)$ diverges in the infrared more strongly than $1/k$ but less than $1/k^3$, Scoccimarro & Frieman [162] demonstrated that any low-q divergences would cancel between the 22 and 13 terms in Galilean-invariant correlation functions. This is part of a more general

cancellation of the low-q contribution [173, 140, 32]. Assuming an Einstein–de Sitter background and focusing on the low-q region we have

$$P_{13} = -\frac{2}{3} D^2 k^2 P^*(k) \int \frac{\mathrm{d}q}{(2\pi)^3} \left[1 + \mathcal{O}\left(\frac{q^2}{k^2}\right)\right] P^*(\mathbf{q}) \tag{2.26a}$$

$$P_{22} = \frac{1}{3} D^2 k^2 \int \frac{\mathrm{d}q}{(2\pi)^3} \left[1 + \mathcal{O}\left(\frac{q^2}{k^2}\right)\right] P^*(\mathbf{q}) P^*(\mathbf{k}-\mathbf{q}). \tag{2.26b}$$

The leading part of (2.26b) comes from regions centred on $\mathbf{q} = 0$ and $\mathbf{q} = \mathbf{k}$ which each give a contribution of the same form as (2.26a), and therefore we have cancellation between these terms. The cancellation between the $\mathcal{O}(q^2/k^2)$ corrections is not exact, so the total one-loop term will diverge in the low-q region if $P^*(k)$ is more divergent than $1/k^3$.

This cancellation means that it is necessary to compute the integrals (2.25a)–(2.25h) with sufficient accuracy that we retain a good estimate of the remainder after cancellation has occurred. Alternatively, they can be grouped in a form in which cancellation is explicit, as described in Ref. [32]. In practice we do not find it is onerous to achieve the required accuracy for realistic input power spectra $P^*(k)$.

2.2.3 Ultraviolet sensitivity and renormalization

Each P_i defined in Eqs. (2.25a)–(2.25i) involves a weighted integral over the power spectrum $P^*(\mathbf{q})$ (or the convolution $P^*(\mathbf{q})P^*(\mathbf{k}-\mathbf{q})$ in the case of integrals contributing to P_{22}), with weighting function given by a combination of the kernels α and γ. The terminology 'one-loop' is borrowed from the diagrammatic expansion of quantum field theory in which similar integrals are encountered. In either case we can regard the loop as an estimate of the average influence of fluctuations over the range $\mathbf{q}$ on the single mode of wavenumber $\mathbf{k}$.

In a free quantum field theory, the typical amplitude of quantum fluctuations of four-momentum q^a decays like $1/q$ for large $|q|$, and therefore the influence of individual high-momentum fluctuations decreases. However, because the number of such fluctuations grows like q^4 their aggregated influence can be very large—indeed, in perturbation theory, the prediction may be unboundedly large. The same behaviour can occur in Eqs. (2.25a)–(2.25i), in which the typical amplitude of fluctuations on scale q decreases like $P^*(q)^{1/2}$. The corresponding contribution to the average may be suppressed or enhanced depending on the details of the weighting function, but since the number of modes grows like q^3 the aggregated effect of high-momentum modes may again be significant or unbounded.

The resolution of this difficulty is to recognize that our predictions for the typical

amplitude of high-wavenumber fluctuations are unreliable.[4] In quantum field theory this is true because of our ignorance of the details of very high energy physics. In applications to structure formation we would (in principle) encounter the same fundamental uncertainty at high enough energies, but in practice our ability to accurately model amplitudes is already compromised at much lower wavenumber because we cannot adequately describe the details of non-linear halo and galaxy formation, gas dynamics, feedback from active galactic nuclei, and so on. Therefore our estimates of the aggregate influence on some low wavenumber $\mathbf{k}$ from much higher wavenumbers $\mathbf{q}$ are not trustworthy even if they are finite.

Although we cannot trust Eqs. (2.25a)–(2.25i) as they stand, we can break them into two parts: first, an integral that aggregates the influence of wavenumbers in a range for which we believe that our estimate of typical amplitudes is adequate; and second, an integral over the remaining $\mathbf{q}$. We cannot evaluate this second integral, but we can parametrize it. Once suitable parameters have been determined, by comparison with observation or simulation, the theory is as predictive as if we had a reliable *ab initio* estimate of the typical amplitude for high-energy fluctuations. This parametrization of unknown high-$\mathbf{q}$ effects is the content of the renormalization programme.

Large q contributions from P_{13} terms.—The first step is to find a suitable parametrization for the ultraviolet part of each integral. The procedure is much the same as for conventional quantum field theory, although complicated by the presence of a time-dependent background.

First consider the large $|\mathbf{q}|$ contributions to $P_D, \ldots, P_{J2}$, given by Eqs. (2.25d)–(2.25i). These contribute to the P_{13} part of the one-loop power spectrum. If there were no time dependence to accommodate, we would express the dimensionless weighting functions in these integrals as a Taylor series in k^2/q^2. Using rotational invariance, it follows immediately that the $q \gg k$ part of each integral can be parametrized as

$$P \overset{\text{UV}}{\supseteq} \sum_{n=0}^{\infty} \frac{k^{2n}}{M_n^{2n}}, \tag{2.27}$$

for some mass scales M_n. (This parametrization may miss effects, associated with the remainder of the Taylor expansion, that vanish for small k faster than any finite power of k. Such effects are not captured by the effective description.[5]) Notice that it does not

[4] In this case, Eqs. (2.25a)–(2.25i) are also unreliable at very low wavenumbers, for which the relativistic corrections in Eqs. (2.2)–(2.4) are no longer small. However, this is an artefact of our gauge choice and may be neglected provided there are no large contributions to the loop from Hubble-scale modes.

[5] In quantum field theory the combination k^2/q^2 is typically replaced by k^2/M^2 for some hard scale M.

matter how we divide the **q** integral and define its untrustworthy $q \gg k$ region, because any change in the division can be absorbed into a redefinition of the mass scales M_n.

The low-energy region $q \lesssim k$ may also generate positive powers of k^2. If so, these are degenerate with the unknown ultraviolet contributions. But unlike the ultraviolet region, the low-energy region may generate terms that are not analytic in k^2. These non-analytic contributions cannot be modified by ultraviolet effects and are unambiguous predictions of the low-energy theory (see, eg., Refs. [53, 54]).

In this picture it would be sufficient to measure six independent mass scales (one for each of $P_D, \ldots, P_{J2}$) for each power of k included in the parametrization. Unfortunately, if our description of the high-wavenumber modes is inadequate to predict their amplitudes, it will also be inadequate to predict their time dependence. Therefore we cannot rely on these modes evolving in the way prescribed by perturbation theory. The result is that, rather than requiring just six numbers to fix the relative size of each contribution to (2.24c), we must allow the coefficient of each power of k to become an arbitrary undetermined function of redshift.[6] This procedure becomes predictive once we have made enough measurements to constrain this function over the redshift range of interest. Depending on the range required this could entail many more than six independent numbers. We will return to this issue in §2.3.6.

The final result must still be independent of how we divide the **q** integrals. For this reason the unknown time-dependent function must contain a component with the same redshift dependence as the $q \gg k$ region of each loop integral. This enables it to subtract any unphysical dependence on the arbitrary upper limit of this region. If we cut off each integral at the same scale Λ, then up to $\mathcal{O}(k^2)$ the $q \gg k$ region of P_{13} behaves like

$$P_{13} \supseteq -DP^*(k)\Big(18D_D + 28D_E - 7D_F - 2D_G - 13\text{Đ}\Big)\frac{k^2}{15\pi^2}\int\limits_{k\ll q\lesssim\Lambda} \mathrm{d}q\, P^*(q) + \cdots\,. \quad (2.28)$$

Notice that the k^0 term is absent [77, 193], which is a consequence of conservation of energy and momentum.[7] Therefore up to $\mathcal{O}(k^2)$ the unknown ultraviolet dependence must take

The remainder term captures effects that are not visible at any finite order in perturbation theory such as $\exp(-M^2/k^2)$.

[6] If we wish, we can apply this statement to each combination such as $D_D(z)P_D(k)$, but all these undetermined functions of time will assemble to give a single undetermined function of time for each term of the form $k^{2n}P^*(k)$ in P_{13}. It is only this single undetermined function that can be constrained. The division of the P_{13} time dependence into D, E, …, J components is part of the structure of low-energy perturbation theory and need not be respected by the ultraviolet terms.

[7] See, eg., Peebles [145]. The argument in this reference amounts to the observation that the large-scale matter distribution feels only tidal effects from small scales. Mercolli & Pajer gave an explicit

the form

$$P_{13} \overset{\text{UV}}{\supseteq} 2D^2k^2P^*(k)\left\{\frac{18D_D + 28D_E - 7D_F - 2D_G - 13\mathcal{D}}{D}Z_{2|\delta} + \zeta_{2|\delta}(z)\right\}$$
$$\equiv -2D^2\frac{k^2}{k_{\rm NL}^2}c_{2|\delta}(z)P^*(k) \tag{2.29}$$

where $Z_{2|\delta}$ is a fixed number of dimension $[\text{mass}]^{-2}$ that effectively takes the place of the mass scale M_n in Eq. (2.27), and $\zeta_{2|\delta}(z)$ is an arbitrary function of z representing any time dependence of the ultraviolet modes that cannot be predicted from perturbation theory at low k. For example, retarded memory effects that are nonlocal in time may contribute to this function [35, 70]. Eq. (2.29) is the *counterterm* needed to renormalize the P_{13} part of the one-loop $\delta\delta$ power spectrum up to k^2.

The quantities $k_{\rm NL}$ and $c_{2|\delta}(z)$ are defined by the second equality in (2.29). Only the combination $c_{2|\delta}/k_{\rm NL}^2$ can be constrained by fitting to data, but the separation of $k_{\rm NL}$ is conceptually useful if all higher-order powers of k are controlled by the same scale. In this case the parametrization orders itself as an expansion in $k/k_{\rm NL}$ with coefficients such as $c_{2|\delta}$ that are not too different from unity. Provided we are satisfied with fixed accuracy, we need only retain sufficiently many terms to make $(k/k_{\rm NL})^{2n}$ suitably small. In this paper we retain only terms up to $\mathcal{O}(k^2)$. We discuss the procedure to fix $c_{2|\delta}$ in §2.2.6.

In principle we can carry this parametrization to as many powers of k as we wish, in which case we would encounter further counterterms involving k^4, k^6, ..., as in Eq. (2.27), all multiplying the combination $D^2P^*(k)$. The time dependence of each term would be analogous to (2.29): a term matching the redshift dependence from the $q \gg k$ part of each integral, and a second arbitrary time-dependent term $\zeta_{4|\delta}$, $\zeta_{6|\delta}$, ..., representing unknown time dependence that cannot be predicted from perturbation theory.

Large q contributions from P_{22} terms.—Now consider the analogous contributions to (2.25a)–(2.25c). These contribute to the P_{22} part of the one-loop power spectrum. Much of the discussion of P_{13} terms also applies to these integrals, with the exception that they do not enter P_{22} in proportion to the input power spectrum $P^*(k)$ as in Eq. (2.29). Instead, their contribution to P_{22} is simply a power series in k^2. After recovery of the correlation function $\xi(\mathbf{r})$ from the Fourier transform of $P(\mathbf{k})$, such powers generate terms proportional to the δ-function $\delta(\mathbf{r})$ and its derivatives. The same applies for 22-type contributions to the power spectrum of any operator, not just δ.

Because these ultraviolet contributions do not enter the power spectrum in combination

demonstration of this property for δ and (under certain circumstances) also the velocity $\mathbf{v}$ [132]. The connexion to tidal forces was made explicitly in §5.2 of Baumann et al. [11].

with $P^*(k)$ they must describe fluctuations that are stochastically independent of δ. To interpret them we should return to the division between a known low-energy sector $q < \Lambda$ and an unknown high-energy sector $q > \Lambda$ described above. These sectors are coupled by processes in which low-energy fluctuations interact to produce high-energy fluctuations or vice-versa. When energy is carried into the high-energy sector by such processes it must be removed from our description, but can later be returned. Because this return of energy is mediated by high-energy interactions it falls below the effective resolution $\sim 1/\Lambda$ of the low-energy description and appears nearly local. In the correlation function its contribution is therefore proportional to $\delta(\mathbf{r})$ and its derivatives, in exactly the manner described above. The presence of such *noise* and *dissipation* effects is well-understood in applications of field theory to condensed matter [67, 27, 28, 29]; for a textbook description, see Kamenev [104]. The application to effective field theories was emphasized by Calzetta & Hu [30, 31].

The conclusion is that we should add extra counterterms that account for fluctuations that are stochastically independent of the long-wavelength part of δ. Baumann et al. called these *stochastic counterterms* [11]. For the $\delta\delta$ power spectrum, the P_{22} contribution for $q \gg k$ begins at $\mathcal{O}(k^4)$. Therefore, in this paper, we assume these stochastic counterterms to be unnecessary at the level of accuracy to which we are working.

2.2.4 Renormalized operators

Renormalized δ operator.—The analysis of §2.2.3 can be rephrased in the language of renormalized operators. By doing so we will able to unify our treatment of the renormalized redshift-space power spectrum with the discussion given here.

The outcome of §2.2.3 was a prescription for computing correlation functions by cutting off each $\mathbf{q}$ integral and parametrizing the ultraviolet region by counterterms. This yields results that are the same as would have been obtained from a modified δ operator that mixes with a $\partial^2\delta$ term,

$$\delta^{\rm R}(\mathbf{x}) = \delta_\Lambda(\mathbf{x}) + \frac{c_{2|\delta}(z)}{k_{\rm NL}^2}\partial^2\delta_\Lambda(\mathbf{x}), \tag{2.30}$$

in which $c_{2|\delta}$ should be treated as one-loop level and therefore any diagram containing $c_{2|\delta}$ need be computed only to tree-level. The subscript Λ is a reminder that loops involving δ_Λ should be cut off for $q \gtrsim \Lambda$. As explained above, the arbitrariness in our choice of Λ can be compensated by a redefinition of the counterterm, but to keep the notation simple we do not write this dependence explicitly. We describe $\delta^{\rm R}$ as the *renormalized* density contrast. If we had retained higher powers k^4, k^6, ..., in the parametrization

of the ultraviolet region then these would appear as mixing with further operators $\partial^4\delta$, $\partial^6\delta$, and so on. In Eq. (2.29) the k^0 term is absent, but if present it would represent a multiplicative adjustment of the normalization of δ on the right-hand side of (2.30); we shall see an example for the velocity power spectrum below. Finally, any stochastic counterterms would appear as additive contributions to δ^{R} that are uncorrelated with δ_Λ.

Renormalized θ operator.—A similar analysis can be given for the velocity. In the potential flow approximation this yields $\mathbf{v} = \mathrm{i}\mathbf{k}(\phi_{\mathbf{k},1} + \phi_{\mathbf{k},2} + \phi_{\mathbf{k},3})$, where

$$\phi_{\mathbf{k},1} = \frac{H}{k^2} f D \delta^*_{\mathbf{k}}, \tag{2.31a}$$

$$\phi_{\mathbf{k},2} = \frac{H}{k^2} \int \frac{\mathrm{d}^3q\,\mathrm{d}^3s}{(2\pi)^6}\, (2\pi)^3\delta(\mathbf{k}-\mathbf{q}-\mathbf{s})\delta^*_{\mathbf{q}}\delta^*_{\mathbf{s}}\Big(D_K(z)\bar\alpha(\mathbf{q},\mathbf{r}) + D_L(z)\bar\gamma(\mathbf{q},\mathbf{r})\Big), \tag{2.31b}$$

and

$$\begin{aligned}\phi_{\mathbf{k},3} = \frac{H}{k^2} \int \frac{\mathrm{d}^3q\,\mathrm{d}^3s\,\mathrm{d}^3t}{(2\pi)^9} (2\pi)^3\delta(\mathbf{k}-\mathbf{q}-\mathbf{s}-\mathbf{t})\delta^*_{\mathbf{q}}\delta^*_{\mathbf{s}}\delta^*_{\mathbf{t}} \\ \times \bigg(2D_M(z)\bar\gamma(\mathbf{s}+\mathbf{t},\mathbf{q})\bar\alpha(\mathbf{s},\mathbf{t}) + 2D_N(z)\bar\gamma(\mathbf{s}+\mathbf{t},\mathbf{q})\bar\gamma(\mathbf{s},\mathbf{t}) \\ + 2D_P(z)\bar\alpha(\mathbf{s}+\mathbf{t},\mathbf{q})\bar\alpha(\mathbf{s},\mathbf{t}) + 2D_Q(z)\bar\alpha(\mathbf{s}+\mathbf{t},\mathbf{q})\bar\gamma(\mathbf{s},\mathbf{t}) \\ + D_R(z)\alpha(\mathbf{s}+\mathbf{t},\mathbf{q})\bar\alpha(\mathbf{s},\mathbf{t}) + D_S(z)\alpha(\mathbf{s}+\mathbf{t},\mathbf{q})\bar\gamma(\mathbf{s},\mathbf{t})\bigg).\end{aligned} \tag{2.31c}$$

The growth functions D_K, …, D_S are defined by

$$D_K \equiv f_A D_A - f D^2, \tag{2.32a}$$

$$D_L \equiv f_B D_B, \tag{2.32b}$$

$$D_M \equiv f_D D_D - f_J \mathcal{D}, \tag{2.32c}$$

$$D_N \equiv f_E D_E, \tag{2.32d}$$

$$D_P \equiv f_F D_F + f_J \mathcal{D} - f D D_A, \tag{2.32e}$$

$$D_Q \equiv f_G D_G - f D D_B, \tag{2.32f}$$

$$D_R \equiv f D^3 + (f - f_A) D D_A - 2 f_J \mathcal{D}, \tag{2.32g}$$

$$D_S \equiv f_J \mathcal{D} + (f - f_B) D D_B. \tag{2.32h}$$

When these functions are replaced by their Einstein–de Sitter counterparts using Table 2.1, the kernels in Eqs. (2.31b) and (2.31c) become the standard expressions $D^2G_2(\mathbf{q},\mathbf{s})$ and $D^3G_3(\mathbf{q},\mathbf{s},\mathbf{t})$ [100, 187, 77, 193, 123, 162, 161].

The one-loop two-point function $\langle v_i v_j\rangle$ can be computed in analogy with §2.2.2, yielding tree, 13 and 22 contributions whose properties match those discussed above. As for

$\langle\delta\delta\rangle$, the ultraviolet $q \gg k$ region of the one-loop integrals must be replaced with a parametrization. This is equivalent to replacing $\mathbf{v}$ with a renormalized velocity,[8]

$$\mathbf{v}^{\mathrm{R}}(\mathbf{x}) = (1 + c_{0|\mathbf{v}})\mathbf{v}_\Lambda(\mathbf{x}) + c_{2|\mathbf{v}}\frac{H}{k_{\mathrm{NL}}^2}\nabla\delta_\Lambda(\mathbf{x}). \tag{2.33}$$

As in Eq. (2.30) we should treat $c_{0|\mathbf{v}}$ and $c_{2|\mathbf{v}}$ as one-loop terms, and therefore it does not matter whether we take $\mathbf{v}$ to mix with $\nabla\delta_\Lambda$ or $\partial^2\mathbf{v}$ because these are related by the tree-level continuity equation (2.8a). The coefficients $c_{0|\mathbf{v}}$ and $c_{2|\mathbf{v}}$ must each contain a component matching the loop-level redshift dependence, and a free function representing the unknown redshift dependence of the ultraviolet modes,

$$c_{0|\mathbf{v}} = \frac{D_R + 2D_S}{fD}Z_{0|\mathbf{v}} + \zeta_{0|\mathbf{v}}(z) \tag{2.34a}$$

$$c_{2|\mathbf{v}} = \Bigg((5f - 12f_A)D_A + (10f - 12f_B)D_B + 12fD^2 - \frac{18f_D D_D + 28f_E D_E - 7f_F D_F - 2f_G D_G - 13f_J \mathcal{D}}{D}\Bigg)Z_{2|\mathbf{v}} + \zeta_{2|\mathbf{v}}(z). \tag{2.34b}$$

(Part of the perturbative time dependence in $c_{2|\mathbf{v}}$ is fixed by the t derivative of the time dependence from $c_{2|\delta}$, but it cannot be expressed as $\mathrm{d}c_{2|\delta}/\mathrm{d}t$ because the coefficient $Z_{2|\mathbf{v}}$ may be different.)

These counterterms are independent of $c_{2|\delta}$. Therfore, as emphasized by Mercolli & Pajer [132], the velocity requires extra counterterms beyond those required to renormalize correlation functions of the density.

Multiplicative renormalization of velocity.—Eq. (2.33) differs from the renormalized density constrast δ^{R} because $\mathbf{v}^{\mathrm{R}}$ mixes not only with the higher-derivative operator $\partial^2\delta$ but also adjusts the normalization of the bare field $\mathbf{v}$ through $c_{0|\mathbf{v}}$. This adjustment is the analogue of field-strength renormalization in quantum field theory, but its appearance here is unexpected because it is known to be absent in Einstein–de Sitter [77, 132].[9] Therefore one might suspect that the combination $D_R + 2D_S$ that controls the perturbative

[8] Notice that each composite operator may have its own, independent counterterms. Formally we couple each composite operator to the Lagrangian with an independent source, and obtain Green's functions for the composite operator by functional differentiation with respect to it. Finally the source is set to zero [91]. Although there is only one operator of the form $\partial^2\delta$, $\partial^4\delta$, $\partial^6\delta$, etc., in the Lagrangian, its coefficient becomes a polynomial in the sources, and this allows the different counterterms to be separated.

[9] The absence of a k^0 term in Einstein–de Sitter has been known empirically for a long time. Mercolli & Pajer showed that this could be justified, without making explicit use of the Einstein–de Sitter background, for a certain microscopic realization of the short-distance velocity field. Although we have not attempted to match our calculation to their microscopic model we believe that our results are not in conflict, since we make different assumptions.

time-dependence of $c_{0|\mathbf{v}}$ could be zero. Although this is not true in general, it *is* always a decaying mode. One can show from Eqs. (2.32g)–(2.32h) and (2.19a)–(2.19b) that

$$D_R + 2D_S = f^*(D^*)^3 \left(\frac{1+z}{1+z^*}\right)^{1/2}, \tag{2.35}$$

where as above a superscript '$*$' indicates evaluation at the time when initial conditions are set for the non-linear evolution. In $\mathbf{v}^{\mathrm{R}}$ this part of the counterterm therefore decays like $(D^*/D)(1+z)^{1/2}/(1+z^*)^{1/2}$, and is identically zero for Einstein–de Sitter in which $z^* \to \infty$. Hence, it is projected out by our choice of initial conditions for the D_i.

In practice, all multiplicative counterterms of this type cancel out of the redshift-space density contrast. Therefore even if we do not adopt Einstein–de Sitter values for the growth factors at the initial time, it is not necessary to introduce an explicit renormalization condition for $c_{0|\mathbf{v}}$.

Renormalized equations of motion.—Similar renormalized counterparts can be defined for each operator appearing in the equations of motion (2.6a)–(2.6c). Beyond linear order this includes the composite operators $\mathbf{v}\delta$ and $(\mathbf{v}\cdot\nabla)\mathbf{v}$. In general, composite operators require extra counterterms to produce finite correlation functions, even when their constituents such as δ and $\mathbf{v}$ have been renormalized [42, 91]. Once renormalized versions have been defined, they may be inserted into Eqs. (2.6a) and (2.6b) to obtain evolution equations. The form of these equations was studied by Mercolli & Pajer, and depends on what relations we take to exist among the counterterms [132].

First consider the continuity equation. For the renormalized operators this reads

$$\frac{\mathrm{d}\delta^{\mathrm{R}}}{\mathrm{d}t} + \nabla\cdot\mathbf{v}^{\mathrm{R}} + \nabla\cdot(\mathbf{v}\delta)^{\mathrm{R}} = \left(\frac{\mathrm{d}c_{2|\delta}}{\mathrm{d}t} + H\left[c_{2|\mathbf{v}} + c_{2|\mathbf{v}\delta}\right]\right)\frac{1}{k_{\mathrm{NL}}^2}\partial^2\delta, \tag{2.36}$$

where we have defined

$$(\mathbf{v}\delta)^{\mathrm{R}} = \mathbf{v}\delta + c_{2|\mathbf{v}\delta}\frac{H}{k_{\mathrm{NL}}^2}\partial^2\delta. \tag{2.37}$$

There is a possible multiplicative renormalization for $\mathbf{v}\delta$, but as for $\mathbf{v}$ it is a decaying mode. Therefore we have omitted it in (2.37). Whether the ordinary continuity equation applies to the renormalized operators depends on whether we take the right-hand side of Eq. (2.36) to vanish.

In general there is no obligation to do so, because we are free to choose the counterterms $c_{2|\delta}$, $c_{2|\mathbf{v}}$ and $c_{2|\mathbf{v}\delta}$ independently. A range of possible choices were surveyed by Mercolli & Pajer [132]. For example, we could use observational data or simulations to measure a velocity correlation function such as $\langle\delta(\mathbf{k}_1)\mathbf{v}(\mathbf{k}_2)\rangle$ or $\langle\mathbf{v}(\mathbf{k}_1)\mathbf{v}(\mathbf{k}_2)\rangle$, and adjust $c_{2|\mathbf{v}}$ to fit the data over some range of k. This is the analogue of an on-shell renormalization scheme.

Alternatively we could impose an arbitrary condition, such as fixing $\langle \mathbf{vv} \rangle$ to a specific value at some wavenumber k_{R}. This would be an analogue of an off-shell scheme such as minimal subtraction. (In an off-shell scheme we require an extra, finite renormalization to express the observable $\mathbf{v}$ in terms of the renormalized operator $\mathbf{v}^{\mathrm{R}}$. We discuss these issues more carefully in §2.2.6.) Depending on our choices, the right-hand side of (2.36) may not be zero.

Second, consider the Euler equation (2.6b). This will become

$$\frac{\mathrm{d}\mathbf{v}^{\mathrm{R}}}{\mathrm{d}t} + \bigl[(\mathbf{v}\cdot\nabla)\mathbf{v}\bigr]^{\mathrm{R}} + 2H\mathbf{v}^{\mathrm{R}} - \frac{1}{a^2}\nabla\Phi^{\mathrm{R}} = \frac{c_s^2(z)}{k_{\mathrm{NL}}^2}\partial^2\delta, \tag{2.38}$$

where c_s^2 is a redshift-dependent function built from the counterterms for each of the operators used in Eqs. (2.6a) and (2.6b). By analogy with the Navier–Stokes equations we can interpret the net counterterm as a viscosity. Its coefficient c_s^2 has dimensions of velocity-squared which justifies the notation, here chosen to match that used in Refs. [11, 34, 33].

Finally, the Poisson constraint (2.6c) is a linear relation between $\nabla^2\Phi$ and δ and is therefore preserved under renormalization. We conclude that renormalization of Φ does not require introduction of any new counterterms.

In Refs. [11, 34, 33, 132], analogues of Eqs. (2.36) and (2.38) were obtained starting from the bare SPT equations (2.6a) and (2.6b) and smoothing them at some arbitrary scale. The smoothed equations parametrize the influence of short-scale modes on those of longer wavelength, and therefore must give the same result as parametrizing the large-$\mathbf{q}$ part of the loop integrals. We should therefore regard equations for renormalized operators, such as Eqs. (2.36) and (2.38), as equivalent to the smoothed equations used in Refs. [11, 34, 33, 132].

In Refs. [165, 116, 148], a smoothing argument was used to obtain the counterterm for δ but composite operators were used to renormalize δ_s. Consequently, it was not immediately clear how these procedures were related. When we discuss the redshift-space density contrast in §2.3 we will employ the methods described in this section, which makes clear that exactly the same procedure is being applied to δ and δ_s.

2.2.5 Resummation schemes

Renormalized operators such as δ^{R} and $\mathbf{v}^{\mathrm{R}}$ correctly parametrize the effect of unknown short-scale modes, but this does not mean that fixed-order perturbation theory in these operators (meaning that we calculate to a fixed order in the loop expansion) will provide

an adequate description. Eqs. (2.25a)–(2.25i) show that the typical magnitude of a loop-level term is set by a weighted integral over the initial power spectrum P^*. For example, Eqs. (2.26a)–(2.26b) show that after making a Taylor expansion in q, each integral can be regarded as a sum of weighted integrals of the form

$$\int_0^\Lambda \frac{\mathrm{d}q}{(2\pi)^3} q^{2n} P^*(q) \tag{2.39}$$

for integer $n \geqslant 0$. In the full power spectrum these terms are enhanced by powers of the growth functions D or D_i.

Contributions with strong ultraviolet weighting $n \gg 0$ will be dominated by the region near the cutoff and can be absorbed by counterterms. But contributions with small n may generate significant contributions from all wavenumbers. Porto, Senatore & Zaldarriaga [151] and Senatore & Zaldarriaga [166] introduced parameters $\epsilon_{s<}$, $\epsilon_{s>}$ and $\epsilon_{\delta<}$ to describe the size of these integrals over different ranges of q,

$$\epsilon_{s<}(z) = k^2 D(z)^2 \int_0^k \frac{\mathrm{d}q}{2\pi^2} P^*(q) \tag{2.40a}$$

$$\epsilon_{s>}(z) = k^2 D(z)^2 \int_k^\Lambda \frac{\mathrm{d}q}{2\pi^2} P^*(q) \tag{2.40b}$$

$$\epsilon_{\delta<}(z) = k^2 D(z)^2 \int_0^\Lambda \frac{\mathrm{d}q}{2\pi^2} q^2 P^*(q). \tag{2.40c}$$

It was shown in Refs. [151, 166] that these parameters could become order unity. Therefore, if they provide an accurate estimate of the size of high-order terms, fixed-order perturbation theory will cease to be a good approximation. Similar difficulties are frequently encountered in field theory. In some cases it is possible to obtain a more statisfactory answer by retaining an infinite subset of terms extending to all orders in the loop expansion. The different strategies for doing so are called resummation schemes.

In practice we will see that although $\epsilon_{s<}$, $\epsilon_{s>}$ and $\epsilon_{\delta<}$ may become individually of order unity, the loop expansion is better behaved because of cancellations. For the real-space density power spectrum to be considered in this section, the effect of resummation is modest—roughly a 2% effect. However, for the redshift-space density power spectrum studied in §2.3 its effects are more significant.

Vlah–Seljak–Chu–Feng resummation

In any practical resummation scheme we require a template that governs the form of some subset of loop corrections to arbitrary order. If the template is sufficiently rigid then it will determine the sum of all terms in the subset from matching to just the lowest few terms of fixed-order perturbation theory. For standard renormalization group flow the template

is provided by the criterion of renormalizability. In other cases, such as factorization in QCD, rigorous theorems control the structure of the high-order terms. For large-scale structure there are not yet any rigorous theorems of this kind but we can still obtain suitable templates from models. The situation is comparable to the use of approximate models to derive properties of correlation functions in QCD [150].

Lagrangian perturbation theory as a model.—The key observation, suggested by Matsubara, is that Lagrangian perturbation theory provides a model from which templates can be derived [125]. In the Lagrangian approach one tracks the displacement $\boldsymbol{\Psi}$ of a particle from some initial comoving location $\mathbf{q}$ to a final location $\mathbf{r}$,

$$\mathbf{r}(\mathbf{q},t) = \mathbf{q} + \boldsymbol{\Psi}(\mathbf{q},t). \tag{2.41}$$

This notation is conventional; note that in this section $\mathbf{q}$ is position-space quantity, and should not be confused with the loop momentum used in Eqs. (2.25a)–(2.25i). The density power spectrum is given in terms of the displacement correlation functions by [24, 181, 182]

$$P(k) = \int \mathrm{d}^3q\, \mathrm{e}^{-\mathrm{i}\mathbf{q}\cdot\mathbf{k}}\Big(\langle \mathrm{e}^{-\mathrm{i}\mathbf{k}\cdot\Delta\boldsymbol{\Psi}}\rangle - 1\Big), \tag{2.42}$$

where $\Delta\boldsymbol{\Psi} \equiv \boldsymbol{\Psi}(\mathbf{q},t) - \boldsymbol{\Psi}(\mathbf{0},t)$. The '$-1$' produces a δ-function that can be dropped at finite wavenumber, while the cumulant expansion theorem can be used to rewrite the expectation of the exponential,

$$P(k) = \int \mathrm{d}^3q\, \mathrm{e}^{-\mathrm{i}\mathbf{q}\cdot\mathbf{k}} \exp\left(\sum_{n=1}^{\infty} \frac{(-\mathrm{i})^n}{n!}\langle(\mathbf{k}\cdot\Delta\boldsymbol{\Psi})^n\rangle_c\right), \tag{2.43}$$

where we have used $\langle\cdots\rangle_c$ to denote a connected correlation function. The Eulerian power spectrum of §2.2.2 can be recovered from Eq. (2.43) by expanding the exponential and collecting terms at the same loop-level [125, 173]. But we can equally regard (2.43) as a template that controls a subset of terms at all orders in the Eulerian loop expansion in terms of the low-order correlation functions of $\Delta\boldsymbol{\Psi}$.

To match the Eulerian power spectrum at one loop requires the two- and three-point correlation functions of $\Delta\boldsymbol{\Psi}$. That gives

$$P(k) = \int \mathrm{d}^3q\, \mathrm{e}^{-\mathrm{i}\mathbf{k}\cdot\mathbf{q}} \exp\left(-\frac{1}{2}k_ik_jA_{ij} + \frac{\mathrm{i}}{6}k_ik_jk_\ell W_{ij\ell} + \cdots\right), \tag{2.44}$$

where A_{ij} and $W_{ij\ell}$ are defined by

$$A_{ij} \equiv \langle[\Delta\boldsymbol{\Psi}(\mathbf{q}) - \Delta\boldsymbol{\Psi}(\mathbf{0})]^2_{ij}\rangle = X(q)\delta_{ij} + Y(q)\hat{q}_i\hat{q}_j. \tag{2.45a}$$

and

$$W_{ij\ell} \equiv \langle[\Delta\boldsymbol{\Psi}(\mathbf{q}) - \Delta\boldsymbol{\Psi}(\mathbf{0})]^3_{ij\ell}\rangle. \tag{2.45b}$$

The lowest-order parts of X and Y are related to the Eulerian power spectrum by

$$X(q) = D(z)^2 \int_0^\infty \frac{\mathrm{d}k}{\pi^2} P^*(k) \left(\frac{1}{3} - \frac{j_1(kq)}{kq}\right) \tag{2.46a}$$

$$Y(q) = D(z)^2 \int_0^\infty \frac{\mathrm{d}k}{\pi^2} P^*(k) j_2(kq), \tag{2.46b}$$

where $j_n(x)$ is the spherical Bessel function of order n. Therefore we can regard X and Y as expansion parameters similar to $\epsilon_{s<}$ $\epsilon_{s>}$, and $\epsilon_{\delta<}$, but with suppression in the region $k \lesssim q$ where the factor multiplying P^* in each integrand is of order $(kq)^2$. For $k \gg q$ the Bessel functions decay, removing any large contributions near the cutoff that may be present in $\epsilon_{\delta<}$. These effects reduce the typical magnitude of high-order loop terms compared to a naïve estimate using (2.40a)–(2.40c).

'Wiggle' and 'no-wiggle' power spectra.—Eqs. (2.44), (2.45a) and (2.46a)–(2.46b) have been used as the basis of a resummation scheme by a number of authors [125, 138, 166, 129, 10, 189, 188]. The scheme originally proposed by Matsubara deduced a template from (2.44) by taking the **q**-independent part of X outside the **q**-integral. This suggests that $P(k)$ should contain a multiplicative damping factor $\exp[-(\epsilon_{s<} + \epsilon_{s>})/3]$. As explained above, this is a 'template' in the sense that the exponential contains terms at all orders in the Eulerian loop expansion but is determined entirely by the Eulerian two-point function. Unfortunately this scheme is quantitatively acceptable only for low k, and causes unphysical overdamping for k in the quasilinear regime of interest [125, 178, 129].

Vlah, Seljak, Chu & Feng proposed an alternative scheme that evades these difficulties [188], based on a division of the power spectrum into 'wiggle' and 'no-wiggle' components. (See also Ref. [23].) These separate the effect of baryonic oscillations from the smooth power spectrum predicted from dark matter alone. We define a 'no-wiggle' form of the initial power spectrum by filtering [188, 10],

$$P^*_{\mathrm{nw}}(k) = \frac{P_{\mathrm{ref}}(k)}{(2\pi\lambda^2)^{1/2}} \int \mathrm{d}\ln q \, \frac{P^*(q)}{P_{\mathrm{ref}}(q)} \exp\left(-\frac{(\ln k/q)^2}{2\lambda^2}\right), \tag{2.47}$$

where $P_{\mathrm{ref}}(k)$ is any suitable smooth reference power spectrum whose broadband power roughly matches P^*. This fixes the normalization of P^*_{nw}. In our numerical work we use the Eisentein & Hu fitting function for the power spectrum with no baryons [59]. The dimensionless scale λ sets the size of the filter window. We use $\lambda = 0.25(k/k_{\mathrm{piv}})^{0.04}$, where $k_{\mathrm{piv}} = 0.05h/\mathrm{Mpc}$ is a fixed reference scale. This choice is intended to match the overall amplitude and scale-dependence suggested in Ref. [188].

Given P^*_{nw}, the 'wiggle' component P^*_{w} is defined by

$$P^*_{\mathrm{w}} \equiv P^* - P^*_{\mathrm{nw}}. \tag{2.48}$$

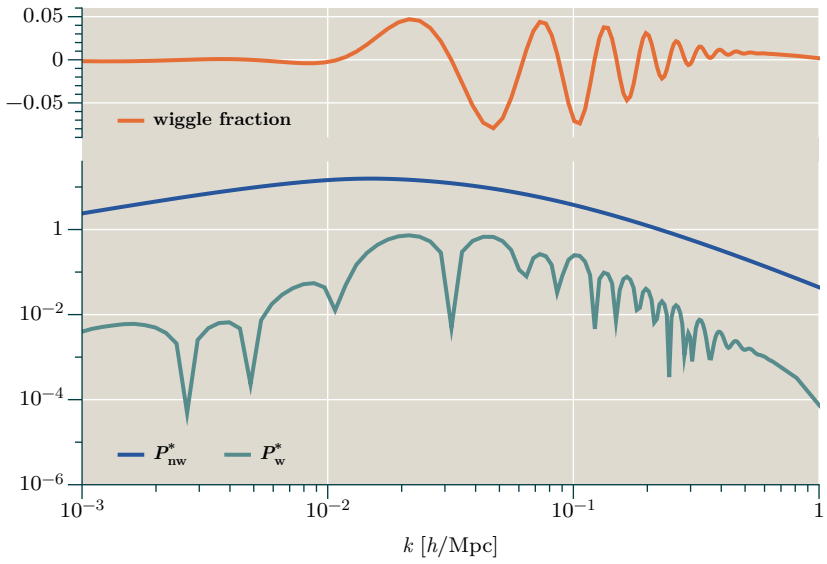

Figure 2.2: **Top panel**: wiggle fraction $P^*_{\rm w}/P^*$. **Bottom panel**: Representative filtered 'wiggle' and 'no-wiggle' power spectra. The initial power spectrum P^* is a Planck2015 cosmology at redshift $z^* = 50$.

We plot the filtered 'wiggle' and 'no-wiggle' components in Fig. 2.2.

Damping the 'wiggle' component.—Once $P^*_{\rm nw}$ has been computed, it can be used to define 'no-wiggle' versions of P_{11}, P_{22} and P_{13}, and corresponding 'wiggle' components by analogy with (2.48). The same can be done for A_{ij} and $W_{ij\ell}$, producing 'wiggle' and 'no-wiggle' components $A^{\rm w}_{ij}$, $A^{\rm nw}_{ij}$, $W^{\rm w}_{ij\ell}$, $W^{\rm nw}_{ij\ell}$.

To extract a template we expand perturbatively, except that we keep the interaction between $A^{\rm nw}_{ij}$ and the 'wiggle' terms to all orders in the Eulerian loop expansion for $A^{\rm nw}_{ij}$. That yields $P^{\leqslant 1\ell}_{vscf}$

$$P^{\leqslant 1\ell}_{vscf}(k) = P^{\leqslant \ell}_{\rm nw} + \int {\rm d}^3q\, {\rm e}^{-{\rm i}\mathbf{k}\cdot\mathbf{q}} \exp\left(-\frac{1}{2}k_ik_jA^{{\rm nw},=\ell 0}_{ij}\right)\left(-\frac{1}{2}k_mk_nA^{{\rm w},\leqslant \ell 1}_{mn} + \frac{\rm i}{6}k_mk_nk_rW^{{\rm w},\leqslant \ell 1}_{mnr}\right), \tag{2.49}$$

where the label '$\leqslant n\ell$' means that the quantity to which it is attached includes terms up to and including level n in the Eulerian loop expansion. If terms at exactly level n are required we write instead '$=n\ell$'. Eq. (2.49) will act as a template if we can rewrite the integral as a combination of the exponential and the 'wiggle' power spectra $P^{=\ell 0}_{\rm w}$ and $P^{=\ell 1}_{\rm w}$.

In general there is no simple way to perform this rewriting. But since the 'wiggle' components have support only over scales near the baryon bump, and $A^{\rm nw}_{ij}$ is relatively slowly varying on these scales, we can *approximately* factorize (2.49) to obtain [189, 188]

$$P^{\leqslant 1\ell}_{vscf}(k) \equiv P^{\leqslant \ell}_{\rm nw} + \exp\left(-\frac{1}{2}\langle\!\langle k_ik_jA^{{\rm nw},=\ell 0}_{ij}\rangle\!\rangle\right)\left(P^{\leqslant \ell}_{\rm w} + \frac{1}{2}\langle\!\langle k_ik_jA^{{\rm nw},=\ell 0}_{ij}\rangle\!\rangle P^{=\ell 0}_{\rm w}\right), \tag{2.50}$$

where $\langle\!\langle k_i k_j A_{ij}^{\mathrm{nw},=\ell 0}\rangle\!\rangle$ is an average of $k_i k_j A_{ij}^{\mathrm{nw},=\ell 0}$ over the range of $\mathbf{q}$ where the 'wiggle' components have support. (We write '$\equiv$' rather than '$=$' to emphasize that this should be regarded as a definition rather than an equality.) The second term in the final bracket has appeared because Eq. (2.48) makes $P_{\mathrm{w}}^{\leqslant\ell}$ contain cross-products between 'wiggle' and 'no-wiggle' components, of which the relevant combination at one-loop is the Zel'dovich-like term $A_{ij}^{\mathrm{w},=\ell 0} A_{mn}^{\mathrm{nw},=\ell 0}$ [173]. This component does not appear in (2.49) and should be subtracted. Its effect makes the expansion of (2.50) up to one-loop agree with the one-loop Eulerian result.

Eq. (2.50) is our template for the resummed power spectrum, with the one-loop terms $P_{\mathrm{nw}}^{\leqslant\ell}$ and $P_{\mathrm{w}}^{\leqslant\ell}$ understood to include counterterms when applied to the effective field theory of §§2.2.3–2.2.4. The precise definition of $\langle\!\langle k_i k_j A_{ij}^{\mathrm{nw},=\ell 0}\rangle\!\rangle$ should be regarded as part of the approximate integration procedure (2.50), but if A_{ij}^{nw} is nearly constant over the relevant $\mathbf{q}$ then any sensible choice will yield nearly the same result. We choose

$$\langle\!\langle k_i k_j A_{ij}^{\mathrm{nw},=\ell 0}\rangle\!\rangle \equiv \frac{k_i k_j}{V(q_{\min}, q_{\max})} \int_{q=q_{\min}}^{q=q_{\max}} \mathrm{d}^3 q \; A_{ij}^{\mathrm{nw}}(\mathbf{q}), \tag{2.51}$$

where $V(a,b)$ is the volume of the three-dimensional spherical shell between radii $r = a$ and $r = b$. We have verified that our results do not strongly depend on the way this integral is weighted. When applied to Eq. (2.45a) and Eqs. (2.46a)–(2.46b) this yields

$$\langle\!\langle k_i k_j A_{ij}^{\mathrm{nw},=\ell 0}\rangle\!\rangle = k^2 \langle\!\langle A^{\mathrm{nw},=\ell 0}\rangle\!\rangle, \tag{2.52}$$

where we have defined

$$\langle\!\langle A^{\mathrm{nw},=\ell 0}\rangle\!\rangle \equiv \frac{D(z)^2}{\pi^2} \frac{1}{q_{\max}^3 - q_{\min}^3} \int_{q_{\min}}^{q_{\max}} \mathrm{d}q \, q^2 \int_0^\infty \mathrm{d}k \, P_{\mathrm{nw}}^*(k) [1 - j_0(kq)]. \tag{2.53}$$

The amplitude of $\langle\!\langle A^{\mathrm{nw},=\ell 0}\rangle\!\rangle$ is inherited from X and Y, which measure the typical amplitude of the displacement $\boldsymbol{\Psi}$ on the scale q. Therefore the degree of damping at momentum k is determined by the ratio k/k_{damp}, where $k_{\mathrm{damp}} \sim \langle\!\langle A^{\mathrm{nw},=\ell 0}\rangle\!\rangle^{-1/2}$ is a wavenumber measuring the typical displacement averaged between the scales $q_{\min}$ and $q_{\max}$. For concrete calculations we choose $q_{\min} = 10h^{-1}\,\mathrm{Mpc}$ and $q_{\max} = 300h^{-1}\,\mathrm{Mpc}$, which roughly bracket the range over which the 'wiggle' component has support in Fig. 2.2. The k-integral is carried up to the same ultraviolet cutoff we use when computing the SPT loops.

The exponential provides efficient damping for $k \gtrsim k_{\mathrm{damp}}$. For a Planck2015-like cosmology we find $k_{\mathrm{damp}} \approx 0.18h/\mathrm{Mpc}$, and by referring to Fig. 2.2 it can be seen that this is comparable to the scales on which baryon acoustic oscillations are visible. Therefore we expect the outcome of this resummation prescription to be modest suppression of these oscillations, while leaving the broadband power unchanged. The underlying physical

reason is that random motions associated with these displacements wash out coherence of the baryon acoustic oscillation [60, 61, 43, 44].

Relation to Senatore–Zaldarriaga resummation.—An alternative resummation prescription was proposed by Senatore & Zaldarriaga [166], which is superficially quite different to the one described here. The relation between these prescriptions was discussed briefly by Vlah et al. [189]. In Appendix 2.A we give a slightly different discussion that emphasizes its relation to the 'wiggle' and 'no-wiggle' filtering procedure described above.

2.2.6 Comparison of results

It was explained in §2.2.5 that the resummed expression Eq. (2.50) is a model, not a theorem about the behaviour of high-order diagrams in SPT. Its utility should be judged on its ability to reproduce observed features of the measured or simulated δ correlation function. In this section we compare Eq. (2.50) with the unresummed effective field theory prediction (2.24a)–(2.24c) and (2.29) and with traditional SPT.

Fitting counterterms.—Like any effective field theory, ours is not predictive until we fix the counterterms. For the δ power spectrum this means that we must assign a value to $c_{2|\delta}/k_{\rm NL}^2$.

As explained in §2.2.4, we can define a renormalized operator $\delta^{\rm R}$ by imposing whatever condition we wish, such as fixing $\langle\delta^{\rm R}\delta^{\rm R}\rangle$ to a prescribed value at some wavenumber $k_{\rm R}$. The physical overdensity would then be related to $\delta^{\rm R}$ by a further finite renormalization, in the same way that the $\overline{\rm MS}$ running mass is related to the physical pole mass by a finite shift. For the level of complexity at which we are working there is nothing to be gained from this freedom, and we may as well choose $\delta^{\rm R}$ to match the observed power spectrum as closely as possible. This was the approach adopted by Carrasco et al. [34, 33]. Therefore we will determine the counterterm by adjusting $\langle\delta^{\rm R}\delta^{\rm R}\rangle$ to match a numerical, non-linear power spectrum over a suitable range of k.

There are several ways this can be done. Carrasco et al. [34, 33] used an ensemble of N-body simulations to estimate the fully non-linear power spectrum. We will adopt this approach in §2.3 when we renormalize the redshift-space power spectrum, for which there is no other way to accurately capture its non-linear effects. For the real-space overdensity there are alternatives, such as use of semianalytic models that are calibrated to match simulations [172, 176]. In this section we illustrate the performance of our models by adjusting the counter-terms to match the **CAMB HALOFIT** power spectrum at $z = 0$ as closely as possible.

Numerical value of $c_{2|\delta}$.—Since we are working at a single redshift there is no need to divide the counterterm into $Z_{2|\delta}$ and $\zeta_{2|\delta}$ components, and we report the single value $c_{2|\delta}(z=0)/k_{\rm NL}^2$.

We estimate the counterterm by performing a least-squares fit over the range $k = 0.15h/\text{Mpc}$ to $k = 0.4h/\text{Mpc}$ where we expect the EFT counterterm to improve the prediction. In Fig. 2.3 we verify that the discrepancy between the one-loop SPT power spectrum P_{SPT} and the **CAMB HALOFIT** power spectrum $P_{\rm NL}$ can be fit by a term with the functional form predicted by the EFT. The red line shows the estimator

$$\frac{c_{2|\delta}}{k_{\rm NL}^2} \approx -\frac{P_{\rm NL} - P_{\mathit{SPT}}}{2k^2 D^2 P^*}, \tag{2.54}$$

which should be approximately k-independent in the fitted region if the predicted functional form is correct. The shaded light-green area shows the region included in the fit, and it can be seen that this region exhibits roughly the expected behaviour. (The oscillations within the shaded region arise from misprediction of the amplitude and phase of the baryon acoustic oscillations, which the EFT counterterm is not expected to improve.) For guidance, the green line shows a power-law fit to the shaded region.

Using a cutoff on the loop momenta of $1.4h/\text{Mpc}$, we find

$$\frac{c_{2|\delta}}{k_{\rm NL}^2} = 1.94h^{-2}\,\text{Mpc}^2 \qquad \text{at } z = 0. \tag{2.55}$$

This compares with the value $(1.62 \pm 0.03)h^{-2}\,\text{Mpc}^2$ reported by Carrasco et al. [33] (although for a different cosmology). In Fig. 2.4 we compare the predictions of SPT with the resummed and unresummed EFT. Our results are consistent with previous analyses, which all found that including the EFT counterterm led to an improved fit [34, 33, 129, 189, 188]. Finally, the suppression of oscillations using the resummed prediction is visible, but improvement in the fit is modest.

2.3 One-loop renormalization of the matter power spectrum in redshift space

Our aim is to use the machinery reviewed in §2.2 to renormalize the two-point function of the redshift-space density contrast, and hence its Legendre multipoles P_ℓ. These are potentially sensitive tests of modified gravity; see, eg., Refs. [95, 26].

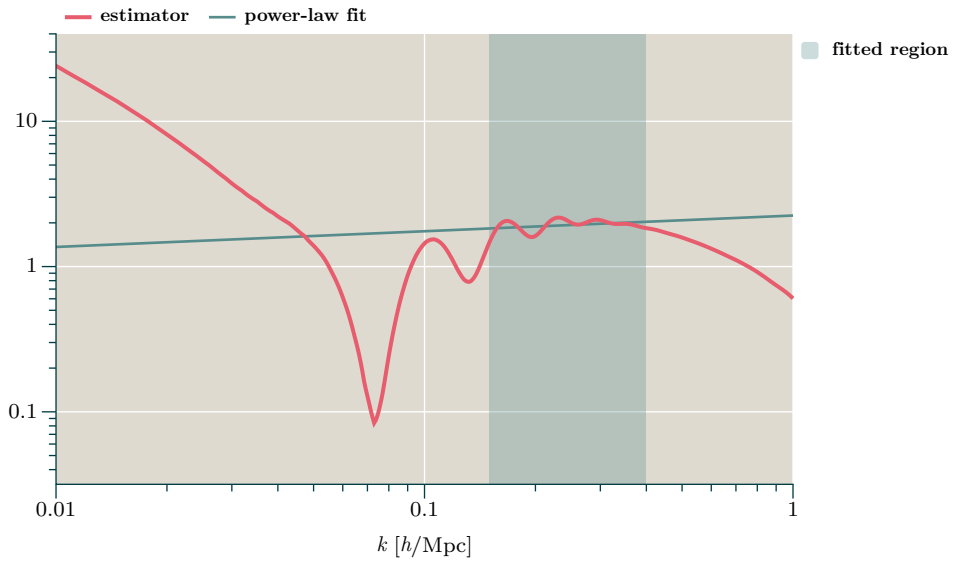

Figure 2.3: Fitting for the counterterm. The red line shows the estimator, $-(P_{\rm NL} - P_{SPT}^{\leqslant \ell 1})/(2k^2 D^2 P^*)$, where $P_{\rm NL}$ is the 'measured' non-linear power spectrum we wish to match. It is approximately constant in a region where the difference between the 1-loop SPT prediction and the measured power spectrum is adequately described by the leading counterterm. To obtain an estimate we optimize the fit in the quasilinear region $0.15h/\text{Mpc} \leqslant k \leqslant 0.4h/\text{Mpc}$, shaded light green, where we expect the EFT counterterm to improve the prediction. The green line shows a least-squares power-law approximation to the estimator in this region, which is $2.246 \times (k/h \times \text{Mpc})^{0.1082}$. As expected, it is nearly k-independent.

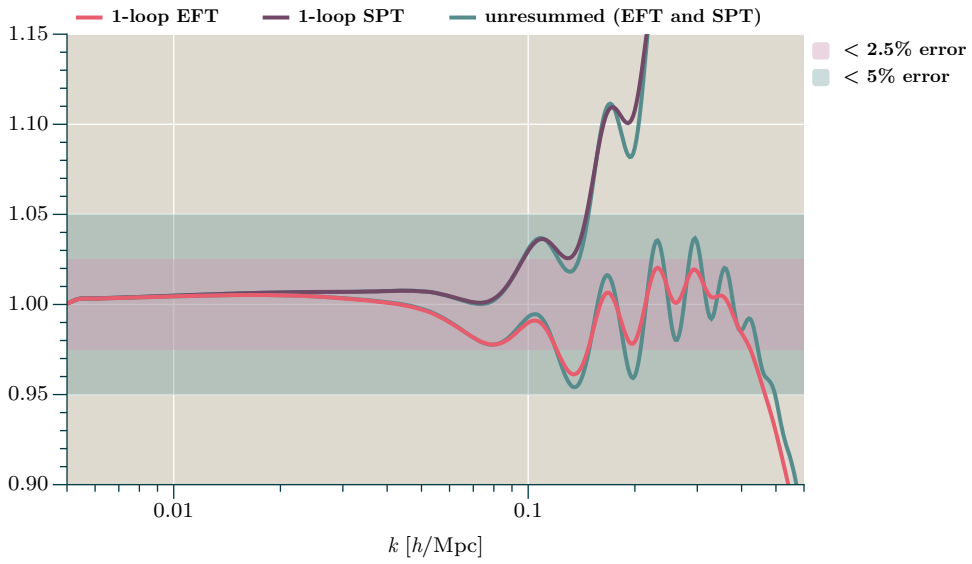

Figure 2.4: Comparison of fit to **CAMB** non-linear (**HALOFIT**) matter power spectrum for 1-loop SPT and 1-loop EFT in their resummed and unresummed variants. The quantity plotted is $P/P_{\rm NL}$, and the cosmology matches the Planck2015 TT+TE+EE+lowP+lensing+ext best-fit parameters [4]. The light-pink region marks where the prediction is within 2.5% of the **CAMB** power spectrum, and the light-green region marks where it is within 5%.

2.3.1 The redshift-space density contrast

Inclusion of redshift-space effects for the two-point function is now well-understood [103, 117, 128, 40]. If the Hubble flow accounted for the entire recession velocity $\mathbf{v}_\mathrm{r}$ of an object at distance $\mathbf{r}$ then it would follow that $\mathbf{v}_\mathrm{r} = H\mathbf{r}$. In practice each object is also embedded in the flow $\mathbf{v}$ described in §2.2.1, and therefore its recession velocity is modified so that $\mathbf{v}_\mathrm{r} = H\mathbf{r} + (\mathbf{v}\cdot\hat{\mathbf{r}})\hat{\mathbf{r}}$. A galaxy survey that measures the redshift corresponding to $\mathbf{v}_\mathrm{r}$ and uses it to infer a distance based on the Hubble flow will assign this galaxy a displaced radial position,

$$\mathbf{s} = \mathbf{r} + \frac{\mathbf{v}\cdot\hat{\mathbf{r}}}{H}\hat{\mathbf{r}}. \tag{2.56}$$

These displacements systematically distort the measured overdensity field.

Redshift-space overdensity.—The mapping between $\mathbf{r}$ and $\mathbf{s}$ conserves mass. Using this property and Eq. (2.56), Scoccimarro showed that [158]

$$\delta_s(\mathbf{k}) = \delta(\mathbf{k}) + \int \mathrm{d}^3 r\; \mathrm{e}^{-\mathrm{i}\mathbf{r}\cdot\mathbf{k}}\left[\exp\left(-\frac{\mathrm{i}}{H}(\mathbf{k}\cdot\hat{\mathbf{r}})[\mathbf{v}(\mathbf{r})\cdot\hat{\mathbf{r}}]\right)\right][1+\delta(\mathbf{r})]. \tag{2.57}$$

As for any operator, it is necessary to exchange δ_s for a renormalized operator $(\delta_s)^\mathrm{R}$ containing counterterms that describe the unknown ultraviolet part of its loop integrals. Because (2.57) is a composite operator in the language of §2.2.4 these counterterms are not fixed by our definition of δ^R. By analogy with (2.30), (2.33) and (2.37) we expect that $(\delta_s)^\mathrm{R}$ could involve both multiplicative renormalization and mixing with $\partial^2\delta$. As in §2.2 we will parametrize ultraviolet effects only up to $\mathcal{O}(k^2)$, and therefore we neglect mixing with $\partial^4\delta$ or higher-derivative operators. In §2.3.6 we determine an upper limit on the region where this approximation is valid.

We will verify below that there is no multiplicative renormalization. In principle there are decaying contributions from $\mathbf{v}$ and $\mathbf{v}\delta$, but these are projected out by our boundary conditions for the D_i as explained in §2.2.2. Therefore, up to one loop, we have

$$(\delta_s)^\mathrm{R} = \delta_s + \frac{c_{2|\delta_s}}{k_\mathrm{NL}^2}\partial^2\delta. \tag{2.58}$$

Inspection of (2.57) shows that the Eulerian expansion of δ_s can be written in the form

$$\delta_s(\mathbf{k}) = \sum_n \hat{r}_{i_1}\cdots\hat{r}_{i_{2n}}(\delta_{s,2n})_{i_1\cdots i_{2n}}, \tag{2.59a}$$

where $(\delta_{s,2n})_{i_1\cdots i_{2n}}$ is an operator that transforms as a rank-$2n$ tensor under spatial rotations. When inserted in a correlation function, isotropy of the background will convert contraction over $i_1\cdots i_{2n}$ into a sum of powers of $\mu^2 = (\hat{\mathbf{k}}\cdot\hat{\mathbf{r}})^2$ with highest power μ^{2n}. Therefore, although δ_s does not itself admit a series expansion in μ^2, the counterterms

needed to make its correlation functions finite will do so. It follows that $c_{2|\delta_s}$ can be written in the form

$$c_{2|\delta_s} = \sum_n c_{2|\delta_s,2n}\mu^{2n}. \tag{2.59b}$$

There is one counterterm for each available power of μ, although these need not be independent at every order in the loop expansion. As usual we expect that averages over ultraviolet modes should respect the symmetries of the low-energy theory and therefore renormalization will not generate odd powers of μ.

One-loop formulae.—To compute $\langle\delta_s\delta_s\rangle$ to one-loop we calculate the expansion (2.59a), dropping operators that contribute only at two loops or higher. This yields [84, 160, 125, 165, 116]

$$\begin{aligned}[\delta_s]_{\mathbf{k}} = [\delta]_{\mathbf{k}} - \frac{\mathrm{i}}{H}(\mathbf{k}\cdot\hat{\mathbf{r}})[\hat{\mathbf{r}}\cdot\mathbf{v}]_{\mathbf{k}} - \frac{\mathrm{i}}{H}(\mathbf{k}\cdot\hat{\mathbf{r}})[\hat{\mathbf{r}}\cdot\mathbf{v}\delta]_{\mathbf{k}} + \frac{1}{2!H^2}(\mathbf{k}\cdot\hat{\mathbf{r}})^2[(\hat{\mathbf{r}}\cdot\mathbf{v})^2]_{\mathbf{k}} \\ + \frac{1}{2!H^2}(\mathbf{k}\cdot\hat{\mathbf{r}})^2[(\hat{\mathbf{r}}\cdot\mathbf{v})^2\delta]_{\mathbf{k}} + \frac{\mathrm{i}}{3!H^3}(\mathbf{k}\cdot\hat{\mathbf{r}})^3[(\hat{\mathbf{r}}\cdot\mathbf{v})^3]_{\mathbf{k}} + \cdots.\end{aligned} \tag{2.60}$$

We have adopted the notation of Ref. [165] in which $[f]_{\mathbf{k}}$ denotes the Fourier transform of f. In principle, based on simple power-counting of $\hat{\mathbf{r}}$, Eq. (2.60) may produce powers of μ^2 up to μ^6, but in practice we will see that for the two-point function at one-loop the highest-order term is absent.

Eq. (2.60) was used by Matsubara [125], and rederived by Senatore & Zaldarriaga [166]. In Refs. [166, 116] the continuity equation was used to exchange the $\mathbf{v}$ and $\mathbf{v}\delta$ terms for $\dot{\delta}$, but this is only possible under the assumption that it is $\boldsymbol{\pi}$ rather than $\mathbf{v}$ that can be written as potential flow. The two are not equivalent, and in SPT the potential flow approximation is normally applied only to $\mathbf{v}$. Therefore we should retain $\mathbf{v}$ and $\mathbf{v}\delta$ separately in Eq. (2.60). With this choice our final result will match that derived by Matsubara after replacing all growth functions by their Einstein–de Sitter counterparts [125]. It also agrees with Perko et al. [148], in which the terms $\mathbf{v}$ and $\mathbf{v}\delta$ were retained.

Role of composite operators.—Eq. (2.60) can be considered as a single composite operator renormalized by the counterterm $c_{2|\delta_s}$. Alternatively, as emphasized in Refs. [165, 116, 148], it may be regarded as a sum of δ and $\mathbf{v}$ with composite operators $\mathbf{v}\delta$, $\mathbf{vv}$, $\mathbf{vv}\delta$ and $\mathbf{vvv}$. In this second point of view we require new renormalization conditions to define $(\mathbf{v}\delta)^{\mathrm{R}}$, $(\mathbf{vv})^{\mathrm{R}}$, $(\mathbf{vv}\delta)^{\mathrm{R}}$ and $(\mathbf{vvv})^{\mathrm{R}}$, in addition to those already used to define δ^{R} and $\mathbf{v}^{\mathrm{R}}$.

As usual, we are free to choose these new renormalization conditions in any convenient fashion. In an 'off shell' scheme we impose arbitrary conditions unrelated to any measured correlation function. Further finite renormalizations would be required at each power of μ^2

to match this off-shell $(\delta_s)^{\mathrm{R}}$ to an observable quantity.[10] Alternatively, we might choose to adjust the definition of one or more composite operators in such a way that $(\delta_s)^{\mathrm{R}}$ is matched to some measured correlation function. This is the choice made in Refs. [116, 148]. If δ_s is broken into a sum of many composite operators then our renormalization conditions need not fix the definition of each operator uniquely. Therefore we should expect degeneracies. These merely reflect the division of δ_s into a collection of independent operators, when only the sum has physical significance. By writing the counterterms as the coefficients of a series expansion in μ^2 we avoid explicit degeneracies of this kind.

The price paid for this convenience is a possibility of overcounting. The requirement that (2.60) is renormalized by mixing with a set of local operators obeying the symmetries of the theory—principally, rotational invariance and Galilean invariance—places restrictions on the $c_{2|\delta_s,2n}$. By explicit calculation using Eqs. (2.82a)–(2.82e) below, or by using the operator product expansion (as in Refs. [165, 116]) to determine how the composite operators in (2.60) mix with $\partial^2\delta$ at one loop, we find that at one-loop level the counterterms satisfy the constraints

$$c_{2|\delta_s,6} = f^3 c_{2|\delta_s,0} - f^2 c_{2|\delta_s,2} + f c_{2|\delta_s,4}, \tag{2.61a}$$

$$c_{2|\delta_s,8} = 0. \tag{2.61b}$$

Therefore (neglecting stochastic counterterms) there is no renormalization of μ^8 at one-loop.

Counterterms for the one-loop power spectrum.—We define the renormalized redshift-space power spectrum P_s^{R} by

$$\langle [\delta_s]^{\mathrm{R}}_{\mathbf{k}_1} [\delta_s]^{\mathrm{R}}_{\mathbf{k}_2} \rangle = (2\pi)^3 \delta(\mathbf{k}_1 + \mathbf{k}_2) P_s^{\mathrm{R}}(k), \tag{2.62}$$

where $k = |\mathbf{k}_1| = |\mathbf{k}_2|$. Bearing the foregoing discussion in mind, it follows that the renormalized δ_s two-point function at one-loop can be written

$$P_s^{\mathrm{R}} = P_s^{SPT,\Lambda} - 2 \sum_{n=0}^{3} c_{2|\delta_s,2n} \mu^{2n} \frac{k^2}{k_{\mathrm{NL}}^2} P, \tag{2.63}$$

where $P_s^{\mathrm{SPT},\Lambda}$ is the one-loop SPT power spectrum following from Eq. (2.60) with the loop integrals cut off at $q \sim \Lambda$. The counterterms $c_{2|\delta_s,0}$, $c_{2|\delta_s,2}$, $c_{2|\delta_s,4}$ and $c_{2|\delta_s,6}$ can be chosen independently subject to the condition (2.61a). (We have dropped the counterterm for μ^8, which is necessarily absent.) However, because δ_s at $\mu = 0$ is equal to δ we will find $c_{2|\delta_s,0} = c_{2|\delta}$.

[10] In Ref. [165], some of the counterterms appearing in the definition of $(\mathbf{vv})^{\mathrm{R}}$, $(\mathbf{vv}\delta)^{\mathrm{R}}$ and $(\mathbf{vvv})^{\mathrm{R}}$ were equated. This choice is too restrictive, as recognized in Refs. [116, 148].

Comparison with Lewandowski et al.—Eq. (2.63) should be compared with Eq. (2.15) of Lewandowski et al. [116]. In this reference, the renormalized δ_s power spectrum was expressed in the form

$$P_s^{\mathrm{R}} = P_s^{SPT,\Lambda} - 2(2\pi)D^2\Big[c_s^2 + \mu^2\Big(2fc_s^2 + \frac{1}{H}\frac{\mathrm{d}c_s^2}{\mathrm{d}t} + \frac{1}{2}\bar{c}_1^2\Big) + \mu^4\Big(f^2c_s^2 + \frac{f}{H}\frac{\mathrm{d}c_s^2}{\mathrm{d}t} + \frac{f}{2}\bar{c}_1^2 + \frac{1}{2}\bar{c}_2^2\Big) + \frac{f}{2}\bar{c}_2^2\mu^6\Big]\frac{k^2}{k_{\mathrm{NL}}^2}P. \tag{2.64}$$

with $P_s^{SPT,\Lambda}$ now understood to be evaluated in the Einstein–de Sitter approximation where all growth functions are replaced by their counterparts from Table 2.1. The counterterms are c_s, $\bar{c}_1$ and $\bar{c}_2$, with $\bar{c}_1$ and $\bar{c}_2$ constructed from degenerate combinations of the counterterms for the composite operators appearing in (2.60) as explained above. Notice that, despite its appearance, the c_s used here does not equal the effective speed of sound appearing in the renormalized Euler equation (2.38). Finally, as usual, D is the linear growth factor.

Eq. (2.64) can be used to map the counterterms $c_{2|\delta_s,2n}$ used in this paper to their counterparts in Ref. [116]. At order-μ^2 it contains contributions involving the μ^0 counterterm c_s and its time derivative $\dot{c}_s$. These appear because Ref. [116] used the continuity equation to eliminate $\mathbf{v}$ and $\mathbf{v}\delta$ in favour of the time derivative $\dot{\delta}$, and included the counterterms for $(\dot{\delta})^{\mathrm{R}}$ among the contributions at μ^2. As explained above, we believe this exchange is not compatible with the assumptions used to obtain Eqs. (2.7a)–(2.7b); instead, $\mathbf{v}$ and $\mathbf{v}\delta$ should be retained separately.

To compute the time derivative $\dot{c}_s$, it was assumed in Ref. [116] that $c_s^2 \propto D^{8/3}$. With this choice, and neglecting further differences in time-dependent factors, the relations are

$$c_{2|\delta_s,0} = 2\pi c_s^2, \tag{2.65a}$$

$$c_{2|\delta_s,2} = 2\pi\Big(\frac{14f}{3}c_s^2 + \frac{1}{2}\bar{c}_1^2\Big), \tag{2.65b}$$

$$c_{2|\delta_s,4} = 2\pi\Big(\frac{11f^2}{3}c_s^2 + \frac{f}{2}\bar{c}_1^2 + \frac{1}{2}\bar{c}_2^2\Big), \tag{2.65c}$$

$$c_{2|\delta_s,6} = \pi f\bar{c}_2^2. \tag{2.65d}$$

Note that these quantities satisfy the linear constraint (2.61a).

2.3.2 Evaluation of the one-loop two-point function

The principal challenge is to compute the one-loop two-point function $P_s^{\mathrm{SPT},\Lambda}$. The calculation is technically straightforward, but very lengthy. Its complexity arises partly from the number of terms that appear in (2.60), but also from the fact that the loop integrals

for the composite operators $\mathbf{v}\delta$, $\mathbf{vv}$, $\mathbf{vv}\delta$ and $\mathbf{vvv}$ are tensorial. In this section we collect the necessary expressions. The computation was first performed by Matsubara using the Einstein–de Sitter approximation described on p.37. Here we give the result with its exact time dependence for the first time.

To simplify the computation we introduce a new method to evaluate the tensor integrals. Matsubara's computation used the traditional approach of rotational covariance to reduce these integrals to scalar form-factors multiplying fixed tensors with the correct transformation properties under rotations. To solve for these form-factors one applies suitable contractions to yield a system of scalar simultaneous equations. This is a standard method, widely used to reduce tensor integrals in field theory [192]. The disadvantage is that the final step of solving for the scalar form-factors can be algebraically expensive. As we now describe, our new method simplifies the calculation by extracting the form factors directly.

Application to 22 integrals.—To illustrate the method, consider the 22-type integration arising from the $\langle[\mathbf{v}\delta]_{\mathbf{k}_1}[\mathbf{v}\delta]_{\mathbf{k}_2}\rangle$ contribution to $\langle\delta_s\delta_s\rangle$. Then

$$P_s(k) \supseteq -f^2D^4k^2\mu^2\int\frac{\mathrm{d}^3q}{(2\pi)^3}\frac{\mathrm{d}^3s}{(2\pi)^3}(2\pi)^3\delta(\mathbf{q}+\mathbf{s}-\mathbf{k}_1)P^*(q)P^*(s)\hat{r}_i\hat{r}_j\left(\frac{q_iq_j}{q^2s^2}-\frac{q_iq_j}{q^4}-\frac{q_ik_{1j}}{q^2s^2}\right) \tag{2.66}$$

In principle the term q_ik_{1j} should be symmetrized over i and j, but since it is contracted with the symmetric combination $\hat{r}_i\hat{r}_j$ there is no need to do so explicitly.

Now replace the δ-function by its Fourier representation, and expand the resulting exponential using the Rayleigh plane wave formula,

$$\mathrm{e}^{\mathrm{i}\mathbf{k}\cdot\mathbf{x}} = \sum_{\ell=0}^{\infty}(2\ell+1)\mathrm{i}^\ell j_\ell(kx)\mathscr{P}_\ell(\hat{\mathbf{k}}\cdot\hat{\mathbf{x}}). \tag{2.67}$$

Here, j_ℓ is the spherical Bessel function of order ℓ and $\mathscr{P}_\ell(x)$ is the ℓ^{th} Legendre polynomial. That yields

$$\begin{aligned}P_s(k) \supseteq{}& -f^2D^4k^2\mu^2\int\frac{\mathrm{d}^3q}{(2\pi)^3}\frac{\mathrm{d}^3s}{(2\pi)^3}\,\mathrm{d}^3x\;P^*(q)P^*(s)\\ &\times\left[\left(\frac{2}{3}\mathscr{P}_2(\hat{\mathbf{q}}\cdot\hat{\mathbf{r}})+\frac{1}{2}\mathscr{P}_0(\hat{\mathbf{q}}\cdot\hat{\mathbf{r}})\right)\left(\frac{1}{s^2}-\frac{1}{q^2}\right)-\frac{k\mu}{qs^2}\mathscr{P}_1(\hat{\mathbf{q}}\cdot\hat{\mathbf{r}})\right]\\ &\times\sum_{\ell,\ell',\ell''}(2\ell+1)(2\ell'+1)(2\ell''+1)\mathrm{i}^{\ell+\ell'+\ell''}j_\ell(sx)j_{\ell'}(kx)j_{\ell''}(qx)\mathscr{P}_\ell(\hat{\mathbf{s}}\cdot\hat{\mathbf{x}})\mathscr{P}_{\ell'}(-\hat{\mathbf{k}}_1\cdot\hat{\mathbf{x}})\mathscr{P}_{\ell''}(\hat{\mathbf{q}}\cdot\hat{\mathbf{x}}).\end{aligned} \tag{2.68}$$

The angular part of the $\mathbf{q}$, $\mathbf{s}$ and $\mathbf{x}$ integrations can be done using the generalized orthogonality relation

$$\int\mathrm{d}^2\hat{\mathbf{x}}\;\mathscr{P}_\ell(\hat{\mathbf{a}}\cdot\hat{\mathbf{x}})\mathscr{P}_{\ell'}(\hat{\mathbf{b}}\cdot\hat{\mathbf{x}}) = \frac{4\pi}{2\ell+1}\delta_{\ell\ell'}\mathscr{P}_\ell(\hat{\mathbf{a}}\cdot\hat{\mathbf{b}}). \tag{2.69}$$

The result is

$$P_s(k) \supseteq -f^2 D^4 k^2 \mu^2 8 \mathscr{P}_2(-\mu) \int \frac{q^2 s^2 \, \mathrm{d}q \, \mathrm{d}s}{(2\pi)^3} P^*(q) P^*(s) \left[\frac{2}{3} \left(\frac{1}{s^2} - \frac{1}{q^2} \right) \mathscr{J}^2_{20} + \frac{k\mu}{qs^2} \mathscr{J}^2_{11} \right], \tag{2.70}$$

where we have defined the 3-Bessel integral $\mathscr{J}^\mu_{\nu\sigma}$ by

$$\mathscr{J}^\mu_{\nu\sigma} \equiv \int_0^\infty \mathrm{d}x \; x^2 j_\mu(kx) j_\nu(qx) j_\sigma(sx). \tag{2.71}$$

To reduce clutter we have suppressed explicit dependence on the wavenumbers k, q and s, but this should be understood via the associations $\mu \mapsto k$, $\nu \mapsto q$ and $\sigma \mapsto s$. The problem of computing these integrals analytically for general k, q and s and arbitrary orders μ, ν and σ was solved by Gervois & Navelet [74] and Fabrikant [62]. We summarize Fabrikant's method in Appendix 2.B, and as part of the bundle of software products accompanying this paper we include a Mathematica notebook that implements the computation.

In general, the $\mathscr{J}^\mu_{\nu\sigma}$ vanish except where k, q and s satisfy the triangle condition $|k-q| < s < |k+q|$. Accordingly we may write $s = (q^2 + k^2 - 2kq\cos\theta)^{1/2}$ and change variable from s to θ. Therefore the $\mathscr{J}^\mu_{\nu\sigma}$ can be regarded as enforcing the δ-function $\delta(\mathbf{q} + \mathbf{s} - \mathbf{k}_1)$ with which we began. The result is a scalar integral over q and θ. The complexities of all tensor form factors have been absorbed by the Legendre polynomial $\mathscr{P}_2(-\mu)$. In more general cases we may encounter a sum of Legendre polynomials if the integrals over $\hat{\mathbf{q}}$, $\hat{\mathbf{s}}$ and $\hat{\mathbf{x}}$ generate nonzero contributions for more than one assignment of ℓ, ℓ' and ℓ''.

Comparison with method of covariance.—Had we used rotational covariance, the first step would have been to introduce form-factors A and B and express the integral (2.66) in the form $A\delta_{ij} + B\hat{k}_{1i}\hat{k}_{1j}$. Next, this should be converted to a system of scalar equations by taking suitable contractions with i and j. Finally, after solving this system for A and B we contract with $\hat{r}_i\hat{r}_j$ to yield the final result $\mu^2 B + A$. The solution will have $A = -B/3$, allowing it to be expressed in the form $-2\mathscr{P}_2(\mu)A$ and reproducing the conclusion of Eq. (2.70). This approach becomes cumbersome because of the manipulations needed to extract the scalar integral A. In our new method these manipulations are replaced by the requirement to compute the integrals $\mathscr{J}^\mu_{\nu\sigma}$, but these are easy to tabulate in advance. The substitution can be automated using a symbolic algebra tool such as Mathematica.

In more complex cases the saving is greater. As the tensor structures become more elaborate, the method of rotational covariance would require us to introduce an increasing number of form factors and decouple the resulting equations. In contrast, the method described here does not suffer from a corresponding increase in algebraic complexity; these

more elaborate structures merely manifest themselves in the appearance of higher-order Legendre polynomials generated by the $\hat{\mathbf{q}}$, $\hat{\mathbf{s}}$ and $\hat{\mathbf{x}}$ integrals. Using Fabrikant's method, the corresponding $\mathscr{J}^{\mu}_{\nu\sigma}$ are no harder to obtain than those of lower order.

A similar procedure can be used to compute any 22-type integral. In some cases we encounter products of Legendre polynomials of the same argument. In order to use the orthogonality relation such products must be rewritten as a sum of individual Legendre polynomials, which can be accomplished using the Neumann–Adams formula or an equivalent [136, 3, 8].

Application to 13 integrals.—A very similar procedure can be used to perform 13-type integrals. These are typically simpler because they involve integration only over $P^*(q)$, not $P^*(q)P^*(|\mathbf{k}-\mathbf{q}|)$ as for a 22-type integral, and therefore the analogue of the $\mathbf{s}$-integral in Eq. (2.66) can be performed analytically using the Fourier transform $\int \mathrm{d}^3 s\, s^{-2} \mathrm{e}^{\mathrm{i}\mathbf{s}\cdot\mathbf{x}} = 2\pi^2/x$. Consequently, 13-type integrals require only 2-Bessel integrals of the form

$$\mathscr{J}_{\mu} \equiv \int_0^{\infty} \mathrm{d}x\; x j_{\mu}(kx) j_{\mu}(qx), \tag{2.72}$$

and not the 3-Bessel form (2.71). Tabulated analytic results for such integrals are relatively easy to obtain; for example, integrals of this type can be performed by Mathematica. (It is also possible to evaluate them by the method described in Appendix 2.B.)

Alternative evaluation techniques.—We remark that the procedure described in this section can be regarded as an alternative to the FAST-PT algorithm recently proposed by McEwen et al. [127, 65]. A similar algorithm was suggested by Schmittful & Vlah [156, 155]. These methods also utilise the Rayleigh expansion (2.67), and agree with our computation of the 13-type integrals. For the 22 case, however, the FAST-PT approach involves re-ordering the integrals to obtain [cf. (2.70)]

$$\int \mathrm{d}q\, \mathrm{d}s\; q^{2+\alpha} s^{2+\beta} P^*(q) P^*(s)\, \mathscr{J}^{\mu}_{\nu\sigma} = \int \mathrm{d}x\; x^2 j_{\mu}(kx) I_{\alpha\nu}(x) I_{\beta\sigma}(x), \tag{2.73}$$

where $I_{\alpha\nu}(x) \equiv \int \mathrm{d}q\, q^{2+\alpha} j_{\nu}(qx) P^*(q)$ is a Hankel transform of the initial power spectrum P^*. This should be contrasted with the direct evaluation of $\mathscr{J}^{\mu}_{\nu\sigma}$ described in Appendix 2.B.

In FAST-PT the computation is reduced to numerical evaluation of the one-dimensional transforms $I_{\alpha\nu}(x)$ and the final one-dimensional x-integral in (2.73). This algorithm therefore has complexity $\mathcal{O}(N_1 \log N_1)$. In comparison, our strategy of direct evaluation leaves a two-dimensional integral over q and s (or q and θ after imposing the triangle condition), and therefore has approximate complexity $\mathcal{O}(N_2^2)$. Notice that the constants N_1 and N_2

measuring the size of the integrals can be different; in practice, we find that $N_2 \sim 10^2$ whereas N_1 is at least an order of magnitude larger. This typically renders the methods equally fast. An advantage of direct evaluation is that (as much as possible) it preserves the algebraic structure of the integrals. In addition, because the Bessel integrals are performed analytically, there are no complications related to convergence of the Hankel transforms $I_{\alpha\nu}$.

Tree-level.—We now summarize the outcome of the complete computation. To all orders, the tree-level contribution is the Kaiser formula,

$$P_s \supseteq D^2(1+f\mu^2)^2 P^*. \tag{2.74}$$

22-type terms.—At loop level we organize the calculation by defining coefficients of a series expansion in μ,

$$P_s \equiv \sum_{n=0}^{\infty} P_{s,2n}\mu^{2n}. \tag{2.75}$$

As explained below Eq. (2.60), in principle the one-loop expression for δ_s includes even powers of μ up to μ^6, and therefore P_s may contain terms in principle up to μ^8. However, in practice, the μ^6 term is missing and therefore at one-loop the only contribution at μ^8 comes from the 22-type term formed from $\langle[\hat{\mathbf{r}}\cdot\mathbf{v}]^2[\hat{\mathbf{r}}\cdot\mathbf{v}]^2\rangle$.

The 22-type contributions can be split into scalar and tensor terms, the latter arising from the composite operators in (2.60). The scalar terms are

$$P_{s,0} \supseteq D_A^2 P_{AA} + D_A D_B P_{AB} + D_B^2 P_{BB}, \tag{2.76a}$$
$$P_{s,2} \supseteq 2D_A D_K P_{AA} + (D_B D_K + D_A D_L)P_{AB} + 2D_B D_L P_{BB}, \tag{2.76b}$$
$$P_{s,4} \supseteq (f_A^2 D_A^2 - fD^2)^2 P_{AA} + f_B D_B (f_A D_A - fD^2)P_{AB} + f_B^2 D_B^2 P_{BB}. \tag{2.76c}$$

The tensor contributions of 22-type can be written in the form

$$P_{s,n} \supseteq \frac{fD^2k^4}{8\pi^2}\int_0^{\Lambda} \mathrm{d}q \int_{-1}^{+1} \frac{\mathrm{d}x}{k^2+q^2-2kqx} P^*(q)P^*[(k^2+q^2-2kqx)^{1/2}]S_n. \tag{2.77}$$

The integrand should be set to zero if the quantity $(k^2+q^2-2kqx)^{1/2}$ exceeds the cutoff Λ. The

quantities S_n are

$$\begin{aligned}
S_2 &= \big[2D_B x(k-qx) + D_A(q+kx-2qx^2)\big]\big[2kx + q(2-f+x^2[f-4])\big] \\
&\quad - \frac{fD^2}{2}(k-2qx)^2(x^2-1), \qquad (2.78a)\\
S_4 &= f(q+2kx-3qx^2)\Big[D_A(q+kx-2qx^2) + 2D_B x(k-qx)\Big] \\
&\quad + \big[fq(x^2-1) + 2(q+kx-2qx^2)\big]\big[D_K q + (D_K+2D_L)kx - 2(D_K+D_L)qx^2\big] \\
&\quad + \frac{fD^2}{8}\big[8q^2 + 8kqx(4-5f+x^2[5f-6]) + q(x^2-1)([8-3f]f + 3[16-16f+f^2]x^2) \\
&\qquad\quad + k^2(12x^2 - 4 - 8f[x^2-1])\Big], \qquad (2.78b)\\
S_6 &= f(q+2kx-3qx^2)\big[D_K q + (D_K+2D_L)kx - 2(D_K+D_L)qx^2\big] \\
&\quad + \frac{f^2D^2}{4}\Big[2k^2(f-2-[f-6]x^2) + 4kqx(7-3f+[3f-11]x^2) \\
&\qquad\quad + q^2(4-3f+18[f-2]x^2 + 5[8-3f]x^4)\Big], \qquad (2.78c)\\
S_8 &= \frac{f^3D^2}{8}\Big[8kqx(3-5x^2) + 4k^2(3x^2-1) + q^2(3-30x^2+35x^4)\Big]. \qquad (2.78d)
\end{aligned}$$

13-type terms.—The same division can be made for 13-type terms. The scalar components are

$$P_{s,0} \supseteq DP^*\Big[(D_D - \text{Đ})P_D + D_E P_E + (D_F + \text{Đ})P_F + D_G P_G + \frac{\text{Đ}}{2}\big[P_{J2} - 2P_{J1}\big]\Big], \qquad (2.79a)$$

$$\begin{aligned}
P_{s,2} \supseteq DP^*\Big[&(D_M + f[D_D - \text{Đ}])P_D + (D_N + fD_E)P_E + (D_P + f[D_F + \text{Đ}])P_F \\
&+ (D_Q + fD_G)P_G + \frac{D_R - 2f\text{Đ}}{2}P_{J1} + \frac{D_S + f\text{Đ}}{2}P_{J2}\Big],
\end{aligned} \qquad (2.79b)$$

$$\begin{aligned}
P_{s,4} \supseteq fDP^*\Big[&(f_D D_D - f_J\text{Đ})P_D + f_E D_E P_E + (f_F D_F + f_J\text{Đ} - fDD_A)P_F + (f_G D_G - fDD_B)P_G \\
&+ ([f-f_A]DD_A + fD^3 - 2f_J\text{Đ})\frac{P_{J1}}{2} + ([f-f_B]DD_B + f_J\text{Đ})\frac{P_{J2}}{2}\Big].
\end{aligned} \qquad (2.79c)$$

The tensor contributions can be written as a single dq integral in the form

$$P_{s,n} = \frac{D^2k^2}{48\pi^2}P^*(k)\int_0^\Lambda \mathrm{d}q\; P^*(q)T_n. \qquad (2.80)$$

The integrands T_n are

$$\begin{aligned}
T_2 &= 3f(D_K+D_L)\frac{k^2}{q^2} + \Big[12(D_K+D_L) - f(16D_A+32D_B+8fD^2+11[D_K+D_L])\Big] \\
&\quad + \Big[16(3D_K+4D_L) - f(16D_A+32D_B+11[D_K+D_L])\Big]\frac{q^2}{k^2} \\
&\quad + 3(f-4)(D_K+D_L)\frac{q^4}{k^4} - \frac{3}{2}(D_K+D_L)\frac{(k^2-q^2)^3}{k^5 q}\Big(f\frac{k^2}{q^2} - f + 4\Big)\ln\left|\frac{1+r}{1-r}\right|, \qquad (2.81a) \\
\frac{T_4}{f} &= 3(1+f)(D_K+D_L)\frac{k^2}{q^2} - \Big[3D_K+19D_L+f(16D_A+32D_B+16fD^2+11[D_K+D_L])\Big] \\
&\quad + \Big[69D_K+85D_L - f(16D_A+32D_B+11[D_K+D_L])\Big]\frac{q^2}{k^2} \\
&\quad + 3(f-7)(D_K+D_L)\frac{q^4}{k^4} - \frac{3}{2}(D_K+D_L)\frac{(k^2-q^2)^3}{k^5 q}\Big[8(1+f)\frac{k^2}{q^2} - f + 7\Big]\ln\left|\frac{1+r}{1-r}\right|, \\
&\qquad (2.81b) \\
\frac{T_6}{f^2} &= -\Big(8f^2D^2 + 15D_K + 31D_L\Big) + (D_K+D_L)\Big(3\frac{k^2}{q^2} + 21\frac{q^2}{k^2} - 9\frac{q^4}{k^4}\Big) \\
&\quad - \frac{3}{2}(D_K+D_L)\frac{(k^2-q^2)^3}{k^5 q}\Big(\frac{k^2}{q^2}+3\Big)\ln\left|\frac{1+r}{1-r}\right|. \qquad (2.81c)
\end{aligned}$$

Counterterms.—The appearance of the counterterms depends on the basis of local operators in which we choose to express δ_s. If we choose to renormalize the basis $(\mathbf{v}\delta)^{\mathrm{R}}$, $(\mathbf{vv})^{\mathrm{R}}$, $(\mathbf{vv}\delta)^{\mathrm{R}}$ and $(\mathbf{vvv})^{\mathrm{R}}$, then the counterterm for each $P_{s,n}$ will be a linear combination of the loop-level time dependence for each of these operators, with coefficients $Z_{2|\mathbf{v}\delta}$, …, $Z_{2|\mathbf{vvv}}$, together with a linear combination of the arbitrary functions $\zeta_{2|\mathbf{v}\delta}$, …, $\zeta_{2|\mathbf{vvv}}$.[11] In this basis we find, suppressing the

[11] If we are using an 'off-shell' scheme in which some or all of the composite operators are defined by arbitrary conditions, then additional finite renormalizations may be needed to allow the $P_{s,n}$ to be matched to measurements.

unknown time-dependent terms $\zeta_{2|\delta}$, …, $\zeta_{2|\mathbf{vvv}}$ associated with each operator,

$$\frac{c_{2|\delta_s,0}}{k_{\rm NL}^2} = -\frac{1}{D}\Big(18D_D + 28D_E - 7D_F - 2D_G - 13\mathcal{D}\Big)Z_{2|\delta}, \tag{2.82a}$$

$$\begin{aligned}\frac{c_{2|\delta_s,2}}{k_{\rm NL}^2} = &-\frac{f}{D}\Big(18D_D + 28D_E - 7D_F - 2D_G - 13\mathcal{D}\Big)Z_{2|\delta}\\ &-\frac{1}{D}\Big(18f_D D_D + 28f_E D_E - 7f_F D_F - 2f_G D_G - 13f_J\mathcal{D} + (12f_A - 5f)DD_A\\ &\quad + (12f_B - 10f)DD_B - 12fD^3\Big)Z_{2|\mathbf{v}}\\ &+\Big((12f_A - 5f)D_A + (12f_B - 10f)D_B - 12fD^2\Big)Z_{2|\mathbf{v}\delta}\\ &-\frac{4f}{3}\Big(f_A D_A + f_B D_B - fD^2\Big)(5Z_{2|\mathbf{vv},A} + Z_{2|\mathbf{vv},B}) - \frac{5}{2}f^2D^2Z_{2|\mathbf{vv}\delta}\end{aligned} \tag{2.82b}$$

$$\begin{aligned}\frac{c_{2|\delta_s,4}}{k_{\rm NL}^2} = &-\frac{f}{D}\Big(18f_D D_D + 28f_E D_E - 7f_F D_F - 2f_G D_G - 13f_J\mathcal{D} + 12(f_A - 5f)DD_A\\ &\quad + 12(f_B - 10f)DD_B - 12fD^3\Big)Z_{2|\mathbf{v}}\\ &+f\Big((12f_A - 5f)D_A + (12f_B - 10f)D_B - 12fD^2\Big)Z_{2|\mathbf{v}\delta}\\ &-\frac{f}{3}\Big((3+4f)f_A D_A + 2(9+2f)f_B D_B - (3+4f)fD^2\Big)Z_{2|\mathbf{vv},B}\\ &-\frac{20f^2}{3}\Big(f_A D_A + f_B D_B - fD^2\Big)Z_{2|\mathbf{vv},A} - \frac{5}{2}f^3D^2(Z_{2|\mathbf{vv}\delta} + Z_{2|\mathbf{vvv}})\end{aligned} \tag{2.82c}$$

$$\frac{c_{2|\delta_s,6}}{k_{\rm NL}^2} = -f^2(f_A D_A + 6f_B D_B - fD^2)Z_{2|\mathbf{vv},B} - \frac{5}{2}f^4D^2Z_{2|\mathbf{vvv}} \tag{2.82d}$$

$$\frac{c_{2|\delta_s,8}}{k_{\rm NL}^2} = 0. \tag{2.82e}$$

Notice that there are two renormalization constants associated with the operator $(\mathbf{vv})^{\rm R}$, because this can mix independently with the tensor factors δ_{ij} and $\hat{k}_i\hat{k}_j$, ie.,

$$(\mathbf{vv})^{\rm R}_{ij} = (\mathbf{vv})_{ij} + \Big(c_{2|\mathbf{vv},A}\delta_{ij} + c_{2|\mathbf{vv},B}\hat{k}_i\hat{k}_j\Big)\frac{H^2}{k_{\rm NL}^2}\frac{1}{k^2}\partial^2\delta. \tag{2.83}$$

The constants $Z_{2|\mathbf{vv},A}$ and $Z_{2|\mathbf{vv},B}$ are the corresponding Z-parameters. These correspond to the Wilson coefficients c_1 and c_2 defined by Lewandowski et al. in their Eq. (6.6) [116]. In principle there could be similar mixing with different tensor factors in the OPE for $(\mathbf{vv}\delta)^{\rm R}$, but at one-loop the $\hat{k}_i\hat{k}_j$ tensor does not enter.

Alternatively, if we choose to renormalize the coefficients of the μ-expansion $(\delta_{s,n})^{\rm R}$, as in Eq. (2.63), then we find, again omitting the possibility of unknown time-dependent terms,

$$\frac{c_{2|\delta_s,0}}{k_{\rm NL}^2} = -\frac{1}{D}\Big(18D_D + 28D_E - 8D_F - 2D_G - 13\mathcal{D}\Big)Z_{2|\delta_s,0}, \tag{2.84a}$$

$$\begin{aligned}\frac{c_{2|\delta_s,2}}{k_{\rm NL}^2} = &-\frac{1}{D}\Big(18(f_D+f)D_D + 28(f_E+f)D_E - 7(f_F+f)D_F - 2(f_G+f)D_G - 13(f_J+J)\mathcal{D}\Big)\\ &+\Big(4(3-2f)(D_K+D_L) - 12f_A D_A - 12f_B D_B + (12 - \frac{5}{2}f)D^2\Big)Z_{2|\delta_s,2},\end{aligned} \tag{2.84b}$$

$$\begin{aligned}\frac{c_{2|\delta_s,4}}{k_{\rm NL}^2} = &-\frac{f}{D}\Big(18f_D D_D + 28f_E D_E - 7f_F D_F - 2f_G D_G - 13f_J\mathcal{D}\Big)\\ &-f\Big(12f_A D_A + 12f_B D_B - 11D_K - 6D_L + f[(5f-12)D^2 + 8D_K + 8D_L]\Big),\end{aligned}$$

$$\frac{c_{2|\delta_s,6}}{k_{\rm NL}^2} = -\frac{f^2}{2}\Big(5f^2D^2 + 2D_K + 12D_L)\Big)Z_{2|\delta_s,6}, \tag{2.84c}$$

$$\frac{c_{2|\delta_s,8}}{k_{\rm NL}^2} = 0. \tag{2.84d}$$

As explained above, these cannot all be varied independently but only subject to the constraint (2.61a). Notice there is no divergence at μ^8 in agreement with (2.61b).

There are no multiplicative renormalizations of the $P_{s,n}$. This can be regarded as a nontrivial check of the computation. Since the mapping between real and redshift space conserves mass, the same conservation-of-mass argument that prohibits multiplicative renormalization of δ will apply to δ_s; see footnote 7 on p.43.

2.3.3 Resummation

If there are large-scale random motions then the redshift-space power spectrum will require resummation for the same reasons described in §2.2.5. This can be accomplished by a modification of the procedure used in real space.

The key tool is still the use of Lagrangian perturbation theory to provide a template. The redshift distortion (2.56) now applies to the Lagrangian picture displacement field $\boldsymbol{\Psi}$ with $\mathbf{v} = \mathrm{d}\boldsymbol{\Psi}/\mathrm{d}t$, so at linear level we have

$$\boldsymbol{\Psi}_{s,1} = \boldsymbol{\Psi}_1 + f(\hat{\mathbf{r}}\cdot\dot{\boldsymbol{\Psi}}_1)\hat{\mathbf{r}} = \mathbf{R}\cdot\boldsymbol{\Psi}_1 \tag{2.85}$$

where $f = \mathrm{d}\ln D/\mathrm{d}\ln a$ is defined by Eq. (2.17) as above and the 'redshift-space distortion tensor' R_{ij} satisfies

$$R_{ij} = \delta_{ij} + f\hat{r}_i\hat{r}_j. \tag{2.86}$$

It follows that correlation functions of $\boldsymbol{\Psi}_1$ can be converted to redshift space by projecting all indices with R_{ij}. Therefore, at lowest order, the two-point function A_{ij} becomes

$$\begin{aligned} A_{s,ij}^{=\ell 0} = \langle[\Delta\boldsymbol{\Psi}_s(\mathbf{q}) - \Delta\boldsymbol{\Psi}_s(\mathbf{0})]^2_{ij}\rangle &= (\delta_{ij} + 2f\hat{r}_i\hat{r}_j + f^2\hat{r}_i\hat{r}_j)X(q) \\ &+ \Big[\hat{q}_i\hat{q}_j + f(\hat{\mathbf{q}}\cdot\hat{\mathbf{r}})(\hat{q}_i\hat{r}_j + \hat{q}_j\hat{r}_i) + f^2(\hat{\mathbf{q}}\cdot\hat{\mathbf{r}})^2\hat{r}_i\hat{r}_j\Big]Y(q), \end{aligned} \tag{2.87}$$

where $X(q)$ and $Y(q)$ continue to be defined by Eqs. (2.46a)–(2.46b).

VSCF formula.—We may now apply the prescription of Vlah, Seljak, Chu & Feng to arrive at an expression for the redshift-space power spectrum analogous to Eq. (2.49),

$$P_{s,vscf}^{\leqslant\ell}(k) \equiv P_{s,\mathrm{nw}}^{\leqslant\ell} + \int \mathrm{d}^3q\, \mathrm{e}^{-\mathrm{i}\mathbf{k}\cdot\mathbf{q}} \exp\left(-\frac{1}{2}k_ik_jA_{s,ij}^{\mathrm{nw},=\ell 0}\right)\left(-\frac{1}{2}k_mk_nA_{s,mn}^{\mathrm{w},\leqslant\ell 1} + \frac{\mathrm{i}}{6}k_mk_nk_rW_{s,mnr}^{\mathrm{w},\leqslant\ell 1}\right). \tag{2.88}$$

The 'wiggle' and 'no-wiggle' combinations have the same meaning used in §2.2.5, with 'no-wiggle' components at one-loop and higher being built exclusively from the 'no-wiggle' initial power spectrum and the 'wiggle' terms absorbing the remainder. The combination

$k_i k_j A^{\mathrm{nw},=\ell 0}_{s,ij}$ can be evaluated using (2.87), which yields

$$k_i k_j A^{\mathrm{nw},=\ell 0}_{s,ij} = k^2\Big([1+f(f+2)\mu^2]X^{\mathrm{nw}}(q)+\Big[(\hat{\mathbf{k}}\cdot\hat{\mathbf{q}})^2+2f\mu(\hat{\mathbf{q}}\cdot\hat{\mathbf{r}})(\hat{\mathbf{q}}\cdot\hat{\mathbf{k}})+f^2\mu^2(\hat{\mathbf{q}}\cdot\hat{\mathbf{r}})^2\Big]Y^{\mathrm{nw}}(q)\Big) \tag{2.89}$$

Eq. (2.89) should be compared with Eq. (4.14) of Lewandowski et al. [116]. Since X^{nw} and Y^{nw} are still slowly varying on scales where the 'wiggle' components have support, we are entitled to perform an approximate integration as in Eq. (2.50), with the result

$$P^{\leqslant\ell}_{s,vscf}(k) = P^{\leqslant\ell}_{s,\mathrm{nw}} + \exp\left(-\frac{1}{2}\langle\!\langle k_i k_j A^{\mathrm{nw},=\ell 0}_{s,ij}\rangle\!\rangle\right)\left(P^{\leqslant\ell}_{s,\mathrm{w}} + \frac{1}{2}\langle\!\langle k_i k_j A^{\mathrm{nw},=\ell 0}_{s,ij}\rangle\!\rangle P^{=\ell 0}_{s,\mathrm{w}}\right) \tag{2.90}$$

The average can be performed as in Eq. (2.51), which yields

$$\langle\!\langle k_i k_j A^{\mathrm{nw},=\ell 0}_{s,ij}\rangle\!\rangle = k^2\Big[1+f(f+2)\mu^2\Big]\langle\!\langle A^{\mathrm{nw},=\ell 0}\rangle\!\rangle \tag{2.91}$$

and $\langle\!\langle A^{\mathrm{nw},=\ell 0}\rangle\!\rangle$ is the same quantity defined in Eq. (2.53) that appears in the real-space resummation template. We evaluate it using the same choices $q_{\mathrm{min}} = 10h^{-1}\,\mathrm{Mpc}$ and $q_{\mathrm{max}} = 300h^{-1}\,\mathrm{Mpc}$ used for the real-space power spectrum, and similarly we perform the k-integration up to the cutoff $k = 1.4h/\mathrm{Mpc}$ used to compute the loops.

Application to renormalized power spectrum.—In practice we wish to apply this resummation prescription to the renormalized power spectrum predicted by the effective field theory. We denote the resulting power spectrum by $P^{\mathrm{R}}_{s,vscf}$. It is defined by Eq. (2.90) with $P^{\leqslant\ell}_{s,\mathrm{nw}}$ and $P^{\leqslant\ell}_{s,\mathrm{w}}$ understood to include the counterterms (2.63), or explicitly

$$P^{\leqslant\ell}_{s,\mathrm{nw}} = P^{\mathit{SPT},\Lambda,\leqslant\ell 1}_{s,\mathrm{nw}} - 2\sum_{n=0}^{4} c_{2|\delta_s,2n}\mu^{2n}\frac{k^2}{k^2_{\mathrm{NL}}}P^{=\ell 0}_{\mathrm{nw}}, \tag{2.92a}$$

$$P^{\leqslant\ell}_{s,\mathrm{w}} = P^{\mathit{SPT},\Lambda,\leqslant\ell 1}_{s,\mathrm{w}} - 2\sum_{n=0}^{4} c_{2|\delta_s,2n}\mu^{2n}\frac{k^2}{k^2_{\mathrm{NL}}}P^{=\ell 0}_{\mathrm{w}}. \tag{2.92b}$$

Fingers-of-God suppression.—It was explained in §2.2.5 that Matsubara's resummation prescription in real space produces a universal damping factor $\sim \exp[(\epsilon_{s<}+\epsilon_{s>})/3]$. In redshift-space the argument of the exponential is modified by the factor $1+f(f+2)\mu^2$ appearing in Eq. (2.91). Matsubara observed [125] that the resulting suppression factor resembled the damping factor $\exp(-k^2\mu^2\sigma_{\mathrm{v}}^2)$ sometimes used as a phenomenological description of power suppression on small scales due to the velocity dispersion σ_{v} within virialized halos, the so-called 'fingers of God' effect [143]. In perturbation theory we can estimate σ_{v} by computing the isotropic part of the velocity two-point function,

$$\sigma^2_{\mathrm{v}} = \langle v_i(\mathbf{x})v_j(\mathbf{x})\rangle_{\mathrm{isotropic}} = f^2D^2\int\frac{\mathrm{d}k}{6\pi^2}P^*(k). \tag{2.93}$$

The scale σ^2_{v} is the same as our factor $\langle\!\langle A^{\mathrm{nw},=\ell 0}\rangle\!\rangle$ if the Bessel function in the integrand of (2.53) is dropped. Matsubara's observation suggests that one could regard the damping

produced by resummation as a description of the power suppression from the 'fingers of God' effect. However, this is not physically satisfactory because the 'fingers of God' damping is an ultraviolet effect that has no clear connexion with the large-scale random motions that necessitate resummation.

As explained in §2.2.5, Matsubara's prescription leads to excessive damping on quasi-linear scales [178]. In an effective field theory description with a Galilean-invariant resummation scheme the conclusion is different. (The details of the resummation scheme do not matter for this argument. The Vlah, Seljak, Chu & Feng scheme described above is one candidate, but this discussion would apply equally to the scheme proposed by Senatore & Zaldarriaga [166] or the schemes discussed in Refs. [189, 129]. See also Taruya, Nishimichi & Saito, who used a different procedure to produce damping of the acoustic oscillations [178].) The damping factor is now applied only to the 'wiggle' component of the power spectrum, and subtraction of power for $\mu \neq 0$ is provided instead by the counterterms $c_{2|\delta_s,2n}$ for $n \geqslant 1$. Therefore the effective field theory description can *separately* accommodate suppression of the baryon acoustic oscillations due to large-scale motions and suppression of the small-scale power due to random motion within halos. This is physically reasonable: the counterterms encode the averaged small-structure of the theory and therefore provide a natural description for the subtraction of power due to virialized velocities.

2.3.4 Multipole power spectra

The outcome of §2.3.3 is a very simple prescription for resummation of the redshift-space power spectrum: the 'no-wiggle' terms are unaffected, whereas the 'wiggle' terms are damped by a term of the form $\exp(-A - B\mu^2)$. The simplicity of this μ-dependence makes it straightforward to extract Legendre modes from Eqs. (2.90)–(2.91). Observational data are typically reported as measurements of these modes. Specifically, Cole, Fisher & Weinberg defined the *multipole power spectra* P_ℓ to satisfy [40]

$$P_s(k,\mu) \equiv \sum_\ell P_\ell(k) \mathscr{P}_\ell(\mu). \tag{2.94}$$

We wish to compute the multipole power spectra for the resummed, renormalized power spectrum, which we denote $P^{\mathrm{R}}_{s,vscf}$. They can be computed using the Legendre orthogonality relation (2.69) with $\mathbf{a} = \mathbf{b}$, which yields

$$P_\ell(k) = \frac{2\ell+1}{2} \int_{-1}^{+1} \mathrm{d}\mu \; P^{\mathrm{R}}_{s,vscf}(k,\mu) \mathscr{P}_\ell(\mu). \tag{2.95}$$

We have not added distinguishing labels to $P_\ell(k)$, but there is no ambiguity because the only multipole power spectra we will discuss are those defined by the resummed, renormalized power spectrum $P^{\rm R}_{s,vscf}$. The P_ℓ are identically zero for odd ℓ because $P^{\rm R}_s$ is a function of μ^2. Measurements exist for the lowest multipoles $\ell = 0$ (the monopole), $\ell = 2$ (the quadrupole) and $\ell = 4$ (the hexadecapole) [195, 22, 137, 18].

Counterterms.—Eqs. (2.95) and (2.92a)–(2.92b) show that we can write

$$P_\ell(k) = P_\ell^{\mathit{SPT},\Lambda,\leqslant \ell 1} - 2d_{2|\delta_s,\ell}\frac{k^2}{k^2_{\rm NL}}P^{=\ell 0}. \tag{2.96}$$

where the labels 'SPT', 'Λ', and '$\leqslant \ell 1$' have their usual meanings, and $P^{=\ell 0}$ is the tree-level power spectrum in real space. As explained above, there is just one counterterm $d_{2|\delta_s,\ell}$ for each multipole ℓ. It is a linear combination of the counterterms $c_{2|\delta_s,2n}$ defined in Eq. (2.63) and associated with the power series expansion in μ^n. If we apply the VSCF resummation scheme to the linear power spectrum $P^{=\ell 0}$ that appears in the counterterms then the coefficients of this combination become weakly dependent on cosmology via the damping factor $\langle\!\langle A^{\rm nw,=\ell 0}\rangle\!\rangle$. In practice, however, it makes very little difference whether or not we choose to apply resummation to the counterterms.

Numerical considerations.—The possibility of analytically extracting the P_ℓ is an advantage of the VSCF resummation prescription. For example, using the resummation scheme proposed by Senatore & Zaldarriaga [166, 116], the resummed expression involves multiple integrations that do not decouple from μ. The Legendre multipoles must be computed by performing the μ integration in (2.95) numerically, giving the final result

$$P_\ell^{\leqslant \ell 1}(k) = \sum_{j=0}^{1}\sum_{\ell'}\int \frac{{\rm d}k'\,(k')^2}{2\pi^2} M_{\|N-j}(k,k')_{\ell\ell'} P^{\rm R}_{\ell'}(k')_j \tag{2.97}$$

where $P^{\rm R}_\ell(k)_j$ is the $\ell^{\rm th}$ multipole of the renormalized power spectrum at order j in the Eulerian expansion, and $M_{\|N-j}(k,k')_{\ell\ell'}$ is a mode-coupling matrix whose definition is given in Eq. (4.18) of Ref. [116]. It involves the μ integral together with a three-dimensional integration over the Lagrangian coordinate $\mathbf{q}$. The final prescription therefore requires five-dimensional integration and summation over ℓ', and is numerically expensive. Lewandowski et al. mitigated this difficulty by developing approximate analytic estimates for some of these integrations, which could be regarded as a counterpart of the approximate integration used in Eq. (2.50). However, their final procedure is still more complex than the VSCF method employed here.

The 'no-wiggle' part of the power spectrum is unchanged by the VSCF procedure. Extracting Legendre multipoles is therefore no more complex than a trivial change-of-

basis in the series representation from μ^n to $\mathscr{P}_\ell(\mu)$. The damped 'wiggle' part requires evaluation of the integrals

$$I_\ell \equiv \frac{2\ell+1}{2}\int_{-1}^{+1} \mathrm{e}^{-A-B\mu^2}\,\mathscr{P}_\ell(\mu)\mu^n\,\mathrm{d}\mu. \tag{2.98}$$

The I_ℓ can be expressed in terms of the incomplete Γ-function $\Gamma_x(s)$, defined by

$$\Gamma_x(a) \equiv \int_x^\infty t^{s-1}\mathrm{e}^{-t}\,\mathrm{d}t. \tag{2.99}$$

The required results are

$$I_0 = \frac{1+(-1)^n}{4}B^{-n_1}\mathrm{e}^{-A}\Big[\Gamma(n_1)-\Gamma_B(n_1)\Big], \tag{2.100}$$

$$I_2 = 5\frac{1+(-1)^n}{16}B^{-n_3}\mathrm{e}^{-A}\Big[(3-2B+3n)\Gamma(n_1)+2B\Gamma_B(n_1)-6\Gamma_B(n_3)\Big], \tag{2.101}$$

$$I_4 = 9\frac{1+(-1)^n}{128}B^{-n_5}\mathrm{e}^{-A}\Big[\big(12B^2-120Bn_1+140n_1n_3\big)\Gamma(n_1)-12B^2\Gamma_B(n_1) -120B\Gamma_B(n_3)+150\Gamma_B(n_5)\Big], \tag{2.102}$$

where $n_p = (n+p)/2$. For numerical evaluation it is sometimes helpful to rewrite the incomplete Γ-function in terms of $\mathrm{erf}(z)$[12] using the recurrence formula $\Gamma_x(n+1) = n\Gamma_x(n) + x^n\mathrm{e}^{-x}$ and

$$\Gamma_x(\tfrac{1}{2}) = \sqrt{\pi}[1-\mathrm{erf}(\sqrt{x})]. \tag{2.103}$$

Effect of resummation.—In Fig. 2.5 we plot the P_ℓ for $\ell = 0$, $\ell = 2$ and $\ell = 4$. We use a background cosmology adjusted to match that used in the MDR1 MultiDark simulation. This is the same background cosmology we will use in §2.3.5 to obtain non-linear estimates for these multipoles from our own simulations.

Whereas the effect of resummation on the real-space power spectrum was small (roughly a percent-level effect), Fig. 2.5 shows that its influence on the redshift-space multipoles is more significant. For the cosmology considered here, the suppression of oscillations in P_0 and P_2 is roughly a 10% effect, and the suppression in P_4 is roughly a 15% effect.

2.3.5 Numerical calculation of the non-linear redshift-space power spectrum

Our task is now to renormalize the multipole power spectra in a similar fashion to §2.2.6. The 'on-shell' scheme consists of adjusting the counterterms to optimize the fit to those P_ℓ for which we have measurements.

[12] The incomplete Γ function itself is not commonly included as a standard function in numerical libraries, but the error function is; eg. it is available as `std::erf()` for $\geqslant$ C++11 .

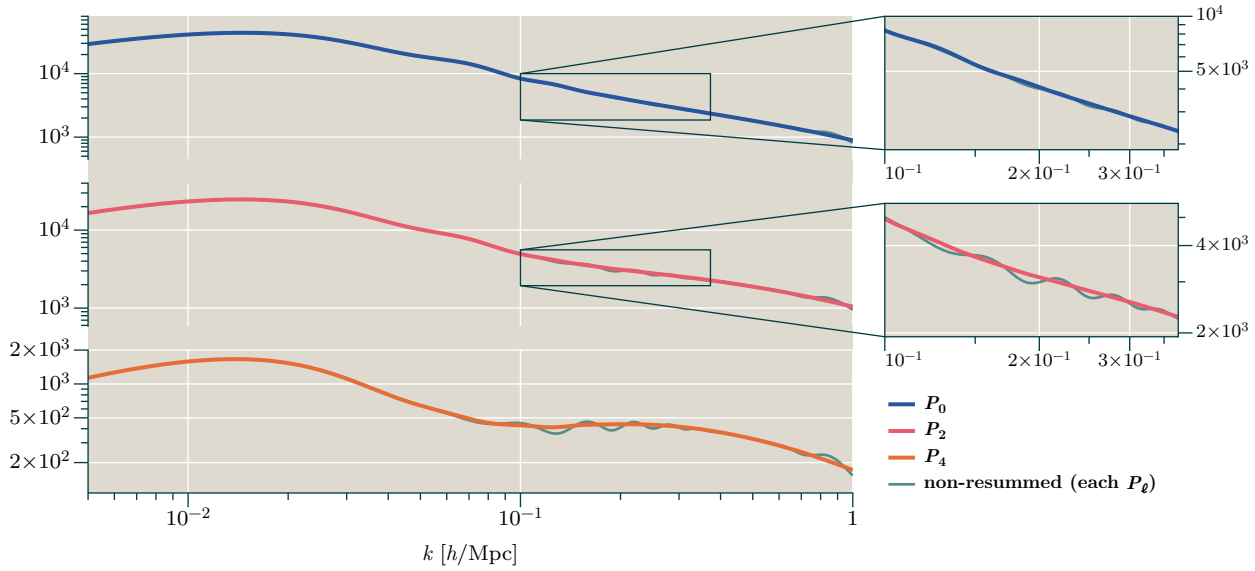

Figure 2.5: Resummed and non-resummed versions of the multipole power spectra P_ℓ. The blue, red and orange lines show the resummed multipoles P_0, P_2 and P_4, respectively. For each multipole, a green line shows the same power spectrum without resummation. Notice that P_2 and P_4 exhibit very significant damping of the 'wiggle' component. The background cosmology matches the MDR1 MultiDark simulation [152] and also our own simulations (§2.3.5).

Power-spectrum methodology

There are not yet any well-calibrated fitting formulae comparable to **HALOFIT** for the non-linear multipole power spectra, and therefore we must obtain direct estimates. To do so we use the public **gevolution** code[13] [2] to perform a custom simulation with 1024^3 particles and a box-size of $(2000\,\mathrm{Mpc}/h)^3$. This corresponds to an N-body particle mass of $\simeq 6 \times 10^{11} M_\odot/h$, approximately matching the mass of Milky Way-sized galaxies. The background cosmology matches the MultiDark MDR1 simulation [152], which we use to cross-check the validity of our results at $z = 0$. Our simulations can be reproduced by downloading a **gevolution** settings file, as explained in Appendix 2.C.

We record snapshots at $z \in \{0, 0.25, 0.5, 0.75, 1\}$. To estimate the real-space power spectrum we construct a density field using cloud-in-cell interpolation of the particle locations. For the redshift-space power spectra we adjust the location of each particle using Eq. (2.56) and construct a density field from these adjusted locations. This can be done in three different ways, by choosing the line-of-sight to be oriented along each of the three axes of the simulation. To reduce numerical noise in the power spectra our final comparisons use an average of these three possibilities.

The amplitude of the real-space power spectrum is estimated by binning Fourier modes of the density field and applying the anti-aliasing prescription of Jeong & Komatsu [96]. The redshift-space power spectra are handled in the same way. To extract multipoles we perform a least-squares fit to the expansion (2.94) in each $\mathbf{k}$-bin. Where the noise is small the outcome of this procedure closely matches the direct projection (2.95). Where the noise is more significant, we find that the least-squares fit produces more stable results.

Difficulties encountered when simulating redshift-space distortions

In the remainder of this paper we discuss only the 1024^3-particle, $(2000\,\mathrm{Mpc}/h)^3$-side simulation. However, to validate our numerical estimates we have tested their convergence using a larger suite of simulations. As part of this procedure we encounter two clear difficulties:

- The transformation from δ to δ_s described by Eq. (2.57) couples different scales: small-scale velocities can affect the redshift-space density on larger scales. While Eq. (2.57) is not explicitly used to construct δ_s from the simulation, our method-

[13] The most interesting feature of **gevolution** is that it can include relativistic effects in the weak field limit. We do not make use of this feature, instead running **gevolution** in Newtonian mode, but in principle this could be used to test the validity of the non-relativistic limit described in §2.2.1.

ology will reproduce its effects. Therefore, accurate redshift-space power spectrum measurements require higher resolution simulations than those needed for the real-space power spectrum.

- The redshift-space power spectrum is sensitive to large-scale bulk flows, for which the sample variance is larger than the sample variance in the density field on the same scales. Therefore, if a simulation does not have sufficiently large volume, the redshift-space power spectrum will differ from the predictions of linear theory even on large scales. Similar issues were discussed in Jennings et al. [94].

To understand these issues we analyse a set of simulations, of which the most relevant are: (*a*) the 1024^3-particle, $(2000\,\mathrm{Mpc}/h)^3$-box simulation already mentioned; (*b*) a 1024^3-particle, $(1000\,\mathrm{Mpc}/h)^3$-box simulation; (*c*) a 1024^3-particle, $(330\,\mathrm{Mpc}/h)^3$-box simulation; and (*d*) a set of 512^3-particle simulations of box size $(1000\,\mathrm{Mpc}/h)^3$.

Small-scale convergence.—We find that, for scales in the range $k = 0.2h/\mathrm{Mpc}$ to $1h/\mathrm{Mpc}$, the 1024^3-particle, $330\,\mathrm{Mpc}/h$-side simulation and the 1024^3-particle, $1000\,\mathrm{Mpc}/h$-side simulation match closely. We interpret this to indicate that velocities on scales smaller than those resolved by the $1000\,\mathrm{Mpc}/h$-side simulation do not contaminate the redshift-space density for this k-range. However, for the $\ell = 2$ mode on the same scales, we observe a difference between these high-resolution simulations and the 512^3-particle, $1000\,\mathrm{Mpc}/h$-side simulation.[14] This suggests that some effects due to the non-linear velocity field are not captured by the resolution of our reference simulation. These scales typically enclose a mass smaller than a Milky Way-sized galaxy. Therefore it is unclear whether observations resolve masses down to the scale where these velocities become relevant. A full investigation of these effects would require an analysis of the redshift-space density field of *halos*. This is beyond the scope of the present analysis, where we study only the dark matter field.

Large-scale convergence.—We find that all the simulations with box sizes smaller than our reference $2000\,\mathrm{Mpc}/h$-side simulation show increased scatter on the largest scales. For example, the $1000\,\mathrm{Mpc}/h$-side simulations exhibit a scatter of $\sim 30\%$ in the $\ell = 2$ mode even for $k \lesssim 0.06h/\mathrm{Mpc}$. We interpret this as a consequence of slow convergence of the

[14] It is difficult to quantify the magnitude of this difference, because the $\ell = 2$ mode undergoes a zero-crossing in the same range. However, at $k = 0.3h/\mathrm{Mpc}$, where the difference is largest (and close to the zero-crossing), the difference in amplitude between the lower- and higher-resolution simulations is $\sim 20\%$ of their shared value at $k = 0.2h/\mathrm{Mpc}$ (far from the crossing).

bulk flows in each simulation. In fact, even for our largest 2000 Mpc/h-side simulation, the scatter in the $\ell = 4$ mode is substantial on the largest scales.

The difficulty entailed by using a box size large enough to suppress sample variance of the bulk flows, while retaining enough resolution to capture the effect of non-linear velocities on small scales, indicates that accurate simulations of redshift-space distortions is computationally expensive.

Covariance.—Finally, the variance in different k-bins of our redshift-space power spectra—primarily in the $\ell = 2$ mode—appears to be correlated, even on large scales. We suspect this occurs because a bulk flow that boosts the power spectrum at one scale will provide a correlated uplift over a range of nearby scales. Where precision fits are made to cosmological models this covariance should be appropriately modelled and taken into account.

In practice this is unlikely to be straightforward. To determine covariances accurately from simulations will require many independent realizations, even for a single cosmological model and choice of background parameters. Determining how the power spectrum and its covariance changes over the entire parameter range of multiple cosmological models will require very many more. In this paper, the computational expense of performing these simulations means that we do not address this issue. Instead, we assign uncorrelated error estimates to each k-bin, in order to assess general properties of the EFT prediction. For precision work, however, the covariances should be taken into account.

2.3.6 Results

In this section we report our measurements of the counterterms at redshift $z = 0$ where the effect of non-linearities is expected to be most pronounced. We express the counterterms in the μ^{2n} basis defined in (2.63) and therefore quote values for the quantities $c_{2|\delta_s,2n}/k_{\rm NL}^2$.[15] Our parameter choices match those in §2.3.3, with an ultraviolet cutoff at $k = 1.4h/\text{Mpc}$. The X and Y parameters used in the infrared resummation are averaged between $q_{\rm min} = 10h^{-1}\,\text{Mpc}$ and $q_{\rm max} = 300h^{-1}\,\text{Mpc}$, and their wavenumber integral is carried up to the ultraviolet cutoff. The non-linear measurements forming our renormalization conditions are taken from the 1024^3-particle, $(2000/h\,\text{Mpc})^3$ simulation volume described in §2.3.5.

[15] It is a matter of convenience whether we renormalize by adjusting the counterterms $c_{2|\delta_s,2n}$ for the power-series expansion in μ [see (2.63)], or for the counterterms $d_{2|\delta_s,\ell}$ defined for the Legendre-mode expansion [see (2.96)]. In practice we will use the $c_{2|\delta_s,2n}$ because $c_{2|\delta_s,0}$ should coincide with the counterterm $c_{2|\delta}$ obtained from renormalizing the real-space power spectrum. This provides a simple way to assess compatibility of the two procedures. In addition, it is straightforward to impose the constraints (2.61a)–(2.61b) in this basis.

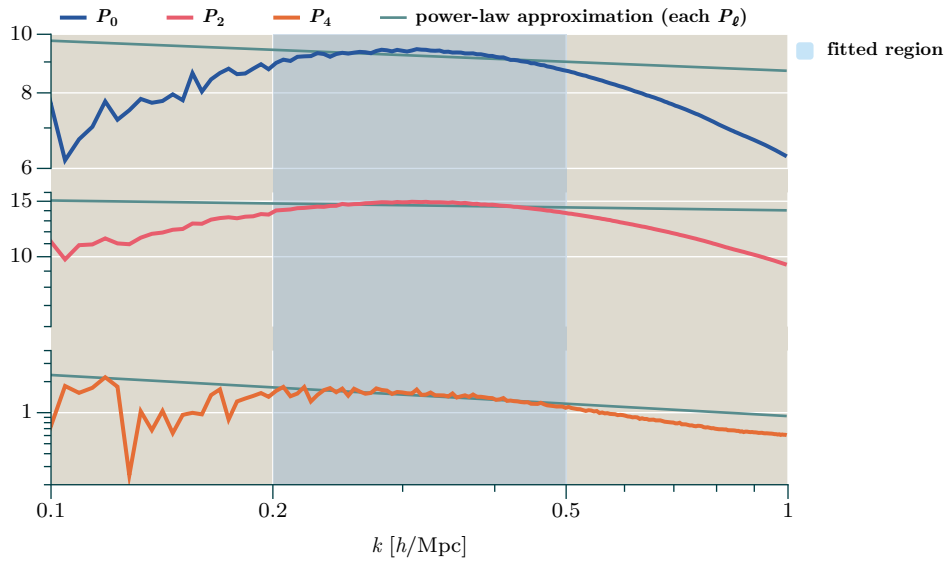

Figure 2.6: Fitting counterterms for the multipole power spectra P_ℓ at $z = 0$. Each panel shows the estimator $-(P_{\rm NL} - P_\ell^{SPT,\leqslant \ell 1})/2k^2 D^2 P^*$, where $P_{\rm NL}$ is the non-linear power spectrum for multipole ℓ obtained from numerical simulations. The green lines show a least-squares power-law approximation to these estimators in the region $0.2h/\text{Mpc} \leqslant k \leqslant 0.5h/\text{Mpc}$ where we optimize the fit (shaded light blue on the plot); the parameters of these fits appear in Table 2.2. The choice of region to be used in the fit should be regarded as part of the renormalization scheme.

As explained in §2.3.5, we reduce noise on the redshift-space multipole measurements by averaging over projections oriented along each of the three coordinate axes.

For most of this section we discuss only the $z = 0$ results. The EFT description for redshifts $z > 0$ is considered in §2.3.6.

Fitting for counterterms

In Fig. 2.6 we plot estimators for the counterterm associated with each multipole at $z = 0$, together with power-law fits to the region included in the optimization. As in §2.2.6, these estimators should be approximately k-independent in a region where the difference between the SPT and N-body power spectra is described by the leading counterterm. Based on the k-dependence of the estimators, we take this fitting region to be $0.2h/\text{Mpc} \leqslant k \leqslant 0.5h/\text{Mpc}$. It is located at marginally higher k than that used for the real-space power spectrum in §2.2.6. The parameters of the power-laws are shown in Table 2.2.

The conclusion is that P_0 and P_2 can be reasonably well-described by the leading counterterm over this region. For $k \gtrsim 0.5h/\text{Mpc}$ the estimators show significant k-dependence,

multipole	**power-law fit** $[0.2h/\mathrm{Mpc} \leqslant k \leqslant 0.5h/\mathrm{Mpc}]$
P_0	$8.701 \times (k/h \times \mathrm{Mpc})^{0.04971}$
P_2	$14.03 \times (k/h \times \mathrm{Mpc})^{-0.03129}$
P_4	$0.9260 \times (k/h \times \mathrm{Mpc})^{-0.3986}$

Table 2.2: Power-law fits to the counterterm estimators of Fig. 2.6 over the region $0.2h/\mathrm{Mpc} \leqslant k \leqslant 0.5h/\mathrm{Mpc}$ at $z = 0$. The estimators for P_0 and P_2 are good fits to a constant, whereas that for P_4 shows residual k-dependence.

which we interpret to mean that higher-order counterterms become relevant. Therefore, if predictions using only the lowest-order counterterm match the measured power spectra on these scales, this should be interpreted as merely accidental. The fit for P_4 is rather less good, with a power-law index of -0.40 over the quasilinear region. There are a number of possible explanations, including the possibility that higher-order counterterms are required, but it may also be caused by difficulties in estimating P_4 from the N-body data. These estimates become increasingly noisy for high multipoles.

Numerical estimates and degeneracies.—To determine numerical values for the counterterms $c_{2|\delta_s,0}$, $c_{2|\delta_s,2}$ and $c_{2|\delta_s,4}$ we have the option to fit simultaneously to both real- and redshift-space power spectra, or use just the redshift-space measurements. In Table 2.3 we list the maximum likelihood estimates for each case. Marginalized constraints obtained from a Monte Carlo Markov chain analysis give similar values. (In this analysis we assume a wide, flat prior on each parameter that comfortably encloses the posterior parameter range.) Notice that $c_{2|\delta_s,0}/k_{\mathrm{NL}}^2 = c_{2|\delta}/k_{\mathrm{NL}}^2$ is not equal to the value derived for this counterterm in §2.2.6 by renormalizing against the Planck2015 cosmology. The correct value is cosmology-dependent [36].

We do not quote error estimates for these counterterms because that would require an estimate for the covariance between the measured $P(k)$ and $P_\ell(k)$. As explained in §2.3.5, to obtain reliable estimates of these covariance matrices would require more simulations than we were able to perform. We hope to return to this issue in the future.

Although $c_{2|\delta_s,0}$ is well-determined no matter what measurements are included in the fit, there is a degeneracy between $c_{2|\delta_s,2}$ and $c_{2|\delta_s,4}$. In Fig. 2.7 we show representative one- and two-σ contours showing the shape of this degeneracy, computed assuming inde-

	$P + P_\ell$		P_ℓ only	P only	Lewandowski et al.[a]
	resummed	**unresummed**			
$c_{2\|\delta_s,0}/k_{\rm NL}^2$ $[h^{-2}\,{\rm Mpc}^2]$	2.28	2.36	2.27	2.32	1.26
$c_{2\|\delta_s,2}/k_{\rm NL}^2$ $[h^{-2}\,{\rm Mpc}^2]$	16.5	16.1	16.5		4.08
$c_{2\|\delta_s,4}/k_{\rm NL}^2$ $[h^{-2}\,{\rm Mpc}^2]$	6.73	6.58	6.73		2.03

[a] Ref. [116]. We have converted their results using a growth factor f matching the Big MultiDark Planck simulation [109], which was used to estimate the non-linear multipole power spectra used as renormalization conditions in this reference.

Table 2.3: Maximum-likelihood estimates for the counterterms $c_{2|\delta_s,0}$, $c_{2|\delta_s,2}$, $c_{2|\delta_s,4}$ at $z = 0$. As explained in §2.3.5, for reasons of computational expense we do not include covariances between k-bins of the different power spectra, but instead assign 5% uncorrelated errors to each bin. However, the results are not strongly sensitive to the size of the error bar we assume.

pendent errors of 5% per bin on the real-space power spectrum, and 20% per bin on each multipole.[16] These are merely fiducial values, so we caution that the *size* of these error ellipses has little meaning. However, unless strong correlations between k-bins change its shape, their *orientation* should be roughly indicative of the direction of the degeneracy.

Accuracy of EFT prediction

In Fig. 2.8 we plot results for the real-space power spectrum, and the P_0 and P_2 modes, using both the resummed, renormalized EFT prediction and SPT. In Fig. 2.9 we show the relative accuracy achieved by each prediction for the same spectra. In both figures the EFT power spectra are taken to be constructed using the $P + P_\ell$ counterterms from Table 2.3. Red lines indicate the resummed EFT prediction; for comparison, their unresummed counterparts are shown in green. We also plot the unresummed SPT prediction in purple. The shaded regions indicate where the prediction has $\leqslant 2.5\%$ accuracy (light pink), $\leqslant 5\%$ accuracy (light green) and $\leqslant 25\%$ accuracy (light blue).

Real-space $P(k)$ and redshift-space $\ell = 0$ mode.—As for the real-space power spectrum, the resummed prediction gives better accuracy for $k \gtrsim 0.1h/{\rm Mpc}$ where SPT tends to

[16] Notice that this error assignment for the P_ℓ is larger than that used to construct Table 2.3. This has been done in order to resolve the contours more clearly. Using these larger estimates shifts the maximum-likelihood $c_{2|\delta_s,0}/k_{\rm NL}^2$ by $+0.03$ to $2.31h^{-2}\,{\rm Mpc}^2$ but leaves $c_{2|\delta_s,2}/k_{\rm NL}^2$ and $c_{2|\delta_s,4}/k_{\rm NL}^2$ unchanged, and therefore makes negligible difference to the predicted power spectra.

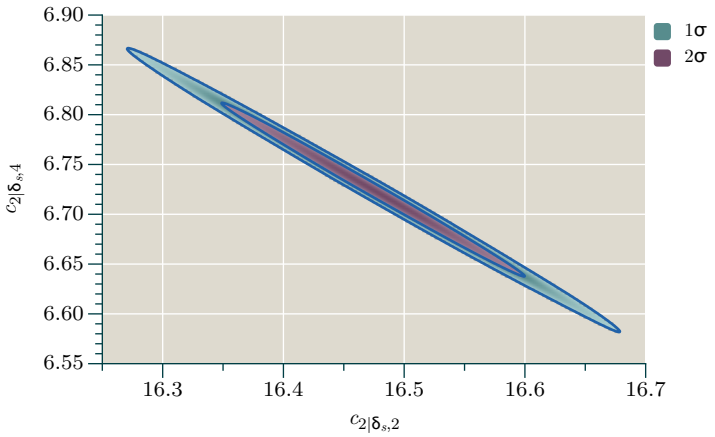

Figure 2.7: Representative degeneracy between $c_{2|\delta_s,2}$ and $c_{2|\delta_s,4}$ counterterms for the redshift-space power spectrum. The size of the error ellipses is merely indicative; they are constructed assuming a wide, flat prior on each parameter and taking independent errors of 5% and 20% per k-bin for the real- and redshift-space power spectra, respectively. (See the discussion in the main text.) With these assumptions, the green ellipse encloses the two-σ region and the purple ellipse encloses the one-σ region.

overpredict the amplitude of baryon oscillations. Although the effect is visible in both real space and redshift space, it is more visible in the redshift-space multipoles. The general performance of the one-loop renormalized result is good. The resummed, renormalized real-space power spectrum is typically within 2.5% of the measured value up to $k \sim 0.4h/\mathrm{Mpc}$. The performance of the P_0 mode is similar but marginally less good, with some excursions into the 5% accuracy band. This is what we should expect based on Fig. 2.6.

Both the real-space power spectrum and P_0 exhibit a downturn near $k \sim 0.5h/\mathrm{Mpc}$, dipping significantly below the measured non-linear result. In the case of P_0 the power spectrum becomes negative near $k = 0.75h/\mathrm{Mpc}$. This is unphysical because the monopole power spectrum should be positive, and therefore its zero-crossing must be removed by higher-order loop corrections or higher-order counterterms that we have not included. Fig. 2.6 already suggests that such contributions become important for $k \gtrsim 0.5h/\mathrm{Mpc}$, but requiring positivity of P_0 implies that we may deduce a firm upper limit for the validity of one-loop EFT predictions using only the leading-order counterterm. For the MDR1 cosmology considered here, higher-order effects must become significant before $k \approx 0.75h/\mathrm{Mpc}$.

Redshift-space $\ell = 2$ mode.—For P_2, which is more strongly sensitive to velocity in-

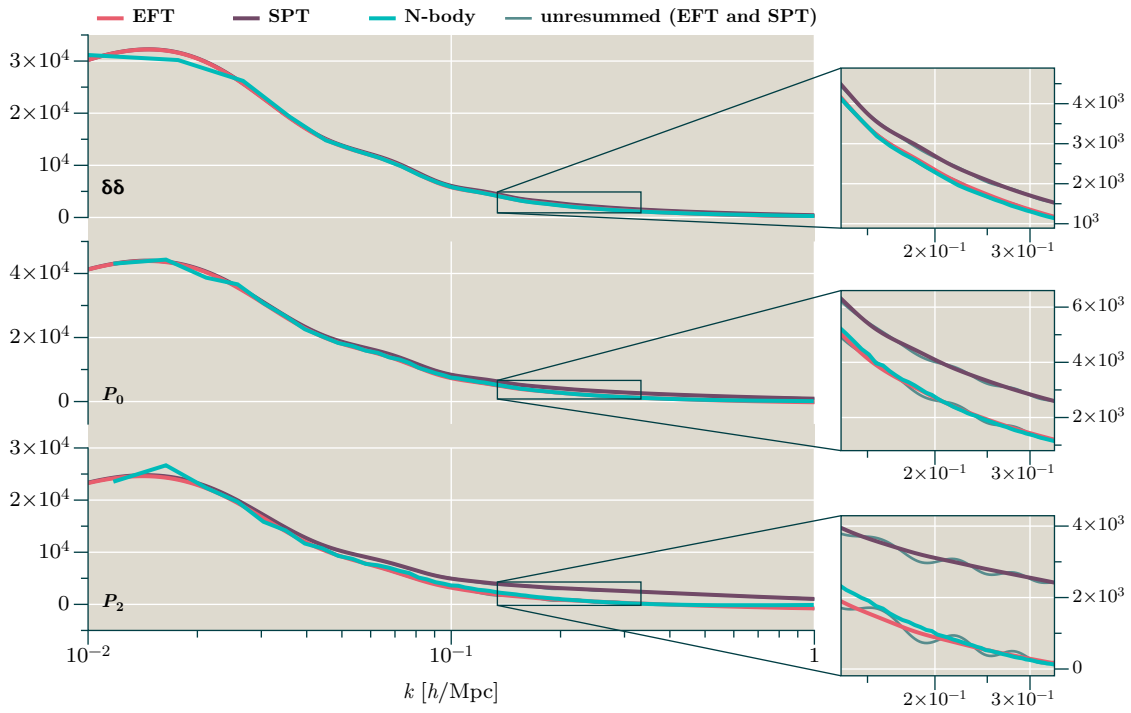

Figure 2.8: Real-space and multipole power spectra P_0 and P_2 predicted by the effective field theory framework (red lines), compared to the predictions in SPT (purple lines). The evaluation is at $z = 0$. The turquoise lines represent the non-linear power spectra recovered from N-body simulations. For both the EFT and SPT predictions, the associated green line shows the unresummed result. The zoomed panels highlight regions where resummation plays a significant role in improving the prediction for P_0 and P_2. As in §2.2.6, its importance for the real-space power spectrum is modest.

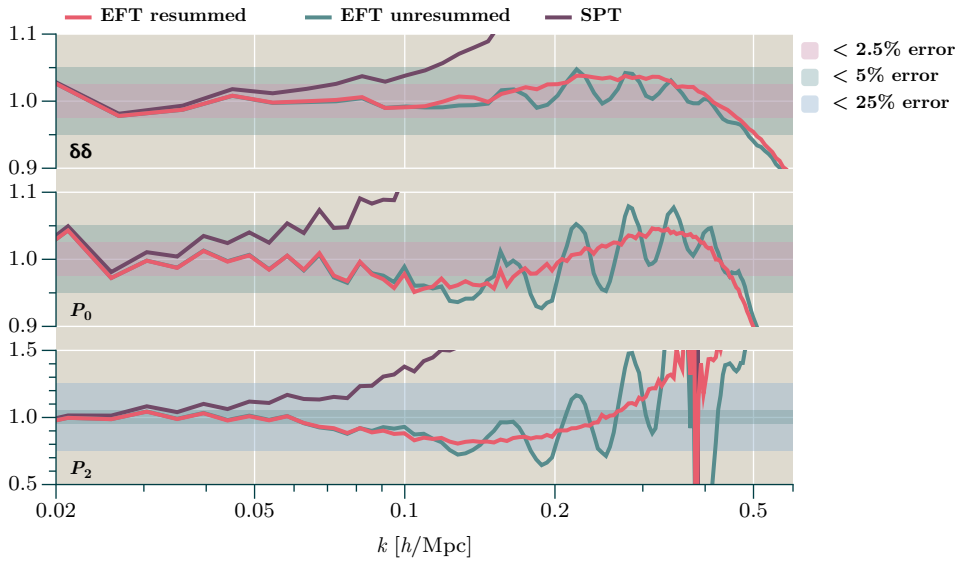

Figure 2.9: Comparison of fit between the predicted one-loop EFT power spectra and the non-linear power spectra at $z = 0$. The EFT predictions are shown in both resummed (red line) and non-resummed (green line) versions. Corresponding results from non-resummed SPT are included for comparison. The quantity plotted is $P/P_{\rm NL}$ and the background cosmology matches the MDR1 MultiDark simulation [152]. The shaded light-pink region marks where the prediction is within 2.5% of the measured value; the light-green region marks where it is within 5%; and the light-blue region marks where it is within 25%.

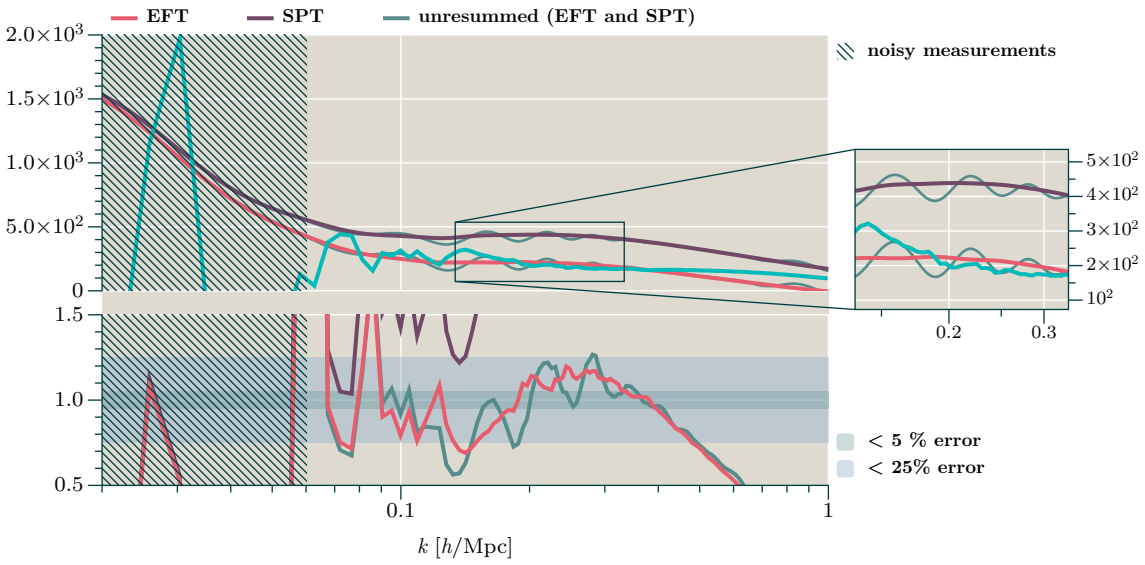

Figure 2.10: **Top panel**: smoothed P_4 power spectrum measured from simulations (turquoise line) compared to EFT predictions (red line) and SPT (purple line). Green lines show the corresponding unresummed predictions. This panel should be compared to Fig. 2.8. Note that although we plot the comparison to a smoothed power spectrum, our fit for the counterterms uses raw measurements. **Bottom panel**: relative accuracy of the P_4 mode compared to the smoothed N-body power spectrum. This panel should be compared to Fig. 2.9. The hatched region $k < 0.06h/\text{Mpc}$ marks where we believe the measurements are too poorly-determined for a comparison to be meaningful.

formation, the EFT prediction is still typically within 25% of the measured value up to $k \sim 0.4h/\text{Mpc}$; this number should be interpreted in light of the discussion in the following paragraph. The feature near $k = 0.4h/\text{Mpc}$ in P_2 arises from a sign change where the $\ell = 2$ mode becomes negative. Unlike the $\ell = 0$ mode, this sign change is physical [40]. It occurs at slightly different locations for the predicted and measured power spectra, causing the relative error to diverge. This divergence is therefore an artefact of the plot and does not have real physical significance. The $\ell = 4$ predictions show similar accuracy to $\ell = 2$ for $k \gtrsim 0.1h/\text{Mpc}$, but at smaller k the data are too noisy to allow a meaningful comparison. We collect the $\ell = 4$ results separately in Fig. 2.10.

Based on inspection of Figs. 2.9 and 2.10, it may appear that we achieve only modest accuracy for P_2 and P_4. While this is true for the *relative* accuracy of the prediction, it should be noted that the improvement compared to SPT is dramatic. However, Fig. 2.8 clearly shows that the amplitude of the one-loop SPT estimate must be adjusted *significantly* downward in the quasilinear region in order to achieve an acceptable prediction. A

similar effect was observed by Taruya, Nishimichi & Saito [178], who compared N-body simulations with the predictions of an 'improved' perturbation theory intended to damp acoustic oscillations in a similar way to the resummation schemes discussed in §§2.2.5 and 2.3.3. Bearing this in mind, the renormalized, resummed EFT prediction is strikingly successful in matching the amplitude of P_2 and P_4 for quasilinear k. However, obtaining a very accurate match to the amplitude of the higher ℓ-modes in this region probably requires the inclusion of higher-order loop contributions and counterterms. A similar conclusion was reached by Lewandowski et al. [116].

Notice also that amplitudes of the P_ℓ become quite small, which inflates the significance of the relative error. Indeed, as stated above, the measured P_2 changes sign: this is a consequence of suppression due to the fingers-of-God effect [40]. In our framework this sign change is not present before renormalization.[17] Its appearance in the final result is entirely attributable to parametrization of small-scale physics by counterterms, as anticipated in the discussion of §2.3.3.

Accuracy of Einstein–de Sitter approximation

Since we retain the full time-dependence of the one-loop redshift-space power spectrum it is possible to assess the accuracy of the Einstein–de Sitter approximation. As discussed in §2.2.2, this consists in replacing the growth functions D_i and growth factors f_i with their counterparts from Table 2.1. In Fig. 2.11 we show the relative accuracy of the Einstein–de Sitter approximation for the real-space power spectrum, and the $\ell = 0, 2, 4$ modes of the redshift-space power spectrum.

For the real-space power spectrum, and the $\ell = 0, 2$ multipoles, the Einstein–de Sitter approximation is excellent up to $k \sim 0.1h/\mathrm{Mpc}$. For P_4 it is excellent up to $k \sim 0.05h/\mathrm{Mpc}$. For larger k the EdS approximation marginally underpredicts the amplitude of the 1-loop SPT power spectrum. The sign of the effect can be understood by comparison with Fig. 2.1, which shows that the largest effect of retaining the full time dependence is a $\sim 2\%$ enhancement for D_F and D_G.

This underprediction does not automatically translate into an underprediction for the EFT power spectrum, because in principle the counterterm subtractions required in this framework can mask the effect. Some compensation is visible for both the real-space power spectrum and P_0. In each case the EFT prediction using the Einstein–de Sitter approximation is very close to EFT prediction using the full time dependence, up to values of

[17] The sign change occurs near $k = 0.38h/\mathrm{Mpc}$, and is therefore well before the scale $k = 0.75h/\mathrm{Mpc}$ where we have reason to believe the linear counterterm leads to oversubtraction.

k where oversubtraction from the leading-order counterterm becomes problematic. Near these scales the Einstein–de Sitter approximation begins to *relatively* overpredict P_0, because the zero-crossing point occurs at smaller k if the full time dependence is used. This causes an unphysical divergence in the relative error, for the same reasons outline above. This dramatic feature would not survive if higher-order counterterms were introduced, and so its presence should be treated with caution.

For P_2 and P_4 the EFT subtractions do not completely absorb the error in the Einstein–de Sitter approximation. For each of these multipoles the EFT power spectrum has a net $\sim 2\%$ underprediction in the region $k \gtrsim 0.1h/\text{Mpc}$. The size of this error is somewhat smaller than the relative error in the EFT prediction itself; see Fig. 2.9. However, if predictions at the $\lesssim 5\%$ level are required for P_2 and P_4, we conclude that the Einstein–de Sitter approximation would no longer be acceptable.

Redshift dependence

Finally, we consider the EFT prediction for $z > 0$. At high redshift we expect nonlinearities to be less significant, and therefore the net contribution of the counterterms to be smaller.

To determine how the counterterms vary with redshift, we extract power spectra at $z \in \{0.25, 0.5, 0.75, 1\}$ to accompany the results at $z = 0$ described above. Fitting for the counterterms independently at each redshift yields the results of Table 2.4, which we plot in Fig. 2.12. In this redshift interval, both the μ^0 and μ^2 counterterm are increasing. In comparison the μ^4 counterterm is very roughly stable, becoming marginally more important at intermediate redshifts $z \sim 0.5$.

It was explained in §2.2.3 that the time dependence of the counterterms is not predicted by the effective theory, because by construction their values depend on the evolution of modes that are not adequately described by the low-energy theory. Nevertheless, one can ask whether the redshift dependence of Table 2.4 *requires* new types of time dependence beyond what is visible in the perturbative description, or whether the perturbative description could already be sufficient. For example, virialized modes are believed to decouple completely from the evolution of perturbations at low wavenumber except for a small renormalization of the background [11]. If this decoupling persists to large enough scales the net effect might be equivalent to a cutoff on the loop integrals at a fairly modest wavenumber, low enough that the time dependence predicted by perturbation theory is not yet inadequate (excepting the possibility of non-local memory effects [35, 70]). A

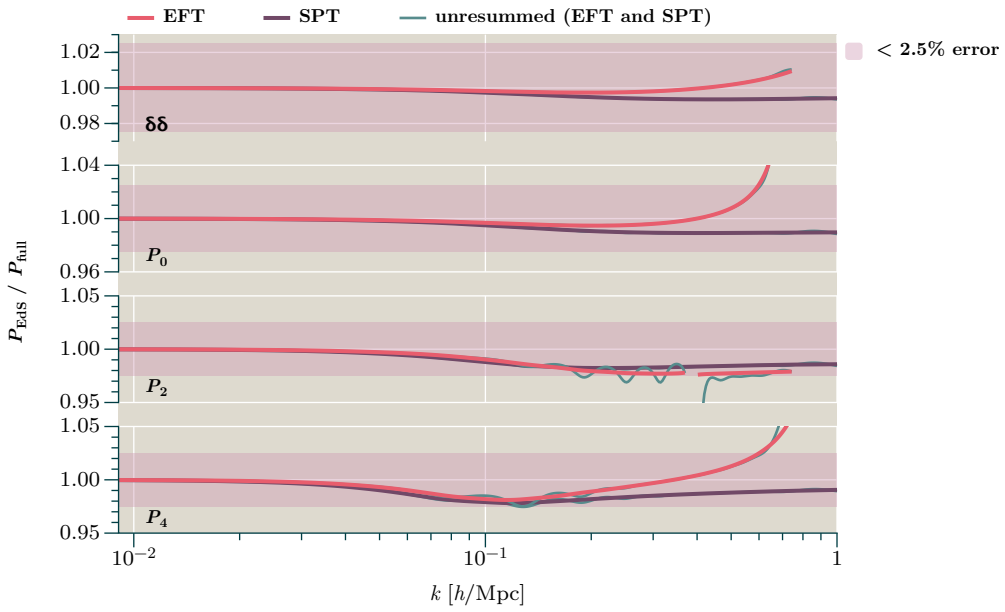

Figure 2.11: Comparison of Einstein–de Sitter approximation with full time-dependence (at $z = 0$) for the effective field theory prediction (red lines) and SPT (purple lines). In each case, the associated green line shows the unresummed result. The plotted quantity is $P_{\rm EdS}/P_{\rm full}$, where $P_{\rm EdS}$ is computed in the Einstein–de Sitter approximation and $P_{\rm full}$ is the result including the full one-loop time dependence. EFT lines are cut off for $k > 0.75h/\text{Mpc}$ where the leading-order counterterm must be supplemented by higher-order contributions. For the EdS–EFT prediction we make a separate fit for the counterterms; they are $c_{2|\delta_s,0} = 2.23h^{-2}\,\text{Mpc}^2$, $c_{2|\delta_s,2} = 16.2h^{-2}\,\text{Mpc}^2$, $c_{2|\delta_s,4} = 6.59h^{-2}\,\text{Mpc}^2$ in the resummed case, and $c_{2|\delta_s,0} = 2.30h^{-2}\,\text{Mpc}^2$, $c_{2|\delta_s,2} = 15.9h^{-2}\,\text{Mpc}^2$ and $c_{2|\delta_s,4} = 6.45h^{-2}\,\text{Mpc}^2$ in the unresummed case. The light-pink shaded region marks where the Einstein–de Sitter approximation is within 2.5% of the prediction using the full time-dependence.

discussion of the time dependence of the counterterms in the context of the Einstein–de Sitter approximation was previously given by Hertzberg [86].

To check whether Table 2.4 is compatible with the perturbative prediction for ultraviolet contributions to the loop integrals, we perform a global fit for the parameters $Z_{2|\delta}$, $Z_{2|\mathbf{v}}$, $Z_{2|\mathbf{v}\delta}$, $Z_{2|\mathbf{vv},A}$, $Z_{2|\mathbf{vv},B}$, $Z_{2|\mathbf{vv}\delta}$ and $Z_{2|\mathbf{vvv}}$, assuming all unpredicted ultraviolet time dependence to be absent. We use the same error estimate of 5% in each k-bin used to measure the $c_{2|\delta_s,2n}$ and impose a flat prior over the interval $[-1, 1]$ on each parameter. We give the marginalized posterior parameter values in Table 2.5 and plot the $c_{2|\delta_s,2n}$ predicted by these values as the points marked 'fitted values' in Fig. 2.12. The fit matches the measured values closely. Notice that under the conditions used to perform the fit, $c_{2|\delta_s,0}$ is determined entirely by $Z_{2|\delta}$ and therefore Fig. 2.12 shows that—in conjunction with the perturbatively-predicted time-dependent factors—this single parameter is enough to fit all five data points accurately. The lines for $c_{2|\delta_s,2}$ and $c_{2|\delta_s,4}$ depend on all seven Z-parameters, but it is still nontrivial that an accurately-fitting combination can be found to match the ten sample points. We find that there are degeneracies between groups of the Z parameters. Their correlation matrix is plotted in Fig. 2.13. (We do not report error bars for the $Z_{2|i}$ for the same reason discussed above, that we do not have reliable estimates of the covariance between our measured power spectra.) The values we have reported include the full time-dependence at one-loop, but the performance of the Einstein–de Sitter approximation is comparable.

It is not possible to draw strong conclusions from this analysis. To the degree that the simulations provide a description of dark-matter clustering in the real universe, there seems no evidence that the time-dependence of deeply ultraviolet modes strongly influences the evolution of modes within the EFT. To some extent, however, this outcome was already embedded in the simulations because these assume that feedback from gas dynamics and other unmodelled baryonic processes does not significantly influence the clustering of modes on much larger scales.

The normalization of the Z-parameters is chosen so that, in the perturbative description, they equal the common value

$$Z = \frac{1}{15\pi^2} \int \mathrm{d}q \; P^*(q). \tag{2.104}$$

Although this is a firm prediction of perturbation theory, we would normally disregard it. The values assumed by the Zs make a statement about the ultraviolet completion, and any such statements derived from the low-energy theory alone cannot be trustworthy. Nevertheless, if the time-dependence predicted by perturbation theory is accurate one

counterterm	$z = 0$	$z = 0.25$	$z = 0.5$	$z = 0.75$	$z = 1$
$c_{2\|\delta_s,0}/k_{NL}^2$ $[h^{-2}\,\mathrm{Mpc}^2]$	2.28	1.94	1.44	1.10	0.894
$c_{2\|\delta_s,2}/k_{NL}^2$ $[h^{-2}\,\mathrm{Mpc}^2]$	16.5	14.0	11.1	8.99	7.14
$c_{2\|\delta_s,4}/k_{NL}^2$ $[h^{-2}\,\mathrm{Mpc}^2]$	6.73	9.23	9.78	9.27	7.96

Table 2.4: Variation of counterterms with redshift. We fit the resummed prediction to the real-space power spectrum and the $\ell = 0, 2, 4$ multipoles over the region $0.2h/\mathrm{Mpc} \leqslant k \leqslant 0.5h/\mathrm{Mpc}$ at each redshift.

$Z_{2\|\delta}$	$Z_{2\|\mathbf{v}}$	$Z_{2\|\mathbf{v}\delta}$	$Z_{2\|\mathbf{vv},A}$	$Z_{2\|\mathbf{vv},B}$	$Z_{2\|\mathbf{vv}\delta}$	$Z_{2\|\mathbf{vvv}}$
1.1×10^{-3}	-1.5×10^{-2}	-7.8×10^{-2}	1.5×10^{-3}	5.8×10^{-3}	1.7×10^{-2}	-1.2×10^{-2}

Table 2.5: Global fit for the Z-parameters. We fit simultaneously to measurements of the real-space power spectrum and the $\ell = 0, 2, 4$ multipoles measured from our simulations at redshifts $z \in \{0, 0.25, 0.5, 0.75, 1\}$. All values are reported in units of $h^{-2}\,\mathrm{Mpc}^2$.

might wonder whether the ultraviolet modes decouple to the extent that approximate equality of the Zs is restored. However, inspection of the values in Table 2.4 shows that this is not the case.

2.4 Conclusions

In this paper we have presented the complete one-loop renormalization of the redshift-space power spectrum and its Legendre multipoles $\ell = 0$, $\ell = 2$ and $\ell = 4$. The same principles apply to modes with $\ell \geqslant 6$, but our numerical results for the hexadecapole are already noisy and present-day observational constraints on this multipole are not yet competitive with the monopole or quadrupole.

The outcome of a similar renormalization has already been reported by Lewandowski et al. [116] in an approximation where all growth functions are replaced by their Einstein–de Sitter counterparts. In this paper we include the exact time dependence for the first time, showing that—at least within the EFT framework, although not for SPT—it is an excellent approximation for the real-space power spectrum and $\ell = 0$ mode, but leads to $\sim 2\%$ errors in the $\ell = 2, 4$ modes for $k \gtrsim 0.1h/\mathrm{Mpc}$. (Results including exact time dependence have been given in Refs. [34, 115], but have not previously been applied to

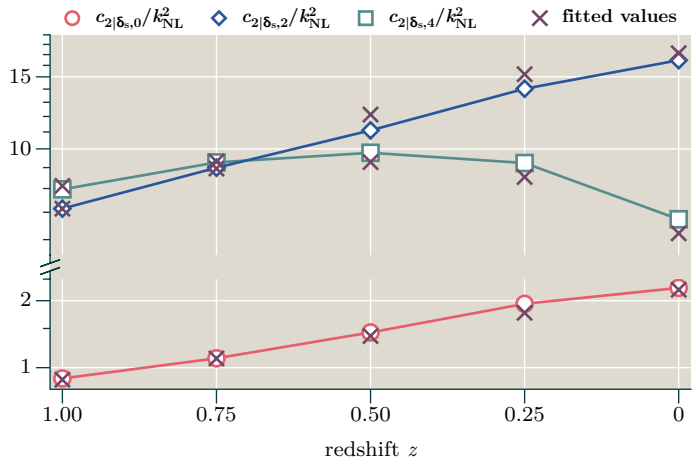

Figure 2.12: Time dependence of EFT counterterms. The plotted values are taken from Table 2.4. The points marked 'fitted values' match the time dependence predicted from Eqs. (2.82a)–(2.82e) assuming no unknown ultraviolet contributions, with values for the constants $Z_{2|i}$ taken from Table 2.5.

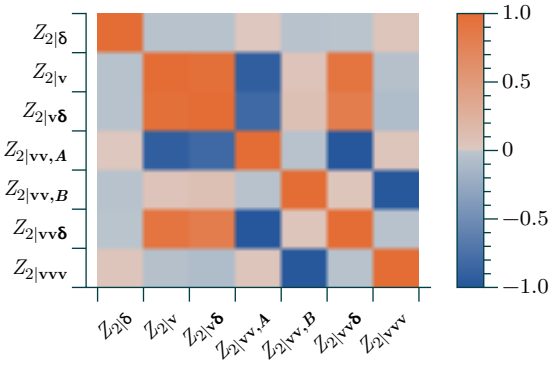

Figure 2.13: Correlation matrix for the $Z_{2|i}$.

the redshift-space power spectrum.) The exact time dependence of the SPT redshift-space power spectrum is already a new result.

Comparison with previous results.—Our formalism is broadly in agreement with the methods used in Refs. [165, 116, 148]. In our presentation we have emphasized the role of the counterterms in parametrizing ultraviolet contributions to loop integrals, rather than arising from smoothed equations of motion. The resulting language is closer to familiar applications of effective field theory in particle physics. In addition, our formalism differs from that presented by Lewandowski et al. [116] in certain technical details, and in our procedure to fit for the counterterms of the redshift-space power spectrum.

For a cosmology matching the MultiDark MDR1 simulation, we find that the real-space power spectrum and the $\ell = 0$ mode of the redshift-space power spectrum can be matched within $\sim 5\%$ using the leading EFT counterterm up to roughly $k \lesssim 0.4h/\mathrm{Mpc}$ at $z = 0$, and with a firm upper limit of $k \lesssim 0.75h/\mathrm{Mpc}$ that follows from imposing positivity of the $\ell = 0$ mode. In practice the higher-order counterterms that restore positivity are presumably already important at substantially smaller wavenumbers.

These maximum k-values are somewhat larger than those found by Lewandowski et al., who reported a fit with $< 2\%$ error to a redshift-space power spectrum extracted from the BigMDPL simulation up to $k \lesssim 0.13h/\mathrm{Mpc}$ at $z = 0.56$. At this redshift, they estimated that higher-order counterterms might already be important at $k = 0.2h/\mathrm{Mpc}$, and suggested that the non-linear scale that controls breakdown of the EFT expansion might sit near $k \approx 0.8h/\mathrm{Mpc}$. Our results are more comparable to those reported by Perko et al., who worked with the halo power spectrum and found a good match up to $k = 0.43h/\mathrm{Mpc}$ at $z = 0.67$. Their fit included more counterterms (roughly, four bias parameters and three stochastic counterterms) and therefore the degree to which our predictions can be compared is not entirely clear. Nevertheless, the qualitative features are very similar.

Our results could also be compared with the 'improved' perturbation theory of Taruya, Nishimichi & Saito [178]. Their prediction can be written as a suppressed Kaiser power spectrum with corrections,

$$P_s = D_{\mathrm{FoG}}(k\mu f\sigma_{\mathrm{v}})\Big(P_{\delta\delta} + 2f\mu^2 P_{\delta\theta} + f^2\mu^4 P_{\theta\theta}\Big) + A(k,\mu) + B(k,\mu), \tag{2.105}$$

where D_{FoG} is a fingers-of-God suppression factor to be chosen by hand, and $A(k,\mu)$ and $B(k,\mu)$ represent a subset of the terms generated by the composite operators $\mathbf{v}\delta$, $\mathbf{vv}$, $\mathbf{vv}\delta$ and $\mathbf{vvv}$ in (2.60). If the power spectra $P_{\delta\delta}$, $P_{\delta\theta}$ and $P_{\theta\theta}$ are evaluated at one-loop and we take $D_{\mathrm{FoG}} \approx \exp(-k^2\mu^2 f^2\sigma_{\mathrm{v}}^2) \approx 1 - k^2\mu^2 f^2\sigma_{\mathrm{v}}^2$, then this very nearly reproduces

Matsubara's SPT result for P_s [178]. Instead, Taruya et al. obtained their improvement by evaluating the power spectra using an alternative prescription [177, 179]. By comparing this model to N-body simulations they were able to demonstrate $\sim 1\%$ accuracy up to $k \lesssim 0.2h/\mathrm{Mpc}$ for the monopole and quadrupole at $z = 0.5$. This model is intended to capture physical effects similar to those used in the EFT model, but these effects appear in different ways: subtraction of power for quasilinear k from D_{FoG} rather than counterterms, and damping of the acoustic oscillations from a combination of D_{FoG} and the modified computation of $P_{\delta\delta}$, $P_{\delta\theta}$, $P_{\theta\theta}$ rather than resummation. The final predictions are broadly comparable, and it would be interesting to understand more clearly how these descriptions are related.

Outlook.—Although we cannot rely on perturbation theory to determine the time-dependence of the counterterms, we show that independent fits for their values at $z \in \{0, 0.25, 0.5, 0.75, 1\}$ are compatible with the time-dependence predicted by the perturbative expansion. In addition, as part of our calculation we have introduced a number of technical innovations:

- We use a new method to decompose the tensor integrals that appear in P_s at one-loop level (§2.3.2), and use it to extract their μ-dependence. This method is based on the Rayleigh plane-wave expansion and analytic integrals over two or three spherical Bessel functions.

- We have extended the resummation scheme proposed by Vlah, Seljak, Chu & Feng [188] to redshift space (§2.3.3). This simplifies calculation of the resummed P_ℓ by comparison with the resummation scheme suggested by Senatore & Zaldarriaga [166].

  In redshift-space this and similar schemes appear similar to the suppression factors used phenomenologically to model the fingers-of-God effect. However we argue that it is more appropriate to interpret the redshift-space counterterms as the source of this suppression, which arises (at least in part) from virialized motions on small scales [158]. Specifically, we show that the redshift-space EFT counterterms successfully reproduce the zero-crossing of the $\ell = 2$ mode, which is associated with this suppression.

We find that the effective field-theory framework successfully produces fits that extend the reach of perturbation theory by a factor of a few in k. While this is a considerable achievement, the practical value of these fitting functions has not yet been demonstrated. First, without a prediction for the time-dependence of the counterterms we are obliged to fit independently at each redshift. This reduces the predictivity of the formalism. Second,

the values of the counterterms vary even between relatively nearby cosmologies such as the Planck2015 and MDR1 models studied in this paper. A proposal to evade the requirement to renormalize on a model-by-model basis has been given by Cataneo, Foreman & Senatore [36]. In cases where this or a similar method can be used, the EFT method may be advantageous for parameter fitting or Fisher forecasts. Specifically, we can reduce the computational requirements if it is possible to produce high-precision predictions over a region of parameter space using sparser coverage with N-body simulations than if we were to achieve the same precision by interpolating the power spectra from these simulations directly.

An alternative use case is to compute covariance matrices that extend to small scales, as suggested by Bertolini et al. [16] and Mohammed, Seljak & Vlah [135]. Our results suggest that accurately modelling redshift-space measurements gives enhanced value to both these use cases. As explained in §2.3.5, we find that bulk flows converge very slowly and exhibit large sample variance, while small-scale velocity effects give important contributions to the redshift-space power spectrum on larger scales. This requirement for high-resolution simulations in large volumes implies that numerical estimation of redshift-space measurements is substantially more expensive than simulation of real-space measurements at the same accuracy. If EFT methods can be used to mitigate this expense then their deployment becomes even more attractive.

Acknowledgments.—The work reported in this paper has been supported by the European Research Council under the European Union's Seventh Framework Programme (FP/2007–2013) and ERC Grant Agreement No. 308082 (DR, DS). LFdlB acknowledges support from the UK Science and Technology Facilities Council via Research Training Grant ST/M503836/1.

Data availability statement.—Computation of the 1-loop matter power spectrum and its multipole decomposition was performed by computer codes, as described in Appendix 2.C. These codes are available for download under open-source licenses. The specific datasets used to construct the EFT power spectra reported in §2.2.6 and §2.3.6 have been made available at zenodo.org. This deposit also includes the **CAMB** parameter files used to construct the linear power spectra, and settings files needed for **gevolution** to perform the N-body simulations described in §2.3.5.

Digital identifiers, attribution information, and licensing conditions are listed in Appendix 2.C for each of these products.

Appendices

2.A Resummation using the Senatore–Zaldarriaga procedure

In §2.2.5 we described the resummation method of Vlah, Seljak, Chu & Feng (the 'VSCF scheme'), which makes explicit use of a decomposition into 'wiggle' and 'no-wiggle' components. This decomposition was critical in allowing the formal Lagrangian-theory expression (2.44) to be rewritten in terms of $P_{\mathrm{w}}^{\leqslant\ell}$ and $P_{\mathrm{nw}}^{\leqslant\ell}$ even when the exponential is not completely expanded. Without this step it would not have been possible to extract a simple, analytic resummation 'template'.

Senatore & Zaldarriaga suggested a different resummation prescription that does not make explicit use of this decomposition [166, 165]. Therefore the relation between these schemes is not completely clear. In this Appendix we briefly sketch the Senatore–Zaldarriaga procedure and explain how it is related to the method of Vlah, Seljak, Chu & Feng.

Isolate infrared contributions.—We define $K(\mathbf{q},\mathbf{k})$ to be the exponential kernel in the Lagrangian formula for the power spectrum,

$$K(\mathbf{q},\mathbf{k}) \equiv \exp\left(-\frac{1}{2}k_i k_j A_{ij} + \frac{\mathrm{i}}{6}k_i k_j k_\ell W_{ij\ell} + \cdots\right). \tag{2.106}$$

The main strategy in the VSCF scheme is to separate the 'no-wiggle' component of K from the remainder; cf. (2.49). Senatore & Zaldarriaga instead chose to isolate the infrared contribution from the two-point function A_{ij}. This yields a new kernel K_{IR} that satisfies

$$K_{\mathrm{IR}}(\mathbf{q},\mathbf{k}) \approx \exp\left(-\frac{1}{2}k_i k_j A_{ij}^{\mathrm{IR}}\right), \tag{2.107}$$

where A_{ij}^{IR} continues to be defined by (2.45a), but with the form-factors X and Y in Eqs. (2.46a)–(2.46b) evaluated at tree-level and restricted to wavenumbers in the infrared. Then the power spectrum (2.44) can be written

$$P(k) = \int \mathrm{d}^3q\, \mathrm{e}^{-\mathrm{i}\mathbf{q}\cdot\mathbf{k}}\Big[K_{\mathrm{IR}}(\mathbf{q},\mathbf{k})\Big]\Big[K_{\mathrm{IR}}^{-1}(\mathbf{q},\mathbf{k})K(\mathbf{q},\mathbf{k})\Big]. \tag{2.108}$$

Notice that both factors in square brackets $[\cdots]$ contain 'wiggle' and 'no-wiggle' contributions, although the 'wiggle' terms in K_{IR} will be very small and could be dropped.

If all quantities were expanded to one-loop then this expression must reproduce the one-loop Eulerian power spectrum. Therefore the infrared-subtracted kernel $K_{\mathrm{IR}}^{-1}K$ by itself can differ from the one-loop Eulerian result only by terms that involve A_{ij}^{IR},

$$\int \mathrm{d}^3q\, \mathrm{e}^{-\mathrm{i}\mathbf{q}\cdot\mathbf{k}}\Big[K_{\mathrm{IR}}^{-1}(\mathbf{q},\mathbf{k})K(\mathbf{q},\mathbf{k})\Big] \approx P^{\leqslant\ell 1}(k) - \Pi_{\mathrm{IR}}(k), \tag{2.109}$$

where $\Pi_{\rm IR}$ is defined by

$$\Pi_{\rm IR}(k) = P_{\rm IR}^{=\ell 0}(k) + \frac{1}{4}\int \mathrm{d}^3q\, \mathrm{e}^{-\mathrm{i}\mathbf{q}\cdot\mathbf{k}}\, k_i k_j k_m k_n A_{ij}^{\rm IR}(\mathbf{q})\Big(A_{mn}^{=\ell 0}(\mathbf{q}) - A_{mn}^{\rm IR}(\mathbf{q})\Big). \tag{2.110}$$

This correction subtracts some of the power in $P^{\leq \ell 1}$ arising from infrared modes. To rewrite the factor $K_{\rm IR}^{-1}K$ in (2.108) using this result, insert a decomposition of unity in the form

$$1 \equiv \int \mathrm{d}^3q'\, \delta_{\rm D}(\mathbf{q}-\mathbf{q}') \equiv \int \frac{\mathrm{d}^3q'\,\mathrm{d}^3k'}{(2\pi)^3}\mathrm{e}^{\mathrm{i}\mathbf{k}'\cdot(\mathbf{q}-\mathbf{q}')}, \tag{2.111}$$

where $\delta_{\rm D}$ is the Dirac δ-function. This yields

$$P(k) = \int \mathrm{d}^3q \int \mathrm{d}^3q' \int \frac{\mathrm{d}^3k'}{(2\pi)^3}\mathrm{e}^{-\mathrm{i}\mathbf{q}\cdot(\mathbf{k}-\mathbf{k}')}\mathrm{e}^{-\mathrm{i}\mathbf{k}'\cdot\mathbf{q}'}K_{\rm IR}(\mathbf{q},\mathbf{k})\Big[K_{\rm IR}^{-1}(\mathbf{q}',\mathbf{k})K(\mathbf{q}',\mathbf{k})\Big]. \tag{2.112}$$

Integrate $K_{\rm IR}$ to a smoothing kernel.—If $K_{\rm IR}$ depends only weakly on $\mathbf{q}$ then the integral over d^3q produces a kernel that has support only in a narrow region where $\mathbf{k} \approx \mathbf{k}'$. This relation becomes exact in the limit that $K_{\rm IR}$ has no dependence on $\mathbf{q}$. Although this is not the case in practice, it gives a simple scenario in which to visualize the outcome of the integration. The kernel is proportional to $\delta_{\rm D}(\mathbf{k}-\mathbf{k}')$ if $K_{\rm IR}$ also has no dependence on $\mathbf{k}$, and convolution with it has no effect. Otherwise, the kernel can be expanded as a series in derivatives of $\delta_{\rm D}(\mathbf{k}-\mathbf{k}')$, and convolution with it represents a local smoothing. For (2.107), the shape of the smoothing kernel is determined by the Gaussian k-dependence of $K_{\rm IR}$, and the width of its smoothing window is determined by the amplitude of X and Y.

Returning finally to the case where X, Y and $K_{\rm IR}$ have weak $\mathbf{q}$-dependence, we can make a Taylor expansion in $\mathbf{q}$ around some fiducial value and exchange explicit powers of $\mathbf{q}$ for further derivatives with respect to $\mathbf{k}$ or $\mathbf{k}'$. Therefore each term in the series expansion integrates to an increasingly high-derivative smoothing kernel. The result can be regarded as a superposition of smoothing kernels with varying widths determined by the variation of X and Y with $\mathbf{q}$. Therefore the smoothing is modulated on the scale of the infrared modes retained in these form-factors. This modulation partially restores the infrared power subtracted by $\Pi_{\rm IR}$.

These arguments are strictly valid only when it is safe to commute limits and summations with the integration over $\mathbf{q}$. Assuming such exchanges to be acceptable, however, we can collect all these together to obtain a net smoothing kernel $M(\mathbf{k},\mathbf{k}')$ defined by

$$M(\mathbf{k},\mathbf{k}') = \int \mathrm{d}^3q\, \mathrm{e}^{-\mathrm{i}\mathbf{q}\cdot(\mathbf{k}-\mathbf{k}')}K_{\rm IR}(\mathbf{q},\mathbf{k}). \tag{2.113}$$

Resummed template is smoothed power spectrum.—The final step is to use the approximation that $M(\mathbf{k},\mathbf{k}')$ has support only near $\mathbf{k} \approx \mathbf{k}'$ to exchange the $\mathbf{k}$-dependence of $K_{\rm IR}^{-1}K$

for $\mathbf{k}'$-dependence. The effect is to average $\mathrm{e}^{\mathrm{i}\mathbf{k}'\cdot\mathbf{q}'}K_{\mathrm{IR}}^{-1}(\mathbf{q}',\mathbf{k}')K(\mathbf{q}',\mathbf{k}')$ over a range of $\mathbf{k}'$ near $\mathbf{k}$. The error in this approximation comes from the inclusion of $\mathrm{e}^{\mathrm{i}\mathbf{k}'\cdot\mathbf{q}'}$ in the average, and can be expressed in terms of gradients of the smoothing kernel in $\mathbf{k}$. If the smoothing does not vary rapidly with wavenumber we may hope it is not large. Proceeding in this way, Senatore & Zaldarriaga obtained the template [166, 116]

$$P_{\mathrm{SZ}}(k) = \int \frac{\mathrm{d}^3k'}{(2\pi)^3} M(\mathbf{k},\mathbf{k}') \left[P^{\leqslant\ell 1}(k') - \Pi_{\mathrm{IR}}(k')\right]. \tag{2.114}$$

If the power spectrum is nearly constant in k then it is unaffected by the smoothing kernel, and therefore the 'no-wiggle' component will be practically unchanged. But the 'wiggle' component is averaged, causing it to be suppressed. Therefore, in the Senatore & Zaldarriaga scheme, the separation into 'wiggle' and 'no-wiggle' components becomes important only in the final average. However, the net effect is still to suppress the acoustic oscillations while leaving the broadband power unchanged.

Note that in the VSCF scheme the amount of suppression applied to the 'wiggle' component at wavenumber k is determined by k/k_{damp}, where as explained in §2.2.5 the wavenumber k_{damp} measures the typical *total* displacement of particles averaged between q_{min} and q_{max}; the infrared modes are not treated separately. In the Senatore–Zaldarriaga scheme we smooth the power spectrum over a window set by the typical displacement induced by infrared modes only, averaged over all scales. The final resummed power spectra are qualitatively similar, but there is no simple relation between the two procedures.

Although the Senatore–Zaldarriaga scheme is elegant, it has computational drawbacks. When applied to redshift-space distortions it is necessary to treat the angular dependence of the integrals numerically. This significantly increases the computational burden. By comparison, in the VSCF scheme the angular dependence can be extracted analytically [cf. Eqs. (2.90) and (2.91)], which simplifies the resummation procedure.

2.B Fabrikant's procedure to evaluate the three-Bessel integrals

In §2.3.2 we described a new procedure for computing the redshift-space one-loop SPT power spectrum P_s^{SPT}, based on the Rayleigh plane-wave expansion. To reduce the resulting expressions to closed form we must integrate over the Bessel functions appearing in the Rayleigh formula. For 13-type integrals this requires weighted integrals over two Bessel functions, which are relatively well-understood. For 22-type integrals it requires

weighted integrals over *three* Bessel functions. These are substantially more difficult to evaluate.

Context.—In 1936, Bailey gave the formula (for positive a, b and c)

$$\int_0^\infty t^{\lambda-1} J_\mu(at) J_\nu(bt) J_\rho(ct)\,\mathrm{d}t = \frac{2^{\lambda-1} a^\mu b^\nu \Gamma(\frac{\lambda+\mu+\nu+\rho}{2})}{c^{\lambda+\mu+\nu}\Gamma(\mu+1)\Gamma(\nu+1)\Gamma(1-\frac{\lambda+\mu+\nu+\rho}{2})} \times F_4\left(\begin{array}{c} [\lambda+\mu+\nu-\rho]/2,\ \mu+1,\ a^2/c^2 \\ [\lambda+\mu+\nu+\rho]/2,\ \nu+1,\ b^2/c^2 \end{array}\right), \tag{2.115}$$

where $\mathrm{Re}(\lambda+\mu+\nu+\rho) > 0$, $\mathrm{Re}(\lambda) < 5/2$, and $c > a+b$; the function F_4 is the fourth type of Appell hypergeometric function,

$$F_4\left(\begin{array}{c} a,\ c_1,\ x \\ b,\ c_2,\ y \end{array}\right) \equiv \sum_{m,n=0}^{\infty} \frac{(a)^{m+n}(b)^{m+n}}{(c_1)^m (c_2)^n m! n!} x^m y^n. \tag{2.116}$$

Here, $(x)^a$ is the Pochhammer symbol (or 'rising factorial') defined by $(x)^a = \Gamma(x+a)/\Gamma(a)$. The condition $c > a+b$ implies that the lengths a, b, c do not form the sides of a triangle. Bailey's methods did not determine the integral when this condition is not satisfied. In particular, there is no reason for the result to be analytic in a, b and c and therefore we cannot extend (2.115) by analytic continuation. (Some results based on analytic continuation are known in special cases; see the discussion in Ref. [74].)

Various extensions of Bailey's results are known. Fabrikant and Dôme used a different computational technique to find integral representations that could be evaluated explicitly [64, 63], but still in the non-triangular case. Mehrem used the Rayleigh plane-wave expansion (3.90) to determine various integrals over two and three spherical Bessel functions, again in the non-triangular case and only when a Clebsch–Gordon coefficient involving the orders μ, ν, σ is not zero [131, 130]. Earlier, Gervois & Navelet [73, 74] had studied the (spherical) three-Bessel integral even in the case where (a, b, c) do form a triangle. Their result appears in its most developed form in Table 2 of Ref. [74], which can be applied whenever $\lambda+\mu+\nu+\rho$ is an integer.

This result of Gervois & Navelet is already sufficient for the purposes of this paper (where μ, ν, σ and λ are individually integers), but in our practical calculations we make use of a more recent formalism due to Fabrikant [62]. The Fabrikant method is equivalent to that of Gervois & Navelet when $\lambda+\mu+\nu+\rho$ is an integer, but is marginally more general because it allows for non-integer λ.

Fabrikant's method.—We briefly summarize the procedure. The aim is to compute a

generalization of the integral (2.71),

$$I = \int_0^\infty t^\lambda j_\mu(kx) j_\nu(qx) j_\sigma(sx), \tag{2.117}$$

where μ, ν and σ are integers, and λ, k, q, and s are real. Fabrikant rewrote the spherical Bessel functions as derivatives of trigonometric functions,

$$j_0(z) = (-1)^{n+1} z^{n+1} \frac{\mathrm{d}^{n+1}}{(z\,\mathrm{d}z)^{n+1}} \cos z, \tag{2.118}$$

which allows I to be expressed in the form

$$I = (-1)^{\mu+\nu+\sigma} a^\mu b^\nu c^\sigma \frac{\partial^\mu}{(a\,\partial a)^\mu} \frac{\partial^\nu}{(b\,\partial b)^\nu} \frac{\partial^\sigma}{(c\,\partial c)^\sigma} \int_0^\infty \frac{\sin at \sin bt \sin ct}{abc\, t^{\mu+\nu+\sigma+3-\lambda}}\,\mathrm{d}t. \tag{2.119}$$

The integral in this expression may be formally divergent, but where I exists the differentiation will yield a finite result. It can be performed using standard trigonometric identities, yielding

$$\begin{aligned} I = (-1)^{\mu+\nu+\sigma} a^\mu b^\nu c^\sigma \cos\frac{\pi}{2}(\mu+\nu+\sigma+3-\lambda) \frac{\partial^\mu}{(a\,\partial a)^\mu} \frac{\partial^\nu}{(b\,\partial b)^\nu} \frac{\partial^\sigma}{(c\,\partial c)^\sigma} \frac{\Gamma(\lambda-\mu-\nu-\sigma-2)}{4abc} \\ \times \Big(|c+a-b|^{\mu+\nu+\sigma+2-\lambda} \operatorname{sgn}(c+a-b) + 2 \text{ cyclic perms} - (a+b+c)^{\mu+\nu+\sigma+2-\lambda} \Big) \end{aligned} \tag{2.120}$$

where $\operatorname{sgn}(x)$ is the sign function, defined by $\operatorname{sgn}(x) = x/|x|$ for $x \neq 0$ and $\operatorname{sgn}(0) = 0$. Compare Eq. (2.120) with Eqs. (3.8), (3.9) and (3.10) of Ref. [74].

If the argument of the cos or Γ functions is zero, then the result should be computed via a limit. The differentiations can be performed using Mathematica, or by using the formula

$$z^{n+1} \frac{\partial^{n+1} f(z)}{(z\,\partial z)^{n+1}} = \sum_{k=0}^{\lfloor n/2 \rfloor} \frac{\Gamma(n+2k+1) f^{(n-2k+1)}(z)}{\Gamma(2k+1)\Gamma(n-2k+1)(2z)^{2k}} - \sum_{k=0}^{\lfloor (n-1)/2 \rfloor} \frac{\Gamma(n+2k+2) f^{(n-2k)}(z)}{\Gamma(2k+2)\Gamma(n-2k)(2z)^{2k+1}}. \tag{2.121}$$

The quantity $\lfloor x \rfloor$ is the floor of x, ie. the largest integer that does not exceed x, and $f^{(n)}(x)$ is the n^{th} derivative of f. As part of the software bundle accompanying this paper we provide a Mathematica notebook to evaluate Eqs. (2.120) and (2.121). It will automatically test the resulting expression against results obtained using Mathematica's built-in integration strategies for highly oscillatory integrals.

Specific results.—We collect the results needed for the computation of $P_s^{\rm SPT}$.

$$\mathscr{J}^0_{00} = \frac{\pi}{4kqs} \tag{2.122a}$$

$$\mathscr{J}^1_{10} = \frac{\pi}{8}\frac{k^2+q^2-s^2}{k^2q^2s} \tag{2.122b}$$

$$\mathscr{J}^2_{20} = \frac{\pi}{32}\frac{3k^4+2k^2(q^2-3s^2)+3(q^2-s^2)^2}{k^3q^3s} \tag{2.122c}$$

$$\mathscr{J}^2_{22} = \frac{\pi}{64}\frac{(3k^4+2k^2q^2+3q^4)s^2+3(k^2+q^2)s^4-3(k^2-q^2)^2(k^2+q^2)-3s^6}{k^3q^3s^3} \tag{2.122d}$$

$$\mathscr{J}^2_{31} = \frac{\pi}{64}\frac{3k^4(q^2+5s^2)+(q^2-s^2)^2(q^2+5s^2)+k^2(q^4+6q^2s^2-15s^4)-5k^6}{k^3q^4s^2} \tag{2.122e}$$

$$\begin{aligned}\mathscr{J}^2_{42} = \frac{\pi}{512}\frac{1}{k^3q^5s^3}\Big(&35k^8-20k^6(3q^2+7s^2)+6k^4(3q^4+10q^2s^2+35s^2)\\&+(q^2-s^2)^2(3q^4+10q^2s^2+35s^4)+4k^2(q^6+3q^4s^2+15q^2s^4-35s^6)\Big)\end{aligned} \tag{2.122f}$$

$$\mathscr{J}^3_{30} = \frac{\pi}{64}\frac{(k^2+q^2-s^2)\big[5k^4+5(q^2-s^2)^2-2k^2(q^2+5s^2)\big]}{k^4q^4s} \tag{2.122g}$$

$$\begin{aligned}\mathscr{J}^4_{40} = \frac{\pi}{512}\frac{1}{k^4q^5s}\Big(&35k^8+20k^2(q^2-7s^2)\big[k^4+(q^2-s^2)^2\big]+35(q^2-s^2)^4\\&+6k^4(3q^4-30q^2s^2+35s^4)\Big)\end{aligned} \tag{2.122h}$$

Index permutations can be obtained by making suitable exchanges of k, q and s; for example, $\mathscr{J}^2_{13}$ can be obtained from (3.93d) by exchanging q and s, and $\mathscr{J}^0_{33}$ can be obtained from (3.94b) by exchanging k and s.

2.C Accompanying software bundle

The calculations needed to obtain the redshift-space power spectrum are complex. To assist those wishing to replicate our results we have made available a large collection of resources, including Mathematica notebooks that summarize (and validate) the calculation of $\langle\delta_s\delta_s\rangle$ in SPT, and software tools to compute the loop integrals needed for numerical evaluation.

2.C.1 Mathematica notebooks

This deposit contains two Mathematica notebooks:

- **FabrikantIntegrals.nb**

  This notebook implements Fabrikant's method for evaluation of the three-Bessel integrals, as described in Appendix 2.B. It will automatically test the resulting analytic formulae against numerical results obtained using Mathematica's built-in integration strategies.

- **SPTPowerSpectrum.nb**

  This notebook summarizes our analytic calculation of the redshift-space power spectrum up to one-loop. It also validates the result against Matsubara's result for the redshift-space power spectrum using the Einstein–de Sitter approximation [125], and with the formulae for the velocity power spectrum given by Makino et al. [123].

2.C.2 One-loop SPT integrals in redshift space

Pipeline A

License	GNU GPL v2.0 or a later version
Author	© University of Sussex 2017. Contributed by David Seery
DOI	DOI 10.5281/zenodo.546725
GitHub	`https://github.com/ds283/LSSEFT`
Git clone	`git clone https://github.com/ds283/LSSEFT.git`

This is a C++ pipeline for computation of the growth factors and loop integrals needed to construct the renormalized redshift-space power spectrum and its multipoles. It implements the Vlah et al. resummation scheme described in §§2.2.5 and 2.3.3.

The implementation is parallelized using MPI and uses adaptive load balancing to spread work over available cores. The Cuba library is used to perform the multidimensional integrations that are required [83], and the SPLINTER library is used to construct B-splines [80]. Results are stored as **SQLite** databases. The counterterm fits are performed using the CosmoSIS parameter-estimation framework and the emcee sampler, for which a Python module is supplied [197]. The power spectra presented in this paper were computed using **git** revision **977e5b03**.

This pipeline shares some code with the **CppTransport** platform for computing correlation functions of inflationary density perturbations [52].

Pipeline B

License	GNU GPL v2.0 or a later version
Author	© University of Sussex 2017. Contributed by Donough Regan
DOI	DOI 10.5281/zenodo.495113
GitHub	https://github.com/DonRegan/PowSpec_EFTofLSS
Git clone	`git clone https://github.com/DonRegan/PowSpec_EFTofLSS.git`

This is a second, independent pipeline that duplicates the functionality of pipeline A, but with slightly different implementation choices. The multidimensional integrations and splines are evaluated using the GNU Scientific Library [72]. The results presented in this paper have been computed using both pipelines A and B, and a third C pipeline implemented using Mathematica. The plots and numerical results are those belonging to pipeline A. The pipeline B results were obtained using **git** revision **1126b040**. We find very good agreement between all pipelines, indicating that our numerics are robust to changes in integration strategy, filtering methods and the counterterm fitting procedure.

2.C.3 Supporting dataset

License	Creative Commons Attribution 4.0 International
Author	Contributed by David Seery and Shaun Hotchkiss
DOI	DOI 10.5281/zenodo.546734
Attribution	Please cite `zenodo.org` DOI and this paper
Download	https://zenodo.org/record/546734

This dataset includes the components necessary to reproduce our numerical results. It comprises:

- **SQLite** databases containing the output of the pipeline described in 2.C.2 for the Planck2015 [4] and MultiDark MDR1 cosmologies [152]. These were used to construct the renormalized real-space power spectrum in §2.2 and the redshift-space power spectrum in §2.3, respectively.

- A settings file for the **gevolution** numerical relativity code, which was used to perform the custom N-body simulations described in §2.3.5. Our results used version 1.1 of

the **gevolution** framework. The initial conditions are generated dynamically from the settings file.

- **CAMB** parameter files for the linear power spectra used to construct our one-loop results, for both the Planck2015 and MDR1 cosmologies. For the Planck2015 model we also include a **CAMB** parameter file to compute the final non-linear power spectrum using **HALOFIT**. These power spectra are also emebedded in the **SQLite** databases containing our numerical results.

Chapter 3

Halo power spectrum in redshift space using effective field theory

Abstract

We study the impact of different bias and redshift-space models on the halo power spectrum, quantifying their effect by comparing the fit to a subset of realizations taken from the **WizCOLA** suite. These provide simulated power spectrum measurements between $k_{\rm min} = 0.03h/{\rm Mpc}$ and $k_{\rm max} = 0.29h/{\rm Mpc}$, constructed using the comoving Lagrangian acceleration method. For the bias prescription we include (i) simple linear bias; (ii) the McDonald & Roy model and (iii) its simpler coevolution variant introduced by Saito et al.; and (iv) a very general model including all terms up to one-loop and corrections from advection. For the redshift-space modelling we include the Kaiser formula with virialization represented by exponential damping and the power spectrum provided by (i) tree-level perturbation theory and (ii) the **HALOFIT** prescription; (iii) one-loop perturbation theory in both clustering and the redshift-space map, also with exponential damping; and (iv) an effective field theory description, also at one-loop in clustering and the redshift-space map, with virialization represented by the EFT subtractions. We quantify the improvement from each layer of modelling by measuring the typical improvement in χ^2 when fitting to a member of the simulation suite. We attempt to detect overfitting by testing for compatibility between the best-fit power spectrum per realization and the best-fit over the entire **WizCOLA** suite. For both bias and the redshift-space map we find that increasingly permissive models yield improvements in χ^2 but with diminishing returns. The most permissive models show modest evidence for overfitting. Accounting for model complexity using the Bayesian Information Criterion, we argue that standard perturbation theory up to one-loop (both in clustering and the redshift-space map), coupled to the Saito et al. coevolution bias model, is likely to provide the best compromise for near-future galaxy surveys such as DESI or LSST.

3.1 Introduction

A new era of large galaxy surveys will soon inaugurate a fertile period for the study of large-scale structure in the Universe. Current or planned surveys include the Dark Energy Survey ('DES'), Euclid, the Dark Energy Spectroscopic Instrument, the Large Synoptic Survey Telescope ('LSST'), the Square Kilometer Array ('SKA') and the 4-metre Multi Object Spectroscopic Telescope ('4MOST') [149, 12, 101, 139, 48]. Each of these surveys measures the distribution of *tracers* of the underlying dark matter distribution. Examples include dark matter haloes and galaxy clusters, but also quasars, the Lyman-α forest, or radiation from the 21-centimetre hyperfine transition of hydrogen. Unfortunately it is not trivial to predict the statistical distribution of these tracers, even if the distribution of dark matter is known accurately, because it involves poorly-understood astrophysical processes such as galaxy formation.

Whatever statistical relation exists between tracers and the underlying dark matter, on scales much larger than the characteristic scale of the tracers it can be expanded in perturbation theory. On these scales the density contrast is small and it is reasonable to expect that an adequate description can be found by retaining only a few low-order terms in the perturbation expansion; for a recent review, see, eg., Ref. [51]. The unknown astrophysical processes that characterize the relationship between tracers and dark matter are encoded in the coefficients of this expansion, but if not too many are required then we can aim to *measure* them rather than predict them from first principles. (See Fig. 3.1.) The disadvantage of this approach is that we must expend some data in constraining the unknown bias coefficients. This inevitably increases the uncertainty with which other physical quantities are measured.

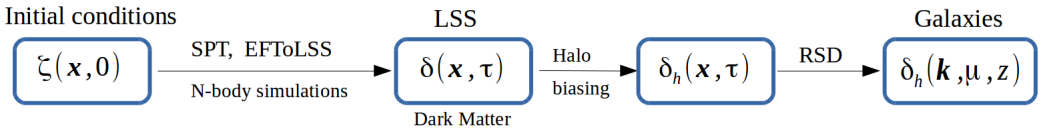

Figure 3.1: Relationship between the primordial initial conditions and large-scale structure observables.

Exactly how many terms must be retained to obtain an adequate description can depend on the properties of the survey and the population of tracers. Failure to model the relationship correctly would impair our ability to extract statistical power from the survey. But conversely, allowing too permissive a relationship would waste this power in

constraining unnecessary coefficients. It also exposes us to the risk of *overfitting*—that is, misinterpreting the random variation between realizations as a meaningful signal. To make best use of the data as it arrives we must find a compromise, balancing simplicity against the minimum level of complexity needed to match the sophistication of next-generation surveys.

What is the appropriate level of complexity for a present-day or near-future survey? A typical previous-generation survey such as WiggleZ would have used a simple linear truncation. More recent surveys have begun to adopt prescriptions that include terms at quadratic order or higher, representing the strength of the tidal gravitational field or related quantities [112, 50, 170, 19, 75]. As surveys probe increasingly small scales these more complex biasing schemes have been found necessary to extract unbiased estimates (in the statistical sense) of the underlying cosmological parameters, or to obtain consistent results between different n-point functions.

Bias modelling.—In this chapter we quantitatively address the question of the appropriate level of modelling sophistication required for analysis of a present-day or near-future galaxy survey. In 'Standard Perturbation Theory' (or 'SPT') we organize each contribution to the bias expansion according to its order in the 'loop expansion'. In this scheme each loop corresponds to an unrestricted average over wavenumbers [100, 187, 69, 77, 174, 123, 162, 161].

Up to one-loop, McDonald & Roy wrote down the most general bias prescription that respects the equivalence principle and is local in the sense of depending on the fields and their spatial derivatives at a single time [126]. The McDonald & Roy scheme therefore bears the same relationship to the linear truncation as one-loop SPT does to tree-level. Their discussion was refined by Chan et al., who phrased their analysis in terms of a slightly different basis of local operators [37]. We give the mapping between the McDonald & Roy and Chan et al. expansions in Appendix 3.A.

Generalizations of McDonald & Roy's prescription are possible. Haloes are assembled over cosmological timescales, so it could happen that the tracer density at time t depends on the advective history of the dark matter fluid at earlier times [191, 164, 134]. This makes the bias expansion more complex. But it could also happen that there are dynamical reasons for different bias coefficients to be related to each other, making the expansion simpler [154].

Redshift-space modelling.—Bias is not the only effect that must be modelled carefully. A galaxy survey does not measure actual spatial configurations, because the radial distance

to each galaxy must be estimated from its redshift. This determination is confused by peculiar motions, giving rise to so-called 'redshift-space distortions' [92, 102]. The large-scale angular distortion due to coherent infall towards local overdensities is known to all orders, assuming non-relativistic motion of the sources [158]. We may account for its effects to as many loop orders as we wish, but these all depend on modelling of local velocities.

Tree-level contributions to the two-point function are well-understood. The analogue of tree-level perturbation theory is the Kaiser formula, which is the basis for most existing treatments [102, 117, 128, 40]. Its reach in k is known to be limited because it does not account for the 'fingers-of-God' suppression at quasi-linear scales to be described below. The extension to one-loop contributions was performed in SPT by Mat

subara [125]. Inclusion of time dependence beyond the Einstein-de Sitter approximation at one-loop was discussed in Ref. [66], and in redshift space in Ref. [49]. A phenomenologically-successful hybrid formula, including some elements of the one-loop SPT result together with other elements of a different origin, was given by Taruya, Nishimichi & Saito [178]. This is commonly known as the 'TNS model'.

Fingers-of-God and Effective Field Theory.—Coherent infall is not the only source of distortion. N-body simulations consistently exhibit strong suppression of power at quasi-linear wavenumbers and above, often ascribed to erasure of correlations due to virialization on subhalo scales. This is the 'fingers-of-God' effect [92, 177]. It is a short-wavelength phenomenon that is not captured at low orders in perturbation theory and must be accounted for in some other way. One option is to introduce an ad hoc phenomenological suppression [142, 143], usually by guessing a suitable functional form. Alternatively, the methods of effective field theory furnish a systematic parametrization of the influence of short-wavelength modes on long-wavelength physics.

This procedure has been elaborated by a number of authors as the 'Effective Field Theory of Large-Scale Structure' [11, 34, 33, 151, 166, 165, 189, 188]. In this framework, as in any application of effective field theory, one introduces counterterms to supply the ultraviolet parts of loop integrals that cannot be estimated reliably on the basis of low-energy perturbation theory. Counterterms due to loops from the redshift-space map should be regarded as the natural means to describe subtraction of power due to short-scale motions. As we shall see, they give a rather more flexible description of the subtraction than the most widely-used phenomenological parametrizations.

Estimates for the power spectrum of a tracer population including some or all of these

effects have appeared in the literature. The one-loop bias corrections to the matter–tracer correlation function and tracer autocorrelation function were computed by McDonald & Roy [126]. Formulae for the same correlation functions including all one-loop effects in clustering and bias (this time accounting for advective contributions from the fluid history) were given by Angulo et al. [6],[1] and after including all one-loop effects in clustering, bias and redshift-space by Perko et al. [148]. These authors worked within the effective field theory framework and determined the counterterms necessary to parametrize unknown short-wavelength effects. They both applied a resummation technique to account for damping of the baryon acoustic oscillation due to large-scale coherent motions.

The modelling burden due to accounting for all these different effects is significant. Taking one-loop effective field theory as an example, we must obtain analytic expressions for the one-loop integrals due to clustering, bias, and redshift-space effects, and use these to deduce the pattern of counterterms. The integrals themselves must be evaluated numerically, usually by Monte Carlo methods, requiring non-negligible compute time. Further integrations are typically required to resum displacements, if this step is performed. Finally, the free counterterms must be determined, either in a 2-step process in which some data is sacrificed for the purpose of obtaining a fit, or by marginalizing over them as nuisance parameters in a larger Markov chain. All this requires a significant investment in analytic calculations, software pipelines, and compute time for parameter fits. Generalization to non-standard scenarios such as modified gravity requires further investment of a similar scale.

Outline.—In this work we study whether this modelling burden is justified. For each combination of bias and redshift-space model, we determine the goodness-of-fit to an ensemble of COLA-accelerated N-body simulations [180]. Our realizations are drawn from the **WizCOLA** simulation suite, which was generated to provide accurate covariance matrices for the WiggleZ galaxy redshift survey [107, 98]. Each mock halo catalogue was used to simulate the power spectrum reconstructed from real WiggleZ measurements, accounting for effects of measurement error, survey geometry, incompleteness, and uncertainties due to the use of spectroscopic redshifts. Therefore our performance measurements will contain a typical selection of effects relevant to a modern galaxy redshift survey, rather than representing the performance of each layer under idealised conditions. We regard this as a significant virtue of the **WizCOLA** suite.

The **WizCOLA** realizations give measurements for the $\ell = 0$, $\ell = 2$ and $\ell = 4$ Legendre

[1] The expressions in this reference were later corrected by Fujita et al. [71].

modes of the redshift-space power spectrum up to $k_{\rm max} = 0.29h/{\rm Mpc}$. With this relatively low value of $k_{\rm max}$, the WiggleZ team found that they could recover unbiased estimates of the underlying cosmological parameters using a linear bias model and the tree-level Kaiser formula for the redshift-space map. The linear power spectrum was estimated using a **HALOFIT** prescription. We take this simple model as the baseline for all our comparisons.

This chapter is organised as follows. In §3.2 we define and review the different models for bias and redshift-space effects that will be used in our our performance analysis. In §3.3 we present our results for fitting to a subsample of ten realizations drawn from the **WizCOLA** suite. We contrast these with fits to the ensemble average over the full set of 600 **WizCOLA** realizations as a means to test for overfitting. Our main conclusions are summmarised in §3.4.

Code availability.—The calculations needed for the complete one-loop power spectrum, including clustering, bias and redshift-space loops, are very lengthy. To validate our results we compare outputs between independent implementations of the entire pipeline.

The first implementation is based on traditional hand-calculation of the loop integrals. These are translated into Mathematica, also by hand. The second implementation uses semi-custom computer algebra methods to automate the computation of all loop integrals directly from an SPT expression for the overdensity δ. Compute code to perform numerical integration is generated automatically to avoid errors due to typos, omissions, or other accidents during translation. We find complete agreement between these pipelines up to the expected variance due to Monte Carlo implementation.

To assist those wishing to replicate our results we have made our codes available. The Mathematica pipeline can be downloaded from Dropbox.

Notation.—Throughout this chapter we use units in which $c = \hbar = 1$. We define the reduced Planck mass to be $M_{\rm P} \equiv (8\pi G)^{-1/2}$. Our Fourier convention is

$$f(\mathbf{x}) = \int {\rm d}^3k\,(2\pi)^{-3}\,f(\mathbf{k}){\rm e}^{{\rm i}\mathbf{k}\cdot\mathbf{x}}, \tag{3.1}$$

$$[f(\mathbf{x})]_{\mathbf{k}} \equiv f(\mathbf{k}) = \int {\rm d}^3x\,f(\mathbf{x}){\rm e}^{-{\rm i}\mathbf{k}\cdot\mathbf{x}}. \tag{3.2}$$

Latin indices a, b, …, from the beginning of the alphabet range over space-time coordinates (t, x, y, z) or $(0, 1, 2, 3)$. Latin indices i, j, …, from the middle of the alphabet range over spatial indices only. Repeated space-time indices are taken to be contracted with the metric g_{ab}. Repeated spatial indices in the 'up' position are contracted with the three-dimensional Euclidean metric δ_{ij}, so that (for example) $v^2 = v^iv^i = \delta_{ij}v^iv^j = \sum_i (v^i)^2$.

Finally, we use subscripts to identify different variants of the same field: s refers to a redshift-space quantity; δ refers to dark matter; h refers to halo quantities; θ refers to the velocity divergence; R denotes a re-normalised operators; and (n) refers to the n^{th} order in perturbation theory.

3.2 Modelling: bias prescriptions and the redshift-space map

Through this section, the most general bias model is fully reviewed, what we call *advective bias*. This model considers space non-local operators, as well as time non-locallity, expanding the biasing up to one-loop to match the one-loop standard perturbation. Finally, stochastic terms are included as well as re-normalisation factors, building the advective bias model combined with the one-loop effective field theory modelling of redshift-space distortions.

3.2.1 Building blocks of non-local Eulerian biasing

Building on work of Assassi et al. [7], we review the scale-independent, space non-local bias model. The halo density at a given location not only depend on the underlying dark matter distribution, tidal tensor and derivatives of the velocity field at that given location. In fact, there exists some influence from the vicinity[2]. The range of influence, k_M, is determined by the mass, M, of the collapsed object, namely $k_M \propto 1/M^{1/3}$. Usually, this length associated to halo mass is different from the scale at which the effective field theory framework breaks down, k_{NL}. In addition, there exist some stochastic contributions, ϵ, coming from the unpredictable injection of noise (and energy) from the bath of modes above the cut-off of the theory.

We now turn to write all the different operators which halo density depends upon. In a matter-dominated universe, the re-scaled gravitational potential is generated by density fluctuations and, for an irrotational velocity field, the velocity potential is sourced by the velocity divergence, $\theta = \partial_i v_i$. The gravitational and velocity potentials, Φ_g and Φ_v

[2]Spatial non-locality comes from considering all halo operators involving exactly two spatial derivatives for the gravitational (or velocity) potential Φ_g (Φ_v).

Order I.	$\delta = \partial^2\Phi_g$
Order II.	$\delta^2 = (\partial^2\Phi_g)^2,$ $\mathcal{G}_2(\Phi_g) \equiv (\partial_i\partial_j\Phi_g)^2 - (\partial^2\Phi_g)^2$
Order III.	$\delta^3, \quad \delta\mathcal{G}_2(\Phi_g), \quad \mathcal{G}_2^{(3)}(\Phi_g),$ $\mathcal{G}_3(\Phi_g) \equiv -\frac{1}{2}\left[2(\partial_i\partial_j\Phi_g)(\partial^i\partial_k\Phi_g)(\partial^k\partial^j\Phi_g) + (\partial^2\Phi_g)^3 - 3(\partial_i\partial_j\Phi_g)^2(\partial^2\Phi_g)\right]$ $\Gamma_3(\Phi_g, \Phi_v) \equiv \mathcal{G}_2(\Phi_g) - \mathcal{G}_2(\Phi_v)$

Table 3.1: List of independent operators that constitute the building blocks of local Eulerian biasing up to third order in perturbation theory [37].

respectively, read

$$\Phi_g = \frac{3\mathcal{H}\Omega_m}{2}\partial^{-2}\delta \to \partial^{-2}\delta, \tag{3.3a}$$

$$\Phi_v = \partial^{-2}\theta, \tag{3.3b}$$

satisfying $\Phi_g^{(1)} = \Phi_v^{(1)}$ at first order. Likewise, the tidal tensor can be defined $\partial_i\partial_j\Phi_\iota$, where $\iota = g, v$. The list of independent operators consistent with the symmetries of the problem up to third order can be read in Table 3.1.

Therefore, the dependence of the halo over-density field on the underlying dark matter distribution, tidal tensor and the rest of operators is given by the functional $\mathtt{F}$

$$\delta_h(\mathbf{x}, t) = \mathtt{F}[\delta, \mathcal{G}_2(\Phi_g), \delta\mathcal{G}_2(\Phi_g), \mathcal{G}_3(\Phi_g), \Gamma_3(\Phi_g, \Phi_v); \epsilon]. \tag{3.4}$$

The explicit expression of the functional $\mathtt{F}$ is generally unknown due to the highly non-linear effects that encodes. Nonetheless, for scales larger than the halo mass scale, $k \ll k_M$, where perturbations are small, the relation above can be Taylor expanded. Consequently, the bias expansion of the space non-local halo density contrast up to third order in Fourier space yields

$$\begin{aligned}
\delta_{\mathbf{k}}^h = \;& b_1\delta_{\mathbf{k}}^{(1)} + \\
+ \;& b_1\delta_{\mathbf{k}}^{(2)} + \frac{b_2}{2!}[\delta^{(1)\,2}]_{\mathbf{k}} + b_{\mathcal{G}_2}[\mathcal{G}_2^{(2)}]_{\mathbf{k}} \\
+ \;& b_1\delta_{\mathbf{k}}^{(3)} + 2\,\frac{b_2}{2!}[\delta^{(1)}\delta^{(2)}]_{\mathbf{k}} + b_{\mathcal{G}_2}[\mathcal{G}_2(3)]_{\mathbf{k}} + \frac{b_3}{3!}[\delta^{(1)\,3}]_{\mathbf{k}} + b_{1\mathcal{G}_2}[\delta\mathcal{G}_2]_{\mathbf{k}} + b_{\mathcal{G}_3}[\mathcal{G}_3]_{\mathbf{k}} + b_{\Gamma_3}[\Gamma_3]_{\mathbf{k}} \\
+ \;& \text{stochastic} + \quad \mathcal{O}(\delta^4)
\end{aligned} \tag{3.5}$$

The stochastic contribution is fully reviewed in section 3.2.4. The set of coefficients

$$\{b_1, b_2, b_3, b_{\mathcal{G}_2}, b_{1\mathcal{G}_2}, b_{\mathcal{G}_3}, b_{\Gamma_3}\}.$$

is known as the set of bias parameters. The main motivation to perform the bias expansion up to third order is to match the loop expansion of standard perturbation theory. Originally, McDonald et al. [126] constructed their bias model based on this premise: to work at the same order in perturbation theory and in the bias expansion.

3.2.2 Adective terms and time non-locality

We have seen how the halo density at a given location depends on the underlying matter distribution, tidal forces, derivatives of velocity field and stochastic noise within a neighbouring region in space. In this section, we review the idea [37, 164] that the halo distribution also depends on the past trajectory of the fluid that ended up collapsing and forming the tracer. The same way there is a scale associated with the length of influence on the halo, one would expect to have a time scale during which the halo is affected by the history of the different fields (refer to Figure 3.2). In other words, in order to obtain an accurate description of the physics of galaxy formation and evolution, the bias model ought to be also non-local in time. Thus the bias expansion given in equation (3.5) needs to be completed.

The average halo density of the past light cone at x reads

$$\delta_h(x) = \int_{\mathcal{I}^-(x)} \mathrm{d}^4x' \kappa(\mathbf{x} - \mathbf{x'})\delta(x') \tag{3.6}$$

where $\mathcal{I}^-(x)$ is the causal past light cone and $\kappa(\mathbf{x}-\mathbf{x'})$ is the memory kernel, encoding the information affecting galaxy formation over the entire displacement along the time flow, from the past at a location x' to the current location x. In case of a infinitely short time scale of influence — the halo is not affected by what happened in the past — , the kernel κ transforms into a Dirac delta. In order to describe advection along the worldline of halo particles, we consider a small packet of fluid with current co-moving coordinate $\mathbf{x}$ that, at a previous time t', would have been located at

$$\mathbf{x}_{fl}(\mathbf{x}, t, t') = \mathbf{x} - \int_{t'}^{t} \mathrm{d}t'' \mathbf{v}[\mathbf{x}_{fl}(\mathbf{x}, t', t'')]. \tag{3.7}$$

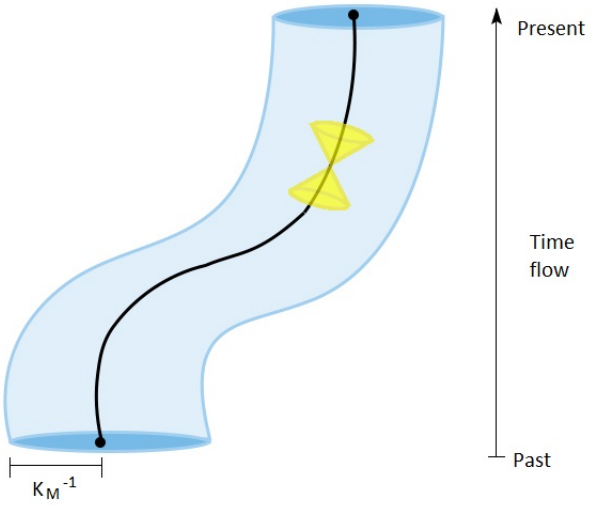

Figure 3.2: History of the collapsed object from the past to today along the worldline, showing the halo mass scale, k_M, and the light cone (in yellow) at a certain location. The image pictures the notion of non-locality in time and space affecting the halo over-density. Image courtesy of M. de la Bella.

For small displacements the equation above can be evaluated perturbatively

$$\begin{aligned}\mathbf{x}_{fl}(\mathbf{x},t,t') = &\mathbf{x} - \int_{t'}^{t} \mathrm{d}t''\mathbf{v}(\mathbf{x},t'') + \int_{t'}^{t}\mathrm{d}t''\int_{t''}^{t'}\mathrm{d}t'''\mathbf{v}(\mathbf{x},t''')\cdot\nabla\mathbf{v}(\mathbf{x},t'') \\ &+\mathcal{O}(\mathbf{v}^3).\end{aligned} \tag{3.8}$$

Working with no loss of generality within the EdS approximation[3], equation (3.8) reads

$$\begin{aligned}\mathbf{x}_{fl}(\mathbf{x},t,t') = &\mathbf{x} - \left(1-\frac{D(t')}{D(t)}\right)\frac{\mathbf{v}^{(1)}}{fH} - \frac{1}{2}\left(1-\frac{D(t')^2}{D(t)^2}\right)\frac{\mathbf{v}^{(2)}}{fH} - \left[\frac{D(t')}{D(t)} - \frac{1}{2}\left(1-\frac{D(t')^2}{D(t)^2}\right)\right]\left(\frac{\mathbf{v}^{(1)}}{fH}\cdot\boldsymbol{\nabla}\right)\frac{\mathbf{v}^{(1)}}{fH} \\ &+\mathcal{O}(\mathbf{v}^3).\end{aligned} \tag{3.9}$$

where $f = \frac{1}{H}\frac{\mathrm{dln}D}{\mathrm{d}t}$ and $D(t)$ is the linear growth function [25, 13].

Applying these corrections to the bias expansion (3.5) would make emerge new contributions to the halo density distribution

$$\delta^h(\mathbf{x},t) \subseteq \int_{t_0}^{t}\mathrm{d}t'\left[b_1(t')\delta(\mathbf{x}_{fl}(\mathbf{x},t')) + b_2(t')\delta(\mathbf{x}_{fl}(\mathbf{x},t'))^2 + \ldots\right]. \tag{3.10}$$

In the case of sub-horizon cold dark matter perturbations in matter domination, we find that time and space (or momentum in Fourier space) factorise at each order[4]. Thus the

[3] Within the Einstein-de Sitter approximation, $\mathbf{v}^{(1)} \propto fDH$, $\mathbf{v}^{(2)} \propto fD^2H$ where $f = \frac{1}{H}\frac{\mathrm{dln}D}{\mathrm{d}t}$.

[4] This is no longer true in any other case and, therefore, one should not expect such factorisation to hold.

above expression can be schematically written in a *quasi-local* form

$$\delta^h(\mathbf{k},t) \sim D(t)A(k) + D(t)^2B(k) + D(t)^3C(k) + \dots \tag{3.11}$$

where $D(t)$, $D(t)^2$, $D(t)^3$, ... schematically represent the time-dependent functions at first, second order, and so on; and $A(k)$, $B(k)$, $C(k)$, etcetera represent the momentum-dependent functions that accompany them. As a clarifying example, we can study the terms associated to the first bias parameter, b_1, in equation (3.10). One can define

$$\int_{t_0}^{t} \mathrm{d}t' b_1(t') D(t') = b_1^{(1)}(t) D(t), \tag{3.12a}$$

$$\int_{t_0}^{t} \mathrm{d}t' b_1(t') D(t')^2 = b_1^{(2)}(t) D(t)^2, \tag{3.12b}$$

$$\int_{t_0}^{t} \mathrm{d}t' b_1(t') D(t')^3 = b_1^{(3)}(t) D(t)^3, \tag{3.12c}$$

then using equations (3.9) and (3.12) in the equation above (3.10) up to third order in perturbations

$$\begin{aligned}
\delta^h(\mathbf{x},t) \subseteq \;& b_1^{(1)}\delta^{(1)}(\mathbf{x},t) \,+\, b_1^{(2)}\delta^{(2)}(\mathbf{x},t) \,+\, b_1^{(3)}\delta^{(3)}(\mathbf{x},t) \\
- \;& \left(b_1^{(1)} - b_1^{(2)}\right) \frac{\mathbf{v}^{(1)}}{fH} \cdot \boldsymbol{\nabla}\delta^{(1)}(\mathbf{x},t) \\
- \;& \frac{1}{2}\left(b_1^{(1)} - b_1^{(3)}\right) \frac{\mathbf{v}^{(2)}}{fH} \cdot \boldsymbol{\nabla}\delta^{(1)}(\mathbf{x},t) \\
- \;& \left(b_1^{(2)} - b_1^{(3)}\right) \frac{\mathbf{v}^{(1)}}{fH} \cdot \boldsymbol{\nabla}\delta^{(2)}(\mathbf{x},t) \\
+ \;& \left[\frac{1}{2}\left(b_1^{(1)} - b_1^{(3)}\right) - b_1^{(2)}\right] \left[\left(\frac{\mathbf{v}^{(1)}}{fH} \cdot \boldsymbol{\nabla}\frac{\mathbf{v}^{(1)}}{fH}\right) \cdot \boldsymbol{\nabla}\delta^{(1)}(\mathbf{x},t) \,+\, \frac{v^{(1)\,i}}{fH}\frac{v^{(1)\,j}}{fH}\partial_i\partial_j\delta^{(1)}(\mathbf{x},t)\right].
\end{aligned} \tag{3.13}$$

Analogously, the terms associated with the second bias parameter, b_2, in equation (3.10) up to third order yield

$$\begin{aligned}
\delta^h(\mathbf{x},t) \subseteq \;& \frac{b_2^{(2)}}{2!}[\delta^{(1)}(\mathbf{x},t)^2]_{\mathbf{k}} \,+\, 2\,\frac{b_2^{(3)}}{2!}[\delta^{(1)}(\mathbf{x},t)\delta^{(2)}(\mathbf{x},t)]_{\mathbf{k}} \\
- \;& 2\left(b_2^{(2)} - b_2^{(3)}\right)\delta^{(1)}(\mathbf{x},t)\frac{\mathbf{v}^{(1)}}{fH} \cdot \boldsymbol{\nabla}\delta^{(1)}(\mathbf{x},t).
\end{aligned} \tag{3.14}$$

And the terms associated with $b_{\mathcal{G}_2}$ read

$$\begin{aligned}
\delta^h(\mathbf{x},t) \subseteq \;& b_{\mathcal{G}_2}^{(2)}[\mathcal{G}_2^{(2)(\mathbf{x},t)}]_{\mathbf{k}} \,+\, b_{\mathcal{G}_2}^{(3)}[\mathcal{G}_2^{(3)(\mathbf{x},t)}]_{\mathbf{k}} \\
- \;& \left(b_{\mathcal{G}_2}^{(2)} - b_{\mathcal{G}_2}^{(3)}\right)\frac{\mathbf{v}^{(1)}}{fH} \cdot \boldsymbol{\nabla}\mathcal{G}_2^{(2)}(\mathbf{x},t).
\end{aligned} \tag{3.15}$$

Corrections associated with b_3, $b_{1\mathcal{G}_2}$, $b_{\mathcal{G}_3}$ and b_{Γ_3} would be higher in order and, therefore, are discarded.

Then the new terms coming from advective effects in Fourier space can be written

$$\delta_A(\mathbf{k}) = \delta_A^{(2)} + \delta_A^{(3)}, \tag{3.16}$$

and employing the short-hand notation given in 3.77, the explicit expressions of $\delta_A^{(2)}$ and $\delta_A^{(3)}$ read

$$\delta_A^{(2)} = \Big(b_1^{(1)} - b_1^{(2)}\Big) D^2 \int_{\mathbf{q},\mathbf{r}}^{\mathbf{k}} \frac{\mathbf{q}\cdot\mathbf{r}}{q^2} \delta^*_{\mathbf{q}}\delta^*_{\mathbf{r}}, \tag{3.17a}$$

$$\begin{aligned}
\delta_A^{(3)} =& \frac{1}{2}\Big(b_1^{(1)} - b_1^{(3)}\Big)\frac{D}{f}\int_{\mathbf{q},\mathbf{r}}^{\mathbf{k}} \frac{\mathbf{q}\cdot\mathbf{r}}{q^2}\int_{\mathbf{s},\mathbf{p}}^{\mathbf{q}} F_{KL}(\mathbf{s},\mathbf{p})\delta^*_{\mathbf{s}}\delta^*_{\mathbf{p}}\delta^*_{\mathbf{r}} \\
&+\Big(b_1^{(2)} - b_1^{(3)}\Big) D \int_{\mathbf{q},\mathbf{r}}^{\mathbf{k}} \frac{\mathbf{q}\cdot\mathbf{r}}{q^2}\int_{\mathbf{s},\mathbf{p}}^{\mathbf{r}} F_{AB}(\mathbf{s},\mathbf{p})\delta^*_{\mathbf{q}}\delta^*_{\mathbf{s}}\delta^*_{\mathbf{p}} \\
&+\left(\frac{b_1^{(1)}+b_1^{(3)}}{2} - b_1^{(2)}\right) D^3 \int_{\mathbf{q},\mathbf{r},\mathbf{s}}^{\mathbf{k}} \frac{\mathbf{r}\cdot\mathbf{s}}{r^2}\,\frac{\mathbf{q}\cdot(\mathbf{r}+\mathbf{s})}{q^2}\delta^*_{\mathbf{q}}\delta^*_{\mathbf{r}}\delta^*_{\mathbf{s}} \\
&+2\Big(\frac{b_2^{(2)}}{2!} - \frac{b_2^{(3)}}{2!}\Big) D^3 \int_{\mathbf{q},\mathbf{r},\mathbf{s}}^{\mathbf{k}} \frac{\mathbf{q}\cdot\mathbf{s}}{q^2}\delta^*_{\mathbf{q}}\delta^*_{\mathbf{r}}\delta^*_{\mathbf{s}} \\
&+\Big(b_{G2}^{(2)} - b_{G2}^{(3)}\Big) D^3 \int_{\mathbf{q},\mathbf{r}}^{\mathbf{k}} \frac{\mathbf{q}\cdot\mathbf{r}}{q^2}\int_{\mathbf{s},\mathbf{p}}^{\mathbf{r}} G_2(\mathbf{s},\mathbf{p})\delta^*_{\mathbf{q}}\delta^*_{\mathbf{s}}\delta^*_{\mathbf{p}}
\end{aligned} \tag{3.17b}$$

Consequently, the bias expansion of the time non-local halo density contrast up to third order in Fourier space yields

$$\begin{aligned}
\delta^h_{\mathbf{k}} =\;& b_1^{(1)}\delta^{(1)}_{\mathbf{k}} + \\
&+\; b_1^{(2)}\delta^{(2)}_{\mathbf{k}} + \frac{b_2^{(2)}}{2!}[\delta^{(1)\,2}]_{\mathbf{k}} + b^{(2)}_{\mathcal{G}_2}[\mathcal{G}_2^{(2)}]_{\mathbf{k}} + \delta_A^{(2)} \\
&+\; b_1^{(3)}\delta^{(3)}_{\mathbf{k}} + 2\,\frac{b_2^{(3)}}{2!}[\delta^{(1)}\delta^{(2)}]_{\mathbf{k}} + b^{(3)}_{\mathcal{G}_2}[\mathcal{G}_2^{(3)}]_{\mathbf{k}} + \frac{b_3}{3!}[\delta^{(1)\,3}]_{\mathbf{k}} + b_{1\mathcal{G}_2}[\delta\mathcal{G}_2]_{\mathbf{k}} + b_{\mathcal{G}_3}[\mathcal{G}_3]_{\mathbf{k}} + b_{\Gamma_3}[\Gamma_3]_{\mathbf{k}} + \delta_A^{(3)} \\
&+ \text{stochastic} + \mathcal{O}(\delta^4)
\end{aligned} \tag{3.18}$$

Therefore, time non-locality becomes the main responsible for splitting the bias parameters in different orders and for new contributions to the halo density. In other words, if halo clustering were local in time: $b_1^{(1)} = b_1^{(2)} = b_1^{(3)} \equiv b_1$, $b_2^{(2)} = b_2^{(3)} \equiv b_2$ and $b^{(2)}_{\mathcal{G}_2} = b^{(3)}_{\mathcal{G}_2} \equiv b_{\mathcal{G}_2}$, reducing the number of bias parameters to seven, and $\delta_A = 0$ — retrieving equation (3.5).

3.2.3 Redshift-space distortions

The addition of redshift-space distortions for the two-point correlation function is now well-understood [103, 117, 128, 40, 49]. Galaxy surveys estimate the radial distance to an object by considering that the Hubble flow is given entirely by the recession velocity

$\mathbf{v}_\mathrm{r}$ of such a source at distance $\mathbf{x}$. It follows that $\mathbf{v}_\mathrm{r} = H\mathbf{x}$. However, each object is also embedded in the peculiar flow $\mathbf{v}$, and therefore its recession velocity is modified so that $\mathbf{v}_\mathrm{r} = H\mathbf{x} + (\mathbf{v}\cdot\hat{\mathbf{x}})\hat{\mathbf{x}}$. Therefore, a galaxy survey that measures the redshift corresponding to $\mathbf{v}_\mathrm{r}$ will assign this galaxy a displaced radial position

$$\mathbf{s} = \mathbf{x} + \frac{\mathbf{v}\cdot\hat{\mathbf{x}}}{H}\hat{\mathbf{x}}. \tag{3.19}$$

where $\hat{\mathbf{x}}$ is a unit vector along the line-of-sight, and $\mathbf{v}/H$ is the peculiar velocity of the galaxy in Hubble units. The real-space matter over-density $\delta(\mathbf{x})$ and the redshift-space over-density $\delta_s(\mathbf{s})$ are related by mass conservation, because the real-to-redshift mapping only moves mass around [158]; it does not change its concentration. Therefore

$$\rho_s(\mathbf{s})\,\mathrm{d}^3 s = \rho(\mathbf{x})\,\mathrm{d}^3 x, \tag{3.20}$$

where ρ_s and ρ are the full density in redshift space and real space, respectively. Hence to first order in perturbations,

$$\rho_{0,s}(\mathbf{s})\Big[1+\delta_s(\mathbf{s})\Big]\,\mathrm{d}^3 s = \rho_0(\mathbf{x})\Big[1+\delta(\mathbf{x})\Big]\,\mathrm{d}^3 x. \tag{3.21}$$

The background density —in real and redshift space, $\rho_{0,s}$ and ρ_0, respectively— is conserved, that is, in the absence of perturbations, matter fields are uniformly and homogeneously distributed in both real and redshift space. Therefore

$$1+\delta_s(\mathbf{s}) = \Big[1+\delta(\mathbf{r})\Big]\,\det\left(\frac{\partial\mathbf{s}}{\partial\mathbf{r}}\right)^{-1}, \tag{3.22}$$

where $\det\left(\frac{\partial\mathbf{s}}{\partial\mathbf{r}}\right) \equiv \det J$ represents the determinant of the Jacobian of the linear transformation, being $\det J = \det\left(\delta^i_k + \hat{r}^i\hat{r}^j\partial_k v_j + O(v^2)\right) \simeq 1 + \hat{r}^i\hat{r}^j\partial_i v_j$, under the *distant observer approximation*. The *distant observer* or plane-parallel approximation establishes that observed galaxies are sufficiently far away that their separations subtend a very small angle at the observer, implying that displacements in redshift space caused by peculiar velocities may be treated as parallels. The halo density reads

$$\delta^h_s(\mathbf{k}) = \delta^h(\mathbf{k}) + \int \mathrm{d}^3 x\; \mathrm{e}^{-\mathrm{i}\mathbf{x}\cdot\mathbf{k}}\left[\mathrm{e}^{-\frac{\mathrm{i}}{H}(\mathbf{k}\cdot\hat{\mathbf{x}})\left[\mathbf{v}(\mathbf{x})\cdot\hat{\mathbf{x}}\right]} - 1\right]\left[1+\delta^h(\mathbf{x})\right], \tag{3.23}$$

where $\mu \equiv \hat{\mathbf{k}}\cdot\hat{\mathbf{x}}$ defines the cosine of the angle of the line of sight. The peculiar velocity is treated as a perturbative parameter, therefore the exponential function in the equation above (3.23) can be expanded up to third order, yielding the redshift-space halo density contrast [84, 160, 125, 165, 116]

$$\begin{aligned}[\delta^h_s]_\mathbf{k} = [\delta^h]_\mathbf{k} &- \frac{\mathrm{i}}{H}(\mathbf{k}\cdot\hat{\mathbf{x}})[\hat{\mathbf{x}}\cdot\mathbf{v}]_\mathbf{k} - \frac{\mathrm{i}}{H}(\mathbf{k}\cdot\hat{\mathbf{x}})[\hat{\mathbf{x}}\cdot\mathbf{v}\delta^h]_\mathbf{k} - \frac{1}{2!H^2}(\mathbf{k}\cdot\hat{\mathbf{x}})^2[(\hat{\mathbf{x}}\cdot\mathbf{v})^2]_\mathbf{k} \\ &- \frac{1}{2!H^2}(\mathbf{k}\cdot\hat{\mathbf{x}})^2[(\hat{\mathbf{x}}\cdot\mathbf{v})^2\delta^h]_\mathbf{k} - \frac{\mathrm{i}}{3!H^3}(\mathbf{k}\cdot\hat{\mathbf{x}})^3[(\hat{\mathbf{x}}\cdot\mathbf{v})^3]_\mathbf{k} + \mathcal{O}(\delta^4).\end{aligned} \tag{3.24}$$

The full expression for the linear, quadratic and cubic part of the redshift-space halo density contrast can be found in Appendix 3.B.

Advective terms.—Using equation (3.19) to map from real to redshift space, the redshift-space advective corrections to the halo density (3.16) yields

$$\delta_s^A(\mathbf{k}) = \delta^A(\mathbf{k}) - \mathrm{i}\frac{\hat{\mathbf{k}}\cdot\hat{\mathbf{x}}}{H}\Big[(\mathbf{v}_p\cdot\hat{\mathbf{x}})^{(1)}\delta_A^{(2)}\Big]_{\mathbf{k}}. \tag{3.25}$$

The second term is the Doppler correction to the advective terms, $\delta^A_{\mathrm{Doppler}}$, whose specific expression reads

$$\delta^A_{\mathrm{Doppler}}(\mathbf{k}) = \left(b_1^{(1)} - b_1^{(2)}\right) D^3 f\mu k \int^{\mathbf{k}}_{\mathbf{q},\,\mathbf{r}} \frac{\mu_{\mathbf{q}}}{q}\int^{\mathbf{r}}_{\mathbf{s},\,\mathbf{p}} \frac{\mathbf{s}\cdot\mathbf{p}}{s^2}\,\delta^*_{\mathbf{q}}\delta^*_{\mathbf{s}}\delta^*_{\mathbf{p}}, \tag{3.26}$$

where we have used the notation given in Appendix 3.B.

3.2.4 Stochasticity

There exists another contribution associated with the impact of small-scale perturbations on galaxy formation. Such contribution is sourced by random noise at microscopical level which does not correlate with other fields, this the so-called *stochastic* field ϵ. According to [34, 33], the stochastic field ought to follow a Poisson distribution with zero mean and to correlate only with itself and not the rest of density and velocity fields. Due to galaxy formation, halo mass and momentum is not conserved and, therefore, the leading stochastic contribution is found at k^0[5]. From the operator product expansion, the stochastic noise involves terms proportional to $\{\epsilon, \epsilon\delta, \epsilon\delta^2\}$ up to third order in perturbations, as well as contributions up to second order in k. That gives

$$\begin{aligned}\delta_h^{(\epsilon)}(\mathbf{k}) = {} & d_1\epsilon + d_2\epsilon\delta + d_3\epsilon\delta^2 + d_4\left(\frac{k}{k_M}\right)^2\epsilon + d_5\left(\frac{k}{k_M}\right)^2\epsilon\delta + d_6\left(\frac{k}{k_M}\right)^2\epsilon\delta^2 \\ & + \mathcal{O}\left(\epsilon^4\right).\end{aligned} \tag{3.27}$$

In order to obtain the stochastic terms in redshift space, the mapping (3.19) is employed once again

$$\delta^{(\epsilon)}_{h,s}(\mathbf{k}) = \delta^{(\epsilon)}_h(\mathbf{k}) + \delta^{(\epsilon)}_{\mathrm{Doppler}}(\mathbf{k}) \tag{3.28}$$

[5] This is not the case for dark matter whose mass and momentum is conserved. In this case, the stochastic term comes into the stress-energy tensor with two spatial derivatives, being suppressed by $(k/k_{NL})^4$ in the power spectrum [34, 33, 148].

where the Doppler contribution reads

$$\begin{aligned}\delta^{(\epsilon)}_{\rm Doppler}(\mathbf{k}) = &-\frac{\mathrm{i}}{H}\mu k[\hat{\mathbf{x}}\cdot\mathbf{v}]_{\mathbf{k}} - \frac{\mathrm{i}}{H}\mu k[\hat{\mathbf{x}}\cdot\mathbf{v}\delta^{(\epsilon)}_h]_{\mathbf{k}} - \frac{1}{2!H^2}(\mu k)^2[(\hat{\mathbf{x}}\cdot\mathbf{v})^2]_{\mathbf{k}} \\ &- \frac{1}{2!H^2}(\mu k)^2[(\hat{\mathbf{x}}\cdot\mathbf{v})^2\delta^{(\epsilon)}_h]_{\mathbf{k}} - \frac{\mathrm{i}}{3!H^3}(\mu k)^3[(\hat{\mathbf{x}}\cdot\mathbf{v})^3]_{\mathbf{k}} \\ &+ \mathcal{O}(\delta^{(\epsilon)\,4}_h).\end{aligned} \tag{3.29}$$

For the velocity divergence[6], it is worth recalling that diffeomorphism invariance requires all the bias terms for the halo velocity to be derivative suppressed. This also applies to the stochastic contributions because in the rest frame of dark matter, the halo simply inherits the dark matter velocity. This property implies that the halo velocity cannot include any constant stochastic term since the dark matter stochastic term is already derivative suppressed. Therefore the leading order contribution to the stochastic halo velocity must be proportional to $\propto \partial^i\epsilon$, and thus the stochastic velocity divergence $\theta^{(\epsilon)}_h \propto \partial^2\epsilon$. Then the following tensors are defined: $\epsilon_i = \partial_i\epsilon$ and $\epsilon_{ij} = (\delta_{ij} + k_ik_j/k^2_M)\epsilon$[7] [148]. In terms of these tensors, the Doppler terms in the redshift-space stochastic distribution yields

$$\mu k[\hat{\mathbf{x}}\cdot\mathbf{v}]_{\mathbf{k}} \propto \mu k f\frac{\hat{\mathbf{x}}\cdot\mathbf{k}^i}{k?M^2}\delta^{(\epsilon)} \propto\ f(\mu k)^2\epsilon, \tag{3.30a}$$

$$\mu k[\hat{\mathbf{x}}\cdot\mathbf{v}\delta^{(\epsilon)}_h]_{\mathbf{k}} \propto \mu k f\,\hat{x}_i(\epsilon^i + k^i\epsilon), \tag{3.30b}$$

$$(\mu k)^2[(\hat{\mathbf{x}}\cdot\mathbf{v})^2]_{\mathbf{k}} \propto (\mu k f)^2\,\hat{x}_i\hat{x}_j(\epsilon^{ij} + k^ik^j\epsilon), \tag{3.30c}$$

$$(\mu k)^2[(\hat{\mathbf{x}}\cdot\mathbf{v})^2\delta^{(\epsilon)}_h]_{\mathbf{k}} \propto (\mu k f)^2\,\hat{x}_i\hat{x}_j\epsilon^{ij}, \tag{3.30d}$$

$$(\mu k)^3[(\hat{\mathbf{x}}\cdot\mathbf{v})^3]_{\mathbf{k}} \propto (\mu k f)^3\,\hat{x}_i\hat{x}_j\hat{x}_\ell\epsilon^i(\epsilon^{j\ell} + k^jk^\ell\epsilon). \tag{3.30e}$$

Therefore, the Doppler stochastic leading term is $\propto f(\mu k)^2\epsilon$, and terms such as $(\mu k)^3[(\hat{\mathbf{x}}\cdot\mathbf{v})^3]_{\mathbf{k}} \propto \mathcal{O}((k/k_M)^4)$ would have null contribution. We can write

$$\delta^{(\epsilon)}_{\rm Doppler}(\mathbf{k}) = d_s f\mu^2\left(\frac{k}{k_M}\right)^2\epsilon, \tag{3.31}$$

where d_s is a stochastic parameter.

---

[6] The velocity divergence is defined as $\theta = \partial_i v^i$ — dimensionless in Hubble units. Furthermore, the velocity for a fluid with vanishing vorticity can be written as the gradient of a scalar potential $v_i = \partial_i\Phi_v$. In addition, at first order in perturbation, $\theta = -f\delta$. Thus the projected velocity along the line of sight can also be written as

$$\hat{\mathbf{x}}\cdot\mathbf{v} = -f\frac{\hat{\mathbf{x}}\cdot\boldsymbol{\nabla}}{\partial^2}\delta.$$

[7] Perko et al. define them as Lorentz invariance while these relations truly are covariant under spatial rotations.

3.2.5 The halo power spectrum

We now turn to compute the halo two-point statistics

$$\langle \delta^{h,s}_{\mathbf{k}} \delta^{h,s}_{\mathbf{k}'} \rangle \equiv (2\pi)^3 \delta(\mathbf{k}+\mathbf{k}') P^{hh}_s(k,z). \tag{3.32}$$

Employing the expression above (3.24) to compute the halo two-point statistics, the one-loop halo power spectrum reads

$$P^{hh}_s(k,z) = P^{hh}_{s,11}(k,z) + P^{hh}_{s,13}(k,z) + P^{hh}_{s,22}(k,z), \tag{3.33}$$

where we need to compute

$$(2\pi)^3 \delta_D(\mathbf{k}+\mathbf{k}') P^{hh}_{s,11}(k) = \langle \delta^{h\,(1)}_{s,\,\mathbf{k}} \delta^{h\,(1)}_{s,\,\mathbf{k}'} \rangle, \tag{3.34a}$$

$$(2\pi)^3 \delta_D(\mathbf{k}+\mathbf{k}') P^{hh}_{s,13}(k) = 2\langle \delta^{h\,(1)}_{s,\,\mathbf{k}} \delta^{h\,(3)}_{s,\,\mathbf{k}'} \rangle, \tag{3.34b}$$

$$(2\pi)^3 \delta_D(\mathbf{k}+\mathbf{k}') P^{hh}_{s,22}(k) = \langle \delta^{h\,(2)}_{s,\,\mathbf{k}} \delta^{h\,(2)}_{s,\,\mathbf{k}'} \rangle. \tag{3.34c}$$

Full details of these calculations can be found in Appendix 3.B.

Advective terms.—In order to compute the advective contributions to the one-loop redshift-space halo power spectrum,

$$P^{A}_s(k) = P^{A}_{s,\,13}(k) + P^{A}_{s,\,22}(k), \tag{3.35}$$

we need to calculate, using equation (3.25), the following two-point functions

$$(2\pi)^3 \delta_D(\mathbf{k}+\mathbf{k}') P^{A}_{s,\,13}(k) = 2\langle \delta^{h\,(1)}_{s,\,\mathbf{k}} \delta^{A\,(3)}_{\mathbf{k}'} \rangle + 2\langle \delta^{h\,(1)}_{s,\,\mathbf{k}} \delta^{A}_{\mathrm{Doppler},\,\mathbf{k}'} \rangle, \tag{3.36a}$$

$$(2\pi)^3 \delta_D(\mathbf{k}+\mathbf{k}') P^{A}_{s,\,22}(k) = 2\langle \delta^{h\,(2)}_{s,\,\mathbf{k}} \delta^{A\,(2)}_{\mathbf{k}'} \rangle + \langle \delta^{A\,(2)}_{\mathbf{k}} \delta^{A\,(2)}_{\mathbf{k}'} \rangle. \tag{3.36b}$$

Again, the reader can refer to Appendix 3.B for the full computations of these correlation functions.

Stochastic terms.—In order to obtain the stochastic part of the halo power spectrum in redshift space, it is necessary the computation of the following correlation functions:

$$\langle \delta^{(\epsilon)}_{h\,s}(\mathbf{k}) \delta^{(\epsilon)}_{h\,s}(\mathbf{k}') \rangle \;=\; \langle \delta^{(\epsilon)}_{h}(\mathbf{k}) \delta^{(\epsilon)}_{h}(\mathbf{k}') \rangle \;+\; 2\,\langle \delta^{(\epsilon)}_{h}(\mathbf{k}) \delta^{(\epsilon)}_{\mathrm{Doppler}}(\mathbf{k}') \rangle \;+\; \langle \delta^{(\epsilon)}_{\mathrm{Doppler}}(\mathbf{k}) \delta^{(\epsilon)}_{\mathrm{Doppler}}(\mathbf{k}') \rangle. \tag{3.37}$$

Bearing in mind that the stochastic field does not correlate with other fields and using

equations (3.27) and (3.29), the stochastic correlation functions read

$$\begin{aligned}\langle\delta_h^{(\epsilon)}(\mathbf{k})\delta_h^{(\epsilon)}(\mathbf{k}')\rangle = &\left[d_1^2 + 2d_1d_4\left(\frac{k}{k_M}\right)^2\right]\langle\epsilon^2\rangle \\ &+ \left[d_2^2 + 2d_2d_5\left(\frac{k}{k_M}\right)^2\right]\langle(\epsilon\delta)^2\rangle \\ &+ \left[2d_1d_3 + (2d_1d_6 + 2d_3d_4)\left(\frac{k}{k_M}\right)^2\right]\langle\epsilon(\epsilon\delta^2)\rangle,\end{aligned} \tag{3.38a}$$

$$\langle\delta_h^{(\epsilon)}(\mathbf{k})\delta_{\text{Doppler}}^{(\epsilon)}(\mathbf{k}')\rangle = 2d_1d_sf\mu^2\left(\frac{k}{k_M}\right)^2\langle\epsilon^2\rangle + 2d_3d_sf\mu^2\left(\frac{k}{k_M}\right)^2\langle\epsilon(\epsilon\delta^2)\rangle \tag{3.38b}$$

$$\langle\delta_{\text{Doppler}}^{(\epsilon)}(\mathbf{k})\delta_{\text{Doppler}}^{(\epsilon)}(\mathbf{k}')\rangle \propto \mathcal{O}\left((k/k_M)^4\right). \tag{3.38c}$$

According to [148], the terms proportional to $\langle(\epsilon\delta)^2\rangle$ and $\langle\epsilon(\epsilon\delta^2)\rangle$ are degenerate with $\langle\epsilon^2\rangle$ — which is a constant $\langle\epsilon^2\rangle = 1/\bar{n}$. Therefore, we can write the one-loop redshift-space stochastic power spectrum

$$\begin{aligned}P_{h,\,s}^{(\epsilon)}(k,z) = &\frac{1}{\bar{n}}\left[d_1^2 + 2\left(d_1d_4 + d_1d_sf\mu^2\right)\left(\frac{k}{k_M}\right)^2\right] \\ &+ \frac{1}{\bar{n}}\left[d_2^2 + 2d_1d_3 + 2\left((d_1d_6 + d_2d_5 + d_3d_4) + d_3d_sf\mu^2\right)\left(\frac{k}{k_M}\right)^2\right]\int^{\Lambda}\mathrm{d}^3qP_{11}(q) \\ &+ \mathcal{O}(k^4).\end{aligned} \tag{3.39}$$

Finally, the total halo power spectrum — considering equation (3.33), the advective (3.35) and stochastic (3.39) contributions — in standard perturbation theory reads

$$P_s^{hh}(k,z) = P_{s,11}^{hh}(k,z) + \left(P_{s,13}^{hh}(k,z) + P_{13}^{A,s}(k,z)\right) + \left(P_{s,22}^{hh}(k,z) + P_{22}^{A,s}(k,z)\right) + P_{h,\,s}^{(\epsilon)}(k,z). \tag{3.40}$$

3.2.6 Renormalised operators

Up to this point we have developed the advective bias model in standard perturbation theory. Notwithstanding, as it happens for the dark matter power spectrum [13], the standard framework seems unable to deal with the physics coming from non-linear scales, $k \gtrsim k_M$[8]. This means that, for scales of interest and visible for current and future surveys of large-scale structures, $k_* \leqslant k \leqslant k_M$ — being k_* the scale at which standard perturbation breaks down —, the standard theory produces unreliable results and therefore becomes unpredictable. Fortunately, the effective field theory is capable of encoding all the ultra-violet

[8] For the halo power spectrum, we adopt a more conservative cut-off scale, the halo mass scale k_M, which may differ from the non-linear scale k_{NL} appearing in the effective field theory applied to dark matter: $k_M \leqslant k_{NL}$.

physics in a finite set of parameters, becoming a more robust and preferable framework to study macroscopic quantities — such as the density distribution — on this mild non-linear regime [140].

Then, as we did for the matter power spectrum [49], we work in the ultra-violet limit to find the correspondent counter-terms of the theory to renormalise the halo power spectrum. Inspection of the redshift-space halo density contrast within this limit reveals that $(\delta_s^h)^R$ could involve multiplicative, $\partial^0\delta$, and mixing renormalisation, $\partial^2\delta$, $\partial^4\delta$ and so on:

$$(\delta_s^h)^R(\mathbf{x},t) = \delta_s^h(\mathbf{x},t) - c_{s0}^2(t)\partial^0\delta(\mathbf{x},t) - c_{s2}^2(t)\partial^2\delta(\mathbf{x},t) - c_{s4}^2(t)\partial^4\delta(\mathbf{x},t) + \dots \tag{3.41}$$

Remarkably, one of the key differences between the halo density field and the dark matter density field is that the halo density has divergences at k^0. For dark matter, these corrections are forbidden by energy-momentum conservation. However, the bias expansion is supposed to be complete at one-loop. Thus any multiplicative counter-term at k^0 would just be absorbed into the bias parameters, $b_1^{(1)}$, $b_1^{(2)}$, $b_1^{(3)}$, etcetera. Therefore, counter-terms at k^0 need not be included in the renormalised operator [148]. In addition, we truncate our expansion up to second order in wavemodes, $\sim (k/k_M)^2$ — higher order in k would absorb the ultra-violet divergences at two-loop and higher levels. Finally, the renormalised halo density contrast reads

$$(\delta_s^h)^R(\mathbf{k}) = \delta_s^h(\mathbf{k}) + c_{2|\delta_s^h}\left(\frac{k}{k_M}\right)^2\delta(\mathbf{k}) + \mathcal{O}(k^4). \tag{3.42}$$

In addition, by inspecting equation (3.23), it was shown in [49] that despite the density contrast itself does not admit a series expansion in μ^2, the counter-terms will do so. It follows that

$$c_{2|\delta_s^h} = \sum_n c_{\delta_s^h|2n}\,\mu^{2n}. \tag{3.43}$$

Renormalisation conditions.—δ_s^h in equation (3.24) can be regarded as the sum of different independent operators [189, 116, 148], $\{\delta_h, \mathbf{v}, \mathbf{v}\delta, \mathbf{vv}, \mathbf{vv}\delta, \mathbf{vvv}\}$. However, only the sum is physically meaningful and should be matched to some observable quantity. Under this perspective, in order to renormalise the sum, every single independent operator need to be renormalised and therefore should have a particular counter-term

$$(\delta^h)^R_{\mathbf{k}} = \delta^h(\mathbf{k}) + c_{\delta|2}\left(\frac{k}{k_M}\right)^2\delta(\mathbf{k}) + \dots \tag{3.44a}$$

$$(v^i)^R_{\mathbf{k}} = v^i(\mathbf{k}) + c_{v|2}\frac{Hf}{k_M^2}k^i\delta(\mathbf{k}) + \dots \tag{3.44b}$$

$$(v^i\delta)^R_{\mathbf{k}} = (v^i\delta)(\mathbf{k}) + c_{v\delta|2}\frac{Hf}{k_M^2}k^i\delta(\mathbf{k}) + \dots \tag{3.44c}$$

Likewise, the composite operators — given by the operator product expansion —

$$[v^i v^j]^R_{\mathbf{k}} = [v^i v^j]_{\mathbf{k}} + \left(c_{12}\,\delta^{ij} + c_{13}\,\hat{k}^i\hat{k}^j\right)\delta^{(1)}(\mathbf{k}) + \dots \tag{3.45a}$$

$$[v^i v^j \delta]^R_{\mathbf{k}} = [v^i v^j \delta]_{\mathbf{k}} + \left(c_{32}\,\delta^{ij} + c_{33}\,\hat{k}^i\hat{k}^j\right)\delta^{(1)}(\mathbf{k}) + \dots \tag{3.45b}$$

$$[v^i v^j v^\ell]^R_{\mathbf{k}} = [v^i v^j v^\ell]_{\mathbf{k}} + c_{21}\left(\delta^{ij}v^\ell(\mathbf{k}) + \delta^{i\ell}v^j(\mathbf{k}) + \delta^{j\ell}v^i(\mathbf{k})\right) + \dots \tag{3.45c}$$

Using these expressions in equation (3.24) at tree level and recalling that $v^i(\mathbf{k}) = \mathrm{i}k^i H f \delta^{(1)}(\mathbf{k})/k_M^2$ at first order, we obtain

$$[\delta^h_s]_{\mathbf{k}} = [\delta^h]_{\mathbf{k}} + \left[-c_{2|\delta} + \mu^2\left(c_{2|v} + c_{2|v\delta} - \frac{c_{12}+c_{32}}{2}\right) + \mu^4\frac{c_{13}+c_{33}-c_{21}f}{2}\right]k^2\delta^{(1)}_{\mathbf{k}} \tag{3.46}$$

Then computing the two-point statistics and identifying the coefficients with equations (3.42) and (3.43), we find the following degeneracies among the renormalisation factors

$$c_{\delta^h_s|6} = f^3 c_{\delta^h_s|0} - f^2 c_{\delta^h_s|2} + f c_{\delta^h_s|4}, \tag{3.47a}$$

$$c_{\delta^h_s|8} = 0. \tag{3.47b}$$

From equation (3.47a) we observe that the factor at μ^6 is degenerate, whereas from equation (3.47b) we conclude there is no renormalisation of μ^8 at one-loop. This means that equation (3.43) would expand up to order μ^6, and the renormalised redshift-space halo power spectrum at one-loop would turn into

$$P^R_{h,s}(k,z) = P^{\mathrm{SPT},\Lambda}_{h,s}(k,z) - \sum_{n=0}^{3} c_{\delta^h_s|2n}\,\mu^{2n}\left(\frac{k}{k_M}\right)^2 P^{\delta\delta}_{11}(k), \tag{3.48}$$

where $P^{\mathrm{SPT},\Lambda}_s$ is the one-loop standard perturbation power spectrum following from Eq. (3.40) with the loop integrals cut-off at $q \sim \Lambda$, and the second term in the right hand side of the equation is the counter-term power spectrum, P^{hh}_{CT}.

Advective renormalisation.—Inspection of the advective terms in the ultra-violet limit indicates that any divergence coming from these contributions are also absorbed by the counter-terms (3.43). This means that their renormalisation would be degenerate with the contribution of the halo stochastic biases up to second order in k.

Stochastic renormalisation.—The possible divergences in the stochastic power spectrum come from the integral $\int^\Lambda \mathrm{d}^3 q P_{11}(q)$ in equation (3.39). Such divergence can be absorbed simply by adjusting the different stochastic parameters. Thus the renormalised stochastic

contribution to the halo power spectrum in redshift space up to one-loop yields

$$P^{(\epsilon)\,R}_{h,\,s}(k,z) = \frac{1}{\bar{n}}\left[c_{\epsilon,1} \,+\, (c_{\epsilon,2} + c_{\epsilon,3} f\mu^2)\left(\frac{k}{k_M}\right)^2\right] + \mathcal{O}(k^4), \tag{3.49}$$

where $c_{\epsilon,1}$, $c_{\epsilon,2}$ and $c_{\epsilon,3}$ are the renormalised factors.

Finally, the total one-loop halo power spectrum in redshift space (3.40) using effective field theory reads

$$P^{hh}_{s\,R}(k,z) = P^{hh}_{s,11}(k,z) + \Big(P^{hh}_{s,13}(k,z) + P^{A,s}_{13}(k,z)\Big) + \Big(P^{hh}_{s,22}(k,z) + P^{A,s}_{22}(k,z)\Big) + P^{(\epsilon)\,R}_{h,\,s}(k,z) + P^{hh}_{CT}(k,z). \tag{3.50}$$

3.3 Analysis

The main goal of this section is the analysis of the different bias models combined with different redshift-space descriptions using data from the **WizCOLA** simulation. In doing so, we decompose the power spectra into different multipoles using Legendre decomposition and we compute the likelihood to find the set of parameters which fit best the dataset. Such analysis would provide a quantitative measure allowing us to make a strong and correct decision on model choice to deal with observational data. This kind of analysis is done for the first time in this work for the effective field theory framework.

Furthermore, all computations and analyses performed throughout this work have been computed independently using automated and handwritten calculations for the theoretical predictions, and employing different programming languages for the chi-square study. This cross-check has allowed us to understand how the apparent spread in the final chi-square values comes from independent implementations of the same formalism (different programming language, different methods of computing loop integrals, different optimisation of the likelihood, etc.).

3.3.1 Comparison with other models

As mentioned, we compare our predictions against different models and theories broadly used in the literature to resemble and adjust the actual distribution of galaxies. We distinguish among frameworks which account for redshift-space distortions (RSD from now on) and, likewise, we study different bias models. Regarding RSD, these theories are:

Kaiser theory in redshift-space.—[102]

$$P^{h}_{s}(k) = P_{\delta\delta}(k) + 2f\mu^2 P_{\delta\theta}(k) + f^2\mu^4 P_{\theta\theta}(k). \tag{3.51}$$

We consider Kaiser tree level (*KaiserTree*)—for which we employ CAMB, $P_{\delta\delta}^{\rm CAMB}$, to compute the linear dark matter power spectrum and also we consider the linear relation between the density field and the velocity divergence—and *KaiserHalo* —for which we use CAMB **HALOFIT**, $P_{\delta\delta}^{\rm Halofit}$.

One-loop standard perturbation theory in redshift space.—(*SPT*) [13]

$$P_s(k,z) = P_{11}^s(k,z) + P_{13}^s(k,z) + P_{22}^s(k,z). \tag{3.52}$$

One-loop effective field theory in redshift space.—(*EFT*) [49]

$$P_s(k,z) = P_{11}^s(k,z) + P_{13}^s(k,z) + P_{22}^s(k,z) + P_{CT}(k,z). \tag{3.53}$$

On top of that, the impact of small scales on large scales are taken into account. The effective field theory framework adjust for this effect through the set of counter-terms. However, Kaiser tree, Kaiser **HALOFIT** and one-loop standard perturbation power spectrum need to be multiplied by an exponential factor: $\mathrm{e}^{-\mu^2 f^2 k^2 \sigma_v^2}$, which phenomenologically describes the power damping on small scales due to the velocity dispersion σ_v—related to random motions within clusters and virialised haloes, the so-called *fingers-of-God effect* [143].

Concerning bias description, we have chosen to study

Linear bias model.—(*Linear*) This is the simplest bias model one could work with. The statistical relation between haloes and the underlying dark matter perturbations in real space [46] becomes linear

$$\delta_h(\mathbf{k}) = b_1 \delta^{(1)}(\mathbf{k}). \tag{3.54}$$

Local McDonald & Roy model.—(*M&Roy*) McDonald et al.'s main motivation to construct this bias model [126] was their concern about the fact that to be consistent with the loop expansion in perturbation, one would need to match the same order in the bias expansion. Therefore,

$$\delta_h(\mathbf{k}) = b_1\delta(\mathbf{k}) + \frac{b_2}{2!}\delta^2(\mathbf{k}) + \frac{b_{s^2}}{2!}s^2(\mathbf{k}) + b_{3nl}[\sigma_3\delta]_{\mathbf{k}}, \tag{3.55}$$

where $\sigma_3^2(k) = \int \ln r \Delta^2(kr) I_R(r)$, further definitions in reference [126]. In our language, $[\sigma_3\delta]_{\mathbf{k}} \equiv \frac{105}{32}\left(s_{ij}t^{ij} + \frac{8}{189}\delta^3\right)$ and, according to the dictionary in appendix 3.A, The McDonald & Roy model reduces to

$$\delta_{\mathbf{k}}^h = b_1\delta_{\mathbf{k}} + \frac{b_2}{2!}\delta_{\mathbf{k}}^2 + b_{\mathcal{G}_2}[\mathcal{G}_2^{(2)}]_{\mathbf{k}} + \frac{b_3}{3!}\delta_{\mathbf{k}}^3 + b_{1\mathcal{G}_2}[\delta\mathcal{G}_2]_{\mathbf{k}} + b_{\Gamma_3}[\Gamma_3]_{\mathbf{k}} \tag{3.56}$$

with the following degeneracies

$$\frac{b_2}{2!} \equiv \frac{b_2}{2!} + \frac{2}{3}\frac{b_{s^2}}{2!}, \quad b_{\mathcal{G}_2} \equiv \frac{b_{s^2}}{2!}, \tag{3.57a}$$

$$\frac{b_3}{3!} \equiv \frac{5}{6}\,b_{3nl}, \quad b_{1\mathcal{G}_2} \equiv -\frac{5}{8}\,b_{3nl}, \quad b_{\Gamma_3} \equiv \frac{105}{64}\,b_{3nl}. \tag{3.57b}$$

Co-evolution.—(*Coevo*) This bias model [154] involves only two free parameters

$$\delta_h(\mathbf{k}) = b_1^{(L)}\delta(\mathbf{k}) + \frac{b_2^{(L)}}{2!}\delta^2(\mathbf{k}). \tag{3.58}$$

The authors of the co-evolution model participate of McDonald et al.'s idea of performing the bias expansion at the same order as the perturbation expansion, however they consider in addition the following degeneracies:

$$b_1 \equiv b_1^{(L)}, \tag{3.59a}$$

$$\frac{b_2}{2!} \equiv \frac{b_2^{(L)}}{2!}, \quad \frac{b_{s^2}}{2!} \equiv -\frac{4}{7}\left(b_1^{(L)} - 1\right), \tag{3.59b}$$

$$b_{3nl} \equiv \frac{32}{315}\left(b_1^{(L)} - 1\right). \tag{3.59c}$$

Advective model.—(*Advective*) We have presented this model in full detail (section 3.2). We also find that the bias parameters for the advective model are not independent but degenerate at one-loop:

$$b_1^{(1)} \longrightarrow b_1^{(1)} + \left[\left(1 + \frac{6D_A + 8D_B}{3D^2}\right) b_2^{(3)} + \frac{1}{2}\,b_3 - \frac{4}{3}\,b_{1\mathcal{G}_2} + \frac{4}{3}\frac{D_A + D_B - f(f_A D_A + f_B D_B) + f^2 D^2}{D_A + D_B} b_{\Gamma_3}\right]\sigma(\Lambda, z)^2 \tag{3.60a}$$

$$b_{\mathcal{G}_2}^{(3)} \longrightarrow b_{\mathcal{G}_2}^{(3)} + \frac{D_A + D_B - f(f_A D_A + f_B D_B) + f^2 D^2}{D_A + D_B} b_{\Gamma_3} \tag{3.60b}$$

where $\sigma(\Lambda, z)^2 \equiv \sigma(\Lambda)^2 D(z)^2$[9]. Whereas, in EdS approximation, the degeneracies transform into

$$b_1^{(1)} \longrightarrow b_1^{(1)} + \left[\frac{55}{21}\,b_2^{(3)} + \frac{1}{2}\,b_3 - \frac{4}{3}\,b_{1\mathcal{G}_2} + \frac{4}{3}\left(1 - \frac{3}{5}f^2\right) b_{\Gamma_3}\right]\sigma(\Lambda, z)^2 \tag{3.61a}$$

$$b_{\mathcal{G}_2}^{(3)} \longrightarrow b_{\mathcal{G}_2}^{(3)} + \left(1 - \frac{3}{5}f^2\right) b_{\Gamma_3}. \tag{3.61b}$$

Consequently, the number of independent bias parameters reduces to six

$$\{b_1^{(1)}, b_1^{(2)}, b_1^{(3)}, b_2^{(2)}, b_{\mathcal{G}_2}^{(2)}, b_{\mathcal{G}_2}^{(3)}\}.$$

With all these models as ingredients, we study different combinations of RSD and BIAS models (RSD+BIAS). For further details of how to compute this grid of models, refer to Table 3.2.

[9] $\sigma(\Lambda)^2 \equiv \int^{\Lambda} \frac{\mathrm{q}}{4\pi^2} q^2 P(q)$.

	Linear	*M&Roy*	*Coevo*	*Advective*
KaiserTree	We use Eq. (3.54) combined with (3.51) $\times \mathrm{e}^{-\mu^2 f^2 k^2 \sigma_v^2}$ and considering $P_{\delta\delta}^{\mathrm{CAMB}}$	Eq. (3.55) with (3.51) $\times \mathrm{e}^{-\mu^2 f^2 k^2 \sigma_v^2}$ and $P_{\delta\delta}^{\mathrm{CAMB}}$	Eq. (3.58) with (3.51) $\times \mathrm{e}^{-\mu^2 f^2 k^2 \sigma_v^2}$ and $P_{\delta\delta}^{\mathrm{CAMB}}$	Eq. (3.24) and (3.25) with (3.51) $\times \mathrm{e}^{-\mu^2 f^2 k^2 \sigma_v^2}$ and $P_{\delta\delta}^{\mathrm{CAMB}}$
KaiserHalo	Eq. (3.54) with (3.51) $\times \mathrm{e}^{-\mu^2 f^2 k^2 \sigma_v^2}$ and $P_{\delta\delta}^{\mathrm{Halofit}}$	Eq. (3.55) with (3.51) $\times \mathrm{e}^{-\mu^2 f^2 k^2 \sigma_v^2}$ and $P_{\delta\delta}^{\mathrm{Halofit}}$	Eq. (3.58) with (3.51) $\times \mathrm{e}^{-\mu^2 f^2 k^2 \sigma_v^2}$ and $P_{\delta\delta}^{\mathrm{Halofit}}$	Eq. (3.24) and (3.25) with (3.51) $\times \mathrm{e}^{-\mu^2 f^2 k^2 \sigma_v^2}$ and $P_{\delta\delta}^{\mathrm{Halofit}}$
SPT	Eq. (3.54) with (3.52) $\times \mathrm{e}^{-\mu^2 f^2 k^2 \sigma_v^2}$	Eq. (3.55) with (3.52) $\times \mathrm{e}^{-\mu^2 f^2 k^2 \sigma_v^2}$	Eq. (3.58) with (3.52) $\times \mathrm{e}^{-\mu^2 f^2 k^2 \sigma_v^2}$	Eq. (3.24) and (3.25) with (3.52) $\times \mathrm{e}^{-\mu^2 f^2 k^2 \sigma_v^2}$
EFT	Eq. (3.54) with (3.53)	Eq. (3.55) with (3.53)	Eq. (3.58) with (3.53)	Eq. (3.50) (this work)

Table 3.2: Grid of different RSD and bias models considered in this analysis. The first row refers to the different bias models, whereas the first column represents the RSD frameworks.

3.3.2 WizCOLA simulations

As we explained above, we utilise the **WizCOLA** simulation in order to analyse our theoretical predictions. **WizCOLA** is a set of simulations[10] designed by the WiggleZ Dark Energy survey to resemble the WiggleZ observational data[11] in the manner in which observations were made[12]—the same angular mask, the same redshift distribution of observed galaxies—and to give an estimate of the covariance matrix. **WizCOLA** amounts to 3600 simulations with different initial random modes, generating 600 independent realisations of mock galaxies for six independent survey regions in the sky [110]. **WizCOLA** cosmology matches that of WMAP5 [111]: $\Omega_m = 0.273$, $\Omega_\Lambda = 0.727$, $\Omega_b = 0.0456$, $h = 0.705$, $\sigma_8 = 0.812$ and $n_s = 0.961$. The data is available in three overlapping redshift bins, $0.2 < z < 0.6$, $0.4 < z < 0.8$ and $0.6 < z < 1.0$. In concrete, in this project we employ the first redshift bin, corresponding to $z = 0.44$, and only 10 realisations. In order to be rigorous, one would need to take into account the relativistic effects arising from observing the past lightcone that alter the observed galaxy number count on cosmological scales. In other words, observations performed along the past lightcone bring in a series of local and non-local corrections, the so-called *General Relativity projection effects*. Traditionally, the Limber approximation [118] has been widely employed to account for these corrections. However, such approximation may not hold any more for scales probed by the next generation of galaxy surveys. Therefore, such effects need to be computed analytically, using a weighted projection down from the light cone. Such computation has never been implemented in the context of the effective field theory; although some work has been done for other power spectrum applications (see for example Bertacca et al. [15]). Unfortunately, our analysis do not consider any of these projection effects; but it will constitute an essential research work in the future. For all these reasons and for the purpose of this study, we consider it is sufficient to compute our theoretical predictions at

[10] The **WizCOLA** simulations employ the so-called COLA algorithm. The acronym COLA stands for CO-moving Lagrangian Acceleration method, which was invented by Tassev et al. [180] to facilitate the generation of large numbers of realisations of cosmological simulations in a reasonable amount of time—reducing the number of time steps by combining second-order Lagrangian perturbation theory and N-body simulation.

[11] The WiggleZ Dark Energy survey was originally designed to detect the scale of the baryon acoustic oscillations at higher redshift than ever [141] and was carried out at the Australian Astronomical Observatory over the course of 276 nights [55], measuring redshifts of up to 225415 galaxy spectra [21].

[12] Of course whether the physics that was assumed for the **WizCOLA** simulations (gravity as we understand it) is the same as the physics that gave rise to the distribution of matter observed by WiggleZ is still an open question.

the median redshift provided by the **WizCOLA** dataset.

The redshift-space galaxy power spectrum $P_g^s(k,\mu)$ in terms of wavenumber k and cosine angle μ can be decomposed in terms of the multipole power spectra

$$P_g^s(k,\mu) = \sum_{\ell=0}^{2n} P_\ell(k)\mathcal{L}_\ell(\mu) \tag{3.62}$$

Where each multipole power spectra is computed through

$$P_\ell(k) = \frac{2\ell+1}{2}\int_{-1}^{1} \mathrm{d}\mu P_g^s(k,\mu)\mathcal{L}_\ell(\mu). \tag{3.63}$$

Additionally, observational data do not represent the actual power spectrum for various reasons. Therefore, the observed power spectrum is then the convolution of a window function with the true underlying power spectrum. This window function represents the anomalous "power" generated simply by selecting galaxies on a past light cone, with some redshift selection function and angular mask. Thus the **WizCOLA** simulations were generated to match as closely as possible the WiggleZ selection function.

Then the likelihood[13] analysis gives

$$-2\mathfrak{L}^{\mathrm{WizCOLA}} = \sum_{i=1}^{6}(\vec{P}_i^{\mathrm{WizCOLA}} - \vec{P}_i^{\mathrm{conv}})^{\mathrm{T}} C_{\mathrm{Wiz},i}^{-1}(\vec{P}_i^{\mathrm{WizCOLA}} - \vec{P}_i^{\mathrm{conv}}), \tag{3.64}$$

where i is the index that refers to the region (1-hr, 3-hr, 9-hr, 11-hr, 15-hr and 22-hr), $\vec{P}^{\mathrm{WizCOLA}}$ is the multipole power spectra measured from the **WizCOLA** simulation, $\vec{P}^{\mathrm{conv}}$ is the convolved power spectra, from the model and the window function and C_{Wiz}^{-1} is the covariance matrix, measured by computing the variation in the multipole spectra over all the realisations from **WizCOLA** [99, 20].

3.3.3 Bayesian information criterion

Fitting multiple models to data entails the necessity of comparing results by using a concrete model selection criterion in order to clarify which model is the most veridical. Quoting Verde [186], a useful fitting procedure should provide a) best fit parameters, b) error estimates on the parameters, c) and statistical measure of the goodness of fit. Obviously, if c) suggests that the model is not adjusting well to the real data, a) and b) are meaningless, therefore this theoretical model ought to be discarded. As the number of model parameters becomes larger, the risk of over-fitting increases. In other words, an over-fitted model contains more parameters that can be justified by the data and, therefore, such model would extract some of the residual variation as if that noise represented

[13] Recall the relation between the likelihood and the chi-square function: $\chi^2 \equiv -2\mathfrak{L}^{\mathrm{WizCOLA}}$.

underlying model structure. The opposite effect could also happen with models with very few parameters. In this case, the under-fitted model cannot adequately capture the structure of the data. Consequently, we need a quantitative measure of incorrect fitting, as well as a quantitative manner to compare models with different numbers of parameters.

The first step would be to compare different models using the evidence for each model — second level of Bayesian inference. In general, the model evidence is not straightforward to compute since it involves integrating out the dependence on model parameters. For y the theoretical data, m a given model and θ the model parameters, it reads

$$p(y|m) = \int p(y, \theta|m) \mathrm{d}\theta \tag{3.65}$$

where $p(y, \theta|m)$ is the likelihood distribution. Bayesian inference derives the posterior probability as a a consequence of two antecedents: the aforementioned likelihood distribution, $p(y, \theta|m)$, and the prior distribution, $p(\theta|m)$. The Bayes' theorem writes the posterior probability as

$$p(\theta|y, m) = \frac{p(y, \theta|m)p(\theta|m)}{p(y|m)}. \tag{3.66}$$

By using this, equation (3.65) reads

$$p(y|m) = \int p(y|\theta, m)p(\theta|m) \mathrm{d}\theta. \tag{3.67}$$

Moreover, taking logarithms to the equation above and employing the Laplace approximation lead to an expression for the log model evidence consisting of an accuracy term and various complexity terms (see appendix A of Penny et al. [147] for further details)

$$\log p(y|m)_L = Acc(m) - Comp(m). \tag{3.68}$$

A simple approximation to the log model evidence is given by the Bayesian information criterion (BIC) [157], for which all terms that do not scale with the number of data points are dropped,

$$BIC = \log p(y|\hat{\theta}, m) - \frac{Np}{2} \log N_d \tag{3.69}$$

where $\hat{\theta}$ is the estimated parameters, N_p is the number of model parameters and N_d refers to the number of data points. The first term on the right hand side would be the accuracy term, whereas the second term would be a complexity term which adds a penalty factor for each parameter.

Yet, another special case of the Laplace approximation is given by the Akaike's information criterion (AIC) [5], which is maximized when the approximating likelihood of a novel data point is closest to the true likelihood,

$$AIC = \log p(y|\hat{\theta}, m) - Np. \tag{3.70}$$

Likewise, one of the most broadly used information criterion is based on the so-called Bayes factors (BF) [106]. The Bayes factors is a summary of the evidence provided by the data in favour of one statistical model as opposed to another. Given models $m = i$ and $m = j$, the BF comparing model i to j is defined as

$$B_{ij} = \frac{p(y|i)}{p(y|j)}. \tag{3.71}$$

When $B_{ij} < 1$, data favour model i over j, otherwise $B_{ij} > 1$ and model j is favoured. Moreover, the Bayes factors can be used to compare non-nested models and allow to quantify evidence in favour of a null hypothesis. However, the main disadvantage of BF is their dependence of the prior distribution on the model parameters. For this reason, either BIC or AIC become better alternatives.

Additionally, in order to make decisions based on BF, some cut-off value is required. In Bayesian decision theory (see [14] for details), the choice of cut-off is guided by a *loss function* or *utility* capturing the costs of making false-positive and false-negative decisions. A conservative strategy would be to compute BF based on BIC and AIC and to make a decision only if both factors agree.

Unfortunately, there seems to be no possibility of implementing the full Bayesian model selection analysis in our case. In other words, the Bayes factor analysis is possible in principle, however it would be absolutely prohibitive in practice because it would take too long to compute. Furthermore, BIC is observed to be biased towards simple models, whereas AIC to complex models [106]. This means BIC pays a heavier parameter penalty than AIC. All things considered, we regard the Bayesian information criterion as the best alternative to the Bayesian evidence for our analysis.

In terms of the chi-square distribution, the Bayesian information criterion for model selection [157] is defined by shifting the χ^2 by a penalty factor $\varpi \equiv N_p \ln N_d$. Specifically, we define

$$BIC = \chi^2 + \varpi. \tag{3.72}$$

Smaller values of the BIC are preferred. Tables 3.3 and 3.4 show the number of parameters and the correspondent penalty factor for each model considered in this work.

Bias model				Redshift-space model			
Linear	*Coevo*	*M&Roy*	*Advective*	*KaiserTree*	*KaiserHalo*	*SPT*	*EFT*
1	2	4	6	1	1^+	1	6

Table 3.3: Number of parameters associated to each RSD and bias parameter. The + sign for Kaiser **HALOFIT** indicates that the power spectrum generated by CAMB **HALOFIT** uses some parameters to calibrate and match data.

	Linear		*Coevo*		*M&Roy*		*Advective*	
KaiserTree	2	11.1	3	16.6	5	27.6	7	38.7
KaiserHalo	2	11.1	3	16.6	5	27.6	7	38.7
SPT	2	11.1	3	16.6	5	27.6	7	38.7
EFT	7	38.7	8	44.2	10	55.3	12	66.4

Table 3.4: Number of parameters (black) and penalty factor (blue) of every model combination, RSD+BIAS.

3.3.4 Results

We now summarise the outcome of our analysis. First, we study the relative performance of each combination of bias and redshift-space model, quantified in units of χ^2. Second, we use the Bayesian Information Criterion to compensate for the number of free parameters involved in each model. We will use a ranking by improvement in BIC to identify which modelling choices represent the best compromise between flexibility to capture physically meaningful adjustments and rigidity to prevent overfitting. For our purposes, 'overfitting' means that the fit per-realisation is sufficiently permissive that it can adjust to match realisation variance. This is an unwanted effect, because it is likely to bias attempts to recover the underlying cosmological parameters by fitting the power spectrum. Finally, we validate our conclusions by comparing the fit per-realisation to the fit to the ensemble average. Where the model is too permissive we should expect these to differ significantly because of adaptation to realisation-specific features.

Improvement in χ^2

For each realisation, we define the χ^2-improvement relative to the WiggleZ baseline model *KaiserHalo+Linear*. This model gives an overall χ^2 of 296.4 ± 25.5 with $\chi^2/\text{dof} \sim 1.176$.

(There are $14 \times 3 \times 6 = 252$ degrees of freedom in the dataset.) While this is a reasonable fit, there is scope for improved modelling to reduce the mean χ^2 by up to ~ 50 to obtain $\chi^2/\mathrm{dof} \sim 1.0$. A significant portion of the variability in fit is attributable to variability in the baryon acoustic oscillation ('BAO') feature. For a survey of size comparable to WiggleZ the BAO feature is not very well resolved in a typical realisation, and can appear with large phase shifts or even be absent entirely. This is a purely statistical effect due to the number of available modes. It has no dependence on the underlying cosmological model. For larger surveys such as DESI or LSST the BAO feature is expected to be defined much more clearly. However, should these surveys elect to subdivide their volume then similar variability could reappear.

For each realisation, the improvement is

$$\Delta\chi^2 \equiv \chi^2(\mathrm{fit}) - \chi^2(\mathrm{base}). \tag{3.73}$$

Here, $\chi^2(\mathrm{base})$ is the χ^2 achieved by the baseline model and $\chi^2(\mathrm{fit})$ is the χ^2 achieved when fitting whatever combination of bias and redshift-space models is under discussion. Occasionally we will refer to the χ^2 for a specific realisation, but generally we quote the mean improvement over all ten realisations. The results are given in Table 3.5 and summarised in Figs. 3.3 and 3.4, which show the improvement due to changes in bias model (with fixed redshift-space model) and redshift-space model (with fixed bias model), respectively.

As we would expect, the most permissive combination *Advective* + *EFT* yields the best overall fit, giving $\chi^2 = 281.9 \pm 23.8$. But given the complexity of the modelling, this improvement is strikingly modest—just ~ 14 units of χ^2 compared to the baseline model. Meanwhile, we note that the variability of fit over the subsample barely changes, no matter which model is in use.

Improvements due to bias model.—To break these results down in detail, consider first Fig. 3.3 which represents the improvement due to modifying the bias model to be more flexible than the simple linear truncation. The models are superclasses of each other in the order *Advective* $\supseteq$ *M&Roy* $\supseteq$ *Coevo*, and therefore we have a strict ordering of improvements: *Advective* $\geqslant$ *M&Roy* $\geqslant$ *Coevo* for all redshift-space models. Because the advective model is most general, it automatically shows the largest improvement.

The breakdown by redshift-space model is more variable, but the structure is similar in each case. The *KaiserHalo* model barely benefits from addition of flexibility in the bias prescription, while the *SPT* model and *KaiserTree* models show very significant improvements that are nearly independent of the model actually chosen. We will comment on

Model	mean $\pm\,\sigma$	χ^2/dof	$\min\chi^2$	$\max\chi^2$
Linear+KaiserTree	$\mathbf{315.0 \pm 28.7}$	1.250	260.2	347.2
Linear+SPT	$\mathbf{312.9 \pm 25.3}$	1.242	256.6	338.0
Linear+KaiserHalo	$\mathbf{296.4 \pm 25.5}$	1.176	240.6	322.7
Linear+EFT	$\mathbf{296.9 \pm 25.2}$	1.178	245.1	322.1
Coevo+KaiserTree	$\mathbf{292.7 \pm 26.0}$	1.162	236.1	321.2
Coevo+SPT	$\mathbf{290.5 \pm 24.7}$	1.153	240.0	316.3
Coevo+KaiserHalo	$\mathbf{296.8 \pm 25.4}$	1.178	241.2	323.0
Coevo+EFT	$\mathbf{287.7 \pm 24.9}$	1.142	238.9	315.5
M&Roy+KaiserTree	$\mathbf{291.6 \pm 25.9}$	1.157	235.2	320.1
M&Roy+SPT	$\mathbf{286.6 \pm 23.5}$	1.137	237.3	309.4
M&Roy+KaiserHalo	$\mathbf{292.8 \pm 25.9}$	1.162	236.7	320.2
M&Roy+EFT	$\mathbf{282.6 \pm 24.0}$	1.121	233.5	310.7
Advective+KaiserTree	$\mathbf{290.1 \pm 25.6}$	1.151	235.3	319.3
Advective+SPT	$\mathbf{284.7 \pm 23.6}$	1.130	236.3	308.7
Advective+KaiserHalo	$\mathbf{288.6 \pm 25.4}$	1.145	234.4	317.2
Advective+EFT	$\mathbf{281.9 \pm 23.8}$	1.119	232.9	309.6

Table 3.5: Summary statistics for fit to subsample of ten realisations from the **WizCOLA** suite.

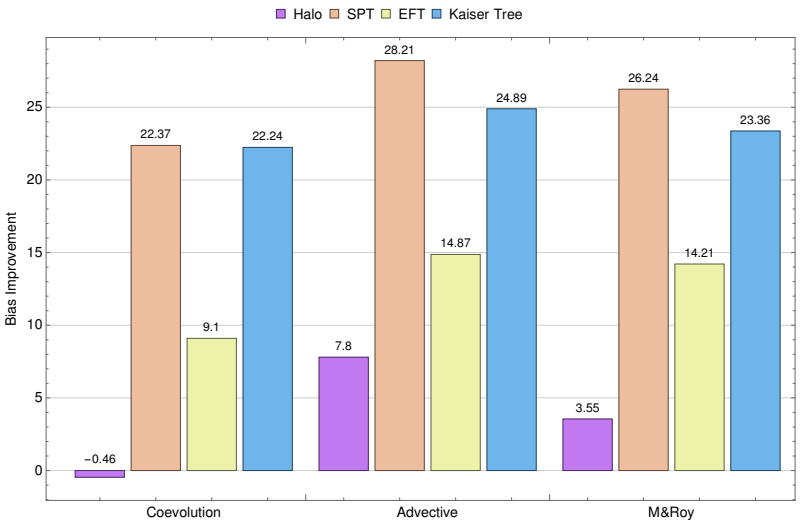

Figure 3.3: Improvement in χ^2 for each bias model, measured relative to the WiggleZ *Linear* baseline with a fixed redshift-space model. Negative values mean that the model performs more poorly than *Linear*.

these features in more detail below.

The performance of these more complex models is similar, and there is little to choose among them. Because the 2-parameter coevolution model already delivers much of the improvement on offer from the other prescriptions, we can guess that it will be favoured after accounting for the number of free parameters.

Improvements due to redshift-space model.—Second, consider Fig. 3.4. This time no one model is a strict superclass of any other, except that the *EFT* model can be regarded as a superclass of *SPT* if terms of order $\mathcal{O}(k^4)$ and higher in the phenomenological fingers-of-God damping term are not relevant. Neither the *EFT* or *SPT* model has a simple relationship to the *KaiserTree* model since there is no continuous parameter that can be varied to connect them.

The most striking features of Fig. 3.4 are the large negative shifts for the *Linear* bias model (yellow bars) in combination with the *SPT* or *KaiserTree* models. Taken together with Fig. 3.3 these show that the relatively rigid *KaiserTree* and *SPT* models do not have the right shape to match the spectral slope of a typical **WizCOLA** power spectrum at both small and large k, even after accounting for fingers-of-God suppression. (See Figs. 3.5 and 3.6 for an explicit demonstration of this in the *KaiserTree* and *SPT* cases, respectively.) This amounts to an adjustment of the slope by a term of the form $k^2P(k)$ at large k.[14]

[14]It is well-known that the tree-level power spectrum significantly underpredicts the nonlinear power spectrum measured from simulations for quasi-linear wavenumbers, and that this underprediction is par-

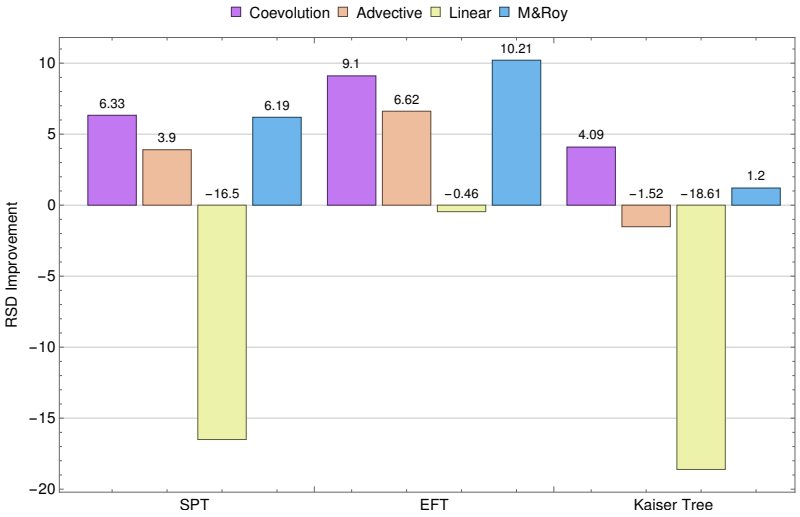

Figure 3.4: Improvement in χ^2 for each redshift-space model, measured relative to the WiggleZ baseline of *KaiserHalo* with a fixed bias model. Negative values mean that the model performs more poorly than *KaiserHalo*.

When used with the *Linear* bias model there is no option to change the shape of the underlying power spectrum; only its normalisation can be adjusted, which explains its poor performance with the *KaiserTree* and *SPT* models. The *KaiserHalo* model is based on the **HALOFIT** power spectrum which is calibrated to match simulations, and therefore does not exhibit a mismatch (at least on these scales). The *EFT* model inherits its shape from *SPT*, but the combination of its additive and multiplicative counterterms can account for some part of the mismatch. Finally, even if we retain the rigid *KaiserTree* or *SPT* models, any of the more complex bias prescriptions is apparently capable of producing the required change of shape.

Typical improvements.—Figs. 3.3 and 3.4 show that, in typical circumstances, the improvement from better bias modelling is comparable to, or perhaps marginally greater than the improvement from better redshift-space modelling. If one is dealing with the *Linear* bias model in conjunction with *KaiserTree* or *SPT* then the gain from moving to *any* other bias model is very significant, as described above—more than 20 units of χ^2. Otherwise, changing the bias model with *KaiserHalo* is worth perhaps ~ 5 units of χ^2 (excluding the *Coevo* model), and with the *EFT* model is worth in the range 10–15 units of χ^2.

Contrast this with the improvements from changing the redshift-space model, as in

tially corrected by the 1-loop term. This underprediction is not directly the source of the mismatch under discussion.

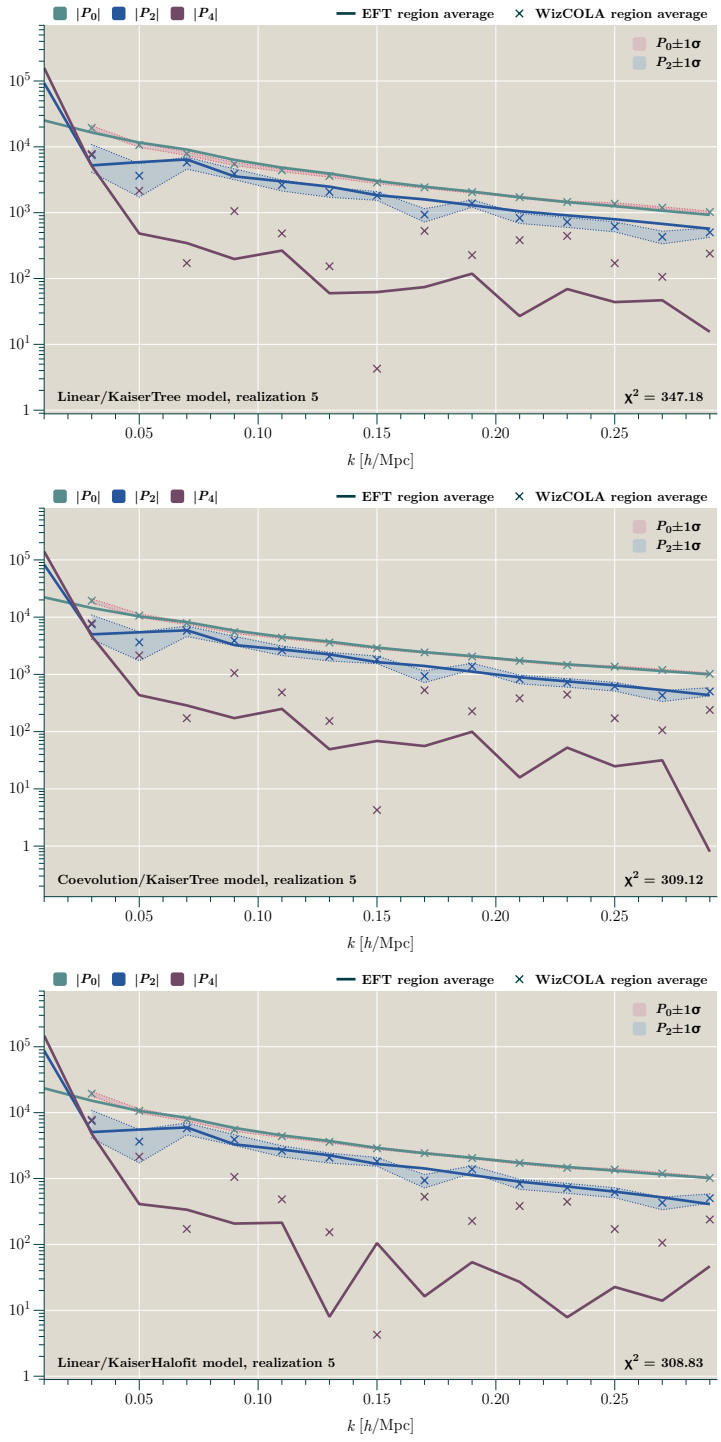

Figure 3.5: Specimen fits for **Realisation 5**. Top panel: *Linear+KaiserTree*. Note the poor fit in P_0 at low k, and for P_2 generally. Middle panel: *Coevo+KaiserTree*. The more general bias model allows a better fit the the low-k spectral slope. Bottom panel: *Linear+KaiserHalo*. Even with linear bias, the *KaiserHalo* model does a better job at low k.

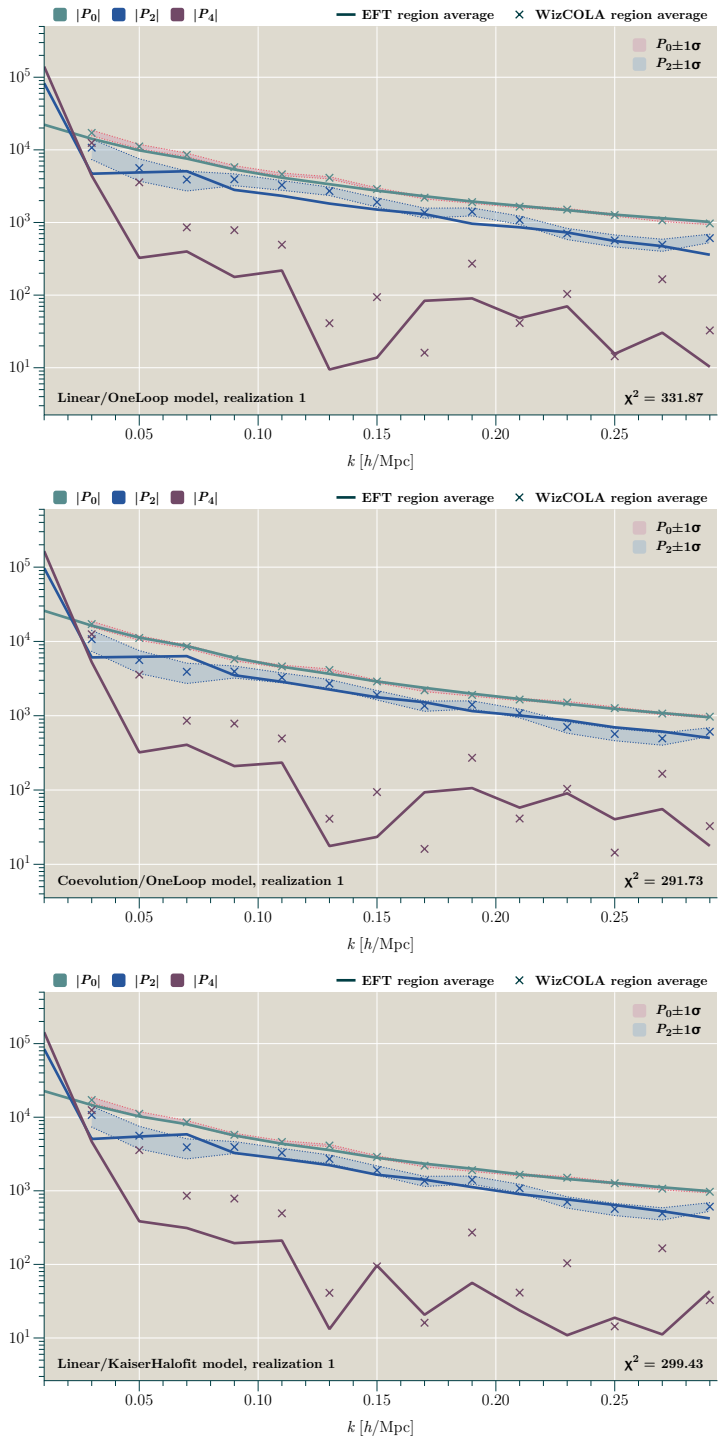

Figure 3.6: Specimen fits for **Realisation 1**. Top panel: *Linear+SPT*. This exhibits similar features to the fit in Fig. 3.5. Middle panel: *Coevo+SPT*. The more general bias model again solves the spectral slope. Bottom panel: *Linear+KaiserHalo*. The **HALOFIT** model is again able to fit the spectral slope at both ends.

Fig. 3.4. Excluding the negative values associated with switching to *KaiserTree* or *SPT* with the *Linear* bias model, these are mostly in the range 0–10 units of χ^2. All of these numbers are comparable to the absolute improvement in best-fit $\Delta\chi^2 = 14.5$ between the WiggleZ baseline and *Advective+EFT*.

The discrepancy between the mean χ^2 obtained from *Advective+EFT* and the target mean $\chi^2 \sim 252$ implies that the **WizCOLA** realisations contain further unmodelled effects. We believe these relate to the variability of the BAO feature in these realisations. In each of our redshift-space models, the phase and amplitude of the BAO feature is a rather rigid part of the template that cannot be adjusted independently—only by adjusting the whole background cosmology. The structure of the BAO feature *can* be adjusted by non-linear terms in a bias model, but these also change the spectral slope. (This is how the nonlinear bias models are able to fix the spectral slope problems of *KaiserTree* and *SPT*.) If the contribution from these non-linear terms is too significant, it will degrade the broadband fit well before it can be compensated by improvements to fitting the BAO feature. Accordingly, variation in the BAO feature due to bias modelling is very modest, giving very limited scope to fit realisation variance. In general, as we now describe, this rigidity is a positive feature that prevents some instances of overfitting.

Bayesian Information Criterion analysis

The analysis of §3.3.4 demonstrates how well each combination of bias and redshift-space model matches the ensemble of realisations at the level of raw χ^2. As expected, the outcome is that the most permissive model gives the best fit. But this does not demonstrate that the large number of parameters required by the model are all physically meaningful; some might match features that vary randomly from realisation to realisation, like the BAO feature. Otherwise might simply lack statistical value. The first case is 'overfitting', which we deal with below. The second is 'overparametrisation'. As explained in §3.3.3, we attempt to detect this using the Bayesian information criterion.

In this analysis, parameter degeneracies play a critical role. The BIC formula (3.72) depends strongly on the number of parameters carried by the model. If degenerate parameters are included in the analysis then they will unfairly downweight the BIC for the corresponding model.

After transformation from raw χ^2 to BIC, Figs. 3.3–3.4 translate to Figs. 3.7–3.8. Notice that many 'improvements' have become negative, implying that the BIC ranks the statistical power of these models lower than the WiggleZ baseline.

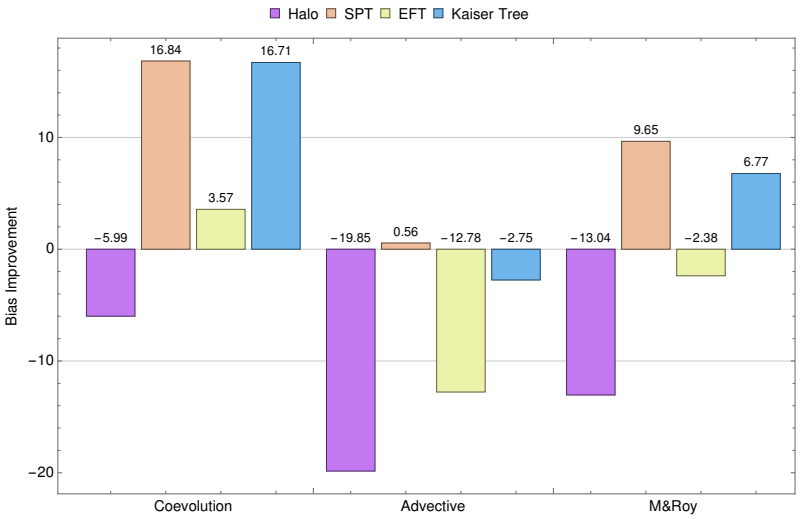

Figure 3.7: Improvement in BIC for each bias model, measured relative to the WiggleZ *Linear* baseline with a fixed redshift-space model.

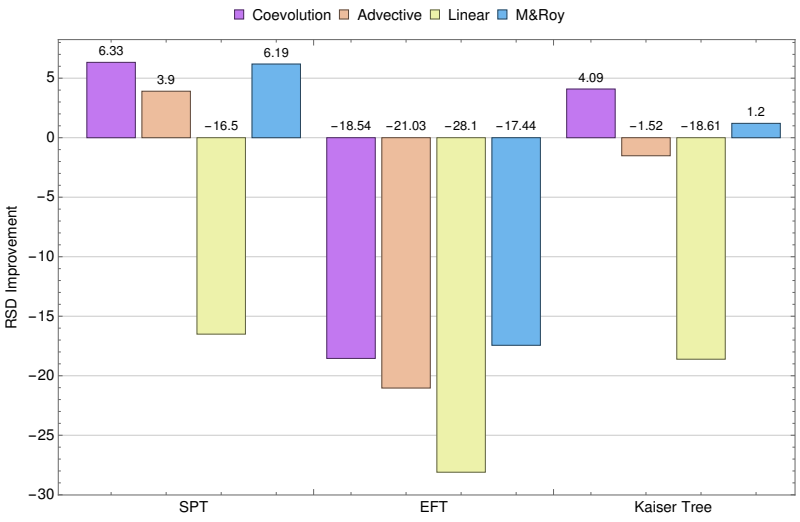

Figure 3.8: Improvement in BIC for each redshift-space model, measured relative to the WiggleZ *KaiserHalo* baseline with a fixed bias model.

Bias models.—Fig. 3.7 shows that there is no statistical value in changing to the *Advective* bias model, and only limited value in switching to the full McDonald & Roy model *M&Roy*. On the other hand there is generally clear value in switching from the *Linear* model to the *Coevo* model. We conclude that a WiggleZ-like survey with a generic redshift-space model would typically benefit from switching to a sufficiently-nonlinear bias model, but there is not yet evidence that the most complex models under consideration are required.

Redshift-space models.—The BIC analysis strongly disfavours the *EFT* model. Reference to Table 3.5 shows that, with a sufficiently permissive bias model, it produces typical χ^2 that are close to the *SPT* model. These models differ only in two respects: (i) in the *SPT* model, suppression of power at quasilinear k is modelled by a single fingers-of-God factor $\exp(-k^2\mu^2 f^2\sigma_{\rm v}^2)$, giving a common suppression for each P_ℓ, whereas in *EFT* there are independent counterterms for each P_ℓ; and (ii) the *EFT* model includes additive stochastic counterterms, but *SPT* does not. The additive counterterms are significant in allowing *EFT* to correct the spectral slopes inherited from *SPT*, but (as described above) this can equally by done by the bias model.

Meanwhile, the similar performance of *EFT* and *SPT* shows that there is no significant benefit from allowing different suppression scales for each of P_0, P_2 and P_4. Under these circumstances there is no significant benefit from using *EFT* in preference to *SPT*. This conclusion likely depends strongly on $k_{\rm max}$. In a survey with large $k_{\rm max}$ the need for different suppression scales associated with each P_ℓ may be more significant, in which case the value of the *EFT* model would need to be revisited.

Overfitting: Comparison to ensemble average

Finally we address the issue of overfitting. For each model combination we compute the best-fit chi-square for each realisation, together with the corresponding parameter choice. We also compute the best-fit to the ensemble average of the full **WizCOLA** suite of over 600 realisations. This enables us to assign a 'shift' to each realisation,

$$\Delta\chi^2 = \chi^2\,(\text{ensemble}) - \chi^2\,(\text{bestfit})\,. \tag{3.74}$$

The sign is chosen so that $\Delta\chi^2$ is typically positive.

We interpret a large shift as evidence that the model is adapting to features present in the power spectrum of a given realisation, but which are *not* present in the ensemble average. In Fig. 3.9 we show the distribution of shifts for each bias and redshift-space model (also refer to Figs. 3.10, 3.11 and 3.12). In the left panel, the *Linear* and *Coevo*

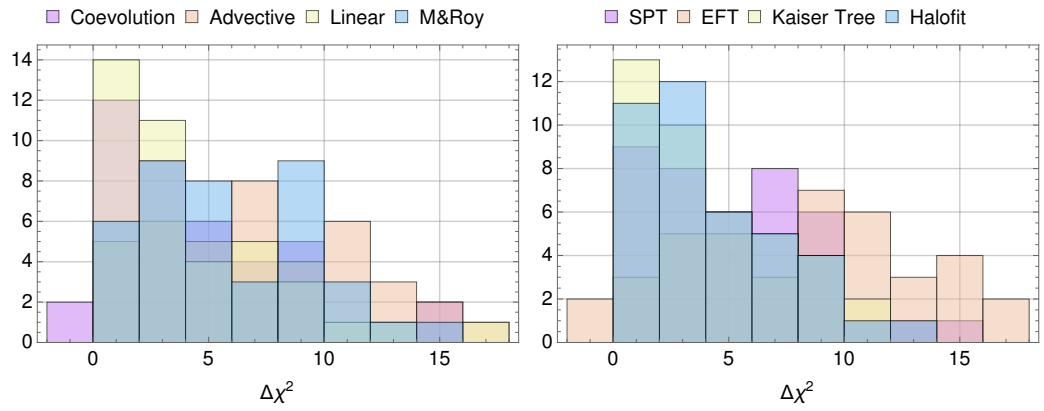

Figure 3.9: Left: Distribution of the shift $\Delta\chi^2$ for each bias model, averaged over redshift-space models. Right: Distribution of $\Delta\chi^2$ for each redshift-space model, averaged over bias models.

models show a sharp peak at low shifts, followed by a tail to large $\Delta\chi^2$. The *M&Roy* and *Advective* distributions are much broader and do not show a clear division into a peak-and-tail structure. In the right panel, the shift distribution of both *KaiserTree* and *KaiserHalo* shows a clearly-defined peak near $\Delta\chi^2 \approx 0$, whereas the *SPT* model shows a near-flat distribution out to $\Delta\chi^2 \approx 10$. The *EFT* model is very broad with a peak near $\Delta\chi^2 \sim 10$.

We interpret these results to mean that the *EFT* redshift-space model, and the *Advective* and *M&Roy* bias models, show modest evidence for overfitting. This analysis would benefit from a larger suite of realisations to obtain better-defined distributions, particularly for *SPT* whose behaviour is a little ambiguous. With the current sample, however, the *EFT* model shows a hint of bimodality. If so, this could be interpreted as a peak near a shift $\Delta\chi^2 \sim 3$ (generated by a cluster of realisations in which there is no significant overfitting), together with a second peak at near $\Delta\chi^2 \sim 7$ (perhaps generated by a cluster of realisations for which modest overfitting occurs). However, to validate these suggestions, we would require a larger sample.

Origin of overfitting.—To test whether overfitting is really occurring, we compare the ensemble-average best-fit with the individual best-fit for Realisation 2 with *Linear+EFT* and Realisation 1 with *Advective+EFT* The shifts are $\Delta\chi^2 = 17.6$ and $\Delta\chi^2 = 16.2$, respectively. See Figs. 3.13–3.14. In Fig. 3.13 the difference between fits appears to be driven by a response to the BAO feature. In comparison with the ensemble average, Realisation 2 has a lower amplitude BAO feature near $k = 0.1h$/Mpc and $k = 0.2h$/Mpc

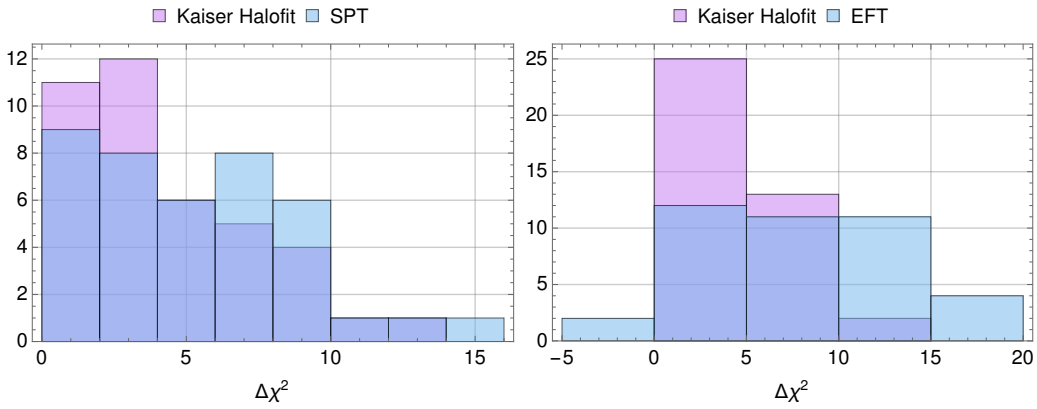

Figure 3.10: Distribution of the shift in the likelihood between the ensemble average and the best fit model. The analysis is performed over all bias models with SPT and Kaiser **HALOFIT** redshift models (left) and EFT and Kaiser **HALOFIT** redshift models (right).

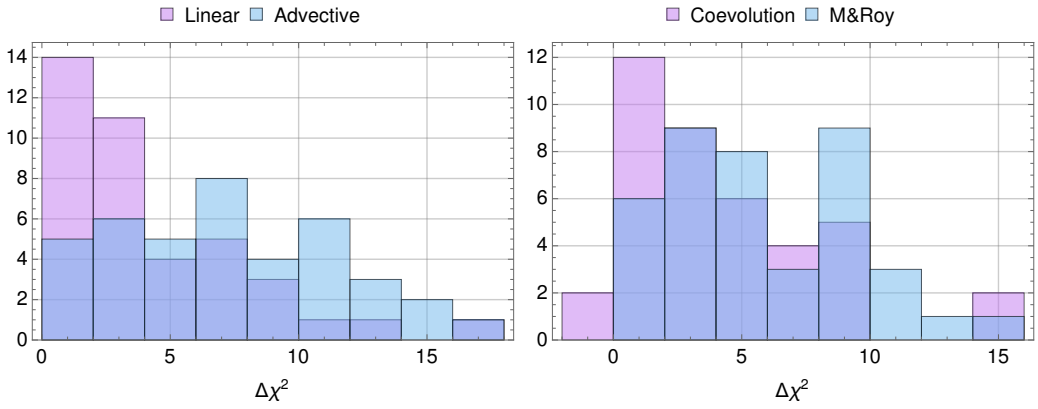

Figure 3.11: Distribution of the shift in the likelihood between the ensemble average and the best fit model. The analysis is performed over all RSD models with Linear and Advective **HALOFIT** redshift models (left) and with co-evolution and M&Roy bias modelss (right).

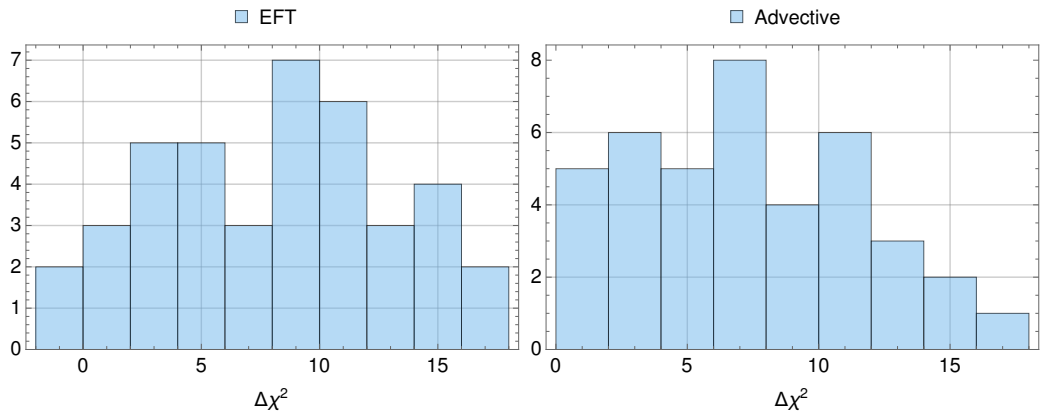

Figure 3.12: Distribution of the shift in the likelihood between the ensemble average and the best fit model. The analysis is performed over all bias combined with an EFT redshift model (left) and over RSD models combined with the advective bias model (right).

in P_0 and near $k = 0.07h/\text{Mpc}$ and $k = 0.2h/\text{Mpc}$ in P_2. Therefore, in this case, we have some evidence for the model adjusting itself to realisation variance in the BAO feature.

In Fig. 3.14 there is a relatively large excursion in the P_0 data to which the individual best-fit responds but the ensemble best-fit does not. Also, there is a generally weaker broadband fit to P_2 in the ensemble average best-fit. This should still count as overfitting, but it is not so clearly a response to the BAO variability.

3.4 Conclusions

In this chapter we have addressed the question: what is an appropriate level of modelling sophistication to extract cosmological information from present-day or next-generation galaxy surveys? A wide array of different models are available to account for biasing or to predict the redshift-space power spectrum, with varying motivations—some empirical, and some motivated by theoretical considerations such as consistency of loop order in the description of clustering, bias, and redshift-space effects.

Our testing uses the **WizCOLA** simulation suite, originally developed to supply realistic covariance matrices for the WiggleZ survey including details of the survey geometry, incompleteness, selection function, and mask. The power spectra and error bars derived from the suite therefore incorporate a wide range of experimental effects that are relevant for state-of-the-art redshift surveys. Therefore our results already account for these effects, rather than providing a (possibly misleading) picture of the performance of each model

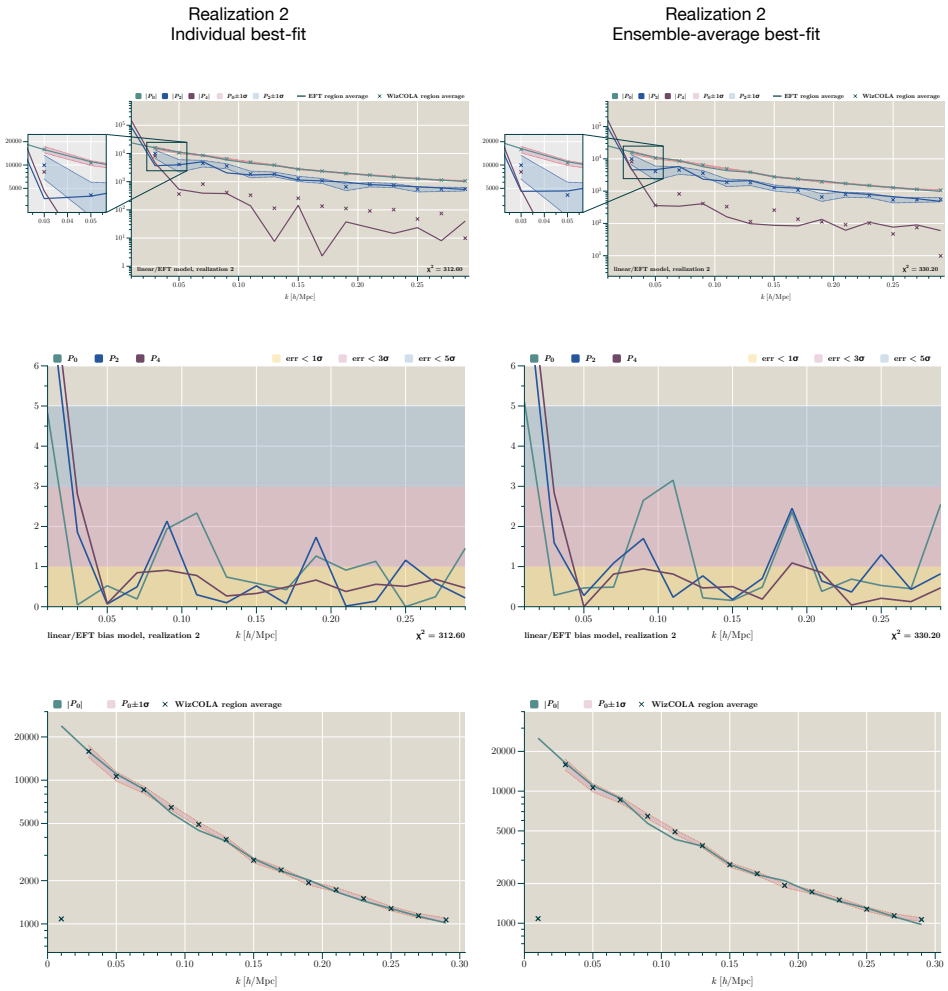

Figure 3.13: EFT+Linear, realisation 02 with $\Delta\chi^2 = 17.6$

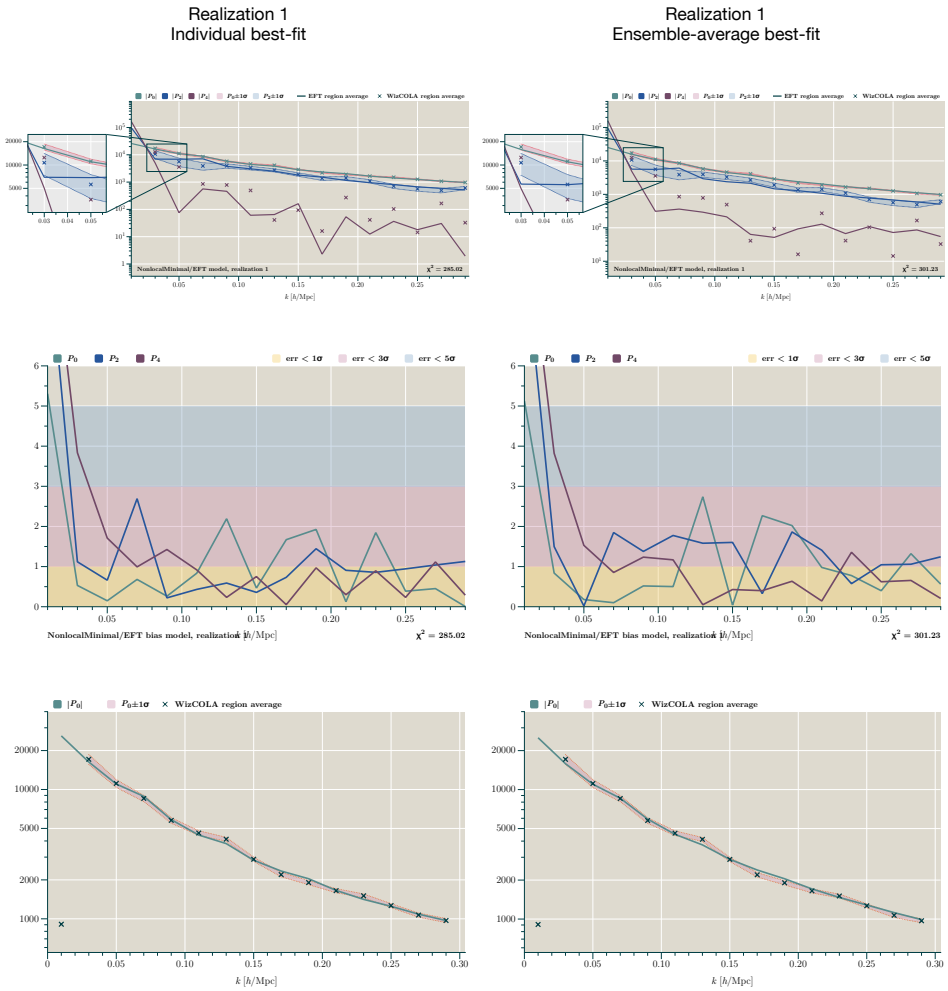

Figure 3.14: EFT+Advective, realisation 01 with $\Delta\chi^2 = 16.2$

under ideal circumstances.

Redshift-space power spectrum.—On the power spectrum side, the most complex model we consider is the effective-field theory of large-scale structure. Its construction is recounted in §3.2. In redshift space the basic power spectrum template matches the one-loop *SPT* model, modified by six subtractions known as 'counterterms'. Our testing shows that it can successfully match both the broadband spectral slope produced by the **WizCOLA** realizations at both large and small k. This cannot be done by the closely-related *SPT* model, which often exhibits a mismatch at small k. (The Monte Carlo fit prioritizes high k, where the error bars are lower. Although the small-k region is likely to be most accurate in perturbation theory this is not accounted for in the fitting, which explains why the region we would naïvely expect to be most accurate is in 'tension' with the data.) We ascribe this to a combination of the additive and multiplicative counterterms that appear in the *EFT* model.

The leading feature of the *EFT* model is its ability to accommodate separate suppression scales for each of the lowest-order multipoles P_0, P_2 and P_4. However, our testing shows that the **WizCOLA** realizations do not make use of this freedom, at least up to $k_{\rm max} = 0.29h/{\rm Mpc}$. This is clearly a strongly $k_{\rm max}$-dependent statement. Since future surveys such as Euclid, DESI and LSST will probe higher $k_{\rm max}$ it would be very interesting to study the $k_{\rm max}$-dependence of the suppression scales. If independent suppression is required then the *EFT* model could become attractive. With $k_{\rm max} = 0.29h/{\rm Mpc}$, however, it does not provide enough statistical return for its extra parameters and is strongly disfavoured by the Bayesian information criterion.

The *SPT* model provides an underlying template that is very similar to the *EFT* model. Its subtler treatment of redshift-space effects compared to tree-level enables it to improve its overall match to the structure of the P_ℓ, and the data do not penalize it for its single suppression scale compared to the multiple suppression scales allowed by *EFT*. When paired with any sufficiently-permissive bias model, to correct problems with the spectral slope, it can nearly reproduce the χ^2 values yielded by the much more permissive *EFT* model. It is favoured by the BIC. We conclude that a model of this type, including **nonlinear redshift-space structure** but only a **common suppression scale for P_0, P_2 and P_4** seems likely to represent a good compromise for present-day or near-future surveys with $k_{\rm max}$ not too dissimilar to $0.3h/{\rm Mpc}$. The 'TNS' model of Tarya, Nishimichi & Saito is of this type [178], and we expect it would perform very similarly to *SPT*.

Bias models.—Our results do not show a preference for complex bias modelling. Increas-

ingly permissive models do give an improvement, but the effect is not large. The critical feature is apparently the inclusion of *some* nonlinearity, which enables small changes to the slope of the power spectrum at large k. Beyond this we do not see significant effects. Accordingly, the BIC prioritizes the simplest nonlinear model we include—the co-evolution model of Saito et al. [154]. As explained in §3.3 this is based on the 1-loop McDonald & Roy model with some nonlinear parameters constrained by matching to analytic arguments and N-body simulations.

One might have imagined that the bias model could provide a means to shift the amplitude and phase of the BAO feature. It was explained in §3.3.4 that this feature is quite variable in the **WizCOLA** realizations. This is simply a statistical effect: too few modes are measured to resolve it clearly. In practice, however, it does not seem possible for nonlinear terms in the bias to change the structure of the BAO feature significantly. This is because such changes would simultaneously change the broadband slope of the power spectrum, at least in some regions, and would therefore significantly degrade the fit. This degradation could not be compensated by the relatively small rewards on offer for providing a better fit to the acoustic oscillation itself.

Discussion.—A striking conclusion from our results is that improvements in modelling are not likely to lead to a significant decrease in the overall χ^2 fit to a simulation suite—in our case we see only a $\Delta\chi^2 \approx 14.5$ decrease even from our best-performing model combination. Since all our models fit the BAO variability equally badly—which, as we have argued, is a good thing to the degree that it prevents overfitting—this conclusion seems unlikely to be altered even in a larger survey where the BAO feature is better resolved. In short, the tree-level Kaiser formula and the **HALOFIT** power spectrum do a surprisingly good job. What could make a difference at larger $k_{\rm max}$ is the appearance of different suppression scales for the low-order Legendre multipoles. At present, however, there are no hints that this is required for the **WizCOLA** realizations.

We see some evidence for overfitting from the most permissive models, the *EFT* model for the power spectrum and the *Advective* model for the bias, although we require a larger sample size to resolve the shape of the distribution with more certainty. We do not see evidence for overfitting from the *Linear*, *Coevo*, *KaiserTree* or *KaiserHalo* models. The *M&Roy* and *SPT* models have poorly-resolved distributions and are slightly ambigious. This risk of overfitting means that one should carefully characterize whether the *EFT* and *Advective* models can really recover unbiased estimates for the underlying cosmological parameters used in a parameter-estimation Monte Carlo. This is an extremely interesting

question to which we hope to return in the future.

Cosmology dependence of the counterterms.—Within the effective field theory framework, we find that not only the counterterms responsible for the parametrization of non-linear phenomena are redshift dependent but also cosmology dependent. Even for nearby cosmologies the variation becomes significant. For example, we find the value of the leading-order counterterm for the matter power spectrum in real space for a Planck 2015 cosmology [4] to be $1.94h^{-2}\mathrm{Mpc}^2$, whereas for the MultiDark MDR1 cosmology [109] the value is $2.32h^{-2}\mathrm{Mpc}^2$. This leads to a considerable 18 % difference between two nearby cosmologies. Therefore, looking into the cosmology dependence of the counterterms becomes of the utmost importance before extending our analysis to higher order in the loop expansion.

Work has been done along these lines, mainly by Cataneo et al. [36] who developed an efficient algorithm to evaluate large-scale observables within the effective field theory framework. Their work is based in two main ideas. First of all, they claim that once any observable is computed with high precision for a reference cosmology, the computation of such observable for a new cosmology with comparable precision is easily performed by adding the difference in that quantity evaluated with much less precision. By doing so, the exploration of the cosmology dependence turns out much less expensive than by performing direct computation. Second and last, since most cosmologies of interest are sufficiently close to the Planck best-fit cosmology, large-scale observables can be obtained from a Taylor expansion around the reference cosmology. All considered, studying the variation of the effective field theory counterterms with the cosmological parameters *à la Cataneo* seems promising and compelling, and will definitely constitute the object of future research.

Acknowledgments The work reported in this paper has been supported by the European Research Council under the European Union's Seventh Framework Programme (FP/2007–2013) and ERC Grant Agreement No. 308082 (DR, DS). LFdlB acknowledges support from the UK Science and Technology Facilities Council via Research Training Grant ST/M503836/1.

Appendices

3.A Bias expansions: Dictionary between McDonald & Roy and Chan et al.

The relation between Assassi et al. bias [7, 37] and Perko et al. bias model [148, 126, 6] is presented in Table 3.6.

	PERKO	**ASSASSI**
Operators	δ , θ, $\eta = \theta - \delta$	$\delta = \partial^2\Phi_g$, $\theta = \partial^2\Phi_v$
	$\Psi = \eta - \eta^{(2)}$	$\mathcal{G}_2(\delta)$
	$s_{ij} = (\partial_i\partial_j\partial^{-2} - \frac{1}{3}\delta_{ij})\delta$	$\Gamma_3(\delta,\theta)$
	$t_{ij} = (\partial_i\partial_j\partial^{-2} - \frac{1}{3}\delta_{ij})\eta$,	$\mathcal{G}_3(\delta)$
$\mathcal{O}_I$	$\delta^{(1)}$	$\delta^{(1)}$
$\mathcal{O}_{II}$	$\delta^{(2)}$, $\delta^{(1)\,2}$, $s^2 = s_{ij}s^{ij}$	$\delta^{(2)}$, $\delta^{(1)\,2}$, $\mathcal{G}_2(\delta)$
$\mathcal{O}_{III}$	$\delta^{(3)}$, $\delta^{(1)}\delta^{(2)}$, $\delta^{(1)\,3}$,	$\delta^{(3)}$, $\delta^{(1)}\delta^{(2)}$, $\delta^{(1)\,3}$,
	$\delta^{(1)}s^2$, $s_{ij}t^{ij}$, Ψ,	$\delta^{(1)}\mathcal{G}_2(\delta)$, $\mathcal{G}_2(\delta)^{(3)}$,
	$s^3 = s_{ij}s^{ik}s^j_k$, $s^{(1)}_{ij}s^{ij\,(2)}$	$\mathcal{G}_3(\delta)$, $\Gamma_3(\delta,\theta)$

Table 3.6: List of independent operators up to order three used by Perko et al. and Assassi et al., respectively, as building blocks of local Eulerian biasing.

Bearing in mind that $\Phi_v^{(1)} = \Phi_g^{(1)}$, the translation from Perko's into Assassi's notation reads

- Order II.

$$s^2 = \frac{2}{3}\delta^{(1)\,2} + \mathcal{G}_2(\delta) \tag{3.75a}$$

- Order III.

$$\delta^{(1)} s^2 = \frac{2}{3}\delta^{(1)\,3} + \delta^{(1)}\mathcal{G}_2(\delta) \tag{3.76a}$$

$$\Psi = \frac{8}{21}\delta^{(1)\,3} - \frac{4}{7}\delta^{(1)} s^2 - \frac{2}{7}\mathcal{G}_2(\delta) \tag{3.76b}$$

$$s_{ij} t^{ij} = \frac{1}{2}\Gamma_3(\delta,\theta) + \frac{1}{3}\delta^2 - \frac{1}{3}\theta^2 \tag{3.76c}$$

$$s^3 = \frac{5}{9}\delta^{(1)\,3} - 2\delta^{(1)}\delta^{(2)} - 2\delta^{(1)}\mathcal{G}_2(\delta) - \mathcal{G}_3(\delta) \tag{3.76d}$$

$$2 s^{(1)}_{ij} s^{ij\,(2)} = \frac{4}{3}\delta^{(1)}\delta^{(2)} + \mathcal{G}_2^{(3)}(\delta) \tag{3.76e}$$

Additionally, Assassi et al. establish the relation $\delta^{(2)} - \theta^{(2)} = -\frac{2}{7}\mathcal{G}_2^{(2)}$.

3.B Redshift-space halo power spectrum: Full calculation

3.B.1 Notation and operators in Fourier space

Throughout this section we employ the following short-hand notation

$$\int^{\mathbf{k}}_{\mathbf{q},\mathbf{r}} \equiv \int \frac{\mathrm{d}^3 q}{(2\pi)^3}\frac{\mathrm{d}^3 r}{(2\pi)^3}(2\pi)^3\delta_D(\mathbf{k}-\mathbf{q}-\mathbf{r}), \tag{3.77a}$$

$$\int^{\mathbf{k}}_{\mathbf{q},\mathbf{s},\mathbf{r}} \equiv \int \frac{\mathrm{d}^3 q\,\mathrm{d}^3 s \mathrm{d}^3 r}{(2\pi)^9}\,(2\pi)^3\delta(\mathbf{k}-\mathbf{q}-\mathbf{s}-\mathbf{r}), \tag{3.77b}$$

as well as $\mu = \hat{\mathbf{k}}\cdot\hat{\mathbf{x}}$ (similarly $\mu_q = \hat{\mathbf{q}}\cdot\hat{\mathbf{x}}$).

We now write down the different operators in Fourier space

$$\delta^{(1)}_{\mathbf{k}} = D(z)\delta^*_{\mathbf{k}}, \tag{3.78a}$$

$$\delta^{(2)}_{\mathbf{k}} = \int^{\mathbf{k}}_{\mathbf{q},\mathbf{r}} F_{AB}(\mathbf{q},\mathbf{r};z)\delta^*_{\mathbf{q}}\delta^*_{\mathbf{r}}, \tag{3.78b}$$

$$[\delta^{(1)\,2}]_{\mathbf{k}} = \int^{\mathbf{k}}_{\mathbf{q},\mathbf{r}} D(z)^2\delta^*_{\mathbf{q}}\delta^*_{\mathbf{r}}, \tag{3.78c}$$

$$[\mathcal{G}^{(2)}_2(\delta)]_{\mathbf{k}} = \int^{\mathbf{k}}_{\mathbf{q},\mathbf{r}} G_2(\mathbf{q},\mathbf{r})D(z)^2\delta^*_{\mathbf{q}}\delta^*_{\mathbf{r}}, \tag{3.78d}$$

$$\delta^{(3)}_{\mathbf{k}} = \int^{\mathbf{k}}_{\mathbf{q},\mathbf{s},\mathbf{r}} T(\mathbf{q},\mathbf{r},\mathbf{r},\mathbf{s}+\mathbf{r};z)\delta^*_{\mathbf{q}}\delta^*_{\mathbf{s}}\delta^*_{\mathbf{r}}, \tag{3.78e}$$

$$[\delta^{(1)}\delta^{(2)}]_{\mathbf{k}} = \int^{\mathbf{k}}_{\mathbf{q},\mathbf{r}}\int^{\mathbf{r}}_{\mathbf{p},\mathbf{s}} F_{AB}(\mathbf{p},\mathbf{s};z)\delta^*_{\mathbf{q}}\delta^*_{\mathbf{p}}\delta^*_{\mathbf{s}}, \tag{3.78f}$$

$$[\delta^{(1)\,3}]_{\mathbf{k}} = \int^{\mathbf{k}}_{\mathbf{q},\mathbf{s},\mathbf{r}} D(z)^3\delta^*_{\mathbf{q}}\delta^*_{\mathbf{s}}\delta^*_{\mathbf{r}}, \tag{3.78g}$$

$$[\delta^{(1)}\mathcal{G}_2(\delta)]_{\mathbf{k}} = \int^{\mathbf{k}}_{\mathbf{q},\mathbf{s},\mathbf{r}} G_2(\mathbf{q},\mathbf{s})D(z)^3\delta^*_{\mathbf{q}}\delta^*_{\mathbf{s}}\delta^*_{\mathbf{r}}, \tag{3.78h}$$

$$[\mathcal{G}^{(3)}_2(\delta)]_{\mathbf{k}} = \int^{\mathbf{k}}_{\mathbf{q},\mathbf{s},\mathbf{r}} G_2(\mathbf{q},\mathbf{s}+\mathbf{r})F_{AB}(\mathbf{s},\mathbf{r};z)\delta^*_{\mathbf{q}}\delta^*_{\mathbf{s}}\delta^*_{\mathbf{r}}, \tag{3.78i}$$

$$[\mathcal{G}_3(\delta)]_{\mathbf{k}} = \int^{\mathbf{k}}_{\mathbf{q},\mathbf{s},\mathbf{r}} G_3(\mathbf{q},\mathbf{s},\mathbf{r})D(z)^3\delta^*_{\mathbf{q}}\delta^*_{\mathbf{s}}\delta^*_{\mathbf{r}}, \tag{3.78j}$$

$$[\Gamma_3(\delta,\theta)]_{\mathbf{k}} = \int^{\mathbf{k}}_{\mathbf{q},\mathbf{r}} G_2(\mathbf{q},\mathbf{r})D(z)\int^{\mathbf{r}}_{\mathbf{p},\mathbf{s}}\left(F_{AB}(\mathbf{p},\mathbf{s};z) - \frac{1}{f}F_{KL}(\mathbf{p},\mathbf{s};z)\right)\delta^*_{\mathbf{q}}\delta^*_{\mathbf{p}}\delta^*_{\mathbf{s}}, \tag{3.78k}$$

where $D(z)$ is the linear growth function related to the growth factor f. Likewise, we define

$$F_{AB}(\mathbf{q},\mathbf{r};z) \equiv D_A(z)\bar{\alpha}(\mathbf{q},\mathbf{r}) + D_B(z)\bar{\gamma}(\mathbf{q},\mathbf{r}), \tag{3.79a}$$

$$F_{KL}(\mathbf{q},\mathbf{r};z) \equiv D_K(z)\bar{\alpha}(\mathbf{q},\mathbf{r}) + D_L(z)\bar{\gamma}(\mathbf{q},\mathbf{r}), \tag{3.79b}$$

$$G_2(\mathbf{q},\mathbf{r}) \equiv -1 + \frac{(\mathbf{q}\cdot\mathbf{r})^2}{q^2r^2}, \tag{3.79c}$$

$$G_3(\mathbf{q},\mathbf{r},\mathbf{s}) \equiv -\frac{1}{2} + \frac{3}{2}\frac{(\mathbf{q}\cdot\mathbf{r})^2}{q^2r^2} - \frac{(\mathbf{q}\cdot\mathbf{r})(\mathbf{q}\cdot\mathbf{s})(\mathbf{r}\cdot\mathbf{s})}{q^2r^2s^2}. \tag{3.79d}$$

As well as

$$\begin{aligned} T(\mathbf{q},\mathbf{r},\mathbf{r},\mathbf{s}+\mathbf{r};z) \equiv\, & 2(D_D(z) - \text{Đ}(z))\bar{\gamma}(\mathbf{s}+\mathbf{r},\mathbf{q})\bar{\alpha}(\mathbf{s},\mathbf{r}) + 2D_E(z)\bar{\gamma}(\mathbf{s}+\mathbf{r},\mathbf{q})\bar{\gamma}(\mathbf{s},\mathbf{r}) \\ & + 2(D_F(z) + \text{Đ}(z))\bar{\alpha}(\mathbf{s}+\mathbf{r},\mathbf{q})\bar{\alpha}(\mathbf{s},\mathbf{r}) + 2D_G(z)\bar{\alpha}(\mathbf{s}+\mathbf{r},\mathbf{q})\bar{\gamma}(\mathbf{s},\mathbf{r}) \\ & + \text{Đ}(z)\alpha(\mathbf{s}+\mathbf{r},\mathbf{q})\bar{\gamma}(\mathbf{s},\mathbf{r}) - 2\text{Đ}(z)\alpha(\mathbf{s}+\mathbf{r},\mathbf{q})\bar{\alpha}(\mathbf{s},\mathbf{r}), \end{aligned} \tag{3.80a}$$

$$\begin{aligned} \tilde{T}(\mathbf{q},\mathbf{s},\mathbf{r},\mathbf{s}+\mathbf{r};z) = & -(1+z)T'(\mathbf{q},\mathbf{s},\mathbf{r},\mathbf{s}+\mathbf{r};z) \\ & - \alpha(\mathbf{q},\mathbf{s}+\mathbf{r})F_{AB}(\mathbf{s},\mathbf{r};z)f - \alpha(\mathbf{s}+\mathbf{r},\mathbf{q})F_{KL}(\mathbf{s},\mathbf{r};z), \end{aligned} \tag{3.80b}$$

where D_ℓ, for $\ell = \{A, B, D, E, F, G, J, K, L\}$, are growth functions associated with their correspondent growth factors, $f_\ell = H^{-1}\partial \ln D_\ell/\partial t$ — whose derivation can be found in

[49], as well as the kernels $\bar{\alpha}(\mathbf{q},\mathbf{s})$ and $\bar{\gamma}(\mathbf{q},\mathbf{s})$ — and $' \equiv D^{-1}\partial/\partial z$. The kernel $\tilde{T}$ will be used later on.

3.B.2 Halo density contrast in redshift space

The linear, quadratic and cubic contributions to the redshift-space halo density contrast read

$$\delta_s^{h\,(1)} = (b_1^{(1)} + f\mu^2)\delta_{\mathbf{k}}^{(1)}, \tag{3.81a}$$

$$\begin{aligned}\delta_s^{h\,(2)} =& b_1^{(2)}\delta_{\mathbf{k}}^{(2)} + \frac{b_2^{(2)}}{2!}[\delta^{(1)\,2}]_{\mathbf{k}} + b_{\mathcal{G}_2}^{(2)}[\mathcal{G}_2^{(2)}]_{\mathbf{k}} \\ &+ \mu^2\int_{\mathbf{q},\mathbf{s}}^{\mathbf{k}} F_{KL}(\mathbf{q},\mathbf{s};z)\delta_{\mathbf{q}}^*\delta_{\mathbf{s}}^* \,+\, \mu^2k^2\frac{(Df)^2}{2}\int_{\mathbf{q},\mathbf{s}}^{\mathbf{k}}\frac{\mu_q\mu_s}{qs}\delta_{\mathbf{q}}^*\delta_{\mathbf{s}}^* \,+\, b_1^{(1)}\,\mu kD^2 f\int_{\mathbf{q},\mathbf{s}}^{\mathbf{k}}\frac{\mu_q}{q}\delta_{\mathbf{q}}^*\delta_{\mathbf{s}}^*,\end{aligned} \tag{3.81b}$$

$$\begin{aligned}\delta_s^{h\,(3)} =& b_1^{(3)}\delta_{\mathbf{k}}^{(3)} + 2\,\frac{b_2^{(3)}}{2!}[\delta^{(1)}\delta^{(2)}]_{\mathbf{k}} + b_{\mathcal{G}_2}^{(3)}[\mathcal{G}_2^{(3)}]_{\mathbf{k}} + \frac{b_3}{3!}[\delta^{(1)\,3}]_{\mathbf{k}} + b_{1\mathcal{G}_2}[\delta\mathcal{G}_2]_{\mathbf{k}} + b_{\mathcal{G}_3}[\mathcal{G}_3]_{\mathbf{k}} + b_{\Gamma_3}[\Gamma_3]_{\mathbf{k}} \\ &+ \mu^2\int_{\mathbf{q},\mathbf{s},\mathbf{r}}^{\mathbf{k}}\tilde{T}(\mathbf{q},\mathbf{s},\mathbf{r},\mathbf{s}+\mathbf{r};z)\delta_{\mathbf{q}}^*\delta_{\mathbf{s}}^*\delta_{\mathbf{r}}^* \,+\, b_1^{(1)}\,\mu kD\int_{\mathbf{q},\mathbf{s}}^{\mathbf{k}}\frac{\mu_q}{q}\int_{\mathbf{q}',\mathbf{s}'}^{\mathbf{q}}F_{KL}(\mathbf{q}',\mathbf{s}';z)\delta_{\mathbf{q}'}^*\delta_{\mathbf{s}'}^*\delta_{\mathbf{s}}^* \\ &+ b_1^{(2)}\,\mu kfD\int_{\mathbf{q},\mathbf{s}}^{\mathbf{k}}\frac{\mu_q}{q}\int_{\mathbf{q}',\mathbf{s}'}^{\mathbf{s}}F_{AB}(\mathbf{q}',\mathbf{s}';z)\delta_{\mathbf{q}}^*\delta_{\mathbf{q}'}^*\delta_{\mathbf{s}'}^* \,+\, \frac{b_2^{(2)}}{2!}\,2\mu kfD^3\int_{\mathbf{q},\mathbf{s},\mathbf{r}}^{\mathbf{k}}\frac{\mu_q}{q}\delta_{\mathbf{q}}^*\delta_{\mathbf{s}}^*\delta_{\mathbf{r}}^* \\ &+ b_{\mathcal{G}_2}^{(2)}\,\mu kfD\int_{\mathbf{q},\mathbf{s},\mathbf{r}}^{\mathbf{k}}\frac{\mu_q}{q}G_2(\mathbf{s},\mathbf{r})\delta_{\mathbf{q}}^*\delta_{\mathbf{s}}^*\delta_{\mathbf{r}}^* \,+\, \mu^2k^2fD\int_{\mathbf{q},\mathbf{s}}^{\mathbf{k}}\int_{\mathbf{q}',\mathbf{s}'}^{\mathbf{s}}F_{KL}(\mathbf{q}',\mathbf{s}';z)\delta_{\mathbf{q}}^*\delta_{\mathbf{q}'}^*\delta_{\mathbf{s}'}^* \\ &+ b_1^{(1)}\,\frac{1}{2}\mu^2k^2f^2D^3\int_{\mathbf{q},\mathbf{s},\mathbf{r}}^{\mathbf{k}}\frac{\mu_q\mu_s}{qs}\delta_{\mathbf{q}}^*\delta_{\mathbf{s}}^*\delta_{\mathbf{r}}^* \,+\, \frac{1}{3}\mu^3k^3f^3D^3\int_{\mathbf{q},\mathbf{s},\mathbf{r}}^{\mathbf{k}}\frac{\mu_q\mu_s\mu_r}{qsr}\delta_{\mathbf{q}}^*\delta_{\mathbf{s}}^*\delta_{\mathbf{r}}^*.\end{aligned} \tag{3.81c}$$

3.B.3 Two-point statistics

First of all, we need to compute the following two-point functions

$$(2\pi)^3\delta_D(\mathbf{k}+\mathbf{k}')P_{s,11}^{hh}(k) = \langle\delta_{s,\,\mathbf{k}}^{h\,(1)}\delta_{s,\,\mathbf{k}'}^{h\,(1)}\rangle, \tag{3.82a}$$

$$(2\pi)^3\delta_D(\mathbf{k}+\mathbf{k}')P_{s,13}^{hh}(k) = 2\langle\delta_{s,\,\mathbf{k}}^{h\,(1)}\delta_{s,\,\mathbf{k}'}^{h\,(3)}\rangle, \tag{3.82b}$$

$$(2\pi)^3\delta_D(\mathbf{k}+\mathbf{k}')P_{s,22}^{hh}(k) = \langle\delta_{s,\,\mathbf{k}}^{h\,(2)}\delta_{s,\,\mathbf{k}'}^{h\,(2)}\rangle. \tag{3.82c}$$

The real-space contributions yield

$$P_{11}^{hh}(k,z) = b_1^{(1)\,2} D(z)^2 P_*(k), \tag{3.83a}$$

$$\begin{aligned} P_{13}^{hh}(k,z) =& \, 4\, b_1^{(1)} b_1^{(3)} D(z) P_*(k) \int \frac{\mathrm{d}^3 q}{(2\pi)^3} T(\mathbf{q},\mathbf{k},-\mathbf{q},\mathbf{k}-\mathbf{q};z) P_*(q) \\ &+ 8\, b_1^{(1)} \frac{b_2^{(3)}}{2!} D(z)^2 P_*(k) \int \frac{\mathrm{d}^3 q}{(2\pi)^3} P_*(q) F_{AB}(\mathbf{k},-\mathbf{q};z) \\ &+ 6\, b_1^{(1)} \frac{b_3}{3!} D(z)^4 P_*(k) \int \frac{\mathrm{d}^3 q}{(2\pi)^3} P_*(q) \\ &+ 4\, b_1^{(1)} b_{1\mathcal{G}_2} D(z)^4 P_*(k) \int \frac{\mathrm{d}^3 q}{(2\pi)^3} P_*(q) G_2(\mathbf{k},-\mathbf{q}) \\ &+ 8\, b_1^{(1)} b_{\mathcal{G}_2}^{(3)} D(z)^2 P_*(k) \int \frac{\mathrm{d}^3 q}{(2\pi)^3} P_*(q) G_2(\mathbf{k},\mathbf{k}-\mathbf{q}) F_{AB}(-\mathbf{q},\mathbf{k};z) \\ &+ 8\, b_1^{(1)} b_{\Gamma_3} D(z)^2 P_*(k) \int \frac{\mathrm{d}^3 q}{(2\pi)^3} P_*(q) G_2(\mathbf{k},\mathbf{k}-\mathbf{q}) \Big(F_{AB}(\mathbf{k},-\mathbf{q};z) - \frac{1}{f} F_{KL}(\mathbf{k},-\mathbf{q};z) \Big), \end{aligned} \tag{3.83b}$$

$$\begin{aligned} P_{22}^{hh}(k,z) =& \, 2\, b_1^{(2)\,2} \int \frac{\mathrm{d}^3 q}{(2\pi)^3} P_*(q) P_*(|\mathbf{k}-\mathbf{q}|) F_{AB}(\mathbf{q},\mathbf{k}-\mathbf{q};z)^2 \\ &+ 2\, \frac{b_2^{(2)\,2}}{2!^2} D(z)^4 \int \frac{\mathrm{d}^3 q}{(2\pi)^3} P_*(q) P_*(|\mathbf{k}-\mathbf{q}|) \\ &+ 2\, b_{\mathcal{G}_2}^{(2)\,2} D(z)^4 \int \frac{\mathrm{d}^3 q}{(2\pi)^3} P_*(q) P_*(|\mathbf{k}-\mathbf{q}|) G_2(\mathbf{q},\mathbf{k}-\mathbf{q})^2 \\ &+ 4\, b_1^{(2)} \frac{b_2^{(2)}}{2!} D(z)^2 \int \frac{\mathrm{d}^3 q}{(2\pi)^3} P_*(q) P_*(|\mathbf{k}-\mathbf{q}|) F_{AB}(\mathbf{q},\mathbf{k}-\mathbf{q};z) \\ &+ 4\, b_1^{(2)} b_{\mathcal{G}_2}^{(2)} D(z)^2 \int \frac{\mathrm{d}^3 q}{(2\pi)^3} P_*(q) P_*(|\mathbf{k}-\mathbf{q}|) F_{AB}(\mathbf{q},\mathbf{k}-\mathbf{q};z) G_2(\mathbf{q},\mathbf{k}-\mathbf{q}) \\ &+ 4\, \frac{b_2^{(2)}}{2!} b_{\mathcal{G}_2}^{(2)} D(z)^4 \int \frac{\mathrm{d}^3 q}{(2\pi)^3} P_*(q) P_*(|\mathbf{k}-\mathbf{q}|) G_2(\mathbf{q},\mathbf{k}-\mathbf{q}). \end{aligned} \tag{3.83c}$$

We turn now to the computations in redshift space:

Tree level.—

$$P_{s,\,11}^{hh}(k,z) = \left(b_1^{(1)} + f\mu^2 \right)^2 D(z)^2 P_*(k). \tag{3.84}$$

13-type correlations.—

$$
\begin{aligned}
P^{hh}_{s,13}(k,z) = &\quad \left(1+f\mu^2/b_1^{(1)}\right) P^{hh}_{13}(k) \\
&+ \quad 4\,D(z)^2 P_*(k)\left(b_1^{(1)}+f\mu^2\right)\mu^2 \int \frac{\mathrm{d}^3q}{(2\pi)^3} P_*(q)\tilde{T}(\mathbf{q},\mathbf{k},-\mathbf{q},\mathbf{k}-\mathbf{q};z) \\
&+ \quad 4\,D(z)^2 P_*(k)\left(b_1^{(1)}+f\mu^2\right) b_1^{(1)}\mu k \int \frac{\mathrm{d}^3q}{(2\pi)^3} P_*(q) F_{KL}(\mathbf{k},-\mathbf{q};z)\frac{k\mu-q\mu_q}{|\mathbf{k}-\mathbf{q}|^2} \\
&+ \quad 4\,D(z)^2 P_*(k)\left(b_1^{(1)}+f\mu^2\right) b_1^{(2)} f\mu k \int \frac{\mathrm{d}^3q}{(2\pi)^3} P_*(q) F_{AB}(\mathbf{k},-\mathbf{q};z)\frac{\mu_q}{q} \\
&+ \quad 4\,D(z)^2 P_*(k)\left(b_1^{(1)}+f\mu^2\right) f\mu^2 k^2 \int \frac{\mathrm{d}^3q}{(2\pi)^3} P_*(q) F_{KL}(\mathbf{k},-\mathbf{q};z)\frac{\mu_q}{q}\frac{k\mu-q\mu_q}{|\mathbf{k}-\mathbf{q}|^2} \\
&+ \quad 2\,D(z)^4 P_*(k)\left(b_1^{(1)}+f\mu^2\right)\frac{b_2^{(2)}}{2!} f\mu^2 \int \frac{\mathrm{d}^3q}{(2\pi)^3} P_*(q) \\
&- \quad D(z)^4 P_*(k)\left(b_1^{(1)}+f\mu^2\right)^2 (f\mu k)^2 \int \frac{\mathrm{d}^3q}{(2\pi)^3} P_*(q)\left(\frac{\mu_q}{q}\right)^2 .
\end{aligned}
\tag{3.85}
$$

22-type correlations.—

$$
\begin{aligned}
P^{hh}_{s,\,22}(k,z) = \;& P^{hh}_{22}(k) \\
+ \;& 4\,b_1^{(2)}\mu^2 \int \frac{\mathrm{d}^3q}{(2\pi)^3} P_*(q)P_*(|\mathbf{k}-\mathbf{q}|)F_{AB}(\mathbf{q},\mathbf{k}-\mathbf{q};z)F_{KL}(\mathbf{q},\mathbf{k}-\mathbf{q};z) \\
+ \;& 2\,\mu^4 \int \frac{\mathrm{d}^3q}{(2\pi)^3} P_*(q)P_*(|\mathbf{k}-\mathbf{q}|)F_{KL}(\mathbf{q},\mathbf{k}-\mathbf{q};z)^2 \\
+ \;& 4\,D(z)^2\frac{b_2^{(2)}}{2!}\mu^2 \int \frac{\mathrm{d}^3q}{(2\pi)^3} P_*(q)P_*(|\mathbf{k}-\mathbf{q}|)F_{KL}(\mathbf{q},\mathbf{k}-\mathbf{q};z) \\
+ \;& 4\,D(z)^2 b_{\mathcal{G}_2}^{(2)}\mu^2 \int \frac{\mathrm{d}^3q}{(2\pi)^3} P_*(q)P_*(|\mathbf{k}-\mathbf{q}|)F_{KL}(\mathbf{q},\mathbf{k}-\mathbf{q};z)G_2(\mathbf{q},\mathbf{k}-\mathbf{q}) \\
+ \;& 4\,D(z)^2 b_1^{(1)}b_1^{(2)} f\mu k \int \frac{\mathrm{d}^3q}{(2\pi)^3} P_*(q)P_*(|\mathbf{k}-\mathbf{q}|)F_{AB}(\mathbf{q},\mathbf{k}-\mathbf{q};z)\frac{\mu_q}{q} \\
+ \;& 4\,D(z)^2 b_1^{(1)}\mu^2 f\mu k \int \frac{\mathrm{d}^3q}{(2\pi)^3} P_*(q)P_*(|\mathbf{k}-\mathbf{q}|)F_{KL}(\mathbf{q},\mathbf{k}-\mathbf{q};z)\frac{\mu_q}{q} \\
+ \;& 2\,D(z)^2 b_1^{(2)}(f\mu k)^2 \int \frac{\mathrm{d}^3q}{(2\pi)^3} P_*(q)P_*(|\mathbf{k}-\mathbf{q}|)F_{AB}(\mathbf{q},\mathbf{k}-\mathbf{q};z)\frac{\mu_q}{q}\frac{\mu_{\mathbf{k}-\mathbf{q}}}{|\mathbf{k}-\mathbf{q}|} \\
+ \;& 2\,D(z)^2\mu^2(f\mu k)^2 \int \frac{\mathrm{d}^3q}{(2\pi)^3} P_*(q)P_*(|\mathbf{k}-\mathbf{q}|)F_{KL}(\mathbf{q},\mathbf{k}-\mathbf{q};z)\frac{\mu_q}{q}\frac{\mu_{\mathbf{k}-\mathbf{q}}}{|\mathbf{k}-\mathbf{q}|} \\
+ \;& 4\,D(z)^4 b_1^{(1)}\frac{b_2^{(2)}}{2!} f\mu k \int \frac{\mathrm{d}^3q}{(2\pi)^3} P_*(q)P_*(|\mathbf{k}-\mathbf{q}|)\frac{\mu_q}{q} \\
+ \;& 4\,D(z)^4 b_1^{(1)}b_{\mathcal{G}_2}^{(2)} f\mu k \int \frac{\mathrm{d}^3q}{(2\pi)^3} P_*(q)P_*(|\mathbf{k}-\mathbf{q}|)G_2(\mathbf{q},\mathbf{k}-\mathbf{q})\frac{\mu_q}{q} \\
+ \;& 2\,D(z)^4\frac{b_2^{(2)}}{2!}(f\mu k)^2 \int \frac{\mathrm{d}^3q}{(2\pi)^3} P_*(q)P_*(|\mathbf{k}-\mathbf{q}|)\frac{\mu_q}{q}\frac{\mu_{\mathbf{k}-\mathbf{q}}}{|\mathbf{k}-\mathbf{q}|} \\
+ \;& 2\,D(z)^4 b_{\mathcal{G}_2}^{(2)}(f\mu k)^2 \int \frac{\mathrm{d}^3q}{(2\pi)^3} P_*(q)P_*(|\mathbf{k}-\mathbf{q}|)G_2(\mathbf{q},\mathbf{k}-\mathbf{q})\frac{\mu_q}{q}\frac{\mu_{\mathbf{k}-\mathbf{q}}}{|\mathbf{k}-\mathbf{q}|} \\
+ \;& 2\,D(z)^4 b_1^{(1)\,2}(f\mu k)^2 \int \frac{\mathrm{d}^3q}{(2\pi)^3} P_*(q)P_*(|\mathbf{k}-\mathbf{q}|)\frac{\mu_q}{q}\left(\frac{\mu_q}{q}+\frac{\mu_{\mathbf{k}-\mathbf{q}}}{|\mathbf{k}-\mathbf{q}|}\right) \\
+ \;& 2\,D(z)^4 b_1^{(1)}(f\mu k)^3 \int \frac{\mathrm{d}^3q}{(2\pi)^3} P_*(q)P_*(|\mathbf{k}-\mathbf{q}|)\left(\frac{\mu_q}{q}\right)^2\frac{\mu_{\mathbf{k}-\mathbf{q}}}{|\mathbf{k}-\mathbf{q}|} \\
+ \;& \frac{1}{2}\,D(z)^4(f\mu k)^4 \int \frac{\mathrm{d}^3q}{(2\pi)^3} P_*(q)P_*(|\mathbf{k}-\mathbf{q}|)\left(\frac{\mu_q}{q}\frac{\mu_{\mathbf{k}-\mathbf{q}}}{|\mathbf{k}-\mathbf{q}|}\right)^2
\end{aligned}
\tag{3.86}
$$

Advective terms.—The advective contributions are the following

$$
(2\pi)^3\delta_D(\mathbf{k}+\mathbf{k}')P^A_{s,\,13}(k) = 2\langle\delta^{h\,(1)}_{s,\,\mathbf{k}}\delta^{A\,(3)}_{\mathbf{k}'}\rangle + 2\langle\delta^{h\,(1)}_{s,\,\mathbf{k}}\delta^{A}_{\mathrm{Doppler},\,\mathbf{k}'}\rangle, \tag{3.87a}
$$

$$
(2\pi)^3\delta_D(\mathbf{k}+\mathbf{k}')P^A_{s,\,22}(k) = 2\langle\delta^{h\,(2)}_{s,\,\mathbf{k}}\delta^{A\,(2)}_{\mathbf{k}'}\rangle + \langle\delta^{A\,(2)}_{\mathbf{k}}\delta^{A\,(2)}_{\mathbf{k}'}\rangle. \tag{3.87b}
$$

Working out the 13-type correlation functions, we find

$$\begin{aligned}
P^A_{s,\,13}(k) = \;& D^2 P_*(k)\, 4\left(b_1^{(1)}+f\mu^2\right)\left(b_1^{(2)}-b_1^{(3)}\right)\int\frac{\mathrm{d}^3q}{(2\pi)^3}P_*(q)\frac{\mathbf{q}\cdot(\mathbf{k}-\mathbf{q})}{q^2}F_{AB}(\mathbf{k},\mathbf{q};z)\\
+\;& D^2 P_*(k)\frac{1}{f}\left(b_1^{(1)}+f\mu^2\right)\left(b_1^{(1)}-b_1^{(3)}\right)\int\frac{\mathrm{d}^3q}{(2\pi)^3}P_*(q)\frac{\mathbf{q}\cdot(\mathbf{k}-\mathbf{q})}{|\mathbf{k}-\mathbf{q}|^2}F_{KL}(\mathbf{k},\mathbf{q};z)\\
+\;& D^4 P_*(k)\, 2\left(b_1^{(1)}+f\mu^2\right)\left(b_1^{(1)}-b_1^{(2)}\right)\mu k\int\frac{\mathrm{d}^3q}{(2\pi)^3}P_*(q)\frac{\mathbf{q}\cdot\mathbf{k}}{q^2}\frac{q^2+k^2}{k^2}\frac{\mu_q}{q}\\
+\;& D^4 P_*(k)\, 2\left(b_1^{(1)}+f\mu^2\right)\left(\frac{b_1^{(1)}+b_1^{(3)}}{2}-b_1^{(2)}\right)\int\frac{\mathrm{d}^3q}{(2\pi)^3}P_*(q)\frac{\mathbf{q}\cdot(\mathbf{k}-\mathbf{q})}{q^2}\left(\frac{k}{q}+\frac{q}{k}\right)\\
+\;& D^4 P_*(k)\, 4\left(b_1^{(1)}+f\mu^2\right)\left(\frac{b_2^{(2)}}{2!}-\frac{b_2^{(3)}}{2!}\right)\int\frac{\mathrm{d}^3q}{(2\pi)^3}P_*(q)\frac{\mathbf{q}\cdot(\mathbf{k}-\mathbf{q})}{q^2}\\
+\;& D^4 P_*(k)\, 4\left(b_1^{(1)}+f\mu^2\right)\left(b_{\mathcal{G}_2}^{(2)}-b_{\mathcal{G}_2}^{(3)}\right)\int\frac{\mathrm{d}^3q}{(2\pi)^3}P_*(q)\frac{\mathbf{q}\cdot(\mathbf{k}-\mathbf{q})}{q^2}G_2(\mathbf{k},\mathbf{q}).
\end{aligned}\tag{3.88}$$

Whereas the 22-type contributions read

$$\begin{aligned}
P^A_{s,\,22}(k) = \;& 4D^2\left(b_1^{(1)}-b_1^{(2)}\right)b_1^{(2)}\int\frac{\mathrm{d}^3q}{(2\pi)^3}P_*(q)P_*(|\mathbf{k}-\mathbf{q}|)\frac{\mathbf{q}\cdot(\mathbf{k}-\mathbf{q})}{q^2}F_{AB}(\mathbf{q},\mathbf{k}-\mathbf{q};z)\\
+\;& 4D^2\left(b_1^{(1)}-b_1^{(2)}\right)\mu^2\int\frac{\mathrm{d}^3q}{(2\pi)^3}P_*(q)P_*(|\mathbf{k}-\mathbf{q}|)\frac{\mathbf{q}\cdot(\mathbf{k}-\mathbf{q})}{q^2}F_{KL}(\mathbf{q},\mathbf{k}-\mathbf{q};z)\\
+\;& 4D^4\left(b_1^{(1)}-b_1^{(2)}\right)\frac{b_2^{(2)}}{2!}\int\frac{\mathrm{d}^3q}{(2\pi)^3}P_*(q)P_*(|\mathbf{k}-\mathbf{q}|)\frac{\mathbf{q}\cdot(\mathbf{k}-\mathbf{q})}{q^2}\\
+\;& 4D^4\left(b_1^{(1)}-b_1^{(2)}\right)b_{\mathcal{G}_2}^{(2)}\int\frac{\mathrm{d}^3q}{(2\pi)^3}P_*(q)P_*(|\mathbf{k}-\mathbf{q}|)\frac{\mathbf{q}\cdot(\mathbf{k}-\mathbf{q})}{q^2}G_2(\mathbf{q},\mathbf{k}-\mathbf{q})\\
+\;& D^4\left(b_1^{(1)}-b_1^{(2)}\right)^2\int\frac{\mathrm{d}^3q}{(2\pi)^3}P_*(q)P_*(|\mathbf{k}-\mathbf{q}|)\left(\frac{\mathbf{q}\cdot(\mathbf{k}-\mathbf{q})}{q^2}\right)^2\frac{q^2+|\mathbf{k}-\mathbf{q}|^2}{|\mathbf{k}-\mathbf{q}|^2}\\
+\;& 2D^4\left(b_1^{(1)}-b_1^{(2)}\right)b_1^{(1)}f\mu k\int\frac{\mathrm{d}^3q}{(2\pi)^3}P_*(q)P_*(|\mathbf{k}-\mathbf{q}|)\frac{\mathbf{q}\cdot(\mathbf{k}-\mathbf{q})}{q^2}\left(\frac{\mu_q}{q}+\frac{\mu_{\mathbf{k}-\mathbf{q}}}{|\mathbf{k}-\mathbf{q}|}\right)\\
+\;& 2D^4\left(b_1^{(1)}-b_1^{(2)}\right)(f\mu k)^2\int\frac{\mathrm{d}^3q}{(2\pi)^3}P_*(q)P_*(|\mathbf{k}-\mathbf{q}|)\frac{\mathbf{q}\cdot(\mathbf{k}-\mathbf{q})}{q^2}\frac{\mu_q\mu_{\mathbf{k}-\mathbf{q}}}{q|\mathbf{k}-\mathbf{q}|}.
\end{aligned}\tag{3.89}$$

3.B.4 Recipe for evaluating the loop integrals

The evaluation of the loop integrals above can be a daunting experience. In this section, we summarise the recipe that we presented in our previous work [49] in order to deal with the challenging evaluation of the tensorial parts of the one-loop correlation functions in redshift space — coming from the composite operators $\mathbf{v}\delta$, $\mathbf{vv}$, $\mathbf{vv}\delta$ and $\mathbf{vvv}$.

1. Replace the Dirac delta by its Fourier representation, and expand the resulting exponential using the Rayleigh plane wave formula,

$$\mathrm{e}^{\mathrm{i}\mathbf{k}\cdot\mathbf{x}} = \sum_{\ell=0}^{\infty}(2\ell+1)\mathrm{i}^\ell j_\ell(kx)\mathscr{P}_\ell(\hat{\mathbf{k}}\cdot\hat{\mathbf{x}}) \tag{3.90}$$

where j_ℓ is the spherical Bessel function of order ℓ and $\mathscr{P}_\ell(x)$ is the ℓ^{th} Legendre polynomial.

2. The angular part of the **q**, **s** and **x** integrations can be done using the generalised orthogonality relation

$$\int \mathrm{d}^2\hat{\mathbf{x}}\; \mathscr{P}_\ell(\hat{\mathbf{a}}\cdot\hat{\mathbf{x}})\mathscr{P}_{\ell'}(\hat{\mathbf{b}}\cdot\hat{\mathbf{x}}) = \frac{4\pi}{2\ell+1}\delta_{\ell\ell'}\mathscr{P}_\ell(\hat{\mathbf{a}}\cdot\hat{\mathbf{b}}). \tag{3.91}$$

3. For P_{22} integrals, involving $P_*(q)P_*(|\mathbf{k}-\mathbf{q}|)$, we use the 3-Bessel integral $\mathscr{J}^\mu_{\nu\sigma}$

$$\mathscr{J}^\mu_{\nu\sigma} \equiv \int_0^\infty \mathrm{d}x\; x^2 j_\mu(kx) j_\nu(qx) j_\sigma(sx), \tag{3.92}$$

where $s = (q^2+k^2-2kq\cos\theta)^{1/2}$ and the different subscripts are associated to the different wavenumbers: $\mu \mapsto k$, $\nu \mapsto q$ and $\sigma \mapsto s$[15]. In general, $\mathscr{J}^\mu_{\nu\sigma} \neq 0$ where k, q and s satisfy the triangle condition $|k-q| < s < |k+q|$. The result is a scalar integral over q and θ.

We collect the results needed for the computation of the power spectrum:

$$\mathscr{J}^0_{00} = \frac{\pi}{4kqs} \tag{3.93a}$$

$$\mathscr{J}^1_{10} = \frac{\pi}{8}\frac{k^2+q^2-s^2}{k^2q^2s} \tag{3.93b}$$

$$\mathscr{J}^2_{20} = \frac{\pi}{32}\frac{3k^4+2k^2(q^2-3s^2)+3(q^2-s^2)^2}{k^3q^3s} \tag{3.93c}$$

$$\mathscr{J}^2_{22} = \frac{\pi}{64}\frac{(3k^4+2k^2q^2+3q^4)s^2+3(k^2+q^2)s^4-3(k^2-q^2)^2(k^2+q^2)-3s^6}{k^3q^3s^3} \tag{3.93d}$$

$$\mathscr{J}^2_{31} = \frac{\pi}{64}\frac{3k^4(q^2+5s^2)+(q^2-s^2)^2(q^2+5s^2)+k^2(q^4+6q^2s^2-15s^4)-5k^6}{k^3q^4s^2} \tag{3.94a}$$

$$\begin{aligned}\mathscr{J}^2_{42} = \frac{\pi}{512}\frac{1}{k^3q^5s^3}\Big(&35k^8-20k^6(3q^2+7s^2)+6k^4(3q^4+10q^2s^2+35s^2)\\&+(q^2-s^2)^2(3q^4+10q^2s^2+35s^4)+4k^2(q^6+3q^4s^2+15q^2s^4-35s^6)\Big)\end{aligned} \tag{3.94b}$$

$$\mathscr{J}^3_{30} = \frac{\pi}{64}\frac{(k^2+q^2-s^2)[5k^4+5(q^2-s^2)^2-2k^2(q^2+5s^2)]}{k^4q^4s} \tag{3.95a}$$

$$\begin{aligned}\mathscr{J}^4_{40} = \frac{\pi}{512}\frac{1}{k^4q^5s}\Big(&35k^8+20k^2(q^2-7s^2)[k^4+(q^2-s^2)^2]+35(q^2-s^2)^4\\&+6k^4(3q^4-30q^2s^2+35s^4)\Big)\end{aligned} \tag{3.95b}$$

[15] The analytical solution to these integrals for general k, q and s and arbitrary orders μ, ν and σ was solved by Gervois & Navelet [74] and Fabrikant [62].

Index permutations can be obtained by making suitable exchanges of k, q and s; for example, $\mathscr{J}^2_{13}$ can be obtained from (3.93d) by exchanging q and s, and $\mathscr{J}^0_{33}$ can be obtained from (3.94b) by exchanging k and s.

4. For P_{13} integrals the procedure is very similar. These are typically simpler because they involve integration only over $P_*(q)$ and therefore can be performed analytically using the Fourier transform

$$\int \mathrm{d}^3 s\, s^{-2} \mathrm{e}^{\mathrm{i}\mathbf{s}\cdot\mathbf{x}} = 2\pi^2/x. \tag{3.96}$$

Consequently, 13-type integrals require only 2-Bessel integrals of the form

$$\mathscr{J}_\mu \equiv \int_0^\infty \mathrm{d}x\; x j_\mu(kx) j_\mu(qx). \tag{3.97}$$

The Bessel functions are easily computable using *Mathematica* for example.

3.B.5 Final results

Power spectrum

Throughout this section we consider the following integral limits: $q \in [q_{IR}, q_{UV}] = [0.001, 1.4]$, $\varphi \in [0, 2\pi)$ and $x \in [-1, 1]$.

13-type integrals.—

- $\mu^{\mathbf{0}}$ **terms**

$$\begin{aligned} b_1^{(1)} b_1^{(3)} \quad \to \quad & -DkP(k) \int_{q_{IR}}^{q_{UV}} \mathrm{d}q \int_{-1}^{1} \mathrm{d}x \, \frac{P(q)}{2\pi^2 \left(k^2 - 2kqx + q^2\right)} \times \\ & \times \Big[x \Big(2D_D \left(k^3 x - k^2 q \left(x^2 + 2 \right) + 3kq^2 x - q^3 x^2 \right) \\ & + 4D_E (kx - q)(k - qx)^2 - D_J \left(k^3 x - 3k^2 q + 3kq^2 x - 2q^3 x^2 + q^3 \right) \Big) \\ & + D_F \left(k^3 x^2 - k^2 q \left(2x^3 + x \right) + kq^2 \left(5x^2 - 2 \right) + q^3 x \left(1 - 2x^2 \right) \right) \\ & + 2D_G \left(k^3 x^2 - 3k^2 q x^3 + kq^2 \left(2x^4 + 2x^2 - 1 \right) + q^3 x \left(1 - 2x^2 \right) \right) \Big] \end{aligned} \tag{3.98a}$$

$$\begin{aligned} b_1^{(1)} b_2^{(3)} \quad \to \quad & -D^2 P(k) \int_{q_{IR}}^{q_{UV}} \mathrm{d}q \int_{-1}^{1} \mathrm{d}x \, \frac{qP(q)}{2\pi^2 k} \times \\ & \times \Big[D_A \left(k^2 x - 2kq + q^2 x \right) + 2D_B \left(k^2 x - kq \left(x^2 + 1 \right) + q^2 x \right) \Big] \end{aligned} \tag{3.98b}$$

$$b_1^{(1)} b_3 \quad \to \quad D^4 P(k) \int_{q_{IR}}^{q_{UV}} \mathrm{d}q \int_{-1}^{1} \mathrm{d}x \, \frac{q^2 P(q)}{4\pi^2} \tag{3.98c}$$

$$b_1^{(1)} b_{1\mathcal{G}_2} \quad \to \quad D^4 P(k) \int_{q_{IR}}^{q_{UV}} \mathrm{d}q \int_{-1}^{1} \mathrm{d}x \, \frac{q^2 \left(x^2 - 1 \right) P(q)}{\pi^2} \tag{3.98d}$$

$$\begin{aligned} b_1^{(1)} b_{\mathcal{G}_2}^{(3)} \quad \to \quad & -D^2 kP(k) \int_{q_{IR}}^{q_{UV}} \mathrm{d}q \int_{-1}^{1} \mathrm{d}x \, \frac{q \left(x^2 - 1 \right) P(q)}{\pi^2 \left(k^2 - 2kqx + q^2 \right)} \times \\ & \times \Big(D_A \left(k^2 x - 2kq + q^2 x \right) + 2D_B \left(k^2 x - kq \left(x^2 + 1 \right) + q^2 x \right) \Big) \end{aligned} \tag{3.98e}$$

$$\begin{aligned} b_1^{(1)} b_{\Gamma_3} \quad \to \quad & -D^2 kP(k) \int_{q_{IR}}^{q_{UV}} \mathrm{d}q \int_{-1}^{1} \mathrm{d}x \, \frac{q \left(x^2 - 1 \right) P(q)}{\pi^2 f \left(k^2 - 2kqx + q^2 \right)} \times \\ & \times \Big[D_A (f - f_A) \left(k^2 x - 2kq + q^2 x \right) + 2D_B (f - f_B) \left(k^2 x - kq \left(x^2 + 1 \right) + q^2 x \right) \\ & + fg^2 \left(k^2 x - 2kq + q^2 x \right) \Big] \end{aligned} \tag{3.98f}$$

- $\mu^{\mathbf{2}}$ **terms**

$$
\begin{aligned}
b_1^{(1)} \quad \rightarrow \quad & - D^2 P(k) \int_{q_{IR}}^{q_{UV}} \mathrm{d}q \int_{-1}^{1} \mathrm{d}x \; - \frac{P(q)}{96\pi^2 k^3 q^3 \left|k^2 - 2kqx + q^2\right|} \times \\
& \times \Big[48k^3q^3 \Big(\Big(- kqx \Big(k^2 (D_A f_A D + 2D_B f_B D + 4D_D f_D + 4D_E f_E + F f_F - 3J f_J) \\
& \quad + q^2 (3A f_A D + 4B f_B D - F f_F - 2D_G f_G + D_J f_J) \Big) \\
& \quad x^2 \Big(k^2 q^2 (D_A f_A D + 4D_B f_B D + 6D_D f_D + 8D_E f_E + 5F f_F + 4D_G f_G - 3J f_J) \\
& \quad + Dq^4 (D_A f_A D + 2D_B f_B D + k^4 \left(2D_D f_D + 4D_E f_E + F f_F + 2D_G f_G - J f_J\right)) \Big) \\
& \quad + 2k^2 q^2 (D_A f_A D + 2D_B f_B D - F f_F - D_G f_G) \Big) \\
& \quad 2fkq \Big(2k^5 q^3 x \left(12D \left(2x^2 (D_A + 3D_B) + 2D_A + 2D_B + D^2 \right) - 11(D_K + D_L) \right) \\
& \quad - 2k^4 q^4 \left(12D \left(x^2 \left(6D_A + 8D_B + D^2 \right) + 4D_B x^4 + 2D^2 \right) - 11(D_K + D_L) \right) \\
& \quad + 2k^3 q^5 x \left(12D \left(2x^2 (D_A + 3D_B) + 2D_A + 2D_B + 3D^2 \right) - 11(D_K + D_L) \right) \\
& \quad + 8k^2 q^6 \left(-3Dx^2 \left(D_A + 2D_B + D^2 \right) + D_K + D_L \right) \\
& \quad + 8k^6 q^2 \left(-3Dx^2 (D_A + 2D_B) + D_K + D_L \right) \\
& \quad - 3k^8 (D_K + D_L) + 6k^7 qx (D_K + D_L) + 6kq^7 x (D_K + D_L) - 3q^8 (D_K + D_L) \Big) \\
& \quad + 3f \left(k^2 - q^2 \right)^4 (D_K + D_L) \left| k^2 - 2kqx + q^2 \right| \log \left| \frac{k+q}{k-q} \right| \Big]
\end{aligned}
\tag{3.99a}
$$

$$
\begin{aligned}
b_1^{(3)} \quad \rightarrow \quad & - fDkP(k) \int_{q_{IR}}^{q_{UV}} \mathrm{d}q \int_{-1}^{1} \mathrm{d}x \, \frac{P(q)}{2\pi^2 \left(k^2 - 2kqx + q^2\right)} \times \\
& \times \Big[x \Big(2D_D \left(k^3 x - k^2 q \left(x^2 + 2 \right) + 3kq^2 x - q^3 x^2 \right) \\
& \quad + 4D_E (kx - q)(k - qx)^2 - D_J \left(k^3 x - 3k^2 q + 3kq^2 x - 2q^3 x^2 + q^3 \right) \Big) \\
& \quad + D_F \left(k^3 x^2 - k^2 q \left(2x^3 + x \right) + kq^2 \left(5x^2 - 2 \right) + q^3 x \left(1 - 2x^2 \right) \right) \\
& \quad + 2D_G \left(k^3 x^2 - 3k^2 q x^3 + kq^2 \left(2x^4 + 2x^2 - 1 \right) + q^3 x \left(1 - 2x^2 \right) \right) \Big]
\end{aligned}
\tag{3.99b}
$$

$$
\begin{aligned}
b_2^{(3)} \quad \rightarrow \quad & - fD^2 P(k) \int_{q_{IR}}^{q_{UV}} \mathrm{d}q \int_{-1}^{1} \mathrm{d}x \, \frac{qP(q)}{2\pi^2 k} \times \\
& \times \Big[D_A \left(k^2 x - 2kq + q^2 x \right) + 2D_B \left(k^2 x - kq \left(x^2 + 1 \right) + q^2 x \right) \Big]
\end{aligned}
\tag{3.99c}
$$

$$b_3 \quad \rightarrow \quad fD^4P(k)\int_{q_{IR}}^{q_{UV}} \mathrm{d}q \int_{-1}^{1} \mathrm{d}x \, \frac{q^2 P(q)}{4\pi^2} \tag{3.100a}$$

$$b_{1\mathcal{G}_2} \quad \rightarrow \quad fD^4P(k)\int_{q_{IR}}^{q_{UV}} \mathrm{d}q \int_{-1}^{1} \mathrm{d}x \, \frac{q^2\left(x^2-1\right)P(q)}{\pi^2} \tag{3.100b}$$

$$\begin{aligned} b_{\mathcal{G}_2}^{(3)} \quad \rightarrow \quad & -fD^2kP(k)\int_{q_{IR}}^{q_{UV}} \mathrm{d}q \int_{-1}^{1} \mathrm{d}x \, \frac{q\left(x^2-1\right)P(q)}{\pi^2\left(k^2-2kqx+q^2\right)}\times \\ & \times\left(D_A\left(k^2x-2kq+q^2x\right)+2D_B\left(k^2x-kq\left(x^2+1\right)+q^2x\right)\right) \end{aligned} \tag{3.100c}$$

$$\begin{aligned} b_{\Gamma_3} \quad \rightarrow \quad & -fD^2kP(k)\int_{q_{IR}}^{q_{UV}} \mathrm{d}q \int_{-1}^{1} \mathrm{d}x \, \frac{q\left(x^2-1\right)P(q)}{\pi^2 f\left(k^2-2kqx+q^2\right)}\times \\ & \times\Big[D_A(f-f_A)\left(k^2x-2kq+q^2x\right)+2D_B(f-f_B)\left(k^2x-kq\left(x^2+1\right)+q^2x\right) \\ & +fg^2\left(k^2x-2kq+q^2x\right)\Big] \end{aligned} \tag{3.100d}$$

$$\begin{aligned} b_1^{(1)}b_1^{(1)} \quad \rightarrow \quad & D^2P(k)\int_{q_{IR}}^{q_{UV}} \mathrm{d}q \int_{-1}^{1} \mathrm{d}x \, \frac{P(q)}{24\pi^2k^3}\times \\ & \times\Big[\frac{3}{q}\left(k^2+q^2\right)\left(k^2-q^2\right)^2(D_K+D_L)\log\left|\frac{k+q}{k-q}\right| \\ & +\frac{2k}{\left|k^2-2kqx+q^2\right|}\Big(6k^5qx\left(-D_Af_A-2D_Bf_B+fg^2\left(fx^2+1\right)+D_K+D_L\right) \\ & +k^4q^2\left(12D_Af_A+12D_Bf_B\left(x^2+1\right)-3fg^2\left(fx^2+4\right)+3D_K+7D_L\right) \\ & -2k^3q^3x\left(3D_Af_A+6D_Bf_B-3fg^2+6D_K+10D_L\right) \\ & -3k^6\left(f^2g^2x^2+D_K+D_L\right)+k^2q^4(3D_K+7D_L) \\ & +6kq^5x(D_K+D_L)-3q^6(D_K+L)\Big)\Big] \end{aligned} \tag{3.101a}$$

$$b_1^{(1)}b_1^{(2)} \quad \rightarrow \quad -fD^2P(k)\int_{q_{IR}}^{q_{UV}} \mathrm{d}q \int_{-1}^{1} \mathrm{d}x \, \frac{P(q)}{3\pi^2}(A+2B)\left(k^2+q^2\right) \tag{3.101b}$$

$$b_1^{(1)}b_2^{(2)} \quad \rightarrow \quad fD^4P(k)\int_{q_{IR}}^{q_{UV}} \mathrm{d}q \int_{-1}^{1} \mathrm{d}x \, \frac{q^2P(q)}{2\pi^2} \tag{3.101c}$$

- **μ^4 terms**

$$
\begin{aligned}
1 \quad \to \quad & -fD^2P(k)\int_{q_{IR}}^{q_{UV}}\mathrm{d}q\int_{-1}^{1}\mathrm{d}x\,-\frac{P(q)}{96\pi^2k^3q^3\left|k^2-2kqx+q^2\right|}\times \\
& \times\Big[48k^3q^3\Big(\Big(-kqx\Big(k^2(D_Af_AD+2D_Bf_BD+4D_Df_D+4D_Ef_E+Ff_F-3Jf_J) \\
& \quad +q^2(3Af_AD+4Bf_BD-Ff_F-2D_Gf_G+D_Jf_J)\Big) \\
& \quad x^2\Big(k^2q^2(D_Af_AD+4D_Bf_BD+6D_Df_D+8D_Ef_E+5Ff_F+4D_Gf_G-3Jf_J) \\
& \quad +Dq^4(D_Af_AD+2D_Bf_BD+k^4\left(2D_Df_D+4D_Ef_E+Ff_F+2D_Gf_G-Jf_J\right)\Big) \\
& \quad +2k^2q^2(D_Af_AD+2D_Bf_BD-Ff_F-D_Gf_G)\Big) \\
& \quad 2fkq\Big(2k^5q^3x\left(12D\left(2x^2(D_A+3D_B)+2D_A+2D_B+D^2\right)-11(D_K+D_L)\right) \\
& \quad -2k^4q^4\left(12D\left(x^2\left(6D_A+8D_B+D^2\right)+4D_Bx^4+2D^2\right)-11(D_K+D_L)\right) \\
& \quad +2k^3q^5x\left(12D\left(2x^2(D_A+3D_B)+2D_A+2D_B+3D^2\right)-11(D_K+D_L)\right) \\
& \quad +8k^2q^6\left(-3Dx^2\left(D_A+2D_B+D^2\right)+D_K+D_L\right) \\
& \quad +8k^6q^2\left(-3Dx^2(D_A+2D_B)+D_K+D_L\right) \\
& \quad -3k^8(D_K+D_L)+6k^7qx(D_K+D_L)+6kq^7x(D_K+D_L)-3q^8(D_K+D_L)\Big) \\
& \quad +3f\left(k^2-q^2\right)^4(D_K+D_L)\left|k^2-2kqx+q^2\right|\log\left|\frac{k+q}{k-q}\right|\Big]
\end{aligned}
\tag{3.102a}
$$

$$
\begin{aligned}
b_1^{(1)} \quad \to \quad & fD^2P(k)\int_{q_{IR}}^{q_{UV}}\mathrm{d}q\int_{-1}^{1}\mathrm{d}x\,\frac{P(q)}{96\pi^2k^3q^3}\times \\
& \times\Big[-3\left(k^2-q^2\right)^3\left(k^2+3q^2\right)(D_K+D_L)\log\left|\frac{k+q}{k-q}\right| \\
& \quad +6k^7q(D_K+D_L)+2k^5q^3(15D_K+31D_L) \\
& \quad +42k^3q^5(D_K+D_L)+18kq^7(D_K+D_L) \\
& \quad +\frac{3}{q}\left(k^2+q^2\right)\left(k^2-q^2\right)^2(D_K+D_L)\log\left|\frac{k+q}{k-q}\right| \\
& \quad +\frac{2k}{\left|k^2-2kqx+q^2\right|}\Big(6k^5qx\left(-D_Af_A-2D_Bf_B+fg^2\left(fx^2+1\right)+D_K+D\right. \\
& \quad \quad +k^4q^2\left(12D_Af_A+12D_Bf_B\left(x^2+1\right)-3fg^2\left(fx^2+4\right)+3D_K+7D_L\right) \\
& \quad \quad -2k^3q^3x\left(3D_Af_A+6D_Bf_B-3fg^2+6D_K+10D_L\right) \\
& \quad \quad -3k^6\left(f^2g^2x^2+D_K+D_L\right)+k^2q^4(3D_K+7D_L) \\
& \quad \quad +6kq^5x(D_K+D_L)-3q^6(D_K+L)\Big]
\end{aligned}
\tag{3.102b}
$$

$$
b_1^{(2)} \quad \to \quad -fD^2P(k)\int_{q_{IR}}^{q_{UV}}\mathrm{d}q\int_{-1}^{1}\mathrm{d}x\,\frac{P(q)}{3\pi^2}(A+2B)\left(k^2+q^2\right) \tag{3.102c}
$$

$$
b_2^{(2)} \quad \to \quad fD^4P(k)\int_{q_{IR}}^{q_{UV}}\mathrm{d}q\int_{-1}^{1}\mathrm{d}x\,\frac{q^2P(q)}{2\pi^2} \tag{3.102d}
$$

- $\mu^{\mathbf{6}}$ **terms**

$$
\begin{aligned}
1 \quad \rightarrow \quad & -f^2 D^2 P(k) \int_{q_{IR}}^{q_{UV}} \mathrm{d}q \int_{-1}^{1} \mathrm{d}x \, \frac{P(q)}{96\pi^2 k^3 q^3} \times \\
& \times \Big[3\left(k^2 - q^2\right)^3 \left(k^2 + 3q^2\right) (D_K + L) \log\left(\left| \frac{k+q}{k-q} \right| \right) \\
& + 2k^5 q^3 \left(12 f^2 D^2 x^2 + 15 D_K + 31 D_L \right) \\
& - 6k^7 q (D_K + D_L) - 42 k^3 q^5 (D_k + D_L) + 18 k q^7 (D_K + D_L) \Big]
\end{aligned}
\tag{3.103}
$$

22-type integrals.—

- $\mu^{\mathbf{0}}$ **terms**

$$
b_1^{(2)} b_1^{(2)} \quad \rightarrow \quad \int_{q_{IR}}^{q_{UV}} \mathrm{d}q \int_{-1}^{1} \mathrm{d}x \, P(q) P\left(|\mathbf{k} - \mathbf{q}|\right) \frac{k^4}{8\pi^2 \left(k^2 - 2kqx + q^2\right)^2} \times \\
\times \left(D_A \left(kx - 2qx^2 + q \right) + 2 D_B x (k - qx) \right)^2 \tag{3.104a}
$$

$$
b_1^{(2)} b_2^{(2)} \quad \rightarrow \quad \int_{q_{IR}}^{q_{UV}} \mathrm{d}q \int_{-1}^{1} \mathrm{d}x \, P(q) P\left(|\mathbf{k} - \mathbf{q}|\right) \frac{D^2 k^2 q}{4\pi^2 \left(k^2 - 2kqx + q^2\right)} \times \\
\times \left(D_A \left(kx - 2qx^2 + q \right) + 2 D_B x (k - qx) \right) \tag{3.104b}
$$

$$
b_1^{(2)} b_{\mathcal{G}_2}^{(2)} \quad \rightarrow \quad \int_{q_{IR}}^{q_{UV}} \mathrm{d}q \int_{-1}^{1} \mathrm{d}x \, P(q) P\left(|\mathbf{k} - \mathbf{q}|\right) \frac{g^2 k^4 q \left(x^2 - 1\right)}{2\pi^2 \left(k^2 - 2kqx + q^2\right)^2} \times \\
\times \left(D_A \left(kx - 2qx^2 + q \right) + 2 D_B x (k - qx) \right) \tag{3.104c}
$$

$$
b_2^{(2)} b_2^{(2)} \quad \rightarrow \quad \int_{q_{IR}}^{q_{UV}} \mathrm{d}q \int_{-1}^{1} \mathrm{d}x \, P(q) P\left(|\mathbf{k} - \mathbf{q}|\right) \frac{D^4 q^2}{8\pi^2} \tag{3.104d}
$$

$$
b_2^{(2)} b_{\mathcal{G}_2}^{(2)} \quad \rightarrow \quad \int_{q_{IR}}^{q_{UV}} \mathrm{d}q \int_{-1}^{1} \mathrm{d}x \, P(q) P\left(|\mathbf{k} - \mathbf{q}|\right) \frac{D^4 k^2 q^2 \left(x^2 - 1\right)}{2\pi^2 \left(k^2 - 2kqx + q^2\right)} \tag{3.104e}
$$

$$
b_{\mathcal{G}_2}^{(2)} b_{\mathcal{G}_2}^{(2)} \quad \rightarrow \quad \int_{q_{IR}}^{q_{UV}} \mathrm{d}q \int_{-1}^{1} \mathrm{d}x \, P(q) P\left(|\mathbf{k} - \mathbf{q}|\right) \frac{D^4 k^4 q^2 \left(x^2 - 1\right)^2}{2\pi^2 \left(k^2 - 2kqx + q^2\right)^2} \tag{3.104f}
$$

- $\mu^{\mathbf{2}}$ **terms**

$$
\begin{aligned}
b_1^{(2)} \quad \to \quad & \int_{q_{IR}}^{q_{UV}} \mathrm{d}q \int_{-1}^{1} \mathrm{d}x\, P(q) P\left(|\mathbf{k}-\mathbf{q}|\right) \frac{1}{64\pi^2 q^2 \left|k^2-2qxk+q^2\right|^3} \times \\
& \times \Big[f^2 g^2 (-(D_A+D_B)) \left|k^2-2qxk+q^2\right|^5 + \\
& f^2 g^2 \left(3D_A k^2 + 4D_A q^2 + 2D_B k^2 + 4D_B q^2\right) \left|k^2-2qxk+q^2\right|^4 \\
& - f^2 g^2 \left(3D_A \left(k^4 + k^2 q^2 + 2q^4\right) + 2D_B q^2 \left(k^2+3q^2\right)\right) \left|k^2-2qxk+q^2\right|^3 \\
& + \Big(D_A \Big(f^2 g^2 \left(k^6 - 2k^4 q^2 - 3k^2 q^4 + 4q^6\right) \left|k^2-2qxk+q^2\right|^2 \\
& \quad + 16 k^4 q^2 \left(D_K \left|kx - 2qx^2 + q\right|^2 + 2D_L x (k-qx)\right) \Big) \\
& \quad + D_B \Big(-2 f^2 g^2 \left(k^6 + k^2 q^4 - 2q^6\right) \left|k^2-2kqx+q^2\right| \\
& \quad + 32 k^4 q^2 x (k-qx) \left(D_K \left|kx - 2qx^2 + q\right| + 2D_L x (k-qx)\right) \Big) \\
& + f^2 g^2 \left(k^2-q^2\right)^3 \left|k^2-2kqx+q^2\right| \left(D_A q^2 + D_B \left(k^2+q^2\right)\right) \Big]
\end{aligned}
\tag{3.105a}
$$

$$
\begin{aligned}
b_2^{(2)} \quad \to \quad & D^2 \int_{q_{IR}}^{q_{UV}} \mathrm{d}q \int_{-1}^{1} \mathrm{d}x\, P(q) P\left(|\mathbf{k}-\mathbf{q}|\right) \frac{1}{32\pi^2 \left|k^2-2kqx+q^2\right|} \times \\
& \times \Big[f^2 g^2 \left|k^2-2qxk+q^2\right| \left(\left|k^2-2qxk+q^2\right| - 2\left(k^2+q^2\right)\right) \\
& + f^2 g^2 \left(k^2-q^2\right)^2 + 8k^2 q \left(kx(D_K+2D_L) - 2qx^2(D_K+D_L) + D_K q\right) \Big]
\end{aligned}
\tag{3.105b}
$$

$$
\begin{aligned}
b_{\mathcal{G}_2}^{(2)} \quad \to \quad & \int_{q_{IR}}^{q_{UV}} \mathrm{d}q \int_{-1}^{1} \mathrm{d}x\, P(q) P\left(|\mathbf{k}-\mathbf{q}|\right) \frac{1}{64\pi^2 q^2 \left|k^2-2kqx+q^2\right|^3} \times \\
& \times \Big[f^2 D^4 \left|k^2-2qxk+q^2\right|^5 \\
& - 4 f^2 D^4 \left(k^2+q^2\right) \left|k^2-2kqx+q^2\right|^4 \\
& + 2 f^2 D^4 \left(3k^4 + 2k^2 q^2 + 3q^4\right) \left|k^2-2qxk+q^2\right|^3 \\
& - 4D^2 \left|k^2-2qxk+q^2\right| \Big(f^2 D^2 \left(k^2-q^2\right)^2 \left(k^2+q^2\right) \left(k^2-2kqx+q^2\right) \\
& \quad - 8k^4 q^3 \left(x^2-1\right) \left(D_K \left(kx - 2qx^2 + q\right) + 2D_L x (k-qx)\right) \Big) \\
& + f^2 g^4 \left(k^2-q^2\right)^4 \left|k^2-2kqx+q^2\right| \Big]
\end{aligned}
\tag{3.105c}
$$

$$b_1^{(1)}b_1^{(1)} \quad \to \quad -f^2D^4\int_{q_{IR}}^{q_{UV}}\mathrm{d}q\int_{-1}^{1}\mathrm{d}x\,P(q)P\left(|\mathbf{k}-\mathbf{q}|\right)\frac{1}{96\pi^2}\left(\frac{1}{q^2}-\frac{1}{k^2-2kqx+q^2}\right)\times$$
$$\times\left(2k^2\left(q^2-3\left|k^2-2qxk+q^2\right|\right)+3\left(q^2-\left|k^2-2qxk+q^2\right|\right)^2+3k^4\right) \tag{3.106a}$$

$$b_1^{(1)}b_1^{(2)} \quad \to \quad fD^2\int_{q_{IR}}^{q_{UV}}\mathrm{d}q\int_{-1}^{1}\mathrm{d}x\,P(q)P\left(|\mathbf{k}-\mathbf{q}|\right)\frac{\left(-\left|k^2-2qxk+q^2\right|+k^2+q^2\right)}{8\pi^2q^2\left|k^2-2qxk+q^2\right|}\times$$
$$\Big[\left|k^2-2qxk+q^2\right|\left(-(D_A+D_B)\left|k^2-2qxk+q^2\right|+2q^2(D_A+D_B)+D_Ak^2\right)$$
$$-q^4(D_A+D_B)+D_Ak^2q^2+D_Bk^4\Big] \tag{3.106b}$$

$$b_1^{(1)}b_2^{(2)} \quad \to \quad fD^4\int_{q_{IR}}^{q_{UV}}\mathrm{d}q\int_{-1}^{1}\mathrm{d}x\,P(q)P\left(|\mathbf{k}-\mathbf{q}|\right)\frac{-\left|k^2-2qxk+q^2\right|+k^2+q^2}{4\pi^2} \tag{3.106c}$$

$$b_1^{(1)}b_{\mathcal{G}_2}^{(2)} \quad \to \quad fD^4\int_{q_{IR}}^{q_{UV}}\mathrm{d}q\int_{-1}^{1}\mathrm{d}x\,P(q)P\left(|\mathbf{k}-\mathbf{q}|\right)\frac{\left((k-q)^2-\left|k^2-2qxk+q^2\right|\right)}{8\pi^2q^2\left|k^2-2qxk+q^2\right|}\times$$
$$\times\left(-\left|k^2-2qxk+q^2\right|+k^2+q^2\right)\left((k+q)^2-\left|k^2-2qxk+q^2\right|\right) \tag{3.106d}$$

- **μ^4 terms**

$$
\begin{aligned}
1 \quad \to \quad & \int_{q_{IR}}^{q_{UV}} \mathrm{d}q \int_{-1}^{1} \mathrm{d}x\, P(q) P\left(|\mathbf{k}-\mathbf{q}|\right) \frac{1}{1024\pi^2 q^2 \left|k^2-2kqx+q^2\right|^2} \times \\
& \times \Big[3f^4 g^4 \left(\left|k^2-2qxk+q^2\right|^2 - 2\left(k^2+q^2\right)\left|k^2-2qxk+q^2\right| + \left(k^2-q^2\right)^2 \right)^2 \\
& + 16 f^2 g^2 \left(\left|k^2-2qxk+q^2\right|^2 - 2\left(k^2+q^2\right)\left|k^2-2qxk+q^2\right| + \left(k^2-q^2\right)^2 \right) \times \\
& \quad \times \Big(\left|k^2-2qxk+q^2\right| \Big(-(D_K+D_L)\left|k^2-2qxk+q^2\right| \\
& \qquad + k^2 D_K + 2q^2(D_K+D_L) \Big) + k^4 D_L + k^2 q^2 D_K - q^4(D_K+D_L) \Big) \\
& + 128 k^4 q^2 \left(kx(D_K+2D_L) - 2qx^2(D_K+D_L) + D_K q \right)^2 \Big]
\end{aligned}
\tag{3.107a}
$$

$$
\begin{aligned}
b_1^{(1)} \quad \to \quad & f D^2 \int_{q_{IR}}^{q_{UV}} \mathrm{d}q \int_{-1}^{1} \mathrm{d}x\, P(q) P\left(|\mathbf{k}-\mathbf{q}|\right) \frac{1}{32\pi^2 q^2 \left|k^2-2qxk+q^2\right|^2} \times \\
& \times \Big(\left|k^2-2qxk+q^2\right|^3 \left(f^2 g^2 \left(7k^2+9q^2\right) + 4(D_K+L)\left(k^2-2kqx+q^2\right) \right) \\
& - 3 f^2 g^2 \left|k^2-2qxk+q^2\right|^4 - \left|k^2-2qxk+q^2\right|^2 \Big(f^2 g^2 \left(5k^4+2k^2q^2+9q^4\right) \\
& \quad + 4\left(k^2-2kqx+q^2\right)\left(k^2(2D_K+L)+3q^2(D_K+L)\right) \Big) \\
& \quad + \left|k^2-2qxk+q^2\right| \Big(f^2 g^2 \left(k^2+3q^2\right)\left(k^2-q^2\right)^2 \\
& \quad + 4\left|k^2-2kqx+q^2\right| \left(k^4(D_K-L) + 2k^2q^2(D_K+L) + 3q^4(D_K+L) \right) \Big) \\
& \quad + 4\left(k^4-q^4\right)\left(k^2-2kqx+q^2\right)\left(k^2 L + q^2(D_K+L)\right) \Big)
\end{aligned}
\tag{3.107b}
$$

$$
\begin{aligned}
b_1^{(2)} \quad \to \quad & f^2 D^2 \int_{q_{IR}}^{q_{UV}} \mathrm{d}q \int_{-1}^{1} \mathrm{d}x\, P(q) P\left(|\mathbf{k}-\mathbf{q}|\right) \frac{1}{64\pi^2 q^2 \left|k^2-2qxk+q^2\right|^2} \times \\
& \times \Big(\Big(-3\left|k^2-2qxk+q^2\right| + 2k^2+6q^2 \Big) \left|k^2-2qk+q^2\right| + k^4 + 2k^2q^2 - 3q^4 \Big) \times \\
& \quad \times \Big[\left|k^2-2qxk+q^2\right| \Big(-(D_A+D_B)\left|k^2-2qxk+q^2\right| + 2q^2(D_A+D_B) + D_A k^2 \Big) \\
& \quad - q^4(D_A+D_B) + D_A k^2 q^2 + D_B k^4 \Big]
\end{aligned}
\tag{3.107c}
$$

$$
\begin{aligned}
b_2^{(2)} \quad \to \quad & f^2 D^4 \int_{q_{IR}}^{q_{UV}} \mathrm{d}q \int_{-1}^{1} \mathrm{d}x\, P(q) P\left(|\mathbf{k}-\mathbf{q}|\right) \frac{1}{32\pi^2 \left|k^2-2kqx+q^2\right|} \times \\
& \times \Big(\Big(-3\left|k^2-2qxk+q^2\right| + 2k^2+6q^2 \Big) \left|k^2-2qxk+q^2\right| + k^4 + 2k^2q^2 - 3q^4 \Big)
\end{aligned}
\tag{3.107d}
$$

$$
\begin{aligned}
b_{\mathcal{G}_2}^{(2)} \quad \to \quad & f^2 D^4 \int_{q_{IR}}^{q_{UV}} \mathrm{d}q \int_{-1}^{1} \mathrm{d}x\, P(q) P\left(|\mathbf{k}-\mathbf{q}|\right) \frac{\left((k-q)^2 - \left|k^2-2qxk+q^2\right|\right)}{64\pi^2 q^2 \left|k^2-2qxk+q^2\right|^2} \times \\
& \Big[\Big((k+q)^2 - \left|k^2-2qxk+q^2\right| \Big) \times \\
& \quad \times \Big(\Big(-3\left|k^2-2qxk+q^2\right| + 2k^2+6q^2 \Big) \left|k^2-2qxk+q^2\right| + k^4 + 2k^2q^2 - 3q^4 \Big) \Big]
\end{aligned}
\tag{3.107e}
$$

$$b_1^{(1)} b_1^{(1)} \quad \to \quad f^2 D^4 k \int_{q_{IR}}^{q_{UV}} \mathrm{d}q \int_{-1}^{1} \mathrm{d}x\, P(q) P\left(|\mathbf{k}-\mathbf{q}|\right) \frac{1}{32\pi^2 q^2 \left|k^2-2kqx+q^2\right|} \times$$
$$\times \Big[\Big|k^2-2qxk+q^2\Big| \Big(3(k-2qx)\Big|k^2-2qxk+q^2\Big| + 12qx\left(k^2+q^2\right)$$
$$- 2k\left(3k^2+5q^2\right)\Big) + 3k^5 - 6k^4qx + 6k^3q^2 - 4k^2q^3x + 7kq^4 - 6q^5x\Big] \tag{3.108a}$$

- **μ^6 terms**

$$1 \quad \to \quad f^2 D^2 \int_{q_{IR}}^{q_{UV}} \mathrm{d}q \int_{-1}^{1} \mathrm{d}x\, P(q) P\left(|\mathbf{k}-\mathbf{q}|\right) \frac{1}{512\pi^2 q^2 \left|k^2-2qxk+q^2\right|^2} \times$$
$$\times \Big[f^2 g^2 \Big(-15\Big|k^2-2qxk+q^2\Big|^4 + 12\left(3k^2+5q^2\right)\Big|k^2-2qxk+q^2\Big|^3$$
$$- 2\left(13k^4+18k^2q^2+45q^4\right)\Big|k^2-2qxk+q^2\Big|^2$$
$$+ 4\left(k^6+k^4q^2-9k^2q^4+15q^6\right)\Big|k^2-2qxk+q^2\Big| + \left(k^2-q^2\right)^2\left(k^4+6k^2q^2-15q^4\right)$$
$$+ 8\Big(-3\Big|k^2-2qxk+q^2\Big|^2 + 2\left(k^2+3q^2\right)\Big|k^2-2qxk+q^2\Big| + k^4+2k^2q^2-3q^4\Big)$$
$$\times \Big(-(D_K+D_L)\Big|k^2-2qxk+q^2\Big|^2 + \Big|k^2-2qxk+q^2\Big|\left(k^2D_K+2q^2(D_K+D_L)\right)$$
$$+ \left(k^2-q^2\right)\left(k^2D_L+q^2(D_K+D_L)\right)\Big)\Big] \tag{3.109a}$$

$$b_1^{(1)} \quad \to \quad f^3 D^4 \int_{q_{IR}}^{q_{UV}} \mathrm{d}q \int_{-1}^{1} \mathrm{d}x\, P(q) P\left(|\mathbf{k}-\mathbf{q}|\right) \frac{1}{32\pi^2 q^2 \left(k^2-2kqx+q^2\right)} \times$$
$$\times \Big[5\Big|k^2-2qxk+q^2\Big|^3 - 3\left(3k^2+5q^2\right)\Big|k^2-2qxk+q^2\Big|^2$$
$$+ 3\left(k^4+2k^2q^2+5q^4\right)\Big|k^2-2qxk+q^2\Big| + k^6+k^4q^2+3k^2q^4-5q^6\Big] \tag{3.109b}$$

- **μ^8 terms**

$$1 \quad \to \quad f^4 D^4 \int_{q_{IR}}^{q_{UV}} \mathrm{d}q \int_{-1}^{1} \mathrm{d}x\, P(q) P\left(|\mathbf{k}-\mathbf{q}|\right) \frac{1}{1024\pi^2 q^2 \left|k^2-2qxk+q^2\right|^2} \times$$
$$\times \Big[35\Big|k^2-2qxk+q^2\Big|^4 - 20\left(3k^2+7q^2\right)\Big|k^2-2qxk+q^2\Big|^3$$
$$+ 6\left(3k^4+10k^2q^2+35q^4\right)\Big|k^2-2qxk+q^2\Big|^2$$
$$+ 4\left(k^6+3k^4q^2+15k^2q^4-35q^6\right)\Big|k^2-2qxk+q^2\Big|$$
$$+ \left(k^2-q^2\right)^2\left(3k^4+10k^2q^2+35q^4\right)\Big] \tag{3.110a}$$

Advective terms

13-type integrals.—We would need the following integrands

$$I1_{13}(k,q,x) = D^2P(k)q^2P(q)\frac{kqx-q^2}{4\pi^2\left(k^2-2kqx+q^2\right)}\Big[\left(1-\frac{1}{2}x\left(\frac{k}{q}+\frac{q}{k}\right)\right)\left(D_Af_A-fg^2\right) + D_Bf_B\left(-\frac{x\left(k^2-2kqx+q^2\right)}{2kq}-\frac{1}{2}x\left(\frac{k}{q}+\frac{q}{k}\right)+1\right)\Big], \tag{3.111a}$$

$$I2_{13}(k,q,x) = D^4xP(k)\left(\frac{k}{q}+\frac{q}{k}\right)P(q)\frac{q^2-kqx}{4\pi^2}, \tag{3.111b}$$

$$I3_{13}(k,q,x) = D^2P(k)P(q)\frac{kqx-q^2}{\pi^2}\Big[D_A\left(1-\frac{1}{2}x\left(\frac{k}{q}+\frac{q}{k}\right)\right) + D_B\left(-\frac{x\left(k^2-2kqx+q^2\right)}{2kq}-\frac{1}{2}x\left(\frac{k}{q}+\frac{q}{k}\right)+1\right)\Big], \tag{3.111c}$$

$$I4_{13}(k,q,x) = D^4P(k)P(q)\frac{kqx-q^2}{2\pi^2}, \tag{3.111d}$$

$$I5_{13}(k,q,x) = D^4\left(x^2-1\right)P(k)P(q)\frac{kqx-q^2}{\pi^2}, \tag{3.111e}$$

$$I6_{13}(k,q,x) = fD^4P(k)\left[-\frac{k}{3q}\left(\frac{k}{q}+\frac{q}{k}\right)-1\right]P(q)\frac{q^2}{2\pi^2}. \tag{3.111f}$$

Then we list the different contributions according to the order in power of μ as well as to the combination of the different bias parameters

- **μ^0 terms**

$$b_1^{(1)}b_1^{(1)} \quad\to\quad \int_{q_{IR}}^{q_{UV}}\mathrm{d}q\int_{-1}^{1}\mathrm{d}x\,2\,\left(\frac{1}{f}I1_{13}(k,q,x)+I2_{13}(k,q,x)\right), \tag{3.112a}$$

$$b_1^{(1)}b_1^{(2)} \quad\to\quad \int_{q_{IR}}^{q_{UV}}\mathrm{d}q\int_{-1}^{1}\mathrm{d}x\,\left(-2I2_{13}(k,q,x)+I3_{13}(k,q,x)\right), \tag{3.112b}$$

$$b_1^{(1)}b_1^{(3)} \quad\to\quad \int_{q_{IR}}^{q_{UV}}\mathrm{d}q\int_{-1}^{1}\mathrm{d}x\,\left(\frac{2}{f}I1_{13}(k,q,x)+2I2_{13}(k,q,x)-I3_{13}(k,q,x)\right), \tag{3.112c}$$

$$b_1^{(1)}b_2^{(2)} \quad\to\quad \int_{q_{IR}}^{q_{UV}}\mathrm{d}q\int_{-1}^{1}\mathrm{d}x\,I4_{13}(k,q,x), \tag{3.112d}$$

$$b_1^{(1)}b_2^{(3)} \quad\to\quad -\int_{q_{IR}}^{q_{UV}}\mathrm{d}q\int_{-1}^{1}\mathrm{d}x\,I4_{13}(k,q,x), \tag{3.112e}$$

$$b_1^{(1)}b_{\mathcal{G}_2}^{(2)} \quad\to\quad \int_{q_{IR}}^{q_{UV}}\mathrm{d}q\int_{-1}^{1}\mathrm{d}x\,I5_{13}(k,q,x), \tag{3.112f}$$

$$b_1^{(1)}b_{\mathcal{G}_2}^{(3)} \quad\to\quad -\int_{q_{IR}}^{q_{UV}}\mathrm{d}q\int_{-1}^{1}\mathrm{d}x\,I5_{13}(k,q,x). \tag{3.112g}$$

- **μ^2 terms**

$$b_1^{(1)} \quad \to \quad \int_{q_{IR}}^{q_{UV}} \mathrm{d}q \int_{-1}^{1} \mathrm{d}x\, 2\, \left(I1_{13}(k,q,x) + fI2_{13}(k,q,x)\right), \tag{3.113a}$$

$$b_1^{(2)} \quad \to \quad \int_{q_{IR}}^{q_{UV}} \mathrm{d}q \int_{-1}^{1} \mathrm{d}x\, \left(-4fI2_{13}(k,q,x) + fI3_{13}(k,q,x)\right), \tag{3.113b}$$

$$b_1^{(3)} \quad \to \quad \int_{q_{IR}}^{q_{UV}} \mathrm{d}q \int_{-1}^{1} \mathrm{d}x\, \left(-2I1_{13}(k,q,x) + 2fI2_{13}(k,q,x) - fI3_{13}(k,q,x)\right), \tag{3.113c}$$

$$b_2^{(2)} \quad \to \quad \int_{q_{IR}}^{q_{UV}} \mathrm{d}q \int_{-1}^{1} \mathrm{d}x\, fI4_{13}(k,q,x), \tag{3.113d}$$

$$b_2^{(3)} \quad \to \quad -\int_{q_{IR}}^{q_{UV}} \mathrm{d}q \int_{-1}^{1} \mathrm{d}x\, fI4_{13}(k,q,x), \tag{3.113e}$$

$$b_{\mathcal{G}_2}^{(2)} \quad \to \quad \int_{q_{IR}}^{q_{UV}} \mathrm{d}q \int_{-1}^{1} \mathrm{d}x\, fI5_{13}(k,q,x), \tag{3.113f}$$

$$b_{\mathcal{G}_2}^{(3)} \quad \to \quad -\int_{q_{IR}}^{q_{UV}} \mathrm{d}q \int_{-1}^{1} \mathrm{d}x\, fI5_{13}(k,q,x), \tag{3.113g}$$

$$b_1^{(1)} b_1^{(1)} \quad \to \quad \int_{q_{IR}}^{q_{UV}} \mathrm{d}q \int_{-1}^{1} \mathrm{d}x\, I6_{13}(k,q,x), \tag{3.113h}$$

$$b_1^{(1)} b_1^{(2)} \quad \to \quad -\int_{q_{IR}}^{q_{UV}} \mathrm{d}q \int_{-1}^{1} \mathrm{d}x\, I6_{13}(k,q,x). \tag{3.113i}$$

- **μ^4 terms**

$$b_1^{(1)} \quad \to \quad \int_{q_{IR}}^{q_{UV}} \mathrm{d}q \int_{-1}^{1} \mathrm{d}x\, fI6_{13}(k,q,x), \tag{3.114a}$$

$$b_1^{(2)} \quad \to \quad -\int_{q_{IR}}^{q_{UV}} \mathrm{d}q \int_{-1}^{1} \mathrm{d}x f\, I6_{13}(k,q,x). \tag{3.114b}$$

22-type integrals.—We define the following integrands

$$I1_{22}(k,q,x) = D^4 P(q) P\left(|\mathbf{k}-\mathbf{q}|\right) \frac{\left(\left|k^2-2qxk+q^2\right|+q^2\right)\left(\left|k^2-2qxk+q^2\right|-k^2+q^2\right)^2}{16\pi^2 q^2\left|k^2-2qxk+q^2\right|} \tag{3.115a}$$

$$I2_{22}(k,q,x) = -D^2 k^2 P(q) P\left(|\mathbf{k}-\mathbf{q}|\right) \frac{(q-kx)\left(D_A\left(kx-2qx^2+q\right)+2D_B x(k-qx)\right)}{2\pi^2\left(k^2-2kqx+q^2\right)} \tag{3.115b}$$

$$I3_{22}(k,q,x) = -D^4 q P(q) P\left(|\mathbf{k}-\mathbf{q}|\right) \frac{(q-kx)}{2\pi^2} \tag{3.115c}$$

$$I4_{22}(k,q,x) = D^4 k^2 P(q) P\left(|\mathbf{k}-\mathbf{q}|\right) \frac{q\left(x^2-1\right)(kx-q)}{\pi^2\left(k^2-2kqx+q^2\right)} \tag{3.115d}$$

$$I5_{22}(k,q,x) = -D^2 k^2 P(q) P\left(|\mathbf{k}-\mathbf{q}|\right) \frac{(q-kx)\left(D_K\left(kx-2qx^2+q\right)+2D_L x(k-qx)\right)}{2\pi^2\left(k^2-2kqx+q^2\right)} \tag{3.115e}$$

$$\begin{aligned} I6_{22}(k,q,x) = {} & f^2 D^4 P(q) P\left(|\mathbf{k}-\mathbf{q}|\right) \Big[\frac{\left(k^2-q^2\right)^3}{32\pi^2 q^2\left|k^2-2qxk+q^2\right|}+ \\ & + \frac{-\left|k^2-2qxk+q^2\right|^2+\left(3k^2+q^2\right)\left|k^2-2qxk+q^2\right|+\left(-3k^4+2k^2q^2+q^4\right)}{32\pi^2 q^2}\Big] \end{aligned} \tag{3.115f}$$

$$\begin{aligned} I7_{22}(k,q,x) = {} & f^2 D^4 P(q) P\left(|\mathbf{k}-\mathbf{q}|\right) \Big[\frac{\left(k^2-q^2\right)^2\left(k^2+3q^2\right)}{32\pi^2 q^2\left|k^2-2qxk+q^2\right|}+ \\ & + \frac{3\left|k^2-2qxk+q^2\right|^2-\left(5k^2+3q^2\right)\left|k^2-2qxk+q^2\right|+\left(k^4+2k^2q^2-3q^4\right)}{32\pi^2 q^2} \end{aligned} \tag{3.115g}$$

$$\begin{aligned} I8_{22}(k,q,x) = {} & f D^4 k P(q) P\left(|\mathbf{k}-\mathbf{q}|\right) \frac{\left(-\left|k^2-2qxk+q^2\right|+k^2-q^2\right)}{8\pi^2 q^2}\times \\ & \times\Big[-(k-2qx)+\frac{(k^2+q^2)(k-2qx)+2kq^2}{\left|k^2-2qxk+q^2\right|}\Big] \end{aligned} \tag{3.115h}$$

Then we list the different contributions according to the order in power of μ as well as to the combination of the different bias parameters

- **μ^0 terms**

$$b_1^{(1)}b_1^{(1)} \quad \to \quad \int_{q_{IR}}^{q_{UV}} \mathrm{d}q \int_{-1}^{1} \mathrm{d}x\, I1_{22}(k,q,x), \tag{3.116a}$$

$$b_1^{(1)}b_1^{(2)} \quad \to \quad \int_{q_{IR}}^{q_{UV}} \mathrm{d}q \int_{-1}^{1} \mathrm{d}x\, \left(-2I1_{22}(k,q,x) + I2_{22}(k,q,x)\right), \tag{3.116b}$$

$$b_1^{(1)}b_2^{(2)} \quad \to \quad \int_{q_{IR}}^{q_{UV}} \mathrm{d}q \int_{-1}^{1} \mathrm{d}x\, I3_{22}(k,q,x), \tag{3.116c}$$

$$b_1^{(1)}b_{\mathcal{G}_2}^{(2)} \quad \to \quad \int_{q_{IR}}^{q_{UV}} \mathrm{d}q \int_{-1}^{1} \mathrm{d}x\, I4_{22}(k,q,x), \tag{3.116d}$$

$$b_1^{(2)}b_1^{(2)} \quad \to \quad \int_{q_{IR}}^{q_{UV}} \mathrm{d}q \int_{-1}^{1} \mathrm{d}x\, \left(I1_{22}(k,q,x) - I2_{22}(k,q,x)\right), \tag{3.116e}$$

$$b_1^{(1)}b_2^{(2)} \quad \to \quad -\int_{q_{IR}}^{q_{UV}} \mathrm{d}q \int_{-1}^{1} \mathrm{d}x\, I3_{22}(k,q,x), \tag{3.116f}$$

$$b_1^{(2)}b_{\mathcal{G}_2}^{(2)} \quad \to \quad -\int_{q_{IR}}^{q_{UV}} \mathrm{d}q \int_{-1}^{1} \mathrm{d}x\, I4_{22}(k,q,x). \tag{3.116g}$$

- **μ^2 terms**

$$b_1^{(1)} \quad \to \quad \int_{q_{IR}}^{q_{UV}} \mathrm{d}q \int_{-1}^{1} \mathrm{d}x\, \left(I5_{22}(k,q,x) + I6_{22}(k,q,x)\right), \tag{3.117a}$$

$$b_1^{(2)} \quad \to \quad -\int_{q_{IR}}^{q_{UV}} \mathrm{d}q \int_{-1}^{1} \mathrm{d}x\, \left(I5_{22}(k,q,x) + I6_{22}(k,q,x)\right), \tag{3.117b}$$

$$b_1^{(1)}b_1^{(1)} \quad \to \quad \int_{q_{IR}}^{q_{UV}} \mathrm{d}q \int_{-1}^{1} \mathrm{d}x\, I8_{22}(k,q,x), \tag{3.117c}$$

$$b_1^{(1)}b_1^{(2)} \quad \to \quad -\int_{q_{IR}}^{q_{UV}} \mathrm{d}q \int_{-1}^{1} \mathrm{d}x\, I8_{22}(k,q,x). \tag{3.117d}$$

- **μ^4 terms**

$$b_1^{(1)} \quad \to \quad \int_{q_{IR}}^{q_{UV}} \mathrm{d}q \int_{-1}^{1} \mathrm{d}x\, I7_{22}(k,q,x), \tag{3.118a}$$

$$b_1^{(2)} \quad \to \quad -\int_{q_{IR}}^{q_{UV}} \mathrm{d}q \int_{-1}^{1} \mathrm{d}x f\, I7_{22}(k,q,x). \tag{3.118b}$$

Chapter 4

Conclusions and outlook

Progress in cosmology comes from the union between a robust theoretical machinery and a technological development associated with observation and probe of the heavens. Along these lines, modern cosmology — in particular, the field of large-scale structure — truly is living a golden age with the most sophisticated theories and the largest number of observational projects in the history of cosmology. My research presented in this thesis is certainly relevant in the study of galaxy clustering, dealing with the adversities present in well-established theoretical frameworks, as well as shedding light on the challenging task of model choice on the observational side. It is well-understood how large-scale surveys observe the distribution of tracers across the universe on different patches of the sky and infer their distance from redshift measurements in their spectra. Furthermore, the existent tight relationship between the distribution of such observed tracers and the underlying dark matter distribution becomes of the utmost importance. Bearing all these ingredients in mind, the machinery constructed throughout this work became complex but more assertive than others in the literature.

As a first step in chapter 2, my work addressed the fact that standard perturbation theory is not sufficient to predict the non-linear behaviour of the matter power spectrum at small scales. Within the standard framework, the equations describing matter perturbations seem inaccurate because the description of dark matter as a perfect fluid only holds on large scales. On smaller scales, the evolution of the long-wavelength modes are significantly affected by short-wavelength modes — ultra-violet physics. Such effect cannot be accurately predicted within the standard theory and enters as the divergence of an effective stress-energy tensor. Borrowing the effective field theory framework from particle physics, we obtained the most general form of the effective stress-energy tensor

as a controlled expansion in terms of powers and derivatives of the long-wavelength fields. Therefore, the ultra-violet divergences are encoded in a set of time-dependent couplings, or counter-terms, which we fit to the CAMB halofit power spectrum. In addition, as mentioned above, surveys estimate the real distance to an object by employing its redshift. However, the random motions of galaxies within clusters are unknown and produce a systematic distortion of the field distribution. Considering such effect, we computed the matter power spectrum in redshift space, including redshift space distortions, and obtaining the different multipoles as a result of a Legendre decomposition.

Notwithstanding the flexibility of the effective field theory, it appears unable to properly adjust the effect of baryon acoustic oscillations. In other words, the theoretical predictions show an oscillatory residual comparing to simulations. These residuals are due to insufficient treatment of the baryon acoustic oscillations. In order to compensate for this inaccuracy, we used the Vlah et al. re-summation scheme, showing the significant effect on the multipole matter power spectra. Our final analysis employs a custom suit of N-body simulations — obtained from the **gevolution** numerical relativity code — in order to fit the re-normalisation factors, or counter-terms. We found that the re-summed redshift-space matter power spectrum within the effective field theory framework is far more capable of adjusting our set of simulations at scales within the mild non-linear regime — scales visible by the current and future large-scale surveys.

The main achievements and innovations derived from chapter 2 are:

- We write the explicit time dependence of the redshift-space matter power spectrum within standard perturbation.
- We compare our results from the full time-dependent effective field theory with that of de Sitter approximation, concluding that the latter is a competent approximation for the real-space matter power spectrum and the monopole power spectrum in redshift space.
- We also find that our results are in good agreements with [165, 116, 148].
- For $z = 0$ and a MultiDark MDR1 cosmology, the real-space matter power spectrum and the monopole in redshift space are matched within five percent using the leading counter-term up to scales $\lesssim 0.4h/\mathrm{Mpc}$. Moreover, this limit can be pushed further up to $k \lesssim 0.74h/\mathrm{Mpc}$ where the monopole becomes non positive. These upper limit

on the range of k is comparable to those of Perko et al. [148] and Taruya et al. [178]; but larger than Lewandowski et al.[116].

- We use a new method based on the Rayleigh plane-wave expansion to decompose the relevant tensor integrals at one-loop and to extract their μ dependence.

- We extend the Vlah et al. re-summation scheme [188] to redshift space, simplifying the Senatore et al. [166] re-summation scheme.

Finally in chapter 3, leaning on our previous results, we considered bias modelling and we addressed the question of the appropriate level of modelling sophistication for analysis of galaxy surveys. Furthermore, such surveys do not measure spatial configuration, but they inferred the radial distance to an object from its redshift, we considered that redshift-space effects — such as redshift-space distortions and finger-of-god suppression— also need to be modelled carefully. Then we reviewed the most representative models to account for biasing — linear bias, McDonald & Roy , Co-evolution and the advective bias — and to predict the redshift-space power spectrum — Kaiser Tree level, Kaiser **HALOFIT**, one-loop standard perturbation and one-loop effective field theory — with varying motivations: some empirical and some motivated by theoretical aspects such as consistency of loop order in the description of clustering and redshift-space effects. Then we studied whether the modelling burden due to accounting for all different effects is justified. We determined for each combination of bias and redshift-space model the goodness-of-fit to an ensemble of COLA-accelerated N-body simulations — from the **WizCOLA** set of simulations, constructed from real WiggleZ data and accounting for measurement error, survey geometry, imcompleteness and uncertainties due to the use of spectroscopic redshifts. Then we contrasted the different fits to the ensemble average over the full set of **WizCOLA** realisations in order to identify signs of overfitting — meaning, the fit per realisation is sufficiently permissive that it can adjust to match realisation variance. Therefore, the main achievements of this chapter 3 are summarised here:

- We study the relative performance of every combination of bias plus redshift-space model, quantified in units of χ^2.

- We use the Bayesian information criterion to compensate for the number of free parameters involved in each model.

- We use a ranking by improvement in the Bayesian information criterion to identify which modelling choices show the best balance between flexibility — to capture the true shape of the power spectrum — and rigidity — to prevent overfitting.

The main conclusions drawn from this work 3 are:

- Regarding the redshift-space power spectrum: the most complex model (the effective field theory) can successfully match the broadband spectral slope produced by the **WizCOLA** realisations at both large and small scales. This cannot be done by the standard perturbation theory which lacks of the re-normalisation factors which provide enough flexibility to do so.

  In addition, we find that although the effective field theory is able to accommodate separate suppression scales for the different multipoles of the power spectrum, the **WizCOLA** realisations do not make use of this freedom, at least up to $k_{\rm max} = 0.29h/\mathrm{Mpc}$. Conversely, the standard perturbation model, including non-linear redshift-space structure but only a common suppression scale for the multipoles, seems likely to represent a good compromise for present-day near-future surveys with $k_{\rm max} \simeq 0.3h/\mathrm{Mpc}$.

- Regarding bias models: the bottom line is that our results do not show a preference for complex bias modelling. However, the BIC prioritizes the simplest non-linear model: the co-evolution model.

- A striking conclusion from our results is that improvements in modelling are not likely to lead to a significant decrease in the overall chi-squared fit to a simulation suite. Besides, since all our models fit the BAO variability equally badly, this conclusion seems unlikely to be altered even in a larger survey where the BAO feature is better resolved.

- We see some evidence for overfitting from the most permissive models, the EFT model for the power spectrum and the Advective model for the bias, although we require a larger sample size to resolve the shape of the distribution with more certainty.

- We have also cross-checked our analysis having two different pipelines for the theoretical predictions and likelihood analysis, coming to the conclusion that the apparent spread in the final chi-square values comes from the use of different implementations of the same formalism.

In spite of the success of the analyses carried out in chapters 2 and 3, several questions still remain, namely

- The full time-dependence of the counter-terms, without which the formalism becomes less predictive.
- A workaround to the model-by-model renormalisation since counter-terms seem to vary even between nearby cosmologies.
- The use of the effective field theory methods to ease the costly numerical estimation of measurements in redshift space.
- The quantification of the impact of baryon acoustic oscillations on the improvement of the likelihood for different bias models.

Bibliography

[1] G. Aad et al. The ATLAS Experiment at the CERN Large Hadron Collider. *JINST*, 3:S08003, 2008. 4

[2] Julian Adamek, David Daverio, Ruth Durrer, and Martin Kunz. General relativity and cosmic structure formation. *Nature Phys.*, 12:346–349, 2016. 75

[3] J. C. Adams. On the Expression of the Product of Any Two Legendre's Coefficients by Means of a Series of Legendre's Coefficients. *Proc. Roy. Soc.*, 27, 1878. 64

[4] P. A. R. Ade et al. Planck 2015 results. XIII. Cosmological parameters. *Astron. Astrophys.*, 594:A13, 2016. 37, 38, 57, 101, 147

[5] H AKAIKE. Information theory and an extension of the maximum likelihood principle. *Petrox, B.N., Caski, F. (Eds.)*, 27:267, 1973. 128

[6] Raul Angulo, Matteo Fasiello, Leonardo Senatore, and Zvonimir Vlah. On the Statistics of Biased Tracers in the Effective Field Theory of Large Scale Structures. *JCAP*, 1509(09):029, 2015. 107, 148

[7] Valentin Assassi, Daniel Baumann, Daniel Green, and Matias Zaldarriaga. Renormalized Halo Bias. *JCAP*, 1408:056, 2014. 29, 109, 148

[8] W. N. Bailey. On the product of two Legendre polynomials. *Mathematical Proceedings of the Cambridge Philosophical Society*, 29(2):173–177, 005 1933. 64

[9] W. N. Bailey. Some infinite integrals involving Bessel functions. *Proceedings of the London Mathematical Society*, s2-40(1):37–48, 1936. 30

[10] Tobias Baldauf, Mehrdad Mirbabayi, Marko Simonović, and Matias Zaldarriaga. Equivalence Principle and the Baryon Acoustic Peak. *Phys. Rev.*, D92(4):043514, 2015. 51

[11] Daniel Baumann, Alberto Nicolis, Leonardo Senatore, and Matias Zaldarriaga. Cosmological Non-Linearities as an Effective Fluid. *JCAP*, 1207:051, 2012. 20, 28, 30, 32, 43, 44, 48, 86, 106

[12] C. Bebeck and collaborators. DESI design report. page 750, 2016. 4, 104

[13] F. Bernardeau, S. Colombi, E. Gaztanaga, and R. Scoccimarro. Large scale structure of the universe and cosmological perturbation theory. *Phys. Rept.*, 367:1–248, 2002. 3, 18, 28, 112, 119, 123

[14] J.M. Bernardo and A.F.M. Smith. *Bayesian Theory*. Wiley, 2000. 129

[15] Daniele Bertacca, Alvise Raccanelli, Nicola Bartolo, Michele Liguori, Sabino Matarrese, and Licia Verde. Relativistic wide-angle galaxy bispectrum on the light-cone. *Phys. Rev.*, D97(2):023531, 2018. 126

[16] Daniele Bertolini, Katelin Schutz, Mikhail P. Solon, Jonathan R. Walsh, and Kathryn M. Zurek. Non-Gaussian Covariance of the Matter Power Spectrum in the Effective Field Theory of Large Scale Structure. *Phys. Rev.*, D93(12):123505, 2016. 93

[17] Edmund Bertschinger and Bhuvnesh Jain. Gravitational instability of cold matter. *Astrophys. J.*, 431:486, 1994. 28

[18] Florian Beutler et al. The clustering of galaxies in the SDSS-III Baryon Oscillation Spectroscopic Survey: Testing gravity with redshift-space distortions using the power spectrum multipoles. *Mon. Not. Roy. Astron. Soc.*, 443(2):1065–1089, 2014. 72

[19] Florian Beutler et al. The clustering of galaxies in the completed SDSS-III Baryon Oscillation Spectroscopic Survey: Anisotropic galaxy clustering in Fourier-space. *Mon. Not. Roy. Astron. Soc.*, 466(2):2242–2260, 2017. 105

[20] Chris Blake, Sarah Brough, Matthew Colless, Carlos Contreras, Warrick Couch, Scott Croom, Tamara Davis, Michael J. Drinkwater, Karl Forster, David Gilbank, Mike Gladders, Karl Glazebrook, Ben Jelliffe, Russell J. Jurek, I-hui Li, Barry Madore, D. Christopher Martin, Kevin Pimbblet, Gregory B. Poole, Michael Pracy, Rob Sharp, Emily Wisnioski, David Woods, Ted K. Wyder, and H. K. C. Yee. The wigglez dark energy survey: the growth rate of cosmic structure since redshift z=0.9. *Monthly Notices of the Royal Astronomical Society*, 415(3):2876–2891, 2011. 127

[21] Chris Blake et al. The WiggleZ Dark Energy Survey: mapping the distance-redshift relation with baryon acoustic oscillations. *Mon. Not. Roy. Astron. Soc.*, 418:1707–1724, 2011. 126

[22] Chris Blake et al. The WiggleZ Dark Energy Survey: the growth rate of cosmic structure since redshift z=0.9. *Mon. Not. Roy. Astron. Soc.*, 415:2876, 2011. 72

[23] Diego Blas, Mathias Garny, Mikhail M. Ivanov, and Sergey Sibiryakov. Time-Sliced Perturbation Theory II: Baryon Acoustic Oscillations and Infrared Resummation. *JCAP*, 1607(07):028, 2016. 51

[24] J. R. Bond and H. M. P. Couchman. $w_{gg}(\theta)$ as a probe of large scale structure. In A. Coley, C. Dyer, and T. Tupper, editors, *Proceedings of the 2nd Canadian Conference on General Relativity and Relativistic Astrophysics*, pages 385–389, 1988. 50

[25] F. R. Bouchet, S. Colombi, E. Hivon, and R. Juszkiewicz. Perturbative Lagrangian approach to gravitational instability. *Astron. Astrophys.*, 296:575, 1995. 112

[26] Clare Burrage, David Parkinson, and David Seery. Beyond the growth rate of cosmic structure: Testing modified gravity models with an extra degree of freedom. 2015. 55

[27] A. O. Caldeira and A. J. Leggett. Influence of dissipation on quantum tunneling in macroscopic systems. *Phys. Rev. Lett.*, 46:211, 1981. 44

[28] A. O. Caldeira and A. J. Leggett. Path integral approach to quantum Brownian motion. *Physica*, 121A:587–616, 1983. 44

[29] A. O. Caldeira and A. J. Leggett. Quantum tunneling in a dissipative system. *Annals Phys.*, 149:374–456, 1983. 44

[30] E. Calzetta and B-L. Hu. Stochastic behavior of effective field theories across threshold. *Phys. Rev.*, D55:3536–3551, 1997. 44

[31] Esteban Calzetta and B. L. Hu. Stochastic dynamics of correlations in quantum field theory: From Schwinger-Dyson to Boltzmann-Langevin equation. *Phys. Rev.*, D61:025012, 2000. 44

[32] John Joseph M. Carrasco, Simon Foreman, Daniel Green, and Leonardo Senatore. The 2-loop matter power spectrum and the IR-safe integrand. *JCAP*, 1407:056, 2014. 40

[33] John Joseph M. Carrasco, Simon Foreman, Daniel Green, and Leonardo Senatore. The Effective Field Theory of Large Scale Structures at Two Loops. *JCAP*, 1407:057, 2014. 20, 28, 30, 32, 48, 54, 55, 106, 116

[34] John Joseph M. Carrasco, Mark P. Hertzberg, and Leonardo Senatore. The Effective Field Theory of Cosmological Large Scale Structures. *JHEP*, 09:082, 2012. 20, 28, 30, 32, 48, 54, 55, 89, 106, 116

[35] Sean M. Carroll, Stefan Leichenauer, and Jason Pollack. Consistent effective theory of long-wavelength cosmological perturbations. *Phys. Rev.*, D90(2):023518, 2014. 43, 86

[36] Matteo Cataneo, Simon Foreman, and Leonardo Senatore. Efficient exploration of cosmology dependence in the EFT of LSS. 2016. 79, 93, 147

[37] Kwan Chuen Chan, Roman Scoccimarro, and Ravi K. Sheth. Gravity and Large-Scale Non-local Bias. *Phys. Rev.*, D85:083509, 2012. 25, 105, 110, 111, 148

[38] Clifford Cheung, Paolo Creminelli, A. Liam Fitzpatrick, Jared Kaplan, and Leonardo Senatore. The Effective Field Theory of Inflation. *JHEP*, 03:014, 2008. 21

[39] Alison L. Coil. Large Scale Structure of the Universe. 2012. 1

[40] Shaun Cole, Karl B. Fisher, and David H. Weinberg. Fourier analysis of redshift space distortions and the determination of Ω. *Mon. Not. Roy. Astron. Soc.*, 267:785, 1994. 58, 71, 84, 85, 106, 114

[41] M. Colless et al. The 2dF Galaxy Redshift Survey: Spectra and redshifts. *Mon. Not. Roy. Astron. Soc.*, 328:1039, 2001. 3

[42] John C. Collins. *Renormalization*, volume 26 of *Cambridge Monographs on Mathematical Physics*. Cambridge University Press, Cambridge, 1986. 47

[43] Martin Crocce and Roman Scoccimarro. Memory of initial conditions in gravitational clustering. *Phys. Rev.*, D73:063520, 2006. 54

[44] Martin Crocce and Roman Scoccimarro. Nonlinear Evolution of Baryon Acoustic Oscillations. *Phys. Rev.*, D77:023533, 2008. 54

[45] H. Curtis. Modern theories of the spiral nebulae. *JRASC*, 14:317, 1920. 2

[46] Efstathiou G. Frenk C. & White D. Davis, M. *ApJ*, 292:371, 1985. 25, 123

[47] Huchra J. Latham D. & Tonry J. Davis, M. *ApJ*, 253:423, 1982. 3

[48] Roelof S. de Jong et al. 4MOST - 4-metre Multi-Object Spectroscopic Telescope. *Proc. SPIE Int. Soc. Opt. Eng.*, 8446:84460T, 2012. 4, 104

[49] Lucía Fonseca de la Bella, Donough Regan, David Seery, and Shaun Hotchkiss. The matter power spectrum in redshift space using effective field theory. *JCAP*, 1711(11):039, 2017. 18, 19, 23, 106, 114, 120, 123, 151, 155

[50] S. de la Torre et al. The VIMOS Public Extragalactic Redshift Survey (VIPERS). Gravity test from the combination of redshift-space distortions and galaxy-galaxy lensing at $0.5 < z < 1.2$. *Astron. Astrophys.*, 608:A44, 2017. 105

[51] Vincent Desjacques, Donghui Jeong, and Fabian Schmidt. Large-Scale Galaxy Bias. 2016. 24, 104

[52] Mafalda Dias, Jonathan Frazer, David J. Mulryne, and David Seery. Numerical evaluation of the bispectrum in multiple field inflation—the transport approach with code. *JCAP*, 1612(12):033, 2016. 100

[53] John F. Donoghue. General relativity as an effective field theory: The leading quantum corrections. *Phys. Rev.*, D50:3874–3888, 1994. 42

[54] John F. Donoghue. Introduction to the effective field theory description of gravity. In *Advanced School on Effective Theories Almunecar, Spain, June 25-July 1, 1995*, 1995. 42

[55] M. J. Drinkwater, R. J. Jurek, C. Blake, D. Woods, K. A. Pimbblet, K. Glazebrook, R. Sharp, M. B. Pracy, S. Brough, M. Colless, W. J. Couch, S. M. Croom, T. M. Davis, D. Forbes, K. Forster, D. G. Gilbank, M. Gladders, B. Jelliffe, N. Jones, I.-H. Li, B. Madore, D. C. Martin, G. B. Poole, T. Small, E. Wisnioski, T. Wyder, and H. K. C. Yee. The WiggleZ Dark Energy Survey: survey design and first data release. *MNRAS*, 401:1429–1452, January 2010. 126

[56] A. Einstein. Cosmological considerations in the general theory of relativity. *Sitzungsber. Preuss. Akad. Wiss. Berlin (Math. Phys.)*, 1917:142–152, 1917. 2

[57] Albert Einstein and Willem de Sitter. On the relation between the expansion and the mean density of the universe. 18(3):213–214, 1932. 18, 19

[58] Daniel J. Eisenstein et al. Detection of the Baryon Acoustic Peak in the Large-Scale Correlation Function of SDSS Luminous Red Galaxies. *Astrophys. J.*, 633:560–574, 2005. 15

[59] Daniel J. Eisenstein and Wayne Hu. Power spectra for cold dark matter and its variants. *Astrophys. J.*, 511:5, 1997. 51

[60] Daniel J. Eisenstein, Hee-jong Seo, Edwin Sirko, and David Spergel. Improving Cosmological Distance Measurements by Reconstruction of the Baryon Acoustic Peak. *Astrophys. J.*, 664:675–679, 2007. 54

[61] Daniel J. Eisenstein, Hee-jong Seo, and Martin J. White. On the Robustness of the Acoustic Scale in the Low-Redshift Clustering of Matter. *Astrophys. J.*, 664:660–674, 2007. 54

[62] V Fabrikant. Elementary exact evaluation of infinite integrals of the product of several spherical Bessel functions, power and exponential. *Quarterly of Applied Mathematics*, 71(3):573–581, 2013. 30, 63, 97, 156

[63] Valery I Fabrikant. Computation of infinite integrals involving three Bessel functions by introduction of new formalism. *ZAMM-Journal of Applied Mathematics and Mechanics/Zeitschrift für Angewandte Mathematik und Mechanik*, 83(6):363–374, 2003. 97

[64] VI Fabrikant and Georges Dôme. Elementary evaluation of certain infinite integrals involving Bessel functions. *Quarterly of Applied Mathematics*, 59(1):1–24, 2001. 97

[65] Xiao Fang, Jonathan A. Blazek, Joseph E. McEwen, and Christopher M. Hirata. FAST-PT II: an algorithm to calculate convolution integrals of general tensor quantities in cosmological perturbation theory. *JCAP*, 1702(02):030, 2017. 64

[66] Matteo Fasiello and Zvonimir Vlah. Nonlinear fields in generalized cosmologies. *Phys. Rev.*, D94(6):063516, 2016. 106

[67] R. P. Feynman and F. L. Vernon, Jr. The Theory of a general quantum system interacting with a linear dissipative system. *Annals Phys.*, 24:118–173, 1963. [Annals Phys.281,547(2000)]. 44

[68] A. Friedmann. Über die Krümmung de Raumes. *Zeitschrift fur Physik*, 10:377–386, 1922. 2

[69] James N. Fry. The Galaxy correlation hierarchy in perturbation theory. *Astrophys. J.*, 279:499–510, 1984. 28, 33, 105

[70] Florian Fuhrer and Gerasimos Rigopoulos. Renormalizing a Viscous Fluid Model for Large Scale Structure Formation. *JCAP*, 1602(02):032, 2016. 43, 86

[71] Tomohiro Fujita, Valentin Mauerhofer, Leonardo Senatore, Zvonimir Vlah, and Raul Angulo. Very Massive Tracers and Higher Derivative Biases. 2016. 107

[72] Mark Galassi et al. GNU Scientific Library Reference Manual (3rd Ed.). `http://savannah.gnu.org/projects/gsl`. 101

[73] A. Gervois and H. Navelet. Some integrals involving three Bessel functions when their arguments satisfy the triangle inequalities. *Journal of Mathematical Physics*, 25(11):3350–3356, 1984. 97

[74] A. Gervois and H. Navelet. Infinite integrals involving three spherical Bessel functions. *SIAM Journal on Mathematical Analysis*, 20(4):1006–1018, 1989. 30, 63, 97, 98, 156

[75] Héctor Gil-Marín, Will J. Percival, Licia Verde, Joel R. Brownstein, Chia-Hsun Chuang, Francisco-Shu Kitaura, Sergio A. Rodríguez-Torres, and Matthew D. Olmstead. The clustering of galaxies in the SDSS-III Baryon Oscillation Spectroscopic Survey: RSD measurement from the power spectrum and bispectrum of the DR12 BOSS galaxies. *Mon. Not. Roy. Astron. Soc.*, 465(2):1757–1788, 2017. 105

[76] Gleyzes, Jérôme and de Putter, Roland and Green, Daniel and Doré, Olivier. Biasing and the search for primordial non-Gaussianity beyond the local type. 2016. 29

[77] M. H. Goroff, Benjamin Grinstein, S. J. Rey, and Mark B. Wise. Coupling of Modes of Cosmological Mass Density Fluctuations. *Astrophys. J.*, 311:6–14, 1986. 28, 37, 42, 45, 46, 105

[78] Dickinson M. & Melott A. J. Gott, J. *ApJ*, 306:341, 1986. 3

[79] L. Gregory, S. & Thompson. *APJ*, 222:784, 1978. 3

[80] Bjarne Grimstad et al. SPLINTER: a library for multivariate function approximation with splines. `http://github.com/bgrimstad/splinter`, 2015. Accessed: 2016-03-20. 100

[81] E. J. Groth and P. J. E. Peebles. Closed-form solutions for the evolution of density perturbations in some cosmological models. *Astron. Astrophys.*, 41:143–145, June 1975. 35

[82] Giulia Gubitosi, Federico Piazza, and Filippo Vernizzi. The Effective Field Theory of Dark Energy. *JCAP*, 1302:032, 2013. [JCAP1302,032(2013)]. 21

[83] T. Hahn. CUBA: A Library for multidimensional numerical integration. *Comput. Phys. Commun.*, 168:78–95, 2005. 100

[84] A. F. Heavens, S. Matarrese, and Licia Verde. The Nonlinear redshift-space power spectrum of galaxies. *Mon. Not. Roy. Astron. Soc.*, 301:797–808, 1998. 59, 115

[85] W. Herschel. On the construction of the Heavens. *Royal Society of London Philosophical Transactions*, I:76,457, 1785. 1

[86] Mark P. Hertzberg. Effective field theory of dark matter and structure formation: Semianalytical results. *Phys. Rev.*, D89(4):043521, 2014. 88

[87] A. Hitchin, N. & Walker. Biographical memoirs of fellows of the Royal Society. 52:413–421, 2006. 2, 6, 9

[88] E. Hubble. Extragalactic nebulae. *APJ*, 64, 1926. 2

[89] E. Hubble. Relation between distance and radial velocity among extra-galactic nebulae. *Proceedings of the National Academy of Science*, 15:168–173, 1929. 11

[90] E. Hubble. *APJ*, 79:8, 1934. 2

[91] C. Itzykson and J. B. Zuber. *Quantum Field Theory*. International Series In Pure and Applied Physics. McGraw-Hill, New York, 1980. 46, 47

[92] J. C. Jackson. Fingers of God: A critique of Rees' theory of primoridal gravitational radiation. *Mon. Not. Roy. Astron. Soc.*, 156:1P–5P, 1972. 29, 106

[93] J. H. Jeans. On the theory of star-streaming and the structure of the universe. *MNRAS*, 76:70–84, December 1915. 14

[94] E. Jennings, C. M. Baugh, and S. Pascoli. Modelling redshift space distortions in hierarchical cosmologies. *MNRAS*, 410:2081–2094, January 2011. 23, 76

[95] Elise Jennings, Carlton M. Baugh, Baojiu Li, Gong-Bo Zhao, and Kazuya Koyama. Redshift space distortions in f(R) gravity. *Mon. Not. Roy. Astron. Soc.*, 425:2128–2143, 2012. 55

[96] Donghui Jeong and Eiichiro Komatsu. Perturbation Theory Reloaded II: Non-linear Bias, Baryon Acoustic Oscillations and Millennium Simulation In Real Space. *Astrophys. J.*, 691:569–595, 2009. 75

[97] Einasto J. & Tago E. Joeveer, M. *MNRAS*, 185:357, 1978. 3

[98] Andrew Johnson, Chris Blake, Jason Dossett, Jun Koda, David Parkinson, and Shahab Joudaki. Searching for Modified Gravity: Scale and Redshift Dependent Constraints from Galaxy Peculiar Velocities. *Mon. Not. Roy. Astron. Soc.*, 458(3):2725–2744, 2016. 107

[99] Andrew Johnson, Chris Blake, Jason Dossett, Jun Koda, David Parkinson, and Shahab Joudaki. Searching for modified gravity: scale and redshift dependent constraints from galaxy peculiar velocities. *Monthly Notices of the Royal Astronomical Society*, 458(3):2725–2744, 2016. 127

[100] R. Juszkiewicz. On the evolution of cosmological adiabatic perturbations in the weakly non-linear regime. *Mon. Not. Roy. Astron. Soc.*, 197:931–940, 1981. 28, 37, 45, 105

[101] S. Kahn and collaborators. LSST Optical design. 2014. 4, 104

[102] N. Kaiser. Clustering in real space and in redshift space. *Mon. Not. Roy. Astron. Soc.*, 227:1–27, 1987. 22, 106, 122

[103] N. Kaiser. Clustering in real space and in redshift space. *Mon. Not. Roy. Astron. Soc.*, 227:1–21, July 1987. 58, 114

[104] Alex Kamenev. *Field theory of non-equilibrium systems.* Cambridge University Press, 2011. 44

[105] I. Kant. Allgemeine Naturgeschiche un Theorie de Himmels, nacg Newtonischen Grundsätzen Abgehandelt. *Johann Friederich Petersen*, 1755. 1

[106] R.E. Kass and A.E. Raftery. Bayes factors and model uncertainty. *Petrox, B.N., Caski, F. (Eds.)*, (254), 1993. 129

[107] Eyal A. Kazin et al. The WiggleZ Dark Energy Survey: improved distance measurements to z = 1 with reconstruction of the baryonic acoustic feature. *Mon. Not. Roy. Astron. Soc.*, 441(4):3524–3542, 2014. 107

[108] Oemler A. & Schechter P. Kischner, R. *AJ*, 83:1549, 1978. 3

[109] A. Klypin, G. Yepes, S. Gottlöber, F. Prada, and S. Heß. MultiDark simulations: the story of dark matter halo concentrations and density profiles. *Mon. Not. Roy. Astron. Soc.*, 457:4340–4359, April 2016. 80, 147

[110] Jun Koda, Chris Blake, Florian Beutler, Eyal Kazin, and Felipe Marin. Fast and accurate mock catalogue generation for low-mass galaxies. *Mon. Not. Roy. Astron. Soc.*, 459(2):2118–2129, 2016. 126

[111] E. Komatsu et al. Five-Year Wilkinson Microwave Anisotropy Probe (WMAP) Observations: Cosmological Interpretation. *Astrophys. J. Suppl.*, 180:330–376, 2009. 126

[112] E. Krause et al. Dark Energy Survey Year 1 Results: Multi-Probe Methodology and Simulated Likelihood Analyses. *Submitted to: Phys. Rev. D*, 2017. 105

[113] J. Lambert. Cosmologische Briefe über die Einrichtung des Weltbauses. *Eberhard Kletts*, 1761. 1

[114] G. Lemaître. Un Universe homogène de masse constante et de rayon croissant rendant compte de la vitesse radiale des nébuleuses extra-galactiques. *Annales de la Société Scientifique de Bruxelles*, 47:49–59, 1927. 2

[115] Matthew Lewandowski and Leonardo Senatore. IR-safe and UV-safe integrands in the EFTofLSS with exact time dependence. 2017. 89

[116] Matthew Lewandowski, Leonardo Senatore, Francisco Prada, Cheng Zhao, and Chia-Hsun Chuang. On the EFT of Large Scale Structures in Redshift Space. 2015. 29, 48, 59, 60, 61, 68, 70, 72, 80, 85, 89, 91, 96, 115, 120, 172, 173

[117] P. B. Lilje and G. Efstathiou. Gravitationally induced velocity fields in the universe. I – Correlation functions. *Mon. Not. Roy. Astron. Soc.*, 236:851–864, February 1989. 58, 106, 114

[118] D. N. Limber. The Analysis of Counts of the Extragalactic Nebulae in Terms of a Fluctuating Density Field. *APJ*, 117:134, January 1953. 126

[119] Eric V. Linder. Cosmic growth history and expansion history. *Phys. Rev.*, D72:043529, 2005. 36

[120] Martin Lopez-Corredoira. Alcock-Paczynski cosmological test. *Astrophys. J.*, 781(2):96, 2014. 21

[121] V. N. Lukash, E. V. Mikheeva, and A. M. Malinovsky. Formation of the large-scale structure of the Universe. *Phys. Usp.*, 54:983–1005, 2011. 12

[122] David H. Lyth and Andrew R. Liddle. *The primordial density perturbation: Cosmology, inflation and the origin of structure*. 2009. 15

[123] Nobuyoshi Makino, Misao Sasaki, and Yasushi Suto. Analytic approach to the perturbative expansion of nonlinear gravitational fluctuations in cosmological density and velocity fields. *Phys. Rev.*, D46:585–602, 1992. 28, 37, 38, 45, 100, 105

[124] Takahiko Matsubara. Correlation function in deep redshift space as a cosmological probe. *Astrophys. J.*, 615:573–585, 2004. 15

[125] Takahiko Matsubara. Resumming Cosmological Perturbations via the Lagrangian Picture: One-loop Results in Real Space and in Redshift Space. *Phys. Rev.*, D77:063530, 2008. 29, 50, 51, 59, 70, 100, 106, 115

[126] Patrick McDonald and Arabindo Roy. Clustering of dark matter tracers: generalizing bias for the coming era of precision LSS. *JCAP*, 0908:020, 2009. 25, 105, 107, 111, 123, 148

[127] Joseph E. McEwen, Xiao Fang, Christopher M. Hirata, and Jonathan A. Blazek. FAST-PT: a novel algorithm to calculate convolution integrals in cosmological perturbation theory. *JCAP*, 1609(09):015, 2016. 64

[128] C. McGill. The redshift projection. I – Caustics and correlation functions. *Mon. Not. Roy. Astron. Soc.*, 242:428–438, February 1990. 58, 106, 114

[129] Matthew McQuinn and Martin White. Cosmological perturbation theory in 1+1 dimensions. *JCAP*, 1601(01):043, 2016. 51, 55, 71

[130] R. Mehrem and A. Hohenegger. A Generalisation For The Infinite Integral Over Three Spherical Bessel Functions. *J. Phys.*, A43(45):9, 2010. 97

[131] Rami Mehrem. The plane wave expansion, infinite integrals and identities involving spherical Bessel functions. *Applied Mathematics and Computation*, 217(12):5360–5365, 2011. 97

[132] Lorenzo Mercolli and Enrico Pajer. On the velocity in the Effective Field Theory of Large Scale Structures. *JCAP*, 1403:006, 2014. 30, 32, 43, 46, 47, 48

[133] P. Mészáros. The behaviour of point masses in an expanding cosmological substratum. *Astron. Astrophys.*, 37:225–228, 1974. 35

[134] Mehrdad Mirbabayi, Fabian Schmidt, and Matias Zaldarriaga. Biased Tracers and Time Evolution. *JCAP*, 1507(07):030, 2015. 105

[135] Irshad Mohammed, Uros Seljak, and Zvonimir Vlah. Perturbative approach to covariance matrix of the matter power spectrum. *Mon. Not. Roy. Astron. Soc.*, 2016. 93

[136] F. E. Neumann. *Beiträge zur Theorie der Kugelfuntionen*. Leipzig, 1878. 64

[137] Akira Oka, Shun Saito, Takahiro Nishimichi, Atsushi Taruya, and Kazuhiro Yamamoto. Simultaneous constraints on the growth of structure and cosmic expansion from the multipole power spectra of the SDSS DR7 LRG sample. *Mon. Not. Roy. Astron. Soc.*, 439:2515–2530, 2014. 72

[138] Tomohiro Okamura, Atsushi Taruya, and Takahiko Matsubara. Next-to-leading resummation of cosmological perturbations via the Lagrangian picture: 2-loop correction in real and redshift spaces. *JCAP*, 1108:012, 2011. 51

[139] SKA organisation. Design process. 2013. 4, 104

[140] Enrico Pajer and Matias Zaldarriaga. On the Renormalization of the Effective Field Theory of Large Scale Structures. *JCAP*, 1308:037, 2013. 40, 120

[141] D. Parkinson, S. Riemer-Sørensen, C. Blake, G. B. Poole, T. M. Davis, S. Brough, M. Colless, C. Contreras, W. Couch, S. Croom, D. Croton, M. J. Drinkwater, K. Forster, D. Gilbank, M. Gladders, K. Glazebrook, B. Jelliffe, R. J. Jurek, I.-h. Li, B. Madore, D. C. Martin, K. Pimbblet, M. Pracy, R. Sharp, E. Wisnioski, D. Woods, T. K. Wyder, and H. K. C. Yee. The WiggleZ Dark Energy Survey: Final data release and cosmological results. *PRD*, 86(10):103518, November 2012. 126

[142] J A Peacock. Statistics of Cosmological Density Fields. In Vicent J Martinez, Miguel Portilla, and Diego Saez, editors, *New Insights into the Universe*, volume 408 of *Lecture Notes in Physics*, pages 1–64. Springer, 1992. 106

[143] J. A. Peacock and S. J. Dodds. Reconstructing the linear power spectrum of cosmological mass fluctuations. *Mon. Not. Roy. Astron. Soc.*, 267:1020–1034, 1994. 70, 106, 123

[144] P. Peebles. *APJ*, 196:647, 1975. 2

[145] P. J. E. Peebles. The Effect of a Lumpy Matter Distribution on the Growth of Irregularities in an Expanding Universe. *Astron. Astrophys.*, 32:391, 1974. 42

[146] P. J. E. Peebles. *The large-scale structure of the universe*. 1980. 15

[147] W.D. Penny, K.E. Stephan, A. Mechelli, and K.J. Friston. Comparing dynamic causal models. *NeuroImage*, 22(3):1157 – 1172, 2004. 128

[148] Ashley Perko, Leonardo Senatore, Elise Jennings, and Risa H. Wechsler. Biased Tracers in Redshift Space in the EFT of Large-Scale Structure. 2016. 29, 48, 59, 60, 91, 107, 116, 117, 119, 120, 148, 172, 173

[149] A. A. Plazas, G. M. Bernstein, and E. S. Sheldon. On-Sky Measurements of the Transverse Electric Fields' Effects in the Dark Energy Camera CCDs. *PASP*, 126:750, 2014. 4, 104

[150] J. C. Polkinghorne. *Models of High Energy Processes*. Cambridge Monographs on Mathematical Physics. Cambridge Univ. Press, Cambridge, UK, 2010. 50

[151] Rafael A. Porto, Leonardo Senatore, and Matias Zaldarriaga. The Lagrangian-space Effective Field Theory of Large Scale Structures. *JCAP*, 1405:022, 2014. 28, 49, 106

[152] Francisco Prada, Anatoly A. Klypin, Antonio J. Cuesta, Juan E. Betancort-Rijo, and Joel Primack. Halo concentrations in the standard LCDM cosmology. *Mon. Not. Roy. Astron. Soc.*, 423:3018–3030, 2012. 74, 75, 83, 101

[153] H. Robertson. On relativistic cosmology. *Philosophical Magazin*, 7:5–835, 1928. 2

[154] Shun Saito, Tobias Baldauf, Zvonimir Vlah, UroÅą Seljak, Teppei Okumura, and Patrick McDonald. Understanding higher-order nonlocal halo bias at large scales by combining the power spectrum with the bispectrum. *Phys. Rev.*, D90(12):123522, 2014. 25, 105, 124, 146

[155] Marcel Schmittfull and Zvonimir Vlah. FFT-PT: Reducing the two-loop large-scale structure power spectrum to low-dimensional radial integrals. *Phys. Rev.*, D94(10):103530, 2016. 64

[156] Marcel Schmittfull, Zvonimir Vlah, and Patrick McDonald. Fast large scale structure perturbation theory using one-dimensional fast Fourier transforms. *Phys. Rev.*, D93(10):103528, 2016. 64

[157] G. Schwarz. Estimating the dimension of a model. *Annals of Statistics*, 6(2):461–464, 1978. 128, 129

[158] Roman Scoccimarro. Redshift-space distortions, pairwise velocities and nonlinearities. *Phys. Rev.*, D70:083007, 2004. 38, 58, 92, 106, 115

[159] Roman Scoccimarro, Stephane Colombi, James N. Fry, Joshua A. Frieman, Eric Hivon, and Adrian Melott. Nonlinear evolution of the bispectrum of cosmological perturbations. *Astrophys. J.*, 496:586, 1998. 37, 38

[160] Roman Scoccimarro, H. M. P. Couchman, and Joshua A. Frieman. The Bispectrum as a Signature of Gravitational Instability in Redshift-Space. *Astrophys. J.*, 517:531–540, 1999. 59, 115

[161] Roman Scoccimarro and Josh Frieman. Loop corrections in nonlinear cosmological perturbation theory 2. Two point statistics and selfsimilarity. *Astrophys. J.*, 473:620, 1996. 37, 38, 45, 105

[162] Roman Scoccimarro and Joshua Frieman. Loop corrections in nonlinear cosmological perturbation theory. *Astrophys. J. Suppl.*, 105:37, 1996. 37, 38, 39, 45, 105

[163] Siebers B. Groth E. & Peebles P. Seldner, M. *AJ*, 82:249, 1977. 3

[164] Leonardo Senatore. Bias in the Effective Field Theory of Large Scale Structures. *JCAP*, 1511(11):007, 2015. 25, 105, 111

[165] Leonardo Senatore and Matias Zaldarriaga. Redshift Space Distortions in the Effective Field Theory of Large Scale Structures. 2014. 28, 29, 48, 59, 60, 91, 94, 106, 115, 172

[166] Leonardo Senatore and Matias Zaldarriaga. The IR-resummed Effective Field Theory of Large Scale Structures. *JCAP*, 1502(02):013, 2015. 20, 28, 49, 51, 54, 59, 71, 72, 92, 94, 96, 106, 173

[167] C. Shane, C. & Wirtanen. *Publications Lick Observatory*, 2:part I, 1967. 2

[168] A. Shapley, H. & Ames. *Annals of Harvard College Observatory*, 88:41, 1932. 2

[169] H Shapley. On the existence of external galaxies. *PASP*, 31:261, 1919. 2

[170] Zachary Slepian et al. Detection of baryon acoustic oscillation features in the large-scale three-point correlation function of SDSS BOSS DR12 CMASS galaxies. *Mon. Not. Roy. Astron. Soc.*, 469(2):1738–1751, 2017. 105

[171] V. Slipher. The radial velocity of andromeda nebula. *Lowell Observatory Bulletin*, 2:56, 1913. 1

[172] R. E. Smith, J. A. Peacock, A. Jenkins, S. D. M. White, C. S. Frenk, F. R. Pearce, P. A. Thomas, G. Efstathiou, and H. M. P. Couchmann. Stable clustering, the halo model and nonlinear cosmological power spectra. *Mon. Not. Roy. Astron. Soc.*, 341:1311, 2003. 54

[173] Naonori S. Sugiyama and David N. Spergel. How does non-linear dynamics affect the baryon acoustic oscillation? *JCAP*, 1402:042, 2014. 40, 50, 53

[174] Yasushi Suto and Misao Sasaki. Quasi nonlinear theory of cosmological selfgravitating systems. *Phys. Rev. Lett.*, 66:264–267, 1991. 28, 38, 39, 105

[175] E. Swedenbohr. Principia Rerum Naturalium Sive Novorum Tentaminum Phaenomena Mundi Elementaris Philosophice Explicandi. *Friderici Hekelli*, 2, 1734. 1

[176] Ryuichi Takahashi, Masanori Sato, Takahiro Nishimichi, Atsushi Taruya, and Masamune Oguri. Revising the Halofit Model for the Nonlinear Matter Power Spectrum. *Astrophys. J.*, 761:152, 2012. 54

[177] Atsushi Taruya and Takashi Hiramatsu. A Closure Theory for Non-linear Evolution of Cosmological Power Spectra. *Astrophys. J.*, 674:617, 2008. 92, 106

[178] Atsushi Taruya, Takahiro Nishimichi, and Shun Saito. Baryon Acoustic Oscillations in 2D: Modeling Redshift-space Power Spectrum from Perturbation Theory. *Phys. Rev.*, D82:063522, 2010. 51, 71, 85, 91, 92, 106, 145, 173

[179] Atsushi Taruya, Takahiro Nishimichi, Shun Saito, and Takashi Hiramatsu. Nonlinear Evolution of Baryon Acoustic Oscillations from Improved Perturbation Theory in Real and Redshift Spaces. *Phys. Rev.*, D80:123503, 2009. 92

[180] Svetlin Tassev, Matias Zaldarriaga, and Daniel Eisenstein. Solving Large Scale Structure in Ten Easy Steps with COLA. *JCAP*, 1306:036, 2013. 107, 126

[181] A. N. Taylor. Statistics of self-gravitating fluctuations. In F. Bouchet and M. Lachieze-Rey, editors, *Cosmic Velocity Fields*, page 585, 1993. 50

[182] A. N. Taylor and A. J. S. Hamilton. Non-linear cosmological power spectra in real and redshift space. *Mon. Not. R. Astron. Soc.*, 282:767–778, October 1996. 50

[183] M. Tegmark and collaborators. *ApJ*, 606:702, 2004. 22

[184] Jean-Philippe Uzan. The big-bang theory: construction, evolution and status. 2016. 4

[185] H. E. S. Velten, R. F. vom Marttens, and W. Zimdahl. Aspects of the cosmological "coincidence problem". *Eur. Phys. J.*, C74(11):3160, 2014. 5

[186] Licia Verde. A practical guide to Basic Statistical Techniques for Data Analysis in Cosmology. 2007. 127

[187] E. T. Vishniac. Why weakly non-linear effects are small in a zero-pressure cosmology. *Mon. Not. Roy. Astron. Soc.*, 203:345–349, 1983. 28, 37, 45, 105

[188] Zvonimir Vlah, Uroš Seljak, Man Yat Chu, and Yu Feng. Perturbation theory, effective field theory, and oscillations in the power spectrum. *JCAP*, 1603(03):057, 2016. 20, 28, 51, 52, 55, 92, 106, 173

[189] Zvonimir Vlah, Martin White, and Alejandro Aviles. A Lagrangian effective field theory. *JCAP*, 1509(09):014, 2015. 20, 28, 51, 52, 54, 55, 71, 106, 120

[190] Robert M Wald. *General relativity*. Chicago Univ. Press, Chicago, IL, 1984. 9

[191] Xin Wang and Alex Szalay. Resummed Perturbation Theory of Galaxy Clustering. *Phys. Rev.*, D86:043508, 2012. 105

[192] Stefan Weinzierl. The Art of computing loop integrals. In *Universality and renormalization: From stochastic evolution to renormalization of quantum fields. Proceedings, Workshop on 'Percolation, SLE and related topics', Toronto, Canada, September 20-24, 2005, and Workshop on 'Renormalization and universality in mathematical physics', Toronto, Canada, October 18-22, 2005*, pages 345–395, 2006. 62

[193] Mark B. Wise. Non-Gaussian Fluctuations. *NATO Sci. Ser. C.*, 219:215–238, 1988. 37, 42, 45

[194] T. Wright. An original theory or new hypothesis of the universe. *H. Chapelle*, 1750. 1

[195] Kazuhiro Yamamoto, Takahiro Sato, and Gert Huetsi. Testing general relativity with the multipole spectra of the SDSS luminous red galaxies. *Prog. Theor. Phys.*, 120:609–614, 2008. 72

[196] Donald G. York et al. The Sloan Digital Sky Survey: Technical Summary. *Astron. J.*, 120:1579–1587, 2000. 3

[197] Joe Zuntz, Marc Paterno, Elise Jennings, Douglas Rudd, Alessandro Manzotti, Scott Dodelson, Sarah Bridle, Saba Sehrish, and James Kowalkowski. CosmoSIS: Modular Cosmological Parameter Estimation. *Astron. Comput.*, 12:45–59, 2015. 100

[198] Herzog E. & Wild P. Zwicky, F. Catalogue of galaxies and cluster of galaxies. *Pasadena: California Institute of Technology*, pages 1961–1968, 1968. 2